

Towards Predictive Simulations of Low-Emission Reactive Solid Fuel Systems

Vom Fachbereich Maschinenbau
an der Technischen Universität Darmstadt
zur
Erlangung des Grades eines Doktor-Ingenieurs (Dr.-Ing.)
genehmigte

D i s s e r t a t i o n

vorgelegt von

Hendrik Nicolai, M.Sc.

aus Wilhelmshaven

Berichterstatter:	Prof. Dr.-Ing. Johannes Janicka
Mitberichterstatter:	Prof. Dr. Luc Vervisch
Mitberichterstatter:	Prof. Dr.-Ing. Christian Hasse
Tag der Einreichung:	17.08.2021
Tag der mündlichen Prüfung:	16.11.2021

Darmstadt 2021

D17

Nicolai, Hendrik: *Towards Predictive Simulations of Low-Emission Reactive Solid Fuel Systems*

Darmstadt, Technische Universität Darmstadt,

Jahr der Veröffentlichung der Dissertation auf TUprints: 2022

URN: urn:nbn:de:tuda-tuprints-210797

Tag der mündlichen Prüfung: 16.11.2021

Veröffentlicht unter CC-BY-NC 4.0 International

<https://creativecommons.org/licenses/>

Hiermit erkläre ich, dass ich die vorliegende Arbeit, abgesehen von den in ihr ausdrücklich genannten Hilfen, selbständig verfasst habe. Ich erkläre außerdem, dass ich bisher noch keinen Promotionsversuch unternommen habe.

Hendrik Nicolai

Darmstadt, den 17. August 2021

Preface

This thesis originates from my work as doctoral candidate at the former Institute for Energy and Power Plant Technology (EKT) at the Technische Universität Darmstadt. First of all, I would like to thank the head of the institute Prof. Dr.-Ing. Johannes Janicka for this opportunity and his confidence in my work. I very much appreciate the freedom he gave me in carrying out my work.

Furthermore, I would like to thank Prof. Dr.-Ing. Christian Hasse not only for reporting on this work but also for many fruitful discussion and cooperations. His encouraging attitude and scientific contribution helped me a lot in accomplishing this work.

I am sincerely grateful to Prof. Dr. Luc Vervisch for his willingness to report on this thesis. Due to his outstanding accomplishments in research and teaching, his interest in my work is a great honor for me.

I would also like to thank my scientific co-workers at the EKT, RSM and STFS, many of whom I call friends. I am much obliged to Dr.-Ing. Guido Künne and Dr.-Ing. Sebastian Ganter for supervising my master thesis in an exemplary fashion and helping me enter the subject matter. Furthermore, I want to thank the remaining members of the former FASTEST group Dr.-Ing. Arne Heinrich, Dr.-Ing. Flavia Calvanti and Dr.-Ing. Robert Knappstein for many helpful discussions. I am also deeply grateful for the companionship with my (former) colleagues and office mates Dennis Kütemeier, Wibke Leudesdorff, Dr.-Ing. Steffen Salenbauch, Dr.-Ing. Martin Pollack, Dr. Xu Wen, Dr. Paulo Debiagi, Johannes Trabold, Dr.-Ing. Sebastian Popp, and Dr.-Ing. Louis Dressler. Also, due to their great character and personality, it was a pleasure to work with them and got to know them as friends. In addition, I would like to thank the five last-named for proofreading and commenting on this manuscript.

For the excellent collaboration with the experimentalists, I would like to thank Henrik Schneider, Christopher Geschwindner, Dr.-Ing. Tao Li, Dr.-Ing. Jan Köser, Dr.-Ing. Benjamin Böhm and Prof. Dr. habil. Andreas Dreizler. They provided valuable insight into the experiments and measurement technologies and thereby contributed to the progress of this work.

Further, I would like my dear parents Helmo and Katrin, for their patience, support and encouragement during this time.

Darmstadt, August 2021

Hendrik Nicolai

Abstract

The increasing worldwide energy demand presents a strong contrast to the required CO₂ reduction to limit global warming. Although renewable energy sources are developing rapidly, fossil solid fuels are expected to still play an essential role in worldwide electricity production in the foreseeable future. Therefore, the decarbonization of the power sector presents a major task for reducing industrial emissions. For this purpose, carbon capture, utilization and storage is considered a key technology for carbon-neutral power generation. Among the possible carbon capture procedures, the oxy-fuel process is one promising technology for rapid CO₂ cutbacks. In the oxy-fuel process, the nitrogen fraction of air is substituted by the much more chemically reactive and radiation-absorbing molecules CO₂, resulting in significant changes in the combustion characteristics. One major advantage of oxy-fuel processes is that flue gases consist almost entirely of CO₂ facilitating its utilization and storage. To exploit the high potential of retrofitting existing plants for applying the oxy-fuel process, comprehensive simulation tools that can accurately predict such systems are required.

Considering the combustion part of the oxy-fuel process, three main modeling pillars can be identified: 1) turbulent mixing and heat transfer, 2) turbulent chemistry interactions, and 3) solid fuel kinetics. Due to the strong coupling of all these processes, the weakest model determines the overall error. Hence, all three modeling pillars must be addressed adequately to contribute to an efficient and predictive holistic model for simulating pulverized solid fuel combustion in air and oxy-fuel conditions. In this work, Large-Eddy Simulation with a detailed chemical description of the gas phase using flamelet-based chemistry tables accounts for the first two pillars. With respect to solid fuel kinetics, besides state-of-the-art coal conversion models, a recently developed seamless multi-step mechanism is used to describe the particle conversion.

A series of different configurations with increasing size and complexity are investigated to validate the developed modeling strategies. First, investigations of particle groups in a laminar flow reactor enable detailed analyses of the ignition and combustion process. Subsequently, at the laboratory burner scale, investigations focus on flame stabilization in complex turbulent flows. Finally, in a pilot-scale burner, the investigation of the overall conversion process is carried out. This step-wise increase of complexity allows for a seamless validation of models under practical relevant conditions. Furthermore, the validated numerical simulations are used to gain new insights into the complex coupled phenomena occurring during solid fuel combustion in an oxy-fuel atmosphere.

Kurzfassung

Der weltweit steigende Energiebedarf steht im starken Kontrast zu der erforderlichen CO₂-Reduzierung zur Begrenzung der globalen Erwärmung. Obwohl erneuerbare Energiequellen sich rasant entwickeln, werden feste fossile Brennstoffe in absehbarer Zukunft weiterhin von Wichtigkeit sein. Daher spielt die Dekarbonisierung des Energiesektors eine wichtige Rolle bei der Verringerung der Industrieemissionen. Hierfür ist die Kohlenstoffabscheidung und -speicherung eine Schlüsseltechnologie. Unter den möglichen Verfahren zur Kohlenstoffabscheidung stellt das Oxyfuel-Verfahren eine der aussichtsreichen Technologien für schnelle CO₂-Einsparungen dar. Beim Oxyfuel-Verfahren wird der Stickstoffanteil der Luft durch CO₂ ersetzt, was zu erheblichen Veränderungen der Verbrennungseigenschaften führt. Ein Vorteil des Verfahrens ist, dass die Abgase fast vollständig aus CO₂ bestehen, was dessen Nutzung und Speicherung erleichtert. Um das große Potenzial der Nachrüstung bestehender Anlagen für das Oxyfuel-Verfahren zu nutzen, sind detaillierte Simulations-Werkzeuge erforderlich, die eine genaue Vorhersage solcher Systeme ermöglichen.

Betrachtet man den Verbrennungsteil des Oxy-Fuel-Prozesses, so lassen sich drei Hauptsäulen für die Modellierung identifizieren: 1) Turbulente Mischung und Wärmeübertragung, 2) Turbulenz Chemie Interaktion und 3) Kinetik des festen Brennstoffes. Aufgrund der starken Kopplung aller Prozesse wird der Gesamtfehler durch das schwächste Modell bestimmt. Daher müssen alle drei Modellierungssäulen angemessen berücksichtigt werden, um zu einem effizienten und prädiktiven ganzheitlichen Modell für die Verbrennung fester Brennstoffe beizutragen. In dieser Arbeit werden die ersten beiden Säulen durch die Large-Eddy-Simulation, gekoppelt mit einer detaillierten Beschreibungen der Gasphasen Chemie mittels eines Flamelet-basierten Modells, abgedeckt. In Bezug auf die Brennstoffkinetik wird neben Standardmodellen insbesondere eine kürzlich entwickelte nahtlose mehrstufigen Kinetik zur Beschreibung der Partikelumwandlung verwendet.

Eine Reihe verschiedener Konfigurationen mit zunehmender Größe und Komplexität werden untersucht, um die entwickelten Modellierungsstrategien zu validieren. Als erster Schritt ermöglicht die Untersuchung von einzelnen Partikeln und Partikelgruppen in einem Reaktor mit laminarer Strömung detaillierte Analysen des Zündungs- und Verbrennungsprozesses. Anschließend konzentrieren sich die Untersuchungen an einem Brenner im Labormaßstab auf die Flammenstabilisierung in komplexen, turbulenten Strömungen. Abschließend wird am Pilotbrenner der gesamte Umwandlungsprozess untersucht. Diese schrittweise Erhöhung der Komplexität ermöglicht eine nahtlose Validierung der Modelle unter praxisrelevanten Bedingungen. Darüber hinaus werden die validierten Simulationen genutzt, um neue Einblicke in die komplexen gekoppelten Phänomene zu gewinnen, die bei der Verbrennung fester Brennstoffe in einer Oxyfuel-Atmosphäre auftreten.

Contents

1. Introduction	1
1.1. Background and Motivation of this Work	1
1.2. State of Research	3
1.3. Aims and Scope of this Work	6
1.4. Structure of this Work	7
2. Mathematical Description and Modeling of Turbulent Reacting Multi-Phase Flows	8
2.1. Governing Equations for Single-Phase Reactive Flows	8
2.1.1. Conservation of Mass	8
2.1.2. Conservation of Momentum	9
2.1.3. Species Transport	9
2.1.4. Energy Balance	10
2.1.5. Equation of State	10
2.1.6. Closure of the Chemical Source Term	11
2.2. Turbulence	12
2.2.1. Numerical Treatment	14
2.2.1.1. Direct Numerical Simulation	15
2.2.1.2. Reynolds Averaged Description	15
2.2.1.3. Large-Eddy Simulation	16
2.3. Multi-Phase Flows	18
2.3.1. Modeling of the Disperse Phase	19
2.3.2. Particle Movement	20
2.3.3. Particle Temperature	21
2.3.4. Interaction with the Gaseous Phase	22
2.4. Thermal Radiation	23
2.4.1. Fundamentals of Thermal Radiation	23
2.4.2. Modeling Thermal Radiation	26
2.4.2.1. RTE in Participating Media	26
2.4.2.2. Radiative Properties	27
2.4.2.3. Turbulence-Radiation-Interaction (TRI)	28
3. Numerical Treatment of Turbulent Flames	30
3.1. Properties of Premixed and Non-Premixed Flames	31
3.1.1. Premixed Laminar Flame Characteristics	31
3.1.2. Non-Premixed Laminar Flame Characteristics	34
3.2. Flamelet-based Tabulation Methods for Turbulent Flames	36
3.3. Flamelet Modeling for PCC	36
3.4. Turbulent Premixed Combustion Modeling	39
3.4.1. Flamelet Generated Manifolds (FGM)	39
3.4.2. Extension for Solid Fuel Combustion	41

3.4.3.	Artificial Thickened Flame Approach	42
3.4.3.1.	Theory	42
3.4.3.2.	Modeling Unresolved Wrinkling	43
3.4.3.3.	Dynamic Thickening	44
3.4.3.4.	Grid and Mixture Adaptive Thickening	45
3.4.4.	Summary Turbulent Premixed Combustion Modeling	46
3.5.	Turbulent Non-Premixed Combustion Modeling	46
3.5.1.	Flamelet Progress Variable Model (FPV)	46
3.5.2.	Extensions for Solid Fuel Combustion	48
3.5.3.	Presumed Probability Density Function Modeling	49
3.5.4.	Summary Turbulent Non-Premixed Combustion Modeling	51
4.	Numerical Treatment of Solid Fuels	53
4.1.	Characterization of Solid Fuels	53
4.2.	Coal Conversion Process	55
4.2.1.	Physical and Chemical Processes: Pyrolysis	56
4.2.2.	Physical and Chemical Processes: Char Conversion	57
4.3.	Modeling of Coal Conversion	58
4.3.1.	Modeling Pyrolysis	58
4.3.1.1.	Empirical Pyrolysis Models	59
4.3.1.2.	Network Pyrolysis Models	60
4.3.1.3.	Chemical Percolation Devolatilization (CPD) Model	60
4.3.2.	Modeling Char Conversion	62
4.3.3.	CRECK-S - Comprehensive Model for Coal Conversion	64
4.4.	Coupling of Solid Fuel Kinetics to the Gas Phase	68
4.4.1.	Indirect Coupling by Simplified Kinetics to CFD	69
4.4.2.	Direct Coupling Detailed Kinetics to CFD	69
4.4.3.	Particle Source Terms for the Gas-phase Equation	72
4.5.	Interaction of Radiation with Solid Fuel Particles	73
4.5.1.	Radiative Properties of Particle Clouds	74
4.5.2.	Scattering Phase Function	75
5.	Numerical Implementations and Verifications	76
5.1.	Carrier Phase Treatment	77
5.1.1.	Finite Volume Discretization of the Transport Equation	77
5.1.2.	Approximations of the Convective Flux	78
5.1.3.	Approximations of the Diffusive Flux	79
5.1.4.	Time Discretization	80
5.1.5.	Pressure Correction	81
5.1.6.	Boundary Conditions	82
5.2.	Treatment of the Disperse Phase	83
5.2.1.	Continuous Phase State at the Particle Position	83
5.2.2.	Temporal Integration Method	83
5.2.3.	Determination of the Particle Grid Position	85
5.2.4.	Euler Source Term	86
5.2.5.	Verification of the Particle-Gas Phase Coupling	87
5.2.6.	Solid Chemistry Treatment	90
5.2.7.	Verification of Solid Fuel Kinetics	90
5.3.	Radiation	92

5.4. Overall Solution Procedure	94
6. Applications	96
6.1. Laminar Flow Reactor [164]	97
6.1.1. Configuration and Boundary Conditions	98
6.1.2. Numerical Model	98
6.1.3. Results and Discussion	100
6.1.3.1. Validation Against Experiment	101
6.1.3.2. Analysis of Heat Transfer Mechanisms	103
6.1.4. Model Sensitivities for Predicting Ignition Delay Times	104
6.1.5. Section Summary	106
6.2. Laboratory-Scale Gas-Assisted Oxy-Coal Swirl-Combustor [163]	107
6.2.1. Configuration and Boundary Conditions	107
6.2.2. Numerical Model	109
6.2.3. Results and Discussion	110
6.2.3.1. Single-Phase Non-Reactive Case (SPNR)	110
6.2.3.2. Single-Phase Reactive Case (SPR)	112
6.2.3.3. Two-Phase Reactive Cases	115
6.2.4. Section Summary	121
6.3. Self-Sustained Oxy-Coal Swirl-Combustor [165]	122
6.3.1. Configuration and Boundary Conditions	122
6.3.2. Numerical Model	124
6.3.3. Results and Discussion	125
6.3.4. Section Summary	137
6.4. Adapted Self-Sustained Oxy-Coal Swirl-Combustor [162]	139
6.4.1. Configuration and Boundary Conditions	139
6.4.2. Numerical Model	139
6.4.3. Results and Discussion	141
6.4.3.1. Validation	143
6.4.3.2. Assessment of the Effects of Solid Fuel Kinetics	148
6.4.4. Section Summary	155
7. Summary and Outlook	156
Bibliography	159
A. Grid Sensitivity of the Uniform Source Term Distribution	186
B. RMS Statistics of Laboratory-Scale Burner	187
C. Influence of the Grid Resolution	191
D. Influence of Radiation	192

Nomenclature

Some variables which are exclusively used locally are not included in this nomenclature. Units which arise from a local context are denoted by \mathcal{U} .

Upper case latin letters		Unit
L	Labile bridges	-
L^*	Reactive intermediate species	-
\mathcal{E}	Efficiency function	-
\mathcal{F}	Thickening of the ATF model	m
\mathcal{G}	Spatial filtering operator	$1/\text{m}^3$
\mathcal{L}	Characteristic length scale	m
\mathcal{P}_{TKE}	Production of the turbulent kinetic energy	m^2/s^3
\mathcal{R}	Ideal gas constant	J/K mol
\mathcal{X}_k	Symbol for species k	-
A_{fr}	Preexponential constant of the Arrhenius law	\mathcal{U}
b	Temperature exponent of the Arrhenius law	-
C	General constant	-
C_P	Projected surface area of the particles	m^2
C_S	Smagorinsky coefficient	-
C_{diff}	Diffusion coefficient	$\text{m}/(\text{s K}^{0.75})$
D_{prt}	Particle diameter	m
D_{ij}	Diffusion coefficient of the species i in the species j	m^2/s
D_i	Mixture-averaged diffusion coefficient of species i	m^2/s
E_A	Activation energy	J/mol
F_i^{D}	Drag force into direction i	$\text{kg m}/\text{s}^2$
F_i^{G}	Gravity force into direction i	$\text{kg m}/\text{s}^2$
G	Incident radiation	W/m^3
I	Total radiative intensity	$\text{W}/(\text{m}^2 \text{sr})$
I_{λ_w}	Spectral radiative intensity	$\text{W}/(\text{m}^3 \text{sr})$
$I_{b\lambda_w}$	Spectral blackbody intensity	$\text{W}/(\text{m}^3 \text{sr})$
k_r	Absorptive index	-
L	Characteristic length scale	m
l_m	Mixing length (Prandtl's mixing-length hypothesis)	m
m_r	Complex index of refraction	-
N_{CV}	Number of control volumes	-
N_{GG}	Number of gray gases	-
N_{prt}	Number of particles	-
N_s	Number of species	-
N_r	Number of reactions	-
$Q_{\text{sca}}, Q_{\text{abs}}, Q_{\text{ext}}$	Efficiency factors for scattering, absorption, and extinction	-
R_{diff}	Diffusion rate coefficient	1/s
R_{reac}	Reaction rate coefficient	1/s
S_{rad}	Radiative source term	$\text{J}/\text{m}^3\text{s}$

Nomenclature

$S_{\text{prt},\Phi}$	Particle source term for gas-phase quantity Φ	\bar{U}
S_{ij}	Rate of strain	1/s
T	Temperature	K
U	Characteristic velocity	m/s
V	General Volume	m^3
V_{prt}	Volume particle	m^3
V_F	Filtering volume	m^3
$V_{k,i}$	Diffusion velocity of the component k into direction i	m/s
W	Mean molar mass of the mixture	kg/mol
W_k	Molar mass of the species k	kg/mol
X_k	Mole fraction of the species k	m/s
Y_{vol}	Volatile mass fraction	-
Y_k	Mass fraction of species k	-
Z	Mixture fraction	-
Lower case latin letters		Unit
\mathcal{Y}	Reaction progress variable	-
a_{HG}	Shape parameter for the Henyey-Greenstein phase function	-
a_n	Weighting factors of gray gas model	-
b_c	Coupling function	-
c	Speed of sound	m/s
c_C	Charred bridge	-
c_l	Speed of light	m/s
c_D	Drag coefficient	-
c_p	Specific heat capacity of the mixture at constant pressure	J/kg K
c_k	Molar concentration of the species k	mol/ m^3
$c_{p,k}$	Specific heat capacity of the species k at constant pressure	J/kg K
E	Total emissive power	W/(m^2 sr)
E_{λ_w}	Spectral emissive power	W/(m^3 sr)
E_{b,λ_w}	Spectral blackbody emissive power	W/(m^3 sr)
g	Acceleration of gravity into direction i	m/s^2
g_1, g_2	Light non-condensable gas	-
g_{HG}	Asymmetry parameter for the Henyey-Greenstein phase function	-
h	Specific enthalpy of the mixture	J/kg
h_{Pl}	Planck's constant	J s
h_k	Specific enthalpy of the species k	J/kg
h_s	Sensible enthalpy of the mixture	J/kg
k	Rate coefficient	\bar{U}
l	General length	m
l_I	Integral length scale	m
l_s	Characteristic system length scale	m
m_k	Mass of the species k	kg
n_r	Refraction index	-
p	Pressure	$\text{kg/s}^2\text{m}$
q_{rad}	Radiative heat flux	W/(m^2)
q_j	Enthalpy flux into direction j	J/ m^2s
$r_{\text{fr}}, r_{\text{br}}$	Reaction rate of the forward and backward reaction	mol/ m^3s
r_{pore}	Pore radius	m
s_T	Turbulent flame speed	m/s

s_i	Unit directional vector in direction i	-
s_l	Laminar flame speed	m/s
u_i	Velocity (into direction i)	m/s
u_i	Velocity (into direction i)	m/s
u_{blow}	Homogeneous devolatilization velocity	m/s
x_i	Cartesian coordinate	m
s	Coordinate in the flame reference frame	m
Upper case greek letters		Unit
$\Delta h_{f,k}^{\text{ref}}$	Enthalpy of formation of the species k	J/kg
Δ_t	Time interval	s
Δ_t	Time step size	s
Δ_t	Time step size	s
Δ_x	Grid size (also Δ_y or Δ_z if direction is relevant)	m
$\Delta_{R,H}$	Reaction enthalpy	J/kg
Δh_{reac}	Heat release by particle reaction	J/s
Γ	General diffusion coefficient	\bar{U}
Ω	Flame sensor	-
Ω_S	Solid angle	sr
Φ	General scalar	\bar{U}
Φ	Thermo-chemical space variables	\bar{U}
Φ_η	Scattering phase function	-
Π	General particle property	\bar{U}
Ψ	Azimuthal angle	sr
Ψ_{char}	The ration of CO to CO ₂ in char off-gas	-
Ψ_{char}	The ration of CO to CO ₂ in char off-gas	-
Θ	Polar angle	sr
Ξ	Wrinkling factor	-
L	General surface	m ²
Lower case greek letters		Unit
α	Heat transfer coefficient	J/m ² Ks
α_1, α_2	Stoichiometric coefficients for the C2SM model	-
α_c	Continuous phase volume fraction	-
α_d	Disperse phase volume fraction	-
β_α	Weighting factor of the coupling function for element α	-
χ	Scalar dissipation rate	s ⁻¹
δ_{SC}	Side chains	-
δ_φ	Flame thickness based on maximum gradient of φ	m
δ_{ij}	Kronecker-symbol	-
$\delta_{\omega,\text{FWHM}}$	Flame thickness based on the FWHM of the source term	m
$\dot{\omega}_k$	Chemical source term of the species k	kg/m ³ s
ϵ_η	Emissivity	-
ϵ_{TKE}	Dissipation of the turbulent kinetic energy	m ² /s ³
ϵ_w	Angular Frequency of a electromagnetic wave	1/m
η	Effectiveness factor	-
η	Wavenumber of a electromagnetic wave	1/m
η_K	Kolmogorov length scale	m
κ	Wave number (in the energy spectrum)	1/m
κ_η	Absorption coefficient	1/m

Nomenclature

λ	Thermal conductivity	W/m K
λ_w	Wavelength of a electromagnetic wave	m
λ_m	Mean free path length	m
μ	Dynamic viscosity	kg/s m
ν	Kinematic viscosity	m ² /s
ν_k''	Stoichiometric coefficient of species k on the product side	-
ν_k'	Stoichiometric coefficient of species k on the reactant side	-
ν_w	Frequency of a electromagnetic wave	1/s
ν_t	Turbulent kinematic viscosity	m ² /s
ω_w	Angular Frequency of a electromagnetic wave	1/m
$\bar{\rho}_c$	Apparent density continuous phase	kg/m ³
$\bar{\rho}_d$	Apparent density disperse phase	kg/m ³
ρ	Density of the mixture	kg/m ³
σ_{SB}	Stefan-Botzmann constant	W/(m ² K ⁴)
$\sigma_{s,\eta}$	Scattering coefficient	1/m
τ	General time scale	s
τ_η	Transmissivity	-
τ_{rad}	Optical thickness	-
τ_{ij}	Components of the viscous stress tensor	kg/s ² m
φ	Thiele number	-
φ_{char}	Ratio of enlarged reactive surface area	-
ζ	Coordinate in the context of the ATF model	m
m_c	Mass of continuous phase	kg
m_d	Mass of disperse phase	kg

Indices

\cdot'	Temporal fluctuation
\cdot_0	Initial value at $t = 0$
\cdot_{Cl}	Cluster
\cdot_{cross}	Crosslinking
\cdot_{fl}, \cdot_{rfl}	Lean and rich flammability limit
\cdot_{meta}	Metaplast
\cdot_{prt}	Particle
\cdot_{REF}	Reference conditions ($T = 298.15$ K, $p = 101\,325$ Pa)
\cdot_{RMS}	Temporal standard deviation (root mean square)
\cdot_b	State in the burnt gas
\cdot_u	State in the unburnt gas
\cdot_{sgs}	Subgrid-scale
$^{13}C-NMR$	Carbon-13 (C13) nuclear magnetic resonance

Operators

$\langle \cdot \rangle$	Temporal average
$\bar{\cdot}$	Spatial (LES) filter
$\tilde{\cdot}$	Density weighted spatial filter

Dimensionless number

Bi_m	Mass transfer Biot number
Da	Damkoehler number
Kn	Knudsen number
Le_k	Lewis number of the species k
Ma	Mach number

Nu_{prt}	Nusselt number
Pr	Prandtl number
Re	Reynolds number
Re_{blow}	Blowing Reynolds number
Re_{prt}	Particle Reynolds number
Sc	Schmidt number
Sc_t	Turbulent Schmidt number
St	Stokes number

Abbreviations

ATF	Artificial thickened flame
BDF	Backward differentiation formulation
C1	Columbian bituminous coal Norte
C2SM	Competing Two Step model
CDS	Central differential scheme
CFD	Computational fluid dynamics
CPD	Chemical Percolation Devolatilization
CPU	Central processing unit
CRECK	Chemical Reaction Engineering and Chemical Kinetics Lab
DAE	Distributed activation energy
daf	Dry and ash free
DNS	Direct Numerical Simulation
FC	Fixed carbon
FDF	Filtered probability density function
FG-DVC	Functional Group-Depolymerization, Vaporization and Crosslinking
FGM	Flamelet generated manifold
FLASHCHAIN	Flash-Distillation Chain-Statistics
FPI	Flame prolongation of ILDM
FPV	Flamelet progress variable model
FVM	Finite volume method
FWHM	Full width at half maximum
ILDM	Intrinsic low-dimension manifolds
ILU	Incomplete lower and upper matrix decomposition
LBL	Line-by-line
LDV	Laser doppler velocimetry
LES	Large Eddy Simulation
LSODE	Livermore Solver for Ordinary Differential Equations
MPI	Message passing interface
OTFA	Optically thin fluctuation assumption
PCC	Pulverized coal combustion
PDE	Partial differential equation
PDF	Probability density function
PIV	Particle image velocimetry
PSD	Particle size distribution
PVM	Proximate volatile matter
RANS	Reynolds averaged Navier Stokes
RL	Rhenish lignite
RTE	Radiative transport equation
SFOR	Single first order reaction model

Nomenclature

SIMPLE	Semi-Implicit Method for Pressure Linked Equations
TCI	Turbulence chemistry interaction
TRI	Turbulence-Radiation-Interactions
TVD	Total variation diminishing
URANS	Unsteady Reynolds averaged Navier Stokes
WSGG	Weighted sum of gray gases

1. Introduction

This work addresses the modeling and simulation of pulverized solid fuel combustion. In the following, the global background leading to the motivation of this work is given. Subsequently, the current state of research with respect to numerical simulation of solid fuels is briefly covered. After that, the specific aims of this work are derived, followed by the structure of this thesis.

1.1. Background and Motivation of this Work

Over the last decades, the world's primary energy demand continuously rose from 5.5 Gtoe¹ in 1971 to 14.3 Gtoe in 2018 [97]. In 2020, the global pandemic and the resulting economic crisis lead to the first significant decrease in energy demand in modern history. However, as the world economy recovers again, the energy demand has already reached pre-pandemic levels. Moreover, it is expected that the energy demand will increase to 17.7 Gtoe in 2040 (+23.8%) according to the *International Energy Agency* (IEA) [97]. This increase will result mainly from developing and emerging countries, such as China and India ($\approx 55\%$ of the increase).

In 2019, out of all produced energy, one of the most significant shares represents burning fossil fuels such as coal. Coal had a share of about 22% of the total primary energy production, right behind oil (30%) and natural gas (25%) [17]. Although renewable energy sources are developing rapidly, coal-fired power plants are expected to still play an essential role in worldwide electricity production in the foreseeable future because coal reserves are more abundant than other fossil fuels [97].

However, the extraction of coal, its conversion for energy production, and the release of byproducts are all associated with adverse effects on health and the environment, including climate change [270]. More specifically, coal conversion represents one of the most significant anthropogenic energy-related sources of carbon dioxide (about 42-44%) emissions in the world [97]. In order to limit global warming to 1.5 °C as set in *The Paris Agreement* [243], a reduction of the global CO₂ emissions from 42 Gt per year in 2017 to roughly 20 Gt per year in 2030 and net-zero by 2055 is required according to the *Intergovernmental Panel on Climate Change* (IPCC) [99]. However, these required CO₂ reductions are in strong contrast to previously discussed increasing primary energy demand predicted by the IEA [97]. Therefore, the IPCC defines four major tasks, tackling the reduction of CO₂ emissions: lowering energy demand, electrifying energy services, decarbonizing the power sector, and decarbonizing non-electric fuel use in energy end-use sectors [99].

Out of these four major tasks stated by the IPCC, this thesis focuses on field of the **decarbonization of the power sector**. For this purpose, carbon capture, utilization and storage (CCUS) presents a key technology for carbon-neutral power generation. Consequently, it is listed as one of the fourteen *Grand Challenges of Engineering by the United States National Academy of Engineering* [159]. Out of the possible carbon capture procedures (pre-combustion or post-combustion, oxy-fuel, chemical looping), the focus is on the oxy-fuel process and, more specifically, on its influence on combustion. In the oxy-fuel process, the nitrogen fraction of air is substituted by the much more chemically reactive and radiation-absorbing molecules CO₂ and

¹tonne oil equivalent (toe)

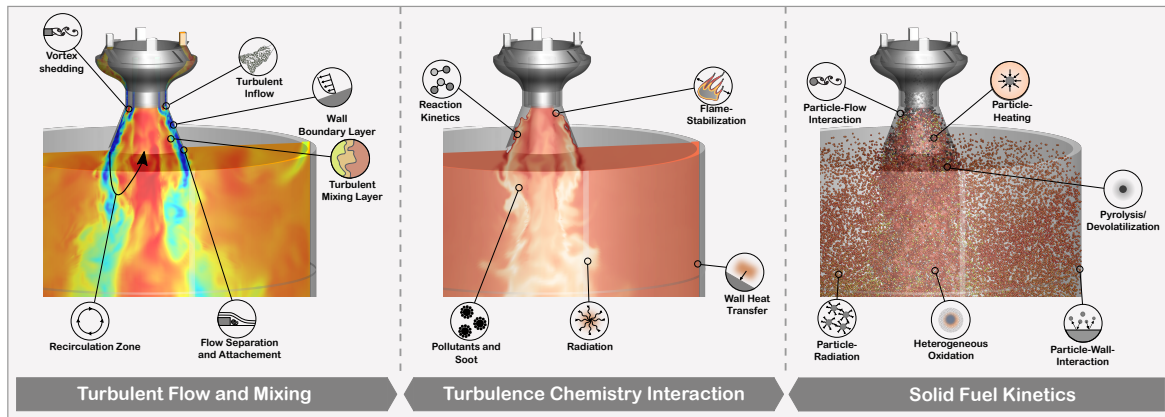


Figure 1.1.: Schematic representation of the physical processes inside a solid fuel combustion chamber [161].

H_2O . Hence, an oxy-fuel atmosphere consists mainly of CO_2 , H_2O and O_2 in the combustion zone resulting in significant changes of the combustion characteristics [29]. One major advantage of oxy-fuel processes is that flue gases consist almost entirely of CO_2 , which facilitates their utilization and storage. Furthermore, a second advantage is a high potential of retrofitting existing plants for the application of the oxy-fuel process, enabling prompt and rapid CO_2 cutbacks.

However, reaction rates, transport processes in the gas phase, and radiative heat transfer are fundamentally influenced by the oxy-fuel process [29]. Hence, the design and development of oxy-fuel technologies require advanced, comprehensive tools that can accurately predict the performance and emissions of such systems [29; 47]. Furthermore, the effective and reliable design of large-scale oxy-fuel combustion systems requires a profound understanding of the relevant chemical and physical processes over various scales: from single molecular reactions over the particle-scale up to the entire combustion chamber.

Gaining this profound understanding purely by experimental investigations is very challenging in pulverized coal combustion (PCC) due to limited optical access. Therefore, numerical simulations and especially 3D-Computational Fluid Dynamics (CFD), can provide insights into the reaction and transport processes in the solid and gaseous phases [50]. In combination with experiments, 3D-CFD simulations enable a deep understanding of oxy-fuel coal combustion at various scales, i.e., from processes on the single-particle scale over particle groups up to reactors on the pilot and industrial scale. Thereby, different experimental and numerical methods can be systematically combined, e.g., detailed measurements of solid kinetics enable the development of suitable submodels that are coupled to CFD simulations of large-scale reactors [86]. The simulations predictive power depends significantly on the quality of the submodels and their interaction, resulting in the total error being determined by the weakest model. Thus, special care must be taken to ensure that each subprocess is modeled with sufficient accuracy. As shown in Figure 1.1, the turbulent combustion of pulverized coal particles can be divided into three main modeling aspects, each involving several fundamental phenomena:

- 1. Turbulent Flow, Mixing and Heat transfer:** The conditions under which the thermochemical conversion of particles takes place are directly determined by the surrounding gas phase. The prediction of the gas phase is particularly difficult as the flow in technologically relevant combustion chambers and reactors is turbulent. Turbulence amplifies the mass, momentum and energy exchange between the gas and the solid phase. Moreover, both heat transfer and turbulent mixing result in inhomogenous states, which significantly

influences the reaction both in the solid and gas-phase.

2. **Turbulence Chemistry Interaction (TCI):** Several gaseous species (volatiles and char off-gases) are released to the gas phase during coal conversion. Their subsequent reactions in the gas phase are strongly influenced by turbulence, usually referred to as turbulence chemistry interaction (TCI). TCI determines the gaseous combustion products, including the pollutants, and therefore is essential to predict the overall emissions of the reactor correctly.
3. **Solid Fuel Kinetics:** The last modeling aspect deals with the thermochemical conversion of coal, namely pyrolysis and char oxidation. These are complex and strongly coupled processes that depend on the molecular structure of the parent coal and the surrounding atmosphere. Since the coal conversion provides the species for the subsequent gas-phase reaction, its modeling is a crucial part of the holistic model.

In addition, all of these phenomena are strongly coupled, which requires not only the assessment of individual models but also the investigation of the interaction of different submodels in the holistic model.

1.2. State of Research

Next, the state of research considering all three modeling pillars is outlined, which provides the starting point of this thesis. Additionally, where possible developments concerning oxy-fuel combustion are also reviewed. Furthermore, benchmark experiments for coal combustion, since these are essential to assess the interaction of submodels, are reviewed, including previous studies and classification of configurations investigated in this thesis.

Simulations of turbulent combustion are conducted at three different detail levels: Direct Numerical Simulations (DNS), Large-Eddy Simulations (LES), and Reynolds- Averaged Navier-Stokes (RANS). Thereby, each approach treats the turbulent fluid motion and mixing differently. DNS provides a description of all instantaneous motions of fluid, heat, and mass in a fully resolved manner. In LES, the turbulence is separated into two scales, enabling the direct computation of the larger scales while the smaller scales are modeled. RANS simulations calculate only averaged flow fields. Hence, models must account for all turbulent motions.

The full direct numerical simulation, which resolves both all turbulent length scales and the solid fuel particles, is restricted to very simplified test cases due to extensive computational cost and numerical challenges. Therefore, only studies focusing on single particle and static particle groups are available in the literature [238–241; 250]. However, results from such studies are challenging to transfer to larger reactors.

An additional DNS concept that emerges to overcome the fully resolved DNS difficulties is applying a carrier phase (CP)-DNS. Thereby, only the fluid motion is fully resolved, whereas particles are described in a point-particle framework. This concept, known from spray combustion [175], was first applied by Luo et al. [135] and Hara et al. [85] in simplified configurations employing reduced chemistry descriptions. Recently, Rieth et al. [201] presented CP-DNS of coal particle ignition in a turbulent mixing layer using detailed kinetics. The results of this study were used in a series of different studies to assess the potential of flamelet modeling for coal combustion [202; 264; 265], which revealed the potential of this method. In addition, several authors [219; 254] employed similar CP-DNS setups to investigate pollutant formation in PCC in detail. Although, computational resources are continuously increasing, the application of DNS to more realistic configurations will remain prohibitive in the foreseeable future.

In large-scale applications, the description of turbulent flow fields was mainly tackled by Reynold-averaged Navier Stokes (RANS) approaches in the past. Hence, numerous studies are available in the literature (e.g., [230; 231; 247]). With respect to oxy-fuel atmospheres, several RANS-based studies were published in the literature dealing with the evaluation of the effects of oxy-fuel atmospheres in comparison to air atmospheres (e.g., [1; 14; 142]).

However, in recent years Large-Eddy Simulation (LES) based approaches have frequently gained attraction for simulating turbulent reacting flows. This is due to their excellent predictive capabilities explainable by the reduced modeling requirements for unclosed terms as summarized in Janicka and Sadiki [100] and Pitsch [179]. After the first LES-based study of PCC by Kurose and Makino [122], several authors adopted this modeling strategy and applied it with different focuses to various configurations. Afterwards, numerous investigations of different configurations highlighted the great predictive capabilities of LES for various configurations (e.g., [120; 121; 257; 269]). Nevertheless, Stein et al. [229] also demonstrated that both numerics and model choices could substantially affect LES results. The available LES studies in the literature already include configurations varying from several kW thermal power up to 2.5 MW thermal power for air-fired systems [172; 189]. However, often simplified models are applied for the remaining physics (i.e., gas-phase and solid reactions). Regarding oxy-fuel combustion first LES studies are available in the literature [28; 48; 68], which however employ simplified coal combustion submodels.

With respect to the second modeling pillar (TCI), the above studies have employed either the eddy break-up model (EBU) [138], or the eddy dissipation concept (EDC) [139] in conjunction with two to three gas-phase reactions. These model combinations represent the state-of-the-art modeling approaches for TCI in PCC. However, such modeling might impose too strong assumptions on the gas-phase reactions (e.g., infinitely fast chemistry). Thus, more advanced descriptions such as transported probability density function (PDF) methods [183] and flamelet-based models [176] are extended from single phase combustion to PCC. In the context of transported PDF models, Stöllinger et al. [230; 231] extended a Lagrange Monte-Carlo method to solve the PDF transport equation for PCC. To overcome the limiting local equilibrium chemistry assumption in the previous model, Zhao and Haworth [276] extended the formulation for finite-rate chemistry. The importance of finite-rate chemistry effects in the gas phase also lead to a series of developments with respect to a flamelet description of the gas phase. Such methods enable the direct application of large kinetic mechanisms at significant reduced computational cost. Independently, different authors proposed tabulated flamelet models based on both non-premixed [65; 204; 249; 250] and premixed flamelets [109–111; 254]. The developed flamelet approaches were applied to several configurations under air-fired conditions and showed promising results.

Considering solid fuel kinetics representing the third modeling pillar, models with various levels of detail are available in the literature [86]. For example, very detailed models such as the chemical percolation devolatilization (CPD) model, which is based on a precise description of the molecular structure of the reference coal, are used to describe devolatilization [60]. However, the increased numerical cost associated with such models leads to the use of simplified one-step and two-step models [8; 113], which account for the global conversion with fewer details. The coefficients of these models must be fitted by selected particle histories obtained from detailed models or experiments. This procedure limits the application range of the simplified models to conditions similar to those of the fitting data [247]. Despite the restricted application range, all previously mentioned large-scale simulations rely on simplified models. Only few studies in small laboratory-scale solid fuel flames using directly coupled detailed solid fuel kinetics were carried out [200; 255]. The coupling of detailed solid fuel conversion models for the entire solid fuel conversion process with LES is not available in literature [86]. One potential reason is the challenging coupling of the detailed devolatilization model with the subsequent char reaction

model. To overcome this challenge, a new seamless model for describing the entire conversion process based on a multi-step approach has been introduced recently [137; 226]. However, the application of the seamless kinetic model is currently limited to simple test cases [239; 256].

To validate the coupling of the previously discussed submodels, detailed measurements are mandatory to assess submodel interactions within the holistic model. However, detailed measurements of the thermo-chemical state for PCC, as known from single phase combustion [9], are beyond the current capabilities of modern laser-based techniques especially considering large-scale applications [260]. The challenging environments (e.g., large and dense particle layers, local soot formation, large (unknown) tars species), and limited optical access prevent detailed measurements. Hence, small-scale experiments in laboratory environments are required to provide experimental insights into the complex process of PCC. Nevertheless, due to different scaling behaviors, the interaction of particles, turbulence, reaction, and radiation might be significantly influenced by the downscaling of the actual reactor [260]. Therefore, developed holistic modeling approaches should be validated in applications with different scales. Firstly, in small-scale laboratory burners, fundamental aspects are validated by detailed experiments. Secondly, the model's predictive capabilities are evaluated in larger-scale processes, where generally less precise measurement data is available. In the following, a brief review of available measurement facilities is given. For more information, the reader is referred to the *Workshop on Measurement and Simulation of Coal and Biomass Conversion* (CBC) [24], where experts in the field of coal combustion meet and decide on target flames.

The coupling and interaction of devolatilization and gas-phase homogeneous ignition modeling are often validated in laminar single-particle configurations. These configurations reduce the complexity of the industrial-scale system significantly by removing the influence of turbulence. Hence, the direct application of detailed numerical models and precise non-intrusive measurements due to optical accessibility are possible. One example for single-particle investigations is the Hencken burner, in which Shaddix and Molina [157; 218] studied the ignition behavior of single particles in a hot laminar coflow experimentally. Their data have been used widely for the validation of numerical models. For instance, Vascellari et al. [250], Goshayeshi and Sutherland [78] and Farazi et al. [51] evaluated the predictability of detailed models for single particle combustion and found decent agreement with the experimental data. An additional promising configuration is the recently developed laminar flat flame burner experimentally investigated by Koeser et al. [114; 115]. A first numerical simulation by Knappstein et al. [109] showed that the applied tabulated flamelet model coupled with a one-step devolatilization model was able to predict the ignition delay correctly.

Subsequently, the next larger scale is the investigation of particle group combustion in a well-defined environment. For instance, the gas-assisted coal jet flame of the Japanese Central Research Institute of Electric Power Industry (CRIEPI) is a very well measured reference case [217]. Therefore, numerous numerical studies were carried out in this configuration focusing on the validation of modeling frameworks for PCC [69; 122; 229; 276]. Additionally, Rieth et al. [200] showed for this configuration that the direct use of a network model in CFD (here CPD) might be advantageous. However, they also concluded that suitably adjusted empirical models provide good results too. Currently, the size of this configuration represents the limit for the direct application of advance solid fuel conversion models.

Since little experience has been gathered on simulating oxy-fuel atmospheres, and as real and semi-industrial combustion chambers are difficult to access, Becker et al. [11] recently designed a new laboratory-scale gas-assisted combustion chamber. This chamber is fully optically accessible, facilitating the application of laser-based measurement methods. Since accurate measurements under fixed boundary conditions are possible, this combustion chamber is very well

suited to gain an insight into oxy-fuel combustion and validate numerical models. The overall design of the burner matches the geometric designs of larger self-sustained burner configurations [236]. To characterize the combustion process inside the chamber, Becker et al. [11; 12] applied different laser measurement techniques in increasingly complex operating modes. On the numerical side, two different studies were carried out [42; 108] considering non-reactive and PCC in air atmospheres, respectively.

At the next larger size, the experimental combustion chamber of the Institute of Heat and Mass Transfer (WSA) from the RWTH Aachen University [236] is situated. This combustion chamber is an appropriate reference case for air and oxy-fuel combustion due to its simple geometry and access points for intrusive and non-intrusive flame measurements [89; 271; 273]. Two previous numerical studies employing this reference case were carried out. First, Franchetti et al. [68] showed that LES coupled with a global reaction mechanism could be used to simulate the combustion process. Second, Sadiki et al. [209] investigated the flow characteristics and turbulence modeling by means of RANS and LES in the chamber.

The fact that LES can be applied to semi-industrial scale combustion chambers was demonstrated by Olenik et al. [172], Rabaçal et al. [189], and Rieth et al. [200; 204]. Employing different modeling strategies, the authors showed that LES could predict a 2.5 MW swirling flame with acceptable accuracy. Although validation of oxy-fuel models at this power level would be beneficial, no precise measurements for oxy-fuel conditions are currently available.

1.3. Aims and Scope of this Work

Generally speaking, this thesis aims to contribute to an efficient and predictive holistic model for simulating pulverized solid fuel combustion in both atmospheric and oxy-fuel conditions. To support establishing the oxy-fuel process on the combustion side, models that describe the fundamental processes involved in solid fuel combustion and apply to both air and oxy-fuel atmospheres are required. In this thesis, such submodels will be assessed, further developed, and coupled, resulting in an overall modeling approach beyond the current state-of-the-art. In particular, two of the three previously introduced modeling pillars will be addressed in detail. As outlined above, all studies considering advanced TCI-models, such as the flamelet model, are solely applied to air-fired combustion. However, more precise models (LES) with more detailed chemical descriptions based on tabulated chemistry are also desirable for oxy-fuel combustion to predict the process with its very different combustion characteristics. Therefore, a combined LES-tabulated flamelet model promising for air-fired combustion will be further developed for application in oxy-fuel atmospheres. Furthermore, with respect to solid fuel kinetics, the accuracy of state-of-the-art coal conversion models will be assessed by comparing simulations employing simpler models to simulations with detailed seamless multi-step kinetics. Summing up, the coupling of the seamless solid fuel kinetics with a flamelet-based description of the gas-phase in the framework of LES and its application to combustion chambers defines the first main objective of this work.

Moreover, gaining a deeper understanding of the physical-chemical processes for the combustion of solid fuels in oxy-fuel atmospheres presents the second objective of this work. Therefore, the developed models are applied to a series of configurations with increasing size and complexity. Starting from single-particle and particle group ignition through gas-assisted laboratory-scale burners to pilot scale burners allows for a seamless validation of models under practical relevant conditions. Furthermore, due to the previously outlined difficulty of measurements in PCC, validated numerical simulations will be employed to provide new insights into the complex coupled phenomena in oxy-coal combustion. In summary, the scientific goals of this thesis are defined

as follows:

- Development of generalized models for turbulent transport phenomena, gas-phase combustion and solid fuel conversion in an oxy-fuel atmosphere, taking relevant effects on each scale into consideration.
- Gaining a comprehensive understanding of relevant mechanisms involved in the combustion of solid pulverized fuels in an oxy-fuel atmosphere.
- Providing a predictive and efficient simulation method to contribute to a knowledge-based design of oxy-fuel combustion in the future.

1.4. Structure of this Work

This thesis is divided into seven chapters. After this general introduction, **Chapter 2** recapitulates the theoretical background on the mathematical description of turbulent reacting multi-phase flows. Next, the two main modeling objectives concerning the numerical treatment of turbulent flames and solid fuel conversion are addressed in detail. In **Chapter 3**, besides the background on modeling turbulent flames, specific extensions developed in this thesis that are required for the accurate simulation of solid fuel combustion are outlined. This is followed by **Chapter 4**, in which the counterpart, namely the modeling of the solid fuel itself, is covered. Furthermore, the chapter addresses further developments of the existing models and their consistent coupling to the remaining model parts. All derived models are implemented in the academic code FASTEST², whose numerics are outlined in **Chapter 5**. In addition, new implementations are verified by means of simple test cases. In **Chapter 6** the developed methodology is applied to series of solid fuel flames with increasing complexity featuring phenomena of practical relevance. In the end, the major findings of this thesis are summarized and an outlook for possible future work is given in **Chapter 7**.

²FASTEST is an acronym for Flow Analysis by Solving Transport Equations with Simulated Turbulence

2. Mathematical Description and Modeling of Turbulent Reacting Multi-Phase Flows

This chapter briefly reviews the governing equations of reactive multi-phase thermo-fluid systems. All given equations are subject to the continuum hypothesis that assumes a sufficiently large number of molecules is inside a given volume, allowing for a description based on macroscopic quantities such as mass density ρ . The continuum hypothesis holds if the ratio of the mean free path of the molecules λ_m to the characteristic system length scale l_s , which is denoted as Knudsen number Kn , is significantly smaller than one

$$Kn = \frac{\lambda_m}{l_s} \ll 1. \quad (2.1)$$

This assumption is valid for most flows in technical applications, including the ones investigated in this thesis.¹

In this chapter, first, the governing equations of reactive single-phase flows are outlined. This is followed by a brief discussion of turbulence a phenomenon closely related to most technical fluid flow applications and its modeling strategies with respect to numerical methods. The consideration of particles in a multi-phase flow is addressed in the subsequent section. Finally, the last section covers the effect and modeling of thermal radiation, which can be an additional heat transfer mechanism in technical systems.

2.1. Governing Equations for Single-Phase Reactive Flows

Single-phase reactive flows are characterized by a set of transport equations for conserved variables and a complementary state equation for the relation between these variables. In addition, material laws, closures for the species diffusion velocities, and chemical source terms are required. This section follows the textbooks by Poinso and Veyante [181], and Bird, Stewart and Lightfoot [15] if not stated otherwise. Throughout this thesis, the notation for Cartesian tensors, as outlined in [228], is employed.

2.1.1. Conservation of Mass

Since mass is conserved, the temporal change of mass in a volume corresponds to the sum of mass fluxes through the surfaces and is in the differential form expressed by

$$\frac{\partial \rho}{\partial t} + \frac{\partial}{\partial x_i} (\rho u_i) = 0. \quad (2.2)$$

Here, ρ represents the density of a mixture and u_i denotes the three Cartesian velocity components.

¹The mean free path of molecules in air at standard conditions is $\approx 68 \cdot 10^{-9}$ m and a typical flame thickness, which can be seen as the systems characteristic length, is approximately $250 \cdot 10^{-6}$ m. For this example, the Knudsen number is $2.72 \cdot 10^{-4}$ and, thus, modeling atmospheric flames by the continuum hypotheses is justifiable.

2.1.2. Conservation of Momentum

Also, the momentum ρu_i is conserved. Hence, a fluid element's temporal momentum is affected by the sum of all forces acting on it and accordingly is given by

$$\frac{\partial}{\partial t} (\rho u_i) + \frac{\partial}{\partial x_j} (\rho u_i u_j) = \frac{\partial}{\partial x_j} \tau_{ij} - \frac{\partial p}{\partial x_i} + \rho g_i \quad i \in \{1, 2, 3\}. \quad (2.3)$$

Here, τ_{ij} represents the stress tensor, p the pressure, and g_i the i -th component of the gravitational acceleration as the only considered volume force. Within this work, only Newtonian fluids are considered, whose material law is given by

$$\tau_{ij} = \mu \left(\frac{\partial u_i}{\partial x_j} + \frac{\partial u_j}{\partial x_i} \right) - \frac{2}{3} \mu \frac{\partial u_k}{\partial x_k} \delta_{ij}, \quad (2.4)$$

where μ denotes the dynamic viscosity.

2.1.3. Species Transport

Since reactive flows usually contain different compositions (e.g., different concentrations of fuel and oxidizer), a quantification of the mixture components is required. For a mixture composed of N_s species, the mass fraction of the species k is defined as

$$Y_k = \frac{m_k}{\sum_{\alpha=1}^{N_s} m_\alpha}. \quad (2.5)$$

The evolution of the mass fraction is described by the following transport equation

$$\frac{\partial}{\partial t} (\rho Y_k) + \frac{\partial}{\partial x_j} (\rho (u_j + V_{k,j}) Y_k) = \dot{\omega}_k. \quad (2.6)$$

Here, both the j -th component of the diffusion velocity $V_{k,j}$ and the chemical source terms $\dot{\omega}_k$ require additional closures, which are detailed in the next paragraph and Section 2.1.6, respectively. Additionally, to ensure continuity, the following conditions must be fulfilled

$$\sum_{\alpha=1}^{N_s} Y_\alpha = 1 \quad \sum_{\alpha=1}^{N_s} \dot{\omega}_\alpha = 0 \quad \sum_{\alpha=1}^{N_s} Y_\alpha V_{\alpha,i} = 0. \quad (2.7)$$

Closures for Diffusion Modeling

To close the diffusion velocity in Equation (2.6), several models with different levels of details are available [181]. In multi-component mixtures, the diffusion velocity can be obtained by solving the Stefan-Maxwell equations [92]. However, the evaluation of this equation results in a linear system of size N_s^2 , which might be too expensive for large-scale simulations.

Concerning a binary mixture, the Stefan-Maxwell equation reduces to

$$V_1 = -\frac{D_{12}}{Y_1} \frac{\partial Y_1}{\partial x_i}, \quad (2.8)$$

also referred to as Fick's law. Commonly, this model is also applied to multi-species mixtures, which yields

$$V_k = -\frac{D_k}{Y_k} \frac{\partial Y_k}{\partial x_i}. \quad (2.9)$$

An additional model simplification is to set the species diffusion D_k equal to the thermal diffusion $\lambda/(\rho c_p)$. Hence, their ratio, referred to as Lewis number $Le = \lambda/(\rho c_p D)$, becomes equal to one. Therefore, this simplification is also called unity Lewis number approach.

2.1.4. Energy Balance

The energy balance can be expressed through different quantities [181]. Within this work, the enthalpy (sum of the sensible enthalpy and the enthalpy of formation) is used, which is defined as

$$h_k = \underbrace{\int_{T_{\text{ref}}}^T c_{p,k} dT}_{h_s} + \Delta h_{f,k}^{\text{ref}}. \quad (2.10)$$

Here, the former temperature-dependent part, represented by the integration of the specific heat capacity at constant pressure, is the sensible part of the enthalpy. The latter part corresponds to the enthalpy of formation $\Delta h_{f,k}^{\text{ref}}$ of the species k at the reference temperature T_{ref} . The enthalpy of a multicomponent mixture is expressed by the mass-weighted sum of the species enthalpies

$$h = \sum_{k=1}^{N_s} h_k Y_k. \quad (2.11)$$

Following the common assumption for low Mach number flows (e.g., enthalpy changes due to pressure variations, viscous heating, and volumetric forces are neglected), the transport equation for the enthalpy yields

$$\frac{\partial}{\partial t} (\rho h) + \frac{\partial}{\partial x_j} (\rho u_j h) = -\frac{\partial q_j}{\partial x_j} + S_{\text{rad}}. \quad (2.12)$$

The first term on the right-hand side denotes the enthalpy flux due to heat conduction and species diffusion

$$q_j = -\lambda \frac{\partial T}{\partial x_j} + \rho \sum_{k=1}^{N_s} h_k Y_k V_{k,j}, \quad (2.13)$$

which, by using (2.9) and (2.11), can be converted to

$$q_j = -\frac{\lambda}{c_p} \frac{\partial h}{\partial x_j} + \sum_{k=1}^{N_s} h_k \frac{\partial Y_k}{\partial x_i} \left(\frac{\lambda}{c_p} - \rho D_k \right). \quad (2.14)$$

Note that if the $Le_k = 1$ assumption is employed, the last term in Equation (2.14) vanishes.

The last term on the right-hand side of Equation (2.12) represents enthalpy changes by thermal radiation. Its closure is discussed in Section 2.4.

2.1.5. Equation of State

In order to close the system of unknowns, a relation between the fluid state variables is required. Since all considered gases are assumed to be ideal, the relation is closed by the thermal equation of state

$$\rho = \frac{p}{T} \frac{W}{\mathcal{R}}, \quad (2.15)$$

where \mathcal{R} denotes the ideal gas constant and W is the mean molar mass of the mixture.

Together with previously introduced equations, the full set of equations enables the description of all physical phenomena, including the propagation of sound waves traveling with the speed of sound c . However, when the flow velocity u is lower than c , the temporal resolution requirements of c significantly increases computational cost. Therefore, special mathematical techniques were developed to remove acoustic waves from the solution [140] and thus enable efficient computation of flows with low Mach numbers

$$Ma = \frac{u}{c}. \quad (2.16)$$

According to (2.15), both pressure and temperature variations lead to changes in the density. In general, flows with $Ma \leq 0.3$ can be considered as incompressible since velocity variations change the pressure by less than 5% [2]. Therefore, it is justifiable to assume a reference pressure p^{ref} in (2.15). On the contrary, the density changes about factor ten due to temperature variation during combustion and, thus, must be considered.

2.1.6. Closure of the Chemical Source Term

Additionally, the chemical source term in Equation (2.6) requires closure. When considered at the molecular level, a chemical reaction describes the breaking of molecular bonds and the formation of new compounds triggered by collisions. This procedure is exemplified by the following equation describing the collision of two products (A_2 and B_2) forming the educts $2AB$



The likelihood of this reaction depends on the temperature. High temperatures lead to high kinetic energies at the molecular level, which results in the breaking of molecular bonds during collisions. The required energy amount is referred to as the activation energy E_A . In the case of an exothermic reaction, an enthalpy surplus remains, which is called the reaction enthalpy $\Delta_{\text{R,H}}$.

The temporal change in species concentration c_k is used to quantify the reaction rate. From this, the forward reaction r_{fr} is then determined by

$$r_{\text{fr}} = \frac{dc_{A_2}}{dt} = \frac{dc_{B_2}}{dt} = -\frac{1}{2} \frac{dc_{AB}}{dt}. \quad (2.18)$$

The reaction rate is proportional to the concentration of molecules participating in the reaction, as these increase the probability of collisions. Using the proportionality constant k_{fr} , the relation is given by

$$r_{\text{fr}} = k_{\text{fr}} c_{A_2} c_{B_2}. \quad (2.19)$$

The proportionality constant is described by an Arrhenius-type equation

$$k_{\text{fr}} = A_{\text{fr}} T^b e^{-\frac{E_A}{\mathcal{R}T}}. \quad (2.20)$$

As indicated by the reaction arrows in Equation 2.17, the reaction occurs also in the other direction r_{bf} . The so-called equilibrium constant can be determined from the ratio of forward reaction to backward reaction

$$k_{\text{eq}} = \frac{k_{\text{fr}}}{k_{\text{br}}}. \quad (2.21)$$

In general, however, fuel and oxidizer are not converted to their educt by a single collision. Instead, multiple collisions take place, leading to several intermediate species. A general reaction system consisting of N_r reactions with N_s species reads

$$\sum_{k=1}^{N_s} \nu'_{k,j} \mathcal{X}_k \rightleftharpoons \sum_{k=1}^{N_s} \nu''_{k,j} \mathcal{X}_k \quad \text{for} \quad j = 1, \dots, N_r, \quad (2.22)$$

where \mathcal{X}_k denotes the species symbol of species k with $\nu'_{k,j}$ and $\nu''_{k,j}$ being the molar stoichiometric coefficients. Accordingly, the reaction rate in Equation (2.19) generalizes to

$$r_j = k_{fr,j} \prod_{k=1}^{N_s} c_k^{\nu'_{k,j}} - k_{br,j} \prod_{k=1}^{N_s} c_k^{\nu''_{k,j}} \quad \text{for} \quad j = 1, \dots, N_r. \quad (2.23)$$

Finally, the required source term for the species transport Equation (2.6) is obtained by summing up the contributions of the individual elementary reaction by

$$\dot{\omega}_k = W_k \sum_{j=1}^{N_r} (\nu''_{k,j} - \nu'_{k,j}) r_j \quad \text{for} \quad j = 1, \dots, N_r. \quad (2.24)$$

Reaction mechanisms are tailored for a specific fuel oxidizer combination. The determination of the reactions and their corresponding preexponential factors A , the temperature exponent b , and the activation energy E_A is covered by the broad research field of reaction kinetics. Already for the simple methane-air combustion, detailed mechanisms contain 53 species and 325 reactions [222]. For more complex fuels, hundreds of species and ten thousand reactions are easily exceeded.

Chemical Reaction Mechanism

In this thesis two chemical reaction mechanism are used:

1. For CH₄-flames: the GRI 3.0 mechanism of Smith et al. [222] (53 species, 325 reactions)
2. For coal-flames: Oxy-fuel mechanism of Cai et al. [21] (100 species, 734 reactions)

2.2. Turbulence

In general, flows are distinguished as either laminar or turbulent. The previously given set of equations can describe both laminar and turbulent flows. However, their respective occurrence involves significantly different characteristics. In particular, the behavior of the flow changes in response to disturbances. In this context, the ratio of inert forces to viscous forces is decisive, which is denoted as the Reynolds number Re . Considering a system with a characteristic velocity U and characteristic length scale \mathcal{L} , the Reynolds number is given by

$$Re = \frac{\rho U \mathcal{L}}{\mu}. \quad (2.25)$$

Based on Reynolds number, the flow is assigned to the laminar or turbulent regime. However, the value where the transition occurs is not fixed as the particular transition Reynolds number depends on the considered problem. Most technical flows in engineering applications are turbulent due to their large dimensions and high operating velocities. Considering combustion systems, turbulence is often deliberate as it promotes the mixing of fuel and oxidizer. This chapter is meant to provide a brief overview of turbulence and its modeling strategies used throughout this work. Admittedly, addressing the full complexity of turbulence is far beyond the scope of this work. A profound treatment of the topic of turbulence is found in the textbook of Pope [184], on which this section bases.

Statistical moments are used to describe the quasi-random and transient nature of turbulent flows. For the description of the arbitrary quantity ϕ , the temporal average is given by

$$\langle \phi \rangle = \frac{1}{\Delta_t} \int_0^{\Delta_t} \phi(t) dt, \quad (2.26)$$

where time interval Δ_t must be sufficiently long. Using the time-average quantity, the corresponding fluctuation is obtained by

$$\phi'(t) = \phi(t) - \langle \phi \rangle. \quad (2.27)$$

The standard deviation (square root of the variance, rms=root mean square) is defined by

$$\phi_{\text{rms}} = \sqrt{\frac{1}{\Delta_t} \int_0^{\Delta_t} \phi'(t)^2 dt}. \quad (2.28)$$

By applying Equation (2.27), the instantaneous velocity is divided into mean and fluctuating parts

$$u = \langle u \rangle + u'. \quad (2.29)$$

Fundamental parts of the turbulent theory bases on the knowledge of the energy related to these fluctuations, the so-called turbulent kinetic energy

$$TKE = \frac{1}{2} \langle u'_i u'_i \rangle. \quad (2.30)$$

It is assumed that the turbulent flow is characterized by various vorticity structures of different sizes l , characteristic velocities u , and timescales t . The largest structures issue from the mean flow and, thus, depend on the geometry. Therefore, these structures have distinct orientations, and their size is in the same order as the characteristic length scale of the system $l_0 = \mathcal{O}(\mathcal{L})$. Accordingly, their characteristic velocity u_0 is in a similar range as the turbulent fluctuation u_{rms} . Based on this description, the production of turbulent kinetic energy \mathcal{P}_{TKE} is calculated from the energy content of this vortices u_0^2 divided by a characteristic time $t_0 = l_0/u_0$, yielding

$$\mathcal{P}_{TKE} \sim \frac{u_0^2}{t_0} = \frac{u_0^3}{l_0}. \quad (2.31)$$

For steady-state flows and homogeneous turbulence [184], the production equals the dissipation of the turbulent kinetic energy ϵ_{TKE}

$$\mathcal{P}_{TKE} = \epsilon_{TKE}. \quad (2.32)$$

However, the larges structures carry too much energy to dissipate directly into heat by viscous processes. Hence, an energy cascade forms in which the energy is transferred to smaller vortices [197]. This cascade remains until the viscous forces lead to energy dissipation. This process is visualized by the energy spectrum in Figure 2.1, using the wavenumber $\kappa = 2\pi/l$ to map the turbulent kinetic energy onto the vortices. The figure indicates that a significant part of the energy belongs to the energy-containing range and the inertial subrange consisting of large vortices. In contrast, the small structures of the dissipation range contain considerably less energy.

The energetic relation between the large-scale eddies and the smallest eddies is given in Equation (2.32). Kolmogorov concludes in his similarity hypothesis that the length scale of the smallest eddies η_K is uniquely determined by the dissipation ϵ_{TKE} and the kinematic viscosity ν . Based on dimensional analysis, the only possible combination of these variables yields

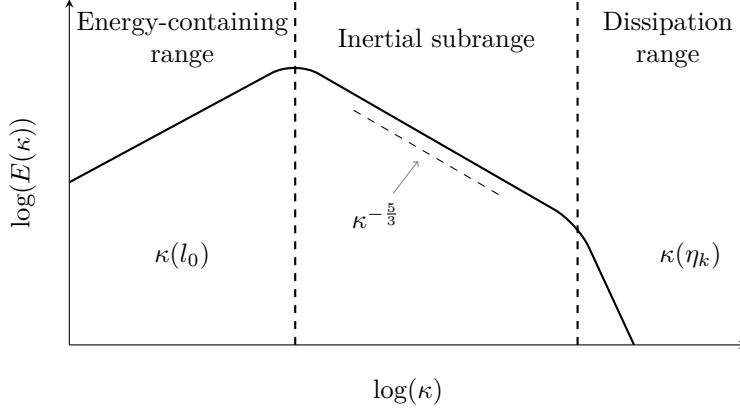


Figure 2.1.: Schematic distribution of the TKE onto different sizes as proposed by the energy cascade of turbulent flows.

$$\eta_K \equiv \left(\frac{\nu^3}{\epsilon_{TKE}} \right)^{1/4}, \quad (2.33)$$

which is referred to as the Kolmogorov length scale.

Another important length to characterize turbulent flows is the integral length scale l_I , which is defined based on the two-point correlation tensor [184]. Similar to the Reynolds number introduced in Equation (2.25), a turbulent Reynolds number is defined by using the integral length scale

$$Re_t = \frac{u_{rms} l_I}{\nu}. \quad (2.34)$$

Combining Equations (2.31), (2.32), and (2.33), the important connection between large and small scales is derived

$$\frac{\eta_K}{l_0} \sim Re_t^{-3/4}. \quad (2.35)$$

2.2.1. Numerical Treatment

To obtain the turbulent flow field, previously given equations together with appropriate boundary and initial conditions must be solved. Since analytic solutions are only available for specific regions (e.g., boundary layers) or require strong assumptions (e.g., potential flows), numerical methods are employed to approximate solutions of these equations. For the numerical solution, a discretization of the domain by several finite volumes, with the dimensions Δ_x , Δ_y , and Δ_z , is performed. Considering a domain with the dimensions \mathcal{L}_x , \mathcal{L}_y , and \mathcal{L}_z the required number of grid points is given by

$$N_{CV} \approx \frac{\mathcal{L}_x}{\Delta_x} \frac{\mathcal{L}_y}{\Delta_y} \frac{\mathcal{L}_z}{\Delta_z}. \quad (2.36)$$

Based on this discretization, which is described in detail in Chapter 5, the system of partial differential equations (PDEs) is converted to a set of algebraic equations enabling the numerical approximation of the unknown quantities in each control volume at discrete time instances. Nevertheless, resolving all turbulent scales in the simulation, referred to as *Direct Numerical Simulation* (DNS), is computationally very expensive. Hence, different techniques have been

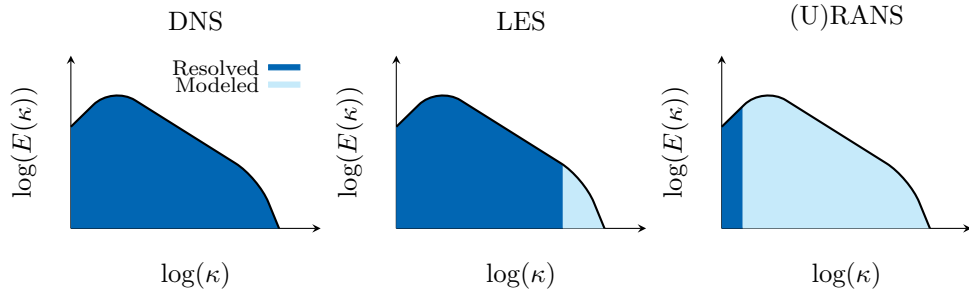


Figure 2.2.: Schematic comparison of the three turbulence modeling approach with respect to the energy spectrum.

established to reduce these costs significantly. The most popular method for dealing with turbulent flows is the *Reynolds averaged Navier Stokes* (RANS) approach. As the name implies, this model only calculates the average quantities, which reduces computational costs drastically. Another method to model turbulent flows, which is to be positioned between DNS and RANS in terms of computational costs, is the *Large-Eddy Simulation* (LES). All three techniques, which are compared by means of the energy spectrum in Figure 2.2, are described in the following. Thereby, the main focus is on LES as this method is used in this work.

2.2.1.1. Direct Numerical Simulation

As previously stated, DNS directly resolves all turbulent scales, which means that the spatial extent of the numerical cell must not exceed the smallest scales. Hence, the grid size must be in the same order as the Kolmogorov scale, introduced in Equation (2.33), and consequently is given by [156]

$$\Delta_{x_i} = C\eta_K \quad \text{with} \quad 1 \leq C \leq 10. \quad (2.37)$$

The required number of control volumes for DNS is estimated by combining Equation (2.35), (2.36) and (2.37) resulting in

$$N_{CV} \propto Re_t^{9/4}, \quad (2.38)$$

illustrating the strong dependency on the Reynolds number. Moreover, to ensure the stability of the numerical solution procedure, the time step Δ_t of the transient method is generally also proportional to the grid size. Combining these two dependencies lead to overall numerical costs being proportional to Re_t^3 , making DNS unfeasible for technical applications, which are characterized by large Reynolds numbers. However, DNS is a valuable tool for academic test cases allowing for detailed fundamental investigations, which are utilized to derive and validate simplified models.

2.2.1.2. Reynolds Averaged Description

For RANS, a time-averaging of the governing equations according to Equation (2.26) is performed. Thus, the mean quantities obtained from the Reynolds decomposition of the flow field are directly computed. Due to the nonlinearity of the convection term, the application of the Reynolds averaging to the Navier Stokes equation leads to additional Reynolds stresses in the governing equation

$$\langle u'_i u'_j \rangle = \langle u_i u_j \rangle - \langle u_i \rangle \langle u_j \rangle, \quad (2.39)$$

which require additional modeling. The model's accuracy is crucial, as errors result in deviation from the correct mean flow field. Most models, such as the well-established $k-\epsilon$ model [124], rely on the so-called Boussinesq approximation, which approximates the Reynolds stresses by a turbulent viscosity and the mean velocity gradient [266].

RANS methods can be extended to unsteady RANS (URANS) to account for large-scale system variations, such as the movement of walls in an internal combustion engine. Hence, this method captures external influences, which are not caused by turbulence.

In industrial environments, RANS methods are state-of-the-art due to their low computational cost. However, RANS approaches have the intrinsic drawback of modeling the entirety of turbulent structures. In particular, large turbulent structures strongly depend on the considered geometry and are difficult to capture with generic models. Therefore, the modeling coefficients must be tuned to predict the flow field correctly. Predictive RANS simulations are even more challenging in reacting multi-phase flows. The need to perform such simulations motivates the development and validation of more sophisticated models.

2.2.1.3. Large-Eddy Simulation

LES aims to include more physical details in the simulation than RANS but having lower computation costs than DNS. Therefore, spatial filtering is applied to the governing equation resulting in the computation of only the large vortices. Thus, the filtering operator removes the small-scale structures associated with high frequencies. Mathematically this is achieved by filtering in spectral space or physical space [184]. However, in LES, this filtering is not explicitly performed but rather approximated by the implicit filtering of the numerical grid. Since the cell size does not reach down to the smallest scales, the filter behavior can be approximated by a box filter in physical space

$$\mathcal{G} = \begin{cases} \frac{1}{V_F} & \text{if } |x_i| \leq \frac{V_F^{1/3}}{2}, \quad i = 1, 2, 3 \\ 0 & \text{else} \end{cases}, \quad (2.40)$$

where V_F is the filtering volume with an edge length corresponding to the physical resolution [210]. To apply the filter to the governing equation, the filter operator must be commutable such that the derivative and the filtering operation are interchangeable

$$\overline{\frac{\partial \phi}{\partial x}} = \frac{\partial \overline{\phi}}{\partial x}. \quad (2.41)$$

Although this is only fulfilled if the filter size stays constant [184], resulting uncertainties are neglected and assumed to be incorporated in subgrid-scale modeling.

Applying the filtering procedure to a variable density flow leads to additional subgrid correlation $\overline{\rho^{sgs} \phi^{sgs}}$, which would require further modeling. To circumvent its occurrence, a density-weighted filter operation, which is called Favre filtering [54], is introduced

$$\tilde{\phi} = \frac{\overline{\rho \phi}}{\overline{\rho}}. \quad (2.42)$$

Using the Favre filter, the splitting of an arbitrary quantity is given by

$$\phi = \tilde{\phi} + \phi^{sgs}, \quad (2.43)$$

where the superscript sgs denotes the contribution to ϕ from the subgrid, residual or unresolved scales. Filtering the non-linear convection term in the transport equation yields an unclosed term

$$\tau_\phi^{sgs} = \left(\widetilde{u_j \phi} - \widetilde{u}_j \widetilde{\phi} \right), \quad (2.44)$$

which requires additional modeling.

Subgrid scale modeling

The subgrid terms are commonly interpreted as an additional diffusion based on their occurrence in the governing equations. Therefore, these terms, caused by the subgrid part of the velocity correlation, are modeled by a turbulent eddy-viscosity. The unresolved momentum fluxes are expressed by the Boussinesq assumption

$$\tau_{ij}^{sgs} - \frac{1}{3} \tau_{kk}^{sgs} = -2\bar{\rho} \nu_t \left(\tilde{S}_{ij} - \frac{1}{3} \tilde{S}_{kk} \delta_{ij} \right), \quad (2.45)$$

where ν_t is denoted as subgrid-scale viscosity. \tilde{S}_{ij} represents the filtered rate of the strain tensor, which is expressed in terms of resolved velocity gradients

$$\tilde{S}_{ij} = \frac{1}{2} \left(\frac{\partial \tilde{u}_i}{\partial x_j} + \frac{\partial \tilde{u}_j}{\partial x_i} \right). \quad (2.46)$$

Following Prandtl's mixing length hypothesis [186], the eddy viscosity must be proportional to a characteristic length scale l_m and the velocity gradients, yielding

$$\nu_t \propto l_m^2 \tilde{S} \quad \text{with} \quad \tilde{S} = \sqrt{2\tilde{S}_{lk}\tilde{S}_{lk}}. \quad (2.47)$$

Smagorinsky model

For LES grids, Smagorinsky suggested using the filter size Δ in conjunction with a proportionality constant to model the characteristic length scale resulting in the following expression

$$\nu_t = (C_S \Delta)^2 \tilde{S}. \quad (2.48)$$

Herein, the constant, commonly referred to as the Smagorinsky coefficient, must be approximated. Typically values of $C_S = 0.13 - 0.18$, depending on the assumptions made, can be analytically derived. However, in inhomogenous flows, these values tend to overestimate the amount of energy transferred to the subgrid scales [184]. To overcome these drawbacks, a dynamic procedure introduced by Germano et al. [73] is employed in this work. The idea of this model is to use an additional test filter, which enables the calculation of the Smagorinsky coefficient based on the locally resolved field as a function of space and time. Details about the numerical treatment and implementation, which relies on the modified version of Lilly [131], are extensively discussed in previous Ph.D. theses by Hahn [83], Olbricht [171], and Kuenne [116]. For the sake of brevity, these details are not repeated here.

Unresolved scalar fluxes

Closure of the scalar transport is achieved through a gradient approach. Thereby, the eddy diffusivity is calculated based on a turbulent eddy viscosity ν_t and a turbulent Schmidt number Sc_t or a turbulent Prandtl number Pr_t . The closure for species mass fractions and enthalpy then reads

$$\tau_{Y_k}^{sgs} = -\frac{\nu_t}{Sc_t} \frac{\partial \widetilde{Y}_k}{\partial x_j} \quad \text{and} \quad \tau_h^{sgs} = -\frac{\nu_t}{Pr_t} \frac{\partial \widetilde{h}}{\partial x_j}. \quad (2.49)$$

2.3. Multi-Phase Flows

In this work, multi-phase flows refer to two-phase flows, where one phase is disperse, i.e., a certain number of discrete elements that are not materially connected. Flows matching this constrain are gas-droplet, gas-particle, and liquid-particle flows, out of which the second case is of importance for this thesis. The essential characteristics of such flows are briefly recapitulated to provide a mathematical background. This section bases on the textbook of Crowe, Schwarzkopf, Sommerfeld, and Tsuji [35].

The volume ratio of the disperse phase (subscript prt) compared to the continuous phase is called the disperse phase volume fraction

$$\alpha_d = \frac{V_{\text{prt}}}{V} = \frac{\sum_{i=1}^{N_{\text{prt}}} V_{\text{prt},i}}{V}, \quad (2.50)$$

where V_{prt} denotes the volume of the disperse phase in the considered volume V . Equally, the volume fraction of the continuous phase is given by

$$\alpha_c = \frac{V_c}{V} = \frac{\sum_{i=1}^{N_{\text{prt}}} V_{\text{prt},i}}{V}, \quad (2.51)$$

where V_c denotes the volume of the continuous phase. Obviously, the sum of both fraction must be unity, i.e. $\alpha_d + \alpha_c = 1$. Similarly, the apparent density of the disperse phase and continuous phase can be defined

$$\bar{\rho}_d = \frac{m_d}{V} \quad \text{and} \quad \bar{\rho}_c = \frac{m_c}{V}. \quad (2.52)$$

Considering a volume, with an edge length of l , containing a spherical particle with the diameter D_{prt} , the volume fraction of the particle is given by

$$\alpha_d = \frac{\pi D_{\text{prt}}^3}{6l^3}. \quad (2.53)$$

Thus, in a lattice arrangement, the particle volume fraction for touching particles is $\pi/6$. With a few mathematical conversions, the ratio of particle spacing to volume fraction yields

$$\frac{l}{D_{\text{prt}}} = \left(\frac{\pi}{6\alpha_d} \right)^{\frac{1}{3}} \quad (2.54)$$

By introducing the disperse mass concentration and material density ratio, the disperse volume fraction can also be expressed as follows

$$\alpha_d = \frac{\bar{\rho}_d}{\rho_d} = \frac{\bar{\rho}_d \bar{\rho}_c \rho_c}{\bar{\rho}_c \rho_c \rho_d} = C \alpha_c \frac{\rho_c}{\rho_d}. \quad (2.55)$$

Further, using $\alpha_c = 1 - \alpha_d$ and defining $\kappa_{\text{prt}} = C \rho_c / \rho_d$, the distance between particles in a disperse flow reads

$$\frac{l}{D_{\text{prt}}} = \left(\frac{\pi}{6} \frac{1 + \kappa_{\text{prt}}}{\kappa_{\text{prt}}} \right)^{\frac{1}{3}}. \quad (2.56)$$

Considering a typical ratio of the gas to the particle density of approximately $1 \cdot 10^{-3}$ and a mass ratio of unity, the corresponding inter-particle spacing is $l/D_{\text{prt}} \approx 10$. According to Crowe et al. [35], such spaced particles do not influence their mutual motion (i.e., through collisions).

Depending on the investigated technical application, this condition is not always fulfilled. For example, fluidized beds are operated under high particle loads resulting in significantly smaller particle spacings. In this work, however, all investigated applications aim for pulverized coal combustion, which generally has low particle loads resulting in $l/D_{\text{prt}} \geq 10$. Thus, particle-particle interactions are considered neglectable.

2.3.1. Modeling of the Disperse Phase

In the most detailed representation of particles, the equations introduced in Section 2.1 require no changes since the simulation fully resolves the particles. In this case, particles are treated as boundary conditions for the flow field. However, this approach is challenging to apply to systems with large particle numbers. Since the boundary conditions must be specified at each particle's surface, the grid generation becomes very cumbersome for particles, continuously changing location, orientation, and size. Although there exist possibilities, such as the cut cell methods on Cartesian grids [70; 214] or unstructured grids [238–241] to circumvent these problems, the demanding computational cost of computing numerous particles restricts the usage to academic test cases, with low particle numbers compared to industrial applications.

Instead methods, that assume point particles are commonly used to describe particle laden flows (e.g., [108; 172; 203; 204; 229]). Thereby, particles are modeled in a Lagrangian framework, whereas the carrier phase description remains Eulerian, resulting in a method commonly referred to as the Euler-Lagrange approach. Since the particles are treated as non-resolved discrete elements, their temporal evolution is solved individually. Accordingly, the flow boundary layers around the particles are not resolved and thus require modeling. Therefore, source terms are introduced in the gas phase equations to account for the interaction between particles and the gas phase. Two prerequisites are commonly required for the consistent application of the Euler-Lagrange approach: 1) The Euler cell size is significantly larger than the particles size, and 2) particles are spherical.

For LES of technical application, the former requirement is fulfilled. In general, the minimum cell size is not below 0.5 mm and thus is larger than the mean particle diameter of around 100 μm . However, for detailed small-scale investigations in academic setups, this assumption is not valid and thus requires additional modeling (see Section 5.2.4). The latter one is also not true as solid fuel particles are not ideally spherical in general. Additional quantities such as orientation and rotation must be computed to include the effect of non-spherical particles. Recently, the inclusion of non-spherical particles into point-particle frameworks was studied in detail by Froehlich et al. [70]. However, considering non-spherical particle shapes increases computational costs significantly. Compared to the other physical effects, the influence of assuming spherical particles on the overall combustion process is considered minor and thus is neglected. Another possible effect, especially for coal particles, is the occurrence of fragmentation. The modeling of fragmentation is complicated and, at the current time, heavily relies on empirical data fitted to experiments. Since no data for the investigated particles are available, fragmentation is not taken into account. Overall, the neglect of non-spherical particle shapes and fragmentation is considered only to have a minor influence and, thus, does not constrain the validity of the results of this work.

In the following, the relevant physics required to describe the evolution of point particles are summarized. Certain parts of the particle model, for instance, modeling the particle conversion, are covered in Chapter 4.

2.3.2. Particle Movement

To track the particle through the computational domain, the following equation is solved for each particle

$$\frac{dx_{\text{prt},i}}{dt} = u_{\text{prt},i}. \quad (2.57)$$

The evolution of the particle velocity in Equation (2.57) is obtained from the sum of all forces acting on its mass center. An overview of all possible forces is given in [35], out of which only the drag F^{D} and gravity force F^{G} are considered within this work. The buoyancy force is not taken into account since the particle density is about three orders of magnitude higher than the gas phase density, $\rho/\rho_{\text{prt}} \ll 1$. Moreover, transient local pressure gradients over the particle are not resolvable, and thus, the resulting force is neglected. Considering the drag and gravity force, the particle velocity equation reads

$$m_{\text{prt}} \frac{du_{\text{prt},i}}{dt} = F_i^{\text{D}} + F_i^{\text{G}}. \quad (2.58)$$

Drag force

The drag force results from two contributions, namely viscous drag and pressure drag. The former one accounts for viscous forces in the particle's boundary layer, which forms due to the no slip condition at the particle surface. The pressure drag is a consequence of the mean pressure distribution around the particle. The drag force is given by

$$F_i^{\text{D}} = c_{\text{D}} \frac{1}{2} \pi \left(\frac{D_{\text{prt}}}{2} \right)^2 \rho |\vec{u} - \vec{u}_{\text{prt}}| (u_i - u_{i,\text{prt}}), \quad (2.59)$$

where c_{D} is the drag coefficient. For the interaction of non-reactive sphere particles with the flow, multiple established correlations exist [158; 228], which are solely a function of the particle Reynolds number

$$Re_{\text{prt}} = \frac{|\vec{u} - \vec{u}_{\text{prt}}| D_{\text{prt}}}{\nu}. \quad (2.60)$$

However, the release of gaseous matter from the particle changes the flow dynamics for reacting solid fuel particles. To extend the non-reacting correlation, an additional blowing Reynolds number is introduced

$$Re_{\text{blow}} = \frac{u_{\text{blow}} D_{\text{prt}}}{\nu} \quad (2.61)$$

where u_{blow} is assumed to be a homogeneous devolatilization velocity according to

$$u_{\text{blow}} = \frac{dm_{\text{prt}}}{dt} \frac{1}{\pi \rho D_{\text{prt}}^2}. \quad (2.62)$$

Using this definition, Bellan and Harstadt [13] derived based on available numerical simulations [31] the following correlation

$$c_{\text{D}} = \frac{24}{Re_{\text{prt}}} \frac{1 + 0.0545 Re_{\text{prt}} + 0.1 \sqrt{Re_{\text{prt}}} (1 - 0.03 Re_{\text{prt}})}{1 + a |Re_{\text{blow}}|^b}, \quad (2.63)$$

with $a = 0.09 + 0.077 \exp(-0.4 Re_{\text{prt}})$ and $b = 0.4 + 0.77 \exp(-0.04 Re_{\text{prt}})$.

Note that Equation (2.63) converges towards the case of a non-reacting particle for $Re_{\text{blow}} = 0$. The validity range of this correlation includes $0 \leq Re_{\text{prt}} \leq 100$ and $0 \leq Re_{\text{blow}} \leq 10$, which is sufficient for all investigated cases in this study.

Gravity force

The gravity is proportional to the particle mass and reads

$$F_i^G = m_{\text{prt}} g_i, \quad (2.64)$$

where g denotes the gravitational acceleration, which is set to 9.81 m/s^2 .

Particle response time

One important parameter to describe the interactions between gas phase and particle is the Stokes number, which is given by

$$St = \frac{\tau_{\text{prt}}}{\tau_F}, \quad (2.65)$$

where τ_{prt} and τ_F are the characteristic time scales of particle and flow, respectively. The flow time scale can be approximated by the ratio of the characteristic length to the characteristic velocity. The particle characteristic time, under the Stokes flow assumption (i.e., $c_D Re_{\text{prt}}/24 \approx 1$), is derived from equation (2.59) and reads

$$\tau_{\text{prt}} = \frac{\rho_{\text{prt}} D_{\text{prt}}^2}{18\mu}. \quad (2.66)$$

2.3.3. Particle Temperature

The evolution of the particle temperature results from summing up the three main contributions:

- heat transfer from/to the gas phase;
- temperature changes due to chemical reactions;
- radiative heat transfer.

These three terms form the right-hand side of the particle temperature equation, which reads

$$\frac{dT_{\text{prt}}}{dt} = \frac{3\alpha}{c_{p,\text{prt}}\rho_{\text{prt}}\frac{D_{\text{prt}}}{2}} \cdot (T - T_{\text{prt}}) + \frac{\Delta h_{\text{reac}}}{m_{\text{reac}}c_{p,\text{prt}}} + \frac{S_{r,\text{prt}}}{c_p\rho_{\text{prt}}}. \quad (2.67)$$

Here, the heat transfer coefficient α is given by

$$\alpha = Nu_{\text{prt}} \frac{\lambda}{D_{\text{prt}}}. \quad (2.68)$$

The Nusselt number Nu_{prt} is calculated from the Ranz Marshall correlation [191; 192], which reads

$$Nu_{\text{prt}} = 2 + 0.552 Re_{\text{prt}}^{1/2} Pr^{1/3}. \quad (2.69)$$

The second term in Equation (2.67) describes the reaction heat from heterogeneous particle reactions, and is discussed in detail in Chapter 4.

Finally, the particle radiative source term is calculated as follows

$$S_{r,\text{prt}} = -\frac{6Q_{\text{abs}}A_{\text{prt}}}{\pi d_p^3} (4\pi I_{b,\text{prt}} - G_{\text{prt}}), \quad (2.70)$$

where the blackbody intensity is computed as $I_{b,\text{prt}} = \sigma T_p^4/(\pi)$ and the variable G_{prt} corresponds to the interpolated incident radiation G in the particle position (see Section 2.4). The determination of the particle adsorption coefficient Q_{abs} is discussed in detail in Section 4.5.

2.3.4. Interaction with the Gaseous Phase

In the reactive multi-phase flows considered in this work, the gas and solid phase interact with each other. More specifically, mass, momentum, and energy are exchanged at their common interface. For the particle, this interaction is represented through the linear interpolation of gas-phase properties to the particle position. In the following, the back coupling from particle to gas phase is described. As previously discussed, this kind of mutual interaction between the two phases is denoted as two-way coupling.

Mass transfer

The mass release of reacting solid fuel particles results from either oxidation of the particle surface or devolatilization. The physical processes at the particle level and the determination of the released particle mass \dot{m}_{prt} are discussed comprehensively in Chapter 4. The mass source term for the gas phase, which acts on Equation (2.2), arises from the sum of released mass from all particles inside the corresponding control volume given by

$$S_{\text{prt},m} = \frac{1}{V_{CV}} \sum^{N_{\text{prt}}} \dot{m}_{\text{prt}}. \quad (2.71)$$

Momentum transfer

The momentum, which is transferred from particles to the gas phase, has two different origins. Firstly, the particles themselves act on the gas phase by viscous forces. Secondly, the released mass by the particle results also in a momentum transfer. Both mechanisms are summarized in the momentum source, which acts on equation (2.3), and read

$$S_{\text{prt},u_i} = \frac{1}{V_{CV}} \sum^{N_{\text{prt}}} (\dot{m}_{\text{prt}} u_i - F_i^D). \quad (2.72)$$

Species transfer

The exchanged masses have specific compositions which are taken into account via source terms in the respective species transport equation, which are as follows

$$S_{\text{prt},Y_k} = \frac{1}{V_{CV}} \sum^{N_{\text{prt}}} (\dot{m}_{\text{prt}} Y_{\text{prt},k}). \quad (2.73)$$

Specifics regarding the composition of the released mass are discussed in Chapter 4.

Heat transfer

Heat exchange occurs by three different mechanisms: thermal radiation, convective heat transfer, and enthalpy source from the released gases. The radiation particle interaction, is treated separately in Section 4.5 due to its high complexity. The second and third terms are directly considered in the gas phase source term for Equation 2.12, which reads

$$S_{\text{prt},h} = \frac{1}{V_{CV}} \sum^{N_{\text{prt}}} (\alpha (T_{\text{prt}} - T) \pi D_{\text{prt}}^2 + \dot{m}_{\text{prt}} h_{\text{release}}). \quad (2.74)$$

Note that generally for solid fuel particles, the enthalpy bounded to the released mass h_{release} does not correspond to $c_{p,\text{prt}} T_{\text{prt}}$ as is often the case for single-component fuels in spray combustion. Hence, it must be computed from the released composition of gases.

2.4. Thermal Radiation

The last unclosed term of the enthalpy balance in Equation (2.12), which describes thermal radiation, is addressed in the following section. Thermal radiation is a crucial mechanism for heat transfer in combustion processes. For instance, it provides a large share of the heat transfer to the walls. Furthermore, thermal radiation influences flame stabilization and overall process temperatures.

The following section briefly reviews the fundamentals of thermal radiation, including emissive power, solid angles, intensity and radiation heat flux, which are essential to describe the closure of the radiation source term in Equation (2.12). Afterwards, the radiative transport equation (RTE) is introduced and strategies to model the spectral dependency are reviewed. Finally, the interaction of radiation with turbulent flows is discussed.

2.4.1. Fundamentals of Thermal Radiation

Thermal radiation describes the energy transfer by electromagnetic waves. Compared to heat conduction (and convection), thermal radiation differs in two main characteristics. First, electromagnetic waves do not need a medium to travel. Hence, thermal radiation becomes dominant in low-pressure (vacuum) applications. Second, thermal radiation is proportional to the fourth power of temperature, while heat conduction and convection depend linearly on the temperature. Therefore, thermal radiation becomes increasingly important in high-temperature processes, such as solid fuel combustion.

In the following, the basics of thermal radiation providing are reviewed. The nomenclature bases on the textbooks of Modest [154] and Modest and Haworth [155].

Electromagnetic Spectrum

From the electromagnetic point of view, thermal radiation is defined as electromagnetic waves emitted by a medium only due to its temperature [154]. The following properties define an electromagnetic wave:

- Frequency (ν_w);
- Wavelength (λ_w);
- Wavenumber (η);
- Angular Frequency (ω_w);

These properties are related as follows

$$\nu_w = \frac{\omega}{2\pi} = \frac{c_l}{\lambda_w} = c_l \eta. \quad (2.75)$$

Here, c_l denotes the speed of light, which corresponds to the propagation speed of radiation. In a vacuum the speed of light is $c_{l,0} = 2.998 \cdot 10^8$ m/s. The ratio of speed light in a medium compared to the vacuum is given by the refraction index $n_r = c_{l,0}/c_l$, which is close to one in most gases for wavelengths in the visible part of the electromagnetic spectrum [154]. The energy ϵ_w of each wave (or photon) is determined from quantum mechanics by the following relation

$$\epsilon_w = h_{\text{Pl}} \nu_w, \quad (2.76)$$

where $h_{\text{Pl}} = 6.626 \cdot 10^{-34}$ J s is denoted as *Planck's constant*.

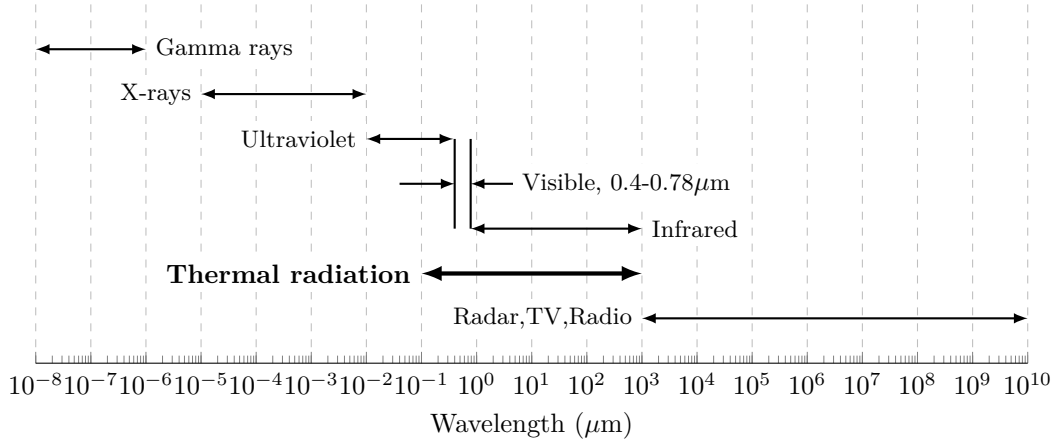


Figure 2.3.: Electromagnetic spectrum indicating the important spectral range of thermal radiation. Adapted from [154].

The electromagnetic spectrum is depicted in Figure 2.3 and shows that the range necessary for heat transfer calculation starts from 0.1 μm up to 100 μm . It spans over parts of the ultraviolet range, includes the complete visible range, and finally reaches the infrared part of the spectrum.

When an electromagnetic wave travels past an interface between two media, the frequency ν_w remains constant, but the wavelength λ_w changes depending on the refraction index n_r . Solid or liquid surfaces that adsorb all incoming radiation within a very thin surface layer are called *opaque*. If additionally radiation is by reflected by an *opaque* surface, it is called *blackbody*.²

Emissive power

The radiative heat flux emitted from a surface, the so-called emissive power E , depends on the temperature and material properties. Both the definition based on the spectral (per unit wavelength) and the total (over the entire spectrum) are valid and related by

$$E(T) = \int_0^{\infty} E_{\lambda_w}(T, \lambda_w) d\lambda_w. \quad (2.77)$$

A blackbody is not only a perfect absorber but also a perfect emitter. Hence, the blackbody emission surpasses those from other surfaces with identical temperatures. The blackbody emissive power is derived from quantum statistics and reads

$$E_{b,\lambda_w}(T, \lambda_w) = \frac{2\pi h_{\text{Pl}} c_{1,0}^2}{n_r^2 \lambda_w^2 [\exp(h_{\text{Pl}} c_{1,0} / n_r \lambda_w k_{\text{Bo}} T) - 1]}, \quad (2.78)$$

where $k_{\text{Bo}} = 1.3806 \cdot 10^{-23}$ J/K is denoted as *Boltzmann's constant*.

Further, the total blackbody emissive power is obtained through integration of Equation (2.78) over the entire spectrum

$$E_b(T) = n_r^2 \sigma_{\text{SB}} T^4, \quad (2.79)$$

with $\sigma_{\text{SB}} = 5.670 \cdot 10^{-8}$ W/(m²K⁴) being the *Stefan-Boltzmann constant*.

²This name originates from the fact that such a surface appears black to the human eye.

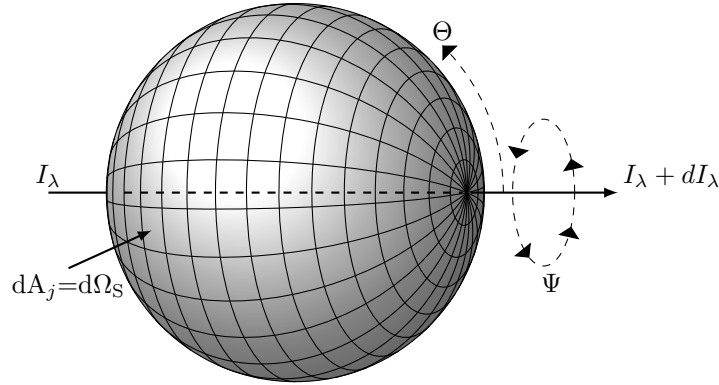


Figure 2.4.: Schematics of the solid angles, adapted from [82].

Solid Angles

Since the radiative flux varies with direction when passing through a point P , a description based on spherical coordinates using the unit directional vector s_i , the polar angle Θ , and the azimuthal angle Ψ is convenient.

On that basis, the solid angle Ω_S of an infinitesimal surface dA_j for a given point P is defined as the projection of the surface dA_j onto a plane normal to the direction vector divided by the distance squared. Considering a unit sphere, the solid angle Ω_S corresponds to the infinitesimal area element of the surface dA_j , as depicted in Figure 2.4. Thus, the infinitesimal solid angle reads

$$d\Omega_S = dA_j = \sin\Theta d\Theta d\Psi. \quad (2.80)$$

The integration over all solid angles for the unit sphere yields 4π , as evident from Figure 2.4.

Radiative Intensity

To describe the directional dependency of the thermal radiation, the radiative intensity I , which can be expressed on a spectral basis or on a total basis, is introduced

$$I(s_i) = \int_0^\infty I_{\lambda_w}(s_i, \lambda_w) d\lambda_w. \quad (2.81)$$

Unlike the emissive power, the radiative intensity I depends not only on the wavelength λ_w but also on the direction vector s_i . Therefore, the intensity must be integrated over all solid angles to obtain the emissive power.

The blackbody intensity, which is by definition directionally independent, can be expressed by the blackbody emissive power

$$I_{b\lambda_w} = \frac{E_{b\lambda_w}}{\pi}. \quad (2.82)$$

Radiative Heat Flux

The encounter of radiation from an infinitesimal solid angle on a surface leads to an infinitesimal heat flow rate per wavelength

$$dQ_{\lambda_w} = I_{\lambda_w}(s_i) d\Omega dA \cos(\theta). \quad (2.83)$$

By combining incoming and outgoing contributions at a given point, the net flux is obtained

$$q_{\text{rad,net}} = \int_{4\pi} I_{\lambda_w}(s_i) \cos(\Theta) d\Omega_S. \quad (2.84)$$

The total radiative heat flux at the surface is derived by replacing $\cos(\Theta)$ with $n_i s_i$ and integrating Equation (2.84) over the entire spectrum

$$q_{\text{rad},i} n_i = \int_0^\infty q_{\lambda,i} n_i = \int_0^\infty \int_{4\pi} I_{\lambda_w}(s_i) s_i n_i d\Omega_S d\lambda_w. \quad (2.85)$$

The surface characterized by the unit vector n_i may be imaginary. Therefore, the radiative heat flux of a participating medium is obtained by removing n_i in Equation (2.85).

The radiative heat source, which is required to close the energy balance in Equation (2.12), is calculated by taking the divergence of the radiative heat flux

$$S_{\text{rad}} = -\frac{\partial q_{\text{rad},i}}{\partial x_i}. \quad (2.86)$$

2.4.2. Modeling Thermal Radiation

The inclusion of thermal radiation into CFD simulations introduces three new challenges:

1. The radiative transfer equation (RTE), an integrodifferential equation in five independent variables, needs to be solved.
2. Absorption coefficients κ_j of the participating species (mainly CO_2 and H_2O) depend strongly on the wavenumber ν .
3. Turbulence-radiation interactions (in particular, the non-local adsorption term) are challenging to model.

The following sections address the treatment of these three aspects.

2.4.2.1. RTE in Participating Media

To evaluate the radiative source term in Equation (2.86), the spectral radiative intensity I_η is required. This radiative intensity is obtained from the RTE [154]

$$\frac{dI_\eta}{ds} = \underbrace{\kappa_\eta I_{b,\eta}}_{\text{emission}} - \underbrace{\kappa_\eta I_\eta}_{\text{adsorption}} - \underbrace{\sigma_{s,\eta} I_\eta}_{\text{outscattering}} + \underbrace{\frac{\sigma_{s,\eta}}{4\pi} \int_{4\pi} I_\eta(\hat{s}_i) \Phi_\eta(\hat{s}_i, s_i) d\Omega_S}_{\text{inscattering}}. \quad (2.87)$$

This equation describes the radiative intensity change along its path s by emission (reduction), adsorption (growth), inscattering (growth), and outscattering (reduction). Here, \hat{s}_i ³ and s_i are the unit vectors, $\sigma_{s,\eta}$ is the spectral scattering coefficient, and Φ_η denotes the scattering phase function. The RTE exhibits that the local spectral intensity I_η depends on non-local quantities, the direction, and the wavenumber.

For multi-phase flows, the scattering effects of the gas phase are significantly smaller compared to the scattering influence of the particles. Therefore, the scattering coefficients of the gas phase are set to zero, and only the particle scattering is taken into account [154]. The details about the evaluation of the radiative particle properties are subject to Section 4.5.

³: denotes a second direction.

The radiation source term in Equation (2.86) is calculated from the difference between local absorption and local emission

$$S_{\text{rad}} = -\frac{\partial q_{\text{rad},i}}{\partial x_i} = -\int_0^\infty \kappa_\eta \left(4\pi I_{b\eta} - \int_{4\pi} I_\eta d\Omega_S \right) d\eta. \quad (2.88)$$

2.4.2.2. Radiative Properties

While radiative transfer characteristics of opaque walls are often described by gray emission (i.e., coefficients have no spectral dependency), for absorption and reflection, the rapidly changing properties of molecular gases prevent the usage of such assumption [49]. Absorption and emission of radiative energy on a molecular level means the rise and drop of the molecule's vibrational or rotational energy levels. Due to the quantification, these energy levels form thousands of discrete lines. The precise energy required is altered by molecular collisions and molecular movement, broadening spectral lines. The locations, strengths, and widths of spectral lines are collected in modern databases (e.g., HITRAN, HITEMP [205; 206]).

In principle, the calculation of the radiative heat flux from the entire spectrum requires the evaluation of the RTE for numerous wavenumbers, denoted as line-by-line (LBL) calculations. Several reduced models were developed to overcome these extensive simulations.

Optically Thin Approximation

The optically thin approximation only considers the emission. Hence, all emission escapes the flame without being adsorbed. This assumption holds if the mean free path of the photon is larger than the absorption coefficient. This ratio is denoted as the optical thickness of a medium. If the optical thickness is small, most photons will leave the flame without being adsorbed, justifying the neglect of self-absorption. With this assumption, the radiative source term (2.88) simplifies to

$$S_{\text{rad}} = -\frac{\partial q_{\text{rad},i}}{\partial x_i} = -4\pi \int_0^\infty \kappa_\eta I_{b,\eta} d\eta = -4\kappa\sigma T^4, \quad (2.89)$$

which always results in local heat losses. This simple model is often used because no RTE needs to be solved. For small laboratory flames, the radiation behavior is predicted reasonably well. However, the model overpredicts radiative heat losses significantly for larger flames and underestimates the flame temperature.

Narrow Band Models

The idea of the narrow band models is to form a narrow band average (with a $\Delta\eta = 4 - 25 \text{ cm}^{-1}$) assuming that the blackbody intensity remains constant within small spectral ranges. If an appropriate approximation for the emissivity is found, the total intensity can be obtained by

$$I(s) = \int_0^\infty I_\eta(s) d\eta = \int_0^\infty \bar{I}_\eta(s) d\eta. \quad (2.90)$$

Several narrow band models, which mainly differ in the band determination, are proposed in the literature. However, all models have in common that the RTE needs to be solved for extensive vast of Narrow-Bands (>10), which might be too expensive for large scale computations [155].

Weighted-Sum-of-Gray-Gases

The weighted-sum-of-gray-gases (WSGG) approach is a global model. Global models integrate over the entire spectrum prior to solving the RTE, leading to a small number of RTE evaluations.

After the initial development of this approach by Hottel for the zonal method [94], the general extension of the model for the RTE by Modest [153] increased the popularity of this approach significantly.

The model assumes that a weighted sum of gray gases can approximate the total emissivity

$$\epsilon(s, T) = \sum_{n=0}^{N_{GG}} a_n(T)(1 - e^{-\kappa_n s}). \quad (2.91)$$

The adsorption coefficients κ_η are constants, whereas the weighting factors a_n are allowed to depend on the temperature. Moreover, the requirement of unity emissivity in an infinitely thick medium requires the sum of the weighting factor to be one $\sum_{n=0}^N a_n = 1$. According to Hottel and Sarofim [94], depending on the quality of the fit, two to three grey gases are sufficient to approximate the emissivity. To consider spectral windows (i.e., $\kappa_\eta \approx 0$), κ_0 is set to zero.

Extending this model for the RTE, the computation of the total radiative intensity from the gray gases is given by

$$I(s) = \sum_{n=0}^{N_{GG}} I_n(s). \quad (2.92)$$

Hence, the solution of the RTE is only required for $N+1$ grey gases, reducing computational efforts significantly. Additionally, the WSGG model may be applied to scattering media and reflecting walls, simply by replacing κ_η and $I_{b,\eta}$ by κ_n and $[a_n I_b](T)$ in Equation 2.87, respectively. Within the WSGG model, scattering and surface properties (e.g., $\sigma_s, \Phi, \epsilon_W$) are assumed to be gray (i.e., constant over the spectrum).

Early WSGG parameters were based on experimental data [154]. However, recently serious efforts were made to obtain coefficients based on HITEMP, especially for high concentrations of radiating gases, which is essential for the oxy-fuel conditions studied in this thesis [16; 43].

2.4.2.3. Turbulence-Radiation-Interaction (TRI)

Due to non-resolved temperature and concentration fluctuations, TRI might significantly influence simulation results, especially for RANS or LES at coarse resolutions. Different techniques can be applied to model TRI, which are summarized in a comprehensive review by Coelho [33]. TRI addresses the treatment of the radiative source term $\overline{S_{rad}}$ in the enthalpy equation in case of averaging (RANS) or filtering (LES). The source term $\overline{S_{rad}}$ is commonly separated into two parts, one containing the emission part $\overline{S_{emi}}$ and one the adsorption part $\overline{S_{ads}}$.

The filtered emission term

$$\overline{S_{emi}} = 4\pi \overline{\kappa(T, p_\alpha) I_b(T)} \quad (2.93)$$

only depends on local scalars (e.g., temperature and species partial pressure). Recent studies by Miranda et al. [151; 152] suggest that for LES, the use of Dirac- δ function for the subgrid contribution is sufficient. Although these results are only reported for single-phase combustion, these approximations have been used through this thesis for multi-phase flows. Further research on the effect of multi-phase subgrid contributions for LES radiation modeling is required to quantify such assumptions.

Absorption TRI is difficult to model due to the non-locality of the incident radiation G_ν

$$S_{abs} = \int_0^\infty \kappa_\eta G_\eta d\eta, \quad \text{with} \quad G_\eta = \int_{4\pi} I_\eta d\Omega. \quad (2.94)$$

However, different studies showed a weak influence of far-field fluctuations on the local absorption [32; 103; 227]. This statement holds if the mean free path for radiation is much larger than the

turbulence length scale. Using this assumption, which is typically referred to as the optically thin eddy approximation or optically thin fluctuation assumption (OTFA), the adsorption term is modeled as

$$\overline{\kappa_\nu G_\nu} \approx \overline{\bar{\kappa}_\nu G_\nu} \quad \text{if} \quad \kappa_\nu l_t \ll 1, \quad (2.95)$$

where l_t is the turbulent length scale.

3. Numerical Treatment of Turbulent Flames

The increase of computational resources in the last few decades significantly contributed to the emergence of CFD as an indispensable tool for efficient engineering designs, not only for aerodynamic applications but also for reacting systems. However, turbulent combustion involves many coupled phenomena at different scales, resulting in several challenges for CFD inclusion. Thereby, four of the main problems associated with turbulent flames in the context of pulverized coal combustion are:

1. The fluid mechanical properties such as the turbulent flow field must be precisely described due to their strong interaction with chemical reactions (turbulence-chemistry-interactions (TCI)) and all transport phenomena occurring in flames.
2. Detailed chemical kinetics are required to correctly predict the consumption rate of the fuel, the combustion zone (i.e., ignition, stabilization or extinction of reactions) and pollutant formation.
3. Multiple fuel streams interact with each other in solid fuel combustion. Hence, the formation of gaseous reactants depends on complex interactions between the release from the solid, turbulent mixing, and combustion.
4. Thermal radiation interacts with the combustion process, particles, and reactor walls.

Concerning modeling of turbulent flow fields, the approach of DNS, where all turbulent scales are directly computed, comes with prohibitive numerical costs as previously outlined in Section 2.2.1. Nevertheless, DNS can still be a valuable tool for model development since no closures for turbulent fluxes and filtered reaction rates are required. With respect to reactive simulations of industrially relevant applications, the development of effective strategies for incorporating chemistry into LES is one main objective of recent research. However, only filtered quantities are available in LES, requiring additional modeling efforts for the turbulence-chemistry interaction at the subgrid-scale (sgs-TCI). To consider the chemical reactions, the straightforward but costly approach consists of taking a suitable chemical kinetic mechanism for the considered fuel, solve scalar transport equations for all species in the mechanism, and model the filtered source term in each equation. However, this direct approach involves solving tens of species and hundreds of reactions already for simple fuels such as methane. This problem is aggravated for solid fuels due to the complex fuel species involved in gas-phase reactions. Unless mechanism reduction methods can significantly reduce the enormous size of the chemical system, solving a multitude of stiffly coupled scalar transport equations remains prohibitive for large-scale simulations. Thus, an essential modeling aspect in LES appears to minimize the number of transported scalar variables required to describe multicomponent diffusion-reaction processes accurately. With this objective, many works have been devoted to turbulent combustion modeling, following a variety of approaches and distinct modeling strategies, which are comprehensively discussed in several review papers [100; 179; 181; 251].

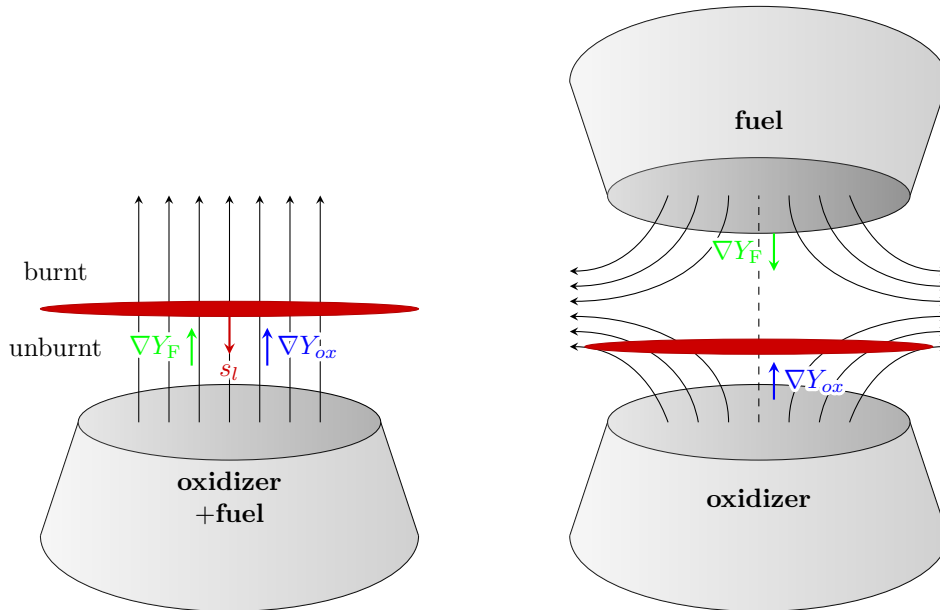


Figure 3.1.: Schematic representation of a premixed flame in a flat flame configuration (left) and a non-premixed flame in a counterflow configuration (right). The characteristic transport of fuel and oxidizer towards the reaction zone is depicted (fuel in green and oxidizer in blue).

In the following, the modeling strategies to deal with the challenges mentioned above are discussed. Besides including TCI (corresponding to the first two points), the focus is on the extension of state-of-the-art single-phase combustion models to multi-phase solid fuel combustion. In particular, the treatment of multiple fuel streams (point three) and the inclusion of substantial heat losses (point four) are addressed. First, the general characteristics of the two main combustion regimes, namely premixed and non-premixed combustion, are discussed. These serve as the foundation for many combustion models, including those employed in this work. After that, the two main strategies to include tabulated chemistry models into simulations and the required extensions for the PCC are discussed. In the end, strategies to model TCI in the LES context are covered.

3.1. Properties of Premixed and Non-Premixed Flames

Depending on how fuel and oxidizer are supplied to the reaction zone, combustion is distinguished into two distinct regimes: premixed and non-premixed. The former describes the reaction of a perfectly premixed oxidizer and fuel mixture. A schematic flat flame configuration for a premixed flame is depicted on the left side of Figure 3.1. On the contrary, for non-premixed combustion, oxidizer and fuel are separated, and a reaction zone is established in the mixing layer. A representative configuration for a non-premixed flame is the counterflow configuration shown on the right-hand side of Figure 3.1.

The main characteristics of both laminar premixed and non-premixed flames are often used in turbulent combustion modeling and are briefly outlined in the following.

3.1.1. Premixed Laminar Flame Characteristics

Considering a path perpendicular through the flat flame in Figure 3.1, an exemplary structure of a laminar premixed flame can be extracted that is depicted on the left-hand side in Figure

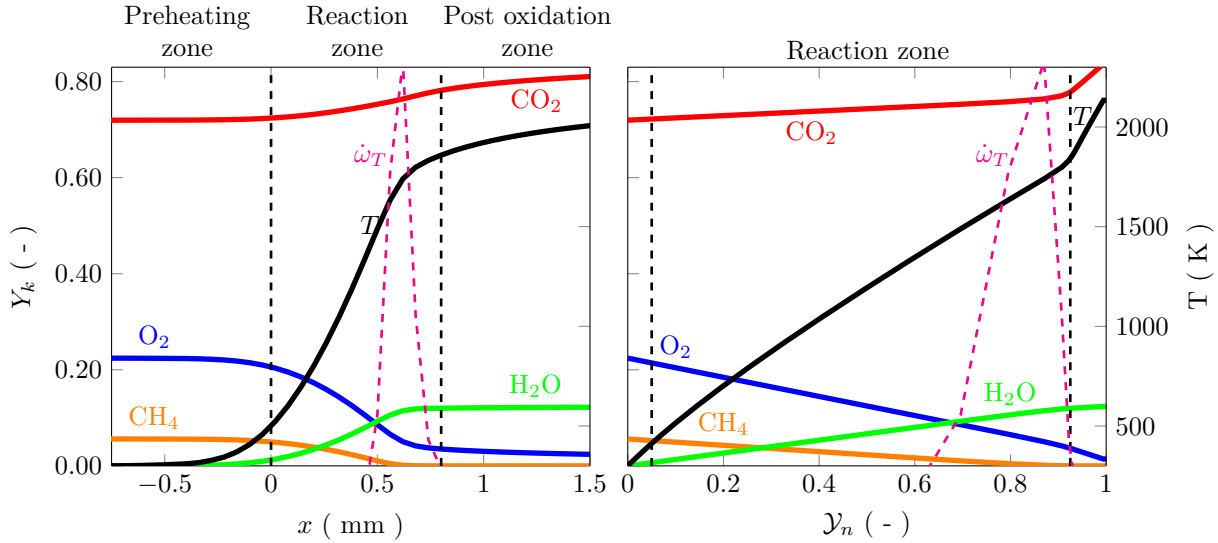


Figure 3.2.: Exemplary premixed flame structure for a stoichiometric methane oxy-fuel mixture. Left: Physical coordinates. Right: Composition space coordinates.

3.2. The considered premixed flame structure illustrates the reaction of methane in an oxy-fuel atmosphere (i.e., oxidizer composed of O_2 and CO_2). A thin reaction zone, indicated by a steep temperature gradient, separates oxidizer and fuel from burnt combustion products. Another essential characteristic of a premixed flame is the propagation towards the fresh gases. The propagation is caused by thermal fluxes originating from the temperature increase, which result in preheating and subsequent reaction of fresh gases. Hence, the premixed flame can be divided into the preheating, reaction, and post-oxidation zones. As depicted in Figure 3.2, in the preheating zone, both oxidizer and fuel are preheated, supplying the energy for the subsequent reaction. After the reaction zone, most of the chemical reactions are completed, and only slow species are formed in the post-oxidation zone until chemical equilibrium is reached. In Figure 3.2, both the fuel and the oxidizer are fully converted, indicating a stoichiometric mixture. However, for lean mixtures, the excess oxygen remains after the flame. Contrary, a rich mixture leads to a fuel surplus in the flue gases. For mixtures outside of the flammability limits, no premixed flames exist.

Considering a one-step irreversible chemical reaction (i.e., reactants \longrightarrow products), the flame can be uniquely defined by a reaction progress variable \mathcal{Y} , which is zero in the fresh gas and unity in the fully burnt products. For this simple reaction, the progress variable may be defined as a reduced temperature or a reduced mass fraction of fuel or oxidizer, which is equivalent for unity Lewis numbers [251]. However, for more complex reaction schemes, more sophisticated progress variable definitions are required. Generally, a weighted linear combination of species mass fractions $\mathcal{Y} = \sum_k b_k Y_k$ is employed. The choice depends on both the investigated operating conditions and the considered fuel. For an appropriate definition of the progress variable, certain conditions must be fulfilled:

- The progress variable must provide a unique relationship with the remaining thermochemical state, i.e., strictly monotonic slope (either positive or negative).
- The entire flame should be covered by the progress variable, which is strictly speaking often not fulfilled due to the formation of minor species in the post-oxidation zone.
- The source term of the progress variable should be well resolvable. However, this condition

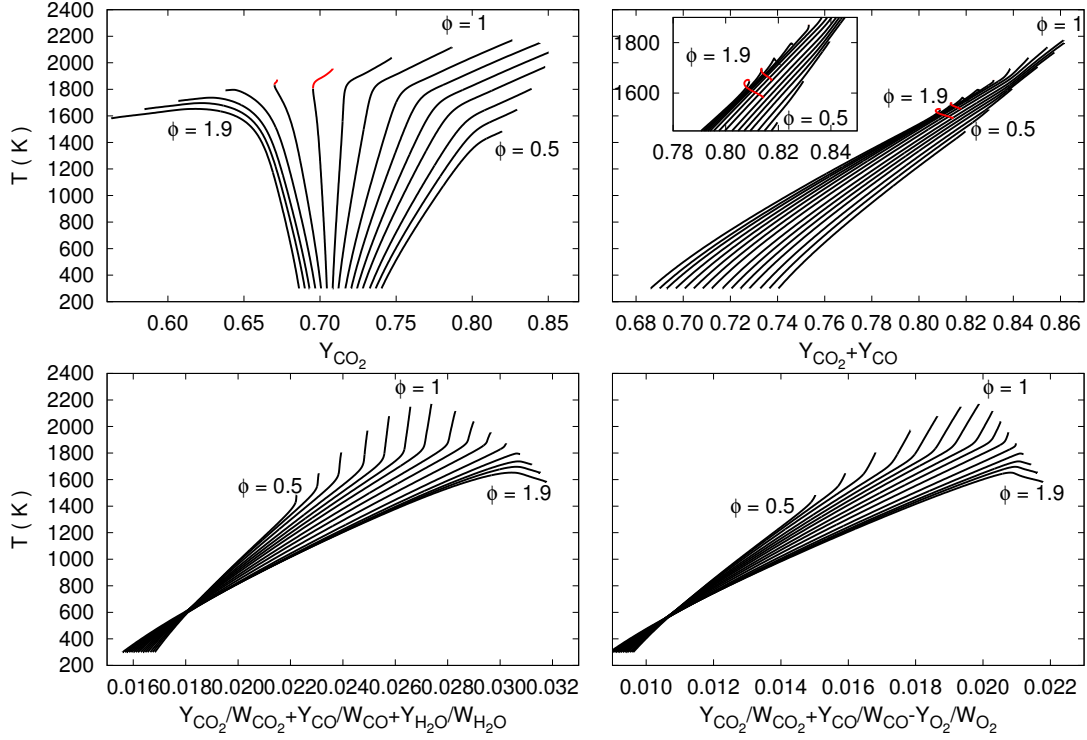


Figure 3.3.: Comparison of monotonicity for the temperature over different progress variables for several equivalence ratios. Non-monotonic parts are marked red.

represents more a numerical advantage rather than an obligation.

As a general rule, the species combinations for the progress variable must be selected specifically for certain reactants. Therefore, this is discussed here for oxy-fuel atmospheres; also because, there are considerable differences when using pure air as the oxidizer. Figure 3.3 shows various progress variables that are classically also used for methane-air combustion [118; 244]. Both CO_2 and the combination of CO_2 and CO exhibit significant non-monotonicity for specific areas (shown in red). Although these progress variables are often used in methane-air combustion, they are not suited for oxy-fuel combustion. The other two progress variables can be used to describe the premixed flame uniquely. In this work, a combination of the massfractions of Y_{CO_2} , Y_{CO} and Y_{O_2} is used

$$\mathcal{Y} = \frac{Y_{\text{CO}_2}}{W_{\text{CO}_2}} + \frac{Y_{\text{CO}}}{W_{\text{CO}}} - \frac{Y_{\text{O}_2}}{W_{\text{O}_2}}, \quad (3.1)$$

which is weight by the molecular weights W_{CO_2} , W_{CO} and W_{O_2} , respectively.

Figure 3.2 depicts premixed flame structure conditioned onto the progress variable. In this representation, the reaction zone is significantly enlarged. In contrast, the preheating and post-oxidation zones are confined to the boundaries of the progress variable.

Besides the structure, global characteristics of premixed flames are beneficial for their modeling and therefore are introduced in the following.

Flame Speed

One important global characteristic of a premixed flame is the flame propagation. Different measures can be introduced to quantify this propagation [181]. For instance, the absolute flame

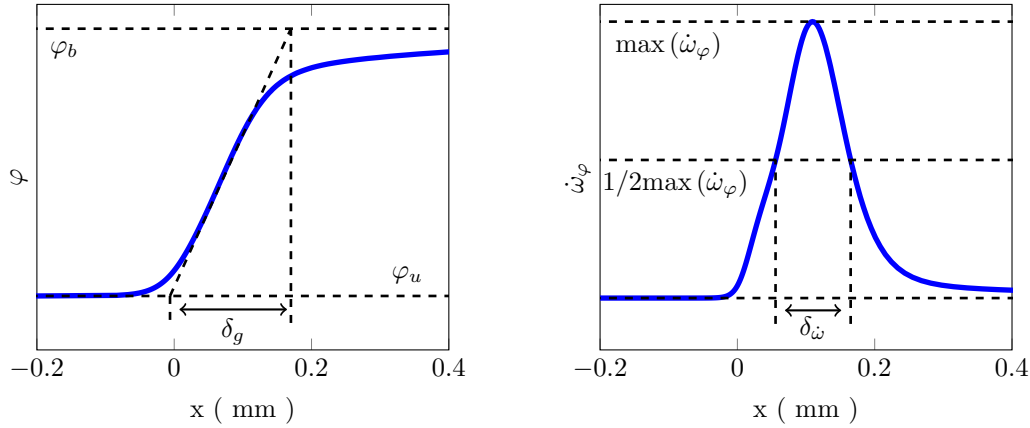


Figure 3.4.: Definitions of flame thicknesses. Left side: Definition based on the maximum gradient of an arbitrary scalar φ . Right side: Definition by means of the source term of the scalar φ .

speed describes the movement of the flame in a fixed reference system. On the other hand, the displacement speed describes the difference between gas and flame front velocity. The laminar burning velocity is an often employed quantity, which is uniquely defined for an undisturbed premixed flame. Hence, it only depends on the fresh gas mixture, temperature, and pressure. A more general definition is the consumption speed, which is calculated from species fluxes and the integration of the species source term

$$s_l = \frac{1}{\rho_u (Y_{k,b} - Y_{k,u})} \int \dot{\omega}_{Y_k} dx. \quad (3.2)$$

Here, u and b denote unburnt and burnt states, respectively.

Flame Thickness

An additional important characteristic of a premixed flame is its thickness. For instance, this property is used to estimate the grid size required to resolve the flame front. Several definitions are available in the literature to define the laminar flame thickness of a premixed flame [181]. The most common ones use the gradient of scalars or the width of species source terms. Based on the profile of the scalar φ , the flame thickness is obtained from the difference between the maximum and minimum value of φ divided by its maximum gradient

$$\delta_\varphi = \frac{\varphi_{\max} - \varphi_{\min}}{\max(\partial\varphi/\partial x)}. \quad (3.3)$$

One often-used scalar in this definition is the temperature, which provides representative flame thicknesses [181]. However, the resolution of the species source term is also essential to preserve the correct flame speed, as shown in the previous paragraph. Hence, the source term width presents an additional suitable quantity to express the flame thickness. Thereby, the thickness of the flame is obtained by taking the full width at half maximum $\delta_{\omega,FWHM}$ [181]. Both thicknesses are schematically depicted in Figure 3.4.

3.1.2. Non-Premixed Laminar Flame Characteristics

In laminar non-premixed flames, fuel and oxidizer are initially separated and the reaction zone forms where fuel and oxidizer are mixed. Thus, the burning rate is determined by the molecular diffusion of the reactants toward the reaction zone. Considering a steady-state counterflow

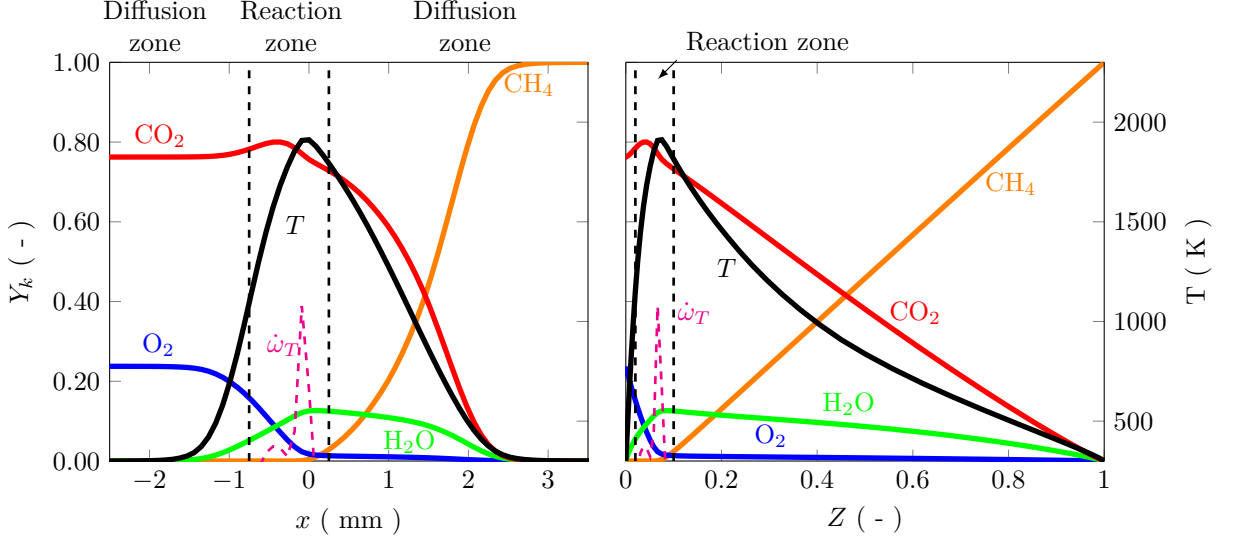


Figure 3.5.: Exemplary non-premixed flame structure for methane reacting in an oxy-fuel atmosphere. Left: Physical coordinates. Right: Composition space coordinates.

configuration, as depicted on the right-hand side of Figure 3.1, the heat amount transported away from the reaction zone equals the heat released by combustion. The flame is established in the vicinity of the stagnation point. Increasing the jets' velocity above a certain critical value results in quenching since heat fluxes leaving the reaction zone are greater than the heat released by combustion. Hence, the flame structure and mixing zone thickness depend on characteristic times representative for molecular diffusion and chemistry [132]. Thus, non-premixed flames do not possess a self-induced propagation mechanism but are controlled by mixing. Furthermore, the thickness of the non-premixed flame depends on the local flow, which is distinctly different from premixed flames.

Figure 3.5 illustrates the non-premixed flame structure along the symmetry axis of a counterflow burner. As discussed previously, a reaction zone forms in the mixing region with a temperature maximum near the stoichiometric condition. The reaction zone is surrounded by two diffusion zones, one on the fuel side and one on the oxidizer side. Consequently, the internal structure of diffusion flames can be characterized by the mixing process. Considering the element fraction, a mixture fraction Z that evolves through the diffusive layer from zero (oxidizer) to unity (fuel) can be derived. First, a coupling function is introduced

$$b_c = \sum_{\alpha=1}^{N_e} \beta_{\alpha} \sum_{k=1}^{N_s} c_{\alpha,k} \frac{W_{\alpha}}{W_k} Y_k, \quad (3.4)$$

where β_{α} is the weighting factor of the element α in the mixture fraction and $c_{\alpha,k}$ denotes the fraction of the element α in the species Y_k . Normalizing the coupling function with its oxidizer and fuel values results in the mixture fraction

$$Z = \frac{b_c - b_{c,ox}}{b_{c,f} - b_{c,ox}}, \quad (3.5)$$

which becomes 0 for pure oxidizer and 1 for pure fuel. For the conserved scalar Z , a transport equation can be derived, which reads

$$\frac{\partial \rho Z}{\partial t} + \frac{\partial \rho u_i Z}{\partial x_i} = \frac{\partial}{\partial x_i} \left(\frac{\lambda}{c_p} \frac{\partial Z}{\partial x_i} \right), \quad (3.6)$$

under the assumption of unity Lewis numbers for all species (i.e., $\rho D_z = \lambda/c_p$). Similar to the premixed flame, the non-premixed flame properties can be expressed in terms of the mixture fraction, as depicted on the right-hand side of Figure 3.5.

3.2. Flamelet-based Tabulation Methods for Turbulent Flames

Due to the high cost associated with directly solving detailed mechanisms, flamelet-based tabulation methods gained attraction over recent years and are also applied in this work for PCC. These models rely on the separation of timescales involved in chemistry and flows. For chemistry, a broad range of scales reaching from 10^{-9} to 10^2 s are present. In contrast, flow timescales take place in a smaller range [136]. The Damkoehler number describes the ratio of both timescales

$$Da = \frac{\tau_t}{\tau_c}, \quad (3.7)$$

where τ_t and τ_c denote the timescale of the turbulence and chemistry, respectively. For large Damkoehler numbers, the interaction of the turbulence with the inner flame structure is considered neglectable and a *thin flame sheet* forms. Hence, only small changes tangentially to the flame front are expected, whereas significant changes occur perpendicular to the flame. Thus, one-dimensional structures, so-called flamelets, can be identified along the flame sheet's normal direction, resulting in the possibility to represent a multidimensional turbulent flame by an ensemble of laminar flamelets [176].

One additional benefit of the flamelet representation of turbulent flames is the possibility to precalculate one-dimensional flame structures that are subsequently parameterized and stored in a flamelet table. Thereby, computational costs associated with solving transport equations for each species in the kinetic mechanism as well as evaluating thermodynamic properties and reaction source terms are significantly reduced since only a reduced set of variables must be solved.

Generally, both of the previously introduced trajectory variables, i.e., progress variable \mathcal{Y} for premixed flames and mixture fraction Z for non-premixed flames, are suitable to represent the flame-normal component. However, by choosing one of the two variables, it is implied that the underlying flame structure is either premixed or non-premixed.

Both, developments on the non-premixed flamelets going back to flamelet model proposed by Peters [176] and developments with respect to premixed flamelets (e.g., *Flamelet Generated Manifolds* (FGM) [244] and *Flame prolongation of ILDM* (FPI) [74]) are available in the literature. Despite the assumption of the underlying flame structure, flamelet-based tabulation has been successfully applied to a wide range of configurations, including partially-premixed, stratified, and spray flames [119; 208; 252]. Low computational costs make tabulated chemistry models also appealing for PCC. However, several extensions are required to apply flamelet-based tabulation models for solid fuel combustion, which are outlined next.

3.3. Flamelet Modeling for PCC

As discussed previously, prior to the application of the flamelet model, one must define the underlying flame structure either as premixed or as non-premixed. However, for PCC, the correct choice is not obvious. While a non-premixed flame structure is expected to form for single-particle combustion, the choice becomes less straightforward for a real burner. Generally, turbulent mixing with the continuous recirculation of flue gases leads to complex premixed and non-premixed combustion interactions. For instance, increased mixing times for fuel and

oxidizer might lead to partially-premixed combustion. To account for partially-premixed combustion, Knudsen and Pitch proposed a flame index [112], that enables a distinction between non-premixed and premixed combustion modes. Based on the flame index, either a non-premixed or a premixed flamelet table is used to obtain the thermo-chemical state. Nevertheless, this method only accounts for the premixed and non-premixed limits accurately, and states associated with multi-mode combustion are not correctly predicted by this approach [20; 185]. To overcome this limitation, Nguyen et al. [160] introduced a promising approach by using a two-dimensional composition space model to obtain the thermo-chemical state. Thereby, the interaction between the mixture fraction and progress variable is described by three dissipation rates (one for each control parameter and one cross dissipation rate), resulting in a five-dimensional table. Although new developments indicate that the table might be reduced by one dimension using orthogonal coordinates [215], these approaches are not yet fully comprehended. Therefore, they are the subject of current research in the case of pure gas-phase combustion. Furthermore, the additional physical effects required for PCC (e.g., multiple fuel streams, heat-losses, and sgs-TCI), the table size exceeds current tabulation capabilities significantly. Considering these challenges, the extension of two-dimensional composition space models to PCC is currently not possible.

Both purely premixed and non-premixed flamelet approaches were used to describe PCC. The main findings of previous studies¹ are summarized Table 3.1. Overall, both premixed and non-premixed flamelet approaches showed promising results in different applications. To compare the performance of both approaches, Messig et al. [147] evaluated the models in a counterflow pulverized coal flame, considering only the devolatilization process. The authors found that both approaches can correctly predict the coal flame. However, in regions beyond the flammability, the premixed table exhibits deviations from the reference solution. Similar results were reported by Wen et al. [264; 265], who assessed the models' performance in the mixing layer DNS data of Rieth et al. [201]. Although both premixed and non-premixed flame structures can be identified in coal flames, the premixed table's overall error was more significant than the non-premixed table. However, these results were obtained only by an *a priori* analysis, i.e., the influence of the coupling in the LES was not considered. Moreover, both studies evaluated simplified configurations, which do not allow for a final evaluation of the most appropriate modeling approach. To conclude, there is still a need for research with respect to *a posteriori* assessment of different flamelet tabulation methods. In particular, the impact of the different flamelet tabulation methods must be evaluated in a fully coupled simulation, which features all physical phenomena of practical relevance. At present, the flamelet structure should be carefully selected considering the configuration under investigation (e.g., laboratory-scale configuration with assisting premixed flames are more suitable for premixed flames, whereas self-sustained coal combustion is predominantly a non-premixed process).

Both premixed and non-premixed flamelet models are applied within this work. However, as evident from the previous discussion, additional physical aspects must be considered before the models can be applied to PCC. First, the employed models (i.e. the *flamelet progress variable model* (FPV) for turbulent non-premixed combustion and the *flamelet generated manifold* model (FGM) for turbulent premixed combustion) are briefly described. Afterwards, a summary of the extensions required to couple these approaches to PCC is given. Among these are the inclusion of strong heat losses and multiple fuel streams in the different models. The specifics of coupling these different models with the LES solver are explained at the end of each section.

¹As indicated by the date of these studies, the field of flamelet modeling for PCC is the subject of current research. Consequently, some of the studies were published during the creation of this work. These studies are also reviewed here since these have influenced modeling choices (e.g., initial development of a premixed flamelet model, which is later exchanged by a non-premixed flamelet model).

Table 3.1.: Literature overview of flamelet models applied to PCC.

Study	Configuration	Solid fuel conversion	Flamelet model	sgs-TCI	Summary
Vascellari et al. [249; 250]	Single-Particle	De-volatilization	unsteady non-premixed	laminar	Good performance for predicting ignition and volatile combustion. Adaption of the analytic expression for the scalar dissipation rate required.
Watanabe et al. [258; 259]	2D coal jet flame; large-scale furnace	dev. char	non-premixed	β -PDF	Overall good agreement with reference simulation and experimental data.
Rieth et al. [202–204]	shear-layer [201]; semi-industrial scale burner	dev. char	non-premixed	β -PDF	Two-mixture fraction model + enthalpy to include heat losses [204]. Subsequently extended to variable scalar dissipation rates [203]. Exchanged the scalar dissipation rate by a progress variable [202]. Overall good agreement with reference data.
Knappstein et al. [108–111]	single-particle; laboratory-scale burner	dev. char	premixed	ATF	Two-mixture fraction model + enthalpy to include heat losses + progress variable. Overall good agreement with reference data.
Wan et al. [254]	planar jet flame	de-volatilization	premixed	fully-resolved	One-mixture fraction model + enthalpy to include heat losses + progress variable. Overall good agreement with reference simulation.
Vascellari et al. [248]	stagnation flame	dev. char	premixed	laminar	Two-mixture fraction model + enthalpy to include heat losses + progress variable. Overall good agreement with reference data.

3.4. Turbulent Premixed Combustion Modeling

A method to include detailed kinetics into turbulent premixed flame simulations with significantly reduced cost is the FGM method, which was introduced by van Oijen et al. [244; 246] for single-phase combustion. Due to the simple use of the model for turbulent premixed flames, it is prevalent and has been used successfully in a wide range of applications, summarized in the recent review by van Oijen et al. [245]. Next, the theory of the FGM method is briefly recapitulated. After that, a description of the required extensions for pulverized solid fuel combustion simulation is given. In the end, the coupling of the FGM method to the LES solver by means of the artificially thickened flame (ATF) approach is discussed.

3.4.1. Flamelet Generated Manifolds (FGM)

The main assumption of the FGM method is that a turbulent premixed flame can be represented by an ensemble of one-dimensional premixed flame structures. First, a new coordinate s , describing a path through the flame, which is perpendicular to the isosurfaces of a particular species mass fraction Y_k , is introduced. The evolution of all species along s is given by

$$m \frac{\partial Y_k}{\partial s} - \frac{\partial}{\partial s} \left(\frac{1}{Le_k} \frac{\lambda}{c_p} \frac{\partial Y_k}{\partial s} \right) = \dot{\omega}_k + P_k, \quad (3.8)$$

where m denotes a constant mass flow rate. Multi-dimensional and transient effects such as flame stretch and curvature are gathered in the perturbation term P_k . Although the perturbation term might become important in some extreme occasions, generally, it is assumed that it is small compared to the other terms and thus is neglected in the flamelet generation procedure. Then, one-dimensional premixed flames can be calculated in physical space. In this work, the detailed chemistry solver Chem1D [26] was used to calculate the flamelets assuming unity Lewis numbers for all species.

To enable further use of the manifold parameterized by s , a single controlling variable, namely the reaction progress variable \mathcal{Y} describing the transition from unburnt to burnt states, is introduced. The reaction progress variable \mathcal{Y} is calculated from a linear combination of species mass fractions. The required unique relation between s and \mathcal{Y} implies that the progress variable must monotonically decrease or increase, as described in Section 3.1.1.

Modeling Mixing in the Context of FGM

In order to capture combustion processes with inhomogeneous mixture compositions, a second parameter is required. Therefore, the mixture fraction Z is also introduced in the context of premixed combustion [244]. By varying the unburnt composition of the flame, i.e., the mixture fraction (or equivalence ratio), a two-dimensional composition space (Z - \mathcal{Y}) is spanned by the flamelet solutions. As depicted in Figure 3.6, the calculation of the flamelets is only possible within the flammability range of the fuel. Hence, a procedure is required to complete the entire composition space between pure fuel and rich flammability limit and between pure oxidizer and lean flammability. For this, linear interpolation, as proposed by Ketelheun et al. [106], is used in this work. Assuming that no reactions occur outside the flammability limits, the species mass fractions in the region are linearly interpolated

$$Y_k = \begin{cases} Y_{k,Z_{\text{lf}}} \frac{Z}{Z_{\text{lf}}} + Y_{k,\text{ox}} \left(1 - \frac{Z}{Z_{\text{lf}}}\right) & \text{if } Z < Z_{\text{lf}} \\ Y_{k,Z_{\text{rf}}} \frac{Z}{Z_{\text{rf}}} + Y_{k,\text{F}} \left(1 - \frac{Z}{Z_{\text{rf}}}\right) & \text{if } Z > Z_{\text{rf}} \end{cases} \quad (3.9)$$

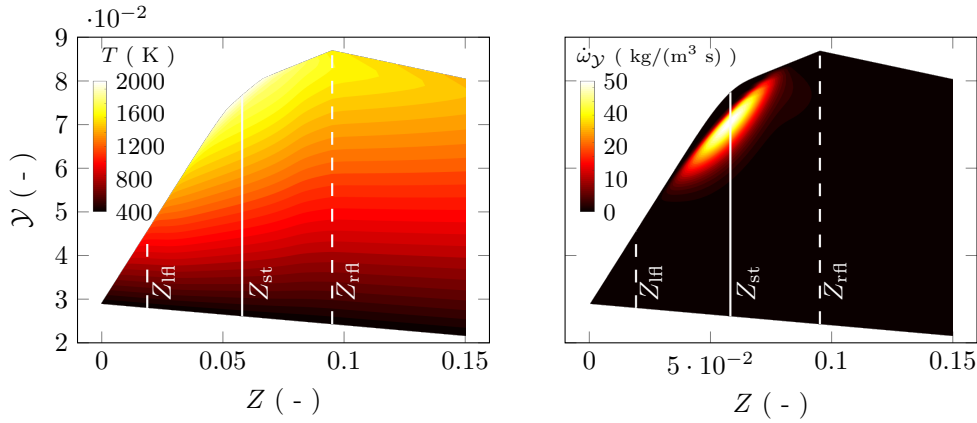


Figure 3.6.: Manifold of premixed flamelets with different equivalence ratios parameterized by mixture fraction Z . The solid line denotes stoichiometry and dashed lines represent lean flammability limit (lf) and rich flammability limit (rfl), respectively. Left: Temperature; Right: Source term of the reaction progress variable.

The temperature is also linearly interpolated, which allows, together with the species composition, the determination of all thermo-physical properties. Lastly, the density is computed from the ideal gas law given by Equation (2.15). At this stage, the thermo-chemical state, i.e., species composition, temperature and thermo-physical properties, is fully characterized by the reaction progress variable and mixture fraction

$$\Phi = \bar{\Phi}(\mathcal{Y}, Z). \quad (3.10)$$

Heat Losses in the Context of FGM

Furthermore, heat losses in the gas phase can be added to the FGM model by including the enthalpy as an additional table parameter. To capture broad enthalpy ranges, three different procedures are employed. To account for reactants' preheating, flamelets with higher temperatures are computed by increasing the fresh gas temperature. Lower enthalpies might also be obtained by reducing the temperature of the fresh gases. However, below a certain temperature, no flamelet solutions can be obtained. Generally, this method is not sufficient to include substantial heat losses in the table. Therefore, different techniques were introduced to obtain lower enthalpies [245]. Initially, van Oijen et al. [244] proposed to use burner stabilized flames, where the stabilization of a premixed flame at an isothermal burner results in heat losses controlled by the unburnt flow velocity. Another method to include heat losses, which is applied in this work, is the recirculation of exhaust gases. Thereby, the exhaust gases of a premixed flame are cooled to ambient temperature and are subsequently mixed with the fresh gases, resulting in a lower enthalpy. By increasing the fraction of exhaust gases in the fresh gases, the enthalpy level is controlled. Compared to burner stabilized flamelets, a similar composition space is obtained [59]. Above a certain level of exhaust gas recirculation, no solution can be obtained anymore. To fill up the remaining composition space, a linear extrapolation procedure adapted from Ketelheun et al. [105] was used. The final table spanned by progress variable and enthalpy is depicted on the left-hand side of Figure 3.7. This approach can be easily extended to multiple mixture fractions, resulting in a thermo-chemical state that is characterized by the reaction progress variable, mixture fraction and enthalpy

$$\Phi = \bar{\Phi}(\mathcal{Y}, Z, h). \quad (3.11)$$

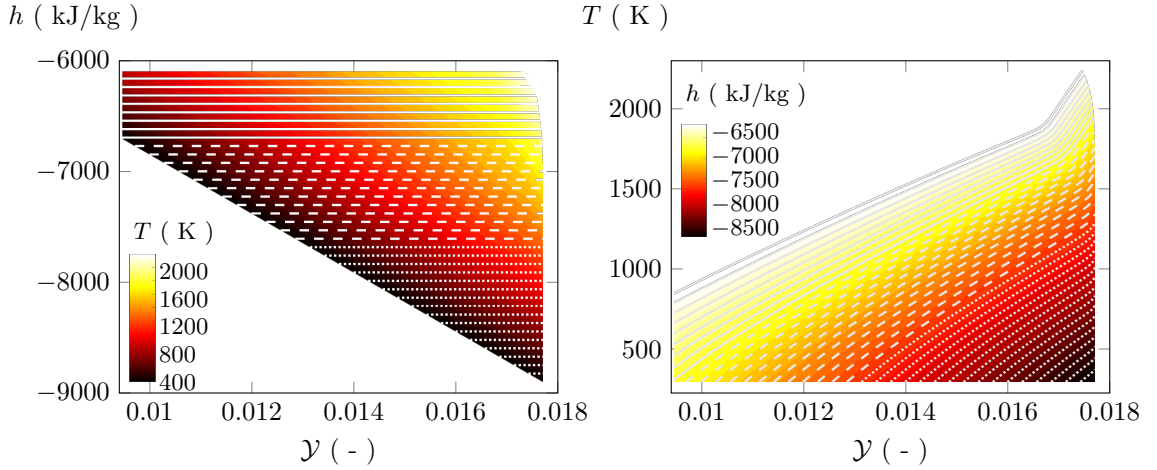


Figure 3.7.: Manifold of premixed flamelets with different enthalpy levels. Solid lines: preheated flamelets. Dashed lines: flamelets with exhaust gas recirculation. Dotted lines: extrapolated "flamelets". Left: temperature contour as a function of enthalpy and progress variable. Right: enthalpy contour as a function of temperature and progress variable for the table access at the boundaries.

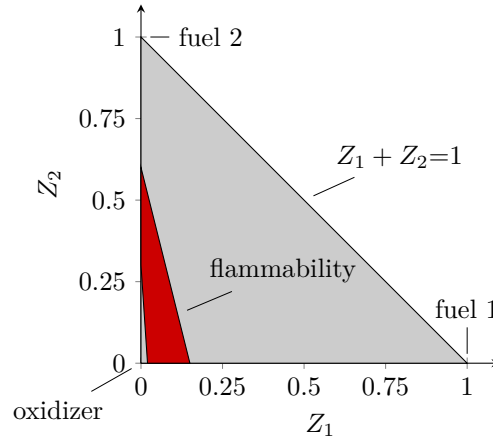


Figure 3.8.: Schematic depiction of composition space spanned by two mixture fractions for a two fuel stream system.

One additional aspect must be considered if walls with temperature boundary conditions are included in the simulation. Since the enthalpy depends on temperature, progress variable, and mixture fraction, it is part of the solution and cannot be prescribed. Therefore, an additional table is constructed, which is solely used at the boundaries of the domains. This table is obtained by remapping the table, shown on the left of Figure 3.7, with respect to temperature instead of enthalpy. Then, the final boundary table depicted on the right of Figure 3.7 is parameterized by temperature, progress variable and mixture fraction

$$\Phi_{BC} = \Phi_{BC}(\mathcal{Y}, Z, T). \quad (3.12)$$

3.4.2. Extension for Solid Fuel Combustion

Due to the changing fuel composition released from the particles (see Chapter 4), further dimensions representing the mixing of multiple fuel streams must be added to the table. For a three stream system (two fuels and the oxidizer), this is achieved by introducing a second

mixture fraction. Figure 3.8 depicts the area covered by the two mixture fractions. The values of $Z_1 = 1$ and $Z_2 = 1$ correspond to fuel 1 and fuel 2, respectively. At the point where both mixture fractions are zero, the atmospheric composition is located. The flammability range of the mixture is shown in red. The grey area corresponds to non-reacting mixing. Each point in this plane represents a two-dimensional table whose dimensions are the progress variable and enthalpy. Outside of the flammability limits, the previously introduced interpolation technique proposed by Ketelheun et al. [106] is adapted and further extended to consider multiple enthalpy levels. The choice of fuels and atmospheric composition is interchangeable in this approach. For instance, fuel 1 could represent both a pilot gas stream or the volatiles released from the solid fuel particle.

Overall, this procedure leads to a four-dimensional representation of the composition space

$$\Phi = \Phi(\mathcal{Y}, Z_1, Z_2, h). \quad (3.13)$$

3.4.3. Artificial Thickened Flame Approach

One issue when coupling FGM to LES is the under-resolved source term of the progress variable due to coarse grid cells resulting in wrong flame propagation. To ensure that the premixed flame structure is resolved on the numerical grid, Butler and O'Rourke [19] and O'Rourke and Bracco [173] proposed a transformation of the transport equation to artificially thicken the flame. Major developments of this approach with respect to the coupling to LES and tabulated chemistry were performed by Kuenne et al. [118; 119] and Kuenne [116].

3.4.3.1. Theory

In the following, the derivation of this model is outlined for a one-dimensional flame. However, the extension to three dimensions is straightforward. First, a new spatial coordinate ζ is introduced, which is related to x by a linear transformation using a constant factor \mathcal{F}

$$\zeta(x) = \mathcal{F}x \quad \text{and} \quad \frac{\partial \zeta}{\partial x} = \mathcal{F}. \quad (3.14)$$

Hence, the spatial derivatives with respect to x may be expressed in terms of ζ by

$$\frac{\partial}{\partial x} = \frac{\partial}{\partial \zeta} \frac{\partial \zeta}{\partial x} = \mathcal{F} \frac{\partial}{\partial \zeta}. \quad (3.15)$$

Applying this transformation to the species transport equation (2.6) yields

$$\frac{\partial \rho Y_k}{\partial t_\zeta} + \frac{\partial}{\partial \zeta} (\rho u Y_k) = \frac{\partial}{\partial \zeta} \left(\rho \mathcal{F} D \frac{\partial Y_k}{\partial \zeta} \right) + \frac{1}{\mathcal{F}} \dot{\omega}_k, \quad (3.16)$$

which still reproduces the flame speed correctly. Until here, this transformation does not modify the physics. However, for the artificial thickening of the flame, Equation (3.16) is solved for x instead of ζ . Thus, ζ is projected onto the x grid, as indicated by Figure 3.9 resulting in a flame thickness increased by the factor \mathcal{F}

$$\delta^\mathcal{F} = \mathcal{F}\delta. \quad (3.17)$$

In turn, this also increases the minimal required grid size to obtain the correct flame dynamics by the factor \mathcal{F}

$$\Delta_{x,\min}^\mathcal{F} = \mathcal{F}\Delta_{x,\min}. \quad (3.18)$$

However, before this approach is applied to 3D-CFD, several further aspects must be addressed, e.g., the treatment of mixing without reactions and the reduced impact of turbulent fluctuations on flame wrinkling. Both aspects are discussed next.

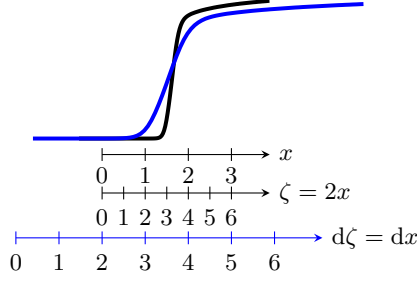


Figure 3.9.: Schematic representation of the transformation of the ATF model for a laminar flame for a thickening factor of $\mathcal{F}=2$. Graphic is adapted from [118].

3.4.3.2. Modeling Unresolved Wrinkling

Although the previously introduced transformation reproduces the laminar flame speed, the interaction of a premixed flame with turbulence is significantly affected by the ATF model. For LES, the interaction of the resolved eddies is damped by the thickening procedure, whereas small eddies do not interact with the flame at all [182]. To account for these effects, Colin et al. [34] proposed an efficiency function \mathcal{E} that modifies the laminar burning velocity to obtain the correct turbulent burning velocity

$$s_T = \mathcal{E} s_l. \quad (3.19)$$

However, the direct application of this equation is not possible in the ATF context since the flame speed is not prescribed but calculated from the species transport. Hence, Colin et al. [34] directly applied the efficiency function to the source term in the species equations. To keep the flame thickness constant, the diffusion term is also multiplied by the efficiency function, which results in the following equation

$$\frac{\partial \rho Y_k}{\partial t} + \frac{\partial}{\partial x_i} (\rho u_i Y_k) = \frac{\partial}{\partial x_i} \left(\rho \mathcal{F} \mathcal{E} D \frac{\partial Y_k}{\partial x_i} \right) + \frac{\mathcal{E}}{\mathcal{F}} \dot{\omega}_k, \quad (3.20)$$

which, according to the premixed flame theory [181], describes a flame with the thickness

$$\delta^F = \mathcal{F} \delta \propto \sqrt{\frac{\mathcal{F} D}{\dot{\omega}/\mathcal{F}}} \quad (3.21)$$

and the turbulent burning velocity

$$s_T = \mathcal{E} s_l \propto \sqrt{\mathcal{F} D \dot{\omega}/\mathcal{F}}. \quad (3.22)$$

The efficiency function is derived from DNS simulations of flame-vortex interactions [4; 145]. The intuitive method to determine the efficiency function is to compare the flame surface of the thickened flame to that of the original flame

$$\mathcal{E} = \frac{\Xi(\delta_l^0)}{\Xi(\delta_l^F)}, \quad (3.23)$$

where Ξ denotes the wrinkling factor. An extension to the initial formulation of Colin et al. [34] was proposed by Charlette et al. [25]. They used a power-law flame wrinkling approach that models the unresolved flame surface in terms of an inner and outer cut-off scale representing the required modeling range. The laminar flame thickness δ_l^0 determines the inner cut-off length,

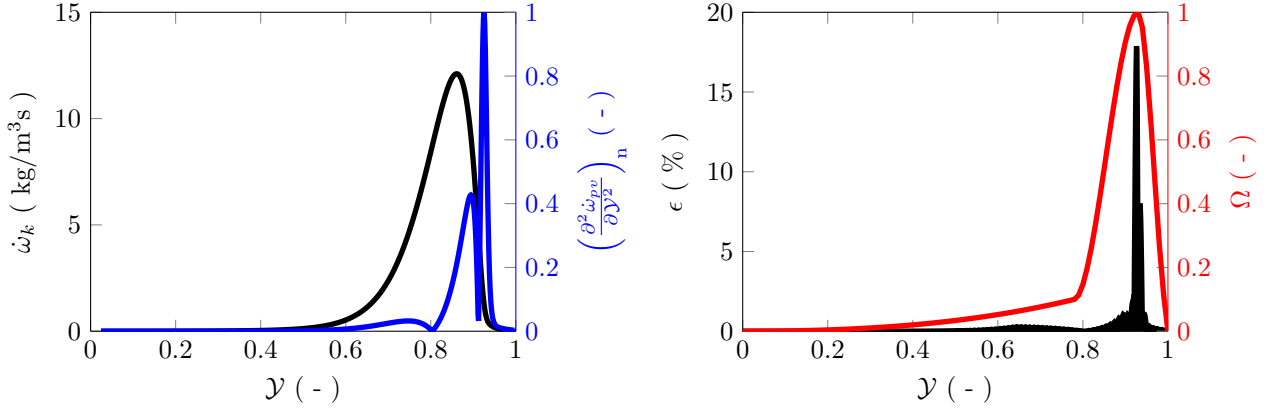


Figure 3.10.: Left: Source term of the reaction progress variable over normalized progress variable for a representative methane flamelet in an oxy-fuel atmosphere. The absolute normalized curvature of the source term is also depicted. Right: Numerically defined flame sensor based on the curvature of the source term. In addition, the error that results from a linear interpolation is presented.

whereas the filter size Δ represents the outer cut-off, which is approximated by the thickened flame $\Delta = \mathcal{F}\delta_l^0$ [25]. Thus, the efficiency function reads

$$\mathcal{E} = \Xi_{\text{Cha}} = \left(1 + \min \left(\frac{\Delta}{\delta_l^0}, \Gamma \frac{u'_\Delta}{s_l} \right) \right)^\beta, \quad (3.24)$$

where u'_Δ and Γ denote the sub-grid velocity fluctuation and efficiency correction, respectively. According to Colin et al. [34] the sub-grid velocity fluctuations in a multidimensional field can be expressed by

$$u'_\Delta = 2\Delta_x^3 \left| \nabla \times (\nabla^2 \vec{u}) \right|. \quad (3.25)$$

The efficiency correction Γ was directly obtained from the flame-vortex interaction DNS. To simplify the use, Charlette et al. [25] provided the following fit for the correction

$$\Gamma \left(\frac{\Delta}{\delta_l^0}, \frac{u'_\Delta}{s_l}, Re_\Delta \right) = \left[\left((f_u^{-a} + f_\Delta^{-a})^{-1/a} \right)^{-b} + f_{Re}^{-b} \right]^{-1/b}, \quad (3.26)$$

where f_u , f_Δ , and f_{Re} are empirical correlation [25] which are for brevity not repeated here. Moreover, these correlations are not evaluated at runtime. Instead, Γ is evaluated prior to the actual simulation and stored in a two-dimensional look-up table as a function of Δ/δ_l^0 and u'_Δ/s_l^0 [117].

3.4.3.3. Dynamic Thickening

The original thickening procedure performs well in premixed flames. However, in the presence of pure mixing outside of the reaction zone, diffusion processes are overestimated. To limit these effects to the local reaction zone, Legier et al. [125] introduced a flame sensor Ω . The flame sensor describes a function that is zero outside the flame and rises to unity within the reaction zone. Using the sensor, it is possible to correctly predict pure mixing and use the thickening procedure to compute the flame on coarse grids.

Due to the new progress variable selected for oxy-fuel conditions, the flame sensor also requires adjustments. For the definition of the flame sensor, there are numerous suggestions in the literature (e.g., [45; 188; 208]). These suggestions often use criteria such as the maximum source

term, the maximum gradient of the progress variable, or the normalized progress variable itself to define the shape of the sensor. These methods provide physically correct results, but finding an optimal shape for the whole state space is challenging. The commonly used sensors are defined over a large normalized progress variable space to ensure sufficient thickening. However, due to the relatively broad area of thickening, a large portion of the flame wrinkling has to be modeled. A generally valid sensor, which is determined numerically based on the curvature, is introduced in the following to minimize this modeling. This sensor provides an optimum flame resolution and minimum modeling. Since the maximum interpolation error increases with the curvature of the target function, as depicted in Figure 3.10, the flame sensor is weighted with the curvature of all physical quantities. Studies of methane mixtures in oxy-fuel atmospheres have shown that the most significant curvature occurs at the source term of the progress variable. Figure 3.10 depicts the progress variable source term and its curvature as functions of the normalized progress variable. Based on the curvature, a higher-order polynomial is determined

$$\Omega = \sum_{n=1}^3 k_n (Z_1, Z_2, h) \mathcal{Y}^n, \quad (3.27)$$

which becomes unity for the maximum curvature. The coefficients k_n are dependent on local composition and become zero outside of the flammability limits. As shown on the right side of Figure 3.10, this sensor covers the errors ϵ that occur during the evaluation of the source term on a coarse grid. The error is estimated by comparing the source terms obtained from a fine grid against a coarse grid. Thus, the flame is always thickened as much as is required for the respective range to minimize interpolation errors.

In summary, the complete thickening factor is defined as follows

$$\mathcal{F} = 1 - \Omega (1 - \mathcal{F}_{\max}), \quad (3.28)$$

where \mathcal{F}_{\max} denotes the maximum thickening factor required for a sufficient resolution of the source term.

3.4.3.4. Grid and Mixture Adaptive Thickening

In general, both local resolution and flame thickness vary significantly within the considered simulation domain. Thus, the lowest flame thickness and the largest cell would determine an overall valid thickening factor. Again, this would lead to increased modeling in terms of efficiency function corrections. Therefore, generally, two extensions are applied to the ATF approach [118]. First, the required thickening factor \mathcal{F}_{\max} is calculated on a local basis considering the cell size and thus is expressed as

$$\mathcal{F}_{\max} = \max \left(\frac{\Delta_{\text{grid}}}{\Delta_{\max}}, 1 \right), \quad (3.29)$$

where Δ_{\max} denotes the required grid resolution to preserve the laminar flame speed. For non-cubic cells, the local grid width is given by $\Delta_{\text{grid}} = (\Delta_x \Delta_y \Delta_z)^{\frac{1}{3}}$.

Second, since the required grid size is connected to the laminar flame thickness, which depends on the local mixture, Δ_{\max} is replaced by δ_l^0/n , where n represents the number of grid points in the flame front. By analyzing several one-dimensional laminar flames for different cell widths and equivalence ratios, the factor is determined as $n = 4$ for oxy-fuel conditions. With this number of cells, the maximum deviation of the laminar flame speed from the reference solution is less than 10%. Applying both procedures, the local maximum thickening factor is calculated as follows

$$\mathcal{F}_{\max} = \max \left(\frac{n \Delta_{\text{grid}}}{\delta_l^0}, 1 \right). \quad (3.30)$$

3.4.4. Summary Turbulent Premixed Combustion Modeling

In summary, in addition to momentum and mass transport, further equations must be solved to describe the mixing, heat losses, and chemical reactions for PCC in the FGM context. Two mixture fractions \tilde{Z}_1 and \tilde{Z}_2 are required to describe the mixing of oxidizer, volatiles, and char products. Additionally, the chemical reaction is described by a reaction progress variable \tilde{Y} . In order to take heat losses into account, the enthalpy \tilde{h} is introduced as a table parameter. The ATF procedure must be applied to all transport equations to ensure a consistent coupling of the equations according to Kuenne et al. [119]. Furthermore, the gradient approach is introduced by weighting it with the flame sensor to obtain the final transport equation [116]. The four ATF-modified transport equations read

$$\frac{\partial (\bar{\rho}\tilde{Z}_1)}{\partial t} + \frac{\partial (\bar{\rho}\tilde{u}_j\tilde{Z}_1)}{\partial x_j} = \frac{\partial}{\partial x_j} \left(\left[\mathcal{F}\mathcal{E} \frac{\bar{\mu}}{S_c} + (1 - \Omega) \frac{\mu_t}{S_{c_t}} \right] \frac{\partial \tilde{Z}_1}{\partial x_j} \right) + \bar{S}_{\text{prt},Z_1}, \quad (3.31)$$

$$\frac{\partial (\bar{\rho}\tilde{Z}_2)}{\partial t} + \frac{\partial (\bar{\rho}\tilde{u}_j\tilde{Z}_2)}{\partial x_j} = \frac{\partial}{\partial x_j} \left(\left[\mathcal{F}\mathcal{E} \frac{\bar{\mu}}{S_c} + (1 - \Omega) \frac{\mu_t}{S_{c_t}} \right] \frac{\partial \tilde{Z}_2}{\partial x_j} \right) + \bar{S}_{\text{prt},Z_2}, \quad (3.32)$$

$$\frac{\partial (\bar{\rho}\tilde{Y})}{\partial t} + \frac{\partial (\bar{\rho}\tilde{u}_j\tilde{Y})}{\partial x_j} = \frac{\partial}{\partial x_j} \left(\left[\mathcal{F}\mathcal{E} \frac{\bar{\mu}}{S_c} + (1 - \Omega) \frac{\mu_t}{S_{c_t}} \right] \frac{\partial \tilde{Y}}{\partial x_j} \right) + \frac{\mathcal{E}}{\mathcal{F}} \bar{\omega}_Y + \bar{S}_{\text{prt},Y}, \quad (3.33)$$

$$\frac{\partial (\bar{\rho}\tilde{h})}{\partial t} + \frac{\partial (\bar{\rho}\tilde{u}_j\tilde{h})}{\partial x_j} = \frac{\partial}{\partial x_j} \left(\left[\mathcal{F}\mathcal{E} \frac{\bar{\mu}}{Pr} + (1 - \Omega) \frac{\mu_t}{Pr_t} \right] \frac{\partial \tilde{h}}{\partial x_j} \right) + \bar{S}_{\text{prt},h}. \quad (3.34)$$

These four transported scalars form the dimensions of the 4-D FGM table, which contains the thermo-chemical states.

3.5. Turbulent Non-Premixed Combustion Modeling

One of the most popular approaches to include non-premixed flamelets into the LES is the flamelet progress variable model (FPV). First, the theory of the model proposed by Pierce and Moin [178] is briefly recapitulated to provide the background. Afterwards, the extension of the model required for solid fuel combustion, such as the inclusion of multiple fuel streams and heat losses, is covered. In the end, the coupling of LES with the flamelet table by means of filtered probability density function modeling is described.

3.5.1. Flamelet Progress Variable Model (FPV)

As mentioned previously, one main objective of turbulent combustion modeling is to reduce the number of transported scalars but retaining the information provided by detailed kinetics. For the non-premixed combustion system, one appropriate choice for such a scalar presents the mixture fraction. Based on a coordinate transformation from physical to mixture fraction space, the one-dimensional flamelet equations can be derived [176]

$$\rho \frac{\partial Y_k}{\partial \tau} = \frac{\rho\chi}{2} \frac{\partial^2 Y_k}{\partial Z^2} + \dot{\omega}_k, \quad (3.35)$$

where τ is a time-like coordinate and χ denotes the scalar dissipation rate. This scalar dissipation rate represents the coupling between the flow field and flamelet solution. The Z -dependent profile

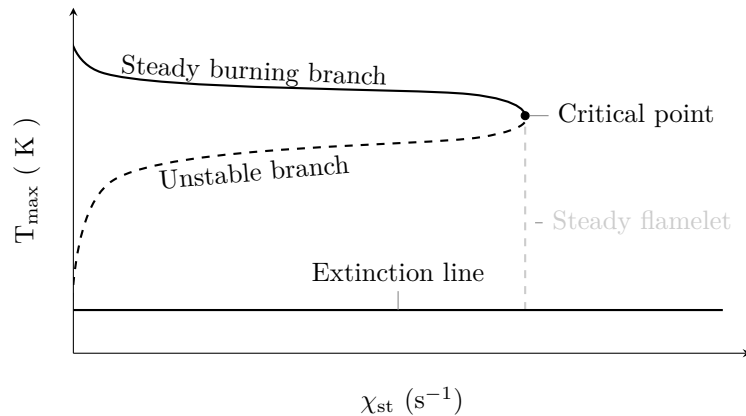


Figure 3.11.: Maximum temperature profile for a complete set of flamelet solutions including the unstable branch, parameterized by the scalar dissipation rate at stoichiometry.

of χ , which must be modeled, can be derived from a steady counterflow flame. Thereby, the stoichiometric scalar dissipation rate χ_{st} is introduced, which enables a unique description of the profile [176]. Hence, different flamelet solutions can be obtained by varying χ_{st} from zero to a critical quenching limit, at which the flame extinguishes. Subsequently, the thermo-chemical state of the non-premixed flamelet is parameterized by the mixture fraction Z and a scalar dissipation rate χ

$$\Phi = \Phi(Z, \chi_{st}). \quad (3.36)$$

However, as depicted in Figure 3.11, the scalar dissipation rate provides no unique relationship for all flamelet solutions. The presented *S-shape* curve is divided into three branches: the stable branch, the unstable branch and the extinction branch. Starting with zero scalar dissipation rate at the stable branch, an increase of χ_{st} results in a reduction of the maximum temperature. At the critical point, the temperature becomes too low to sustain the chemical kinetics. Thus, a further increase of the scalar dissipation rate leads to an extinction of the flame. To maintain the balance between transport processes and chemical reaction, further temperature reduction must be accompanied by lower scalar dissipation rates, which is represented by the unstable branch [178]. At the extinction line, the dependency of the scalar dissipation rate vanishes since chemistry effects are neglectable. Considering the parameterization given by Equation (3.36), it becomes evident that the intermediate states between the stable burning branch and the extinction branch are not included adequately in the database for the steady flamelet model (dashed grey line). To overcome this limitation, Pierce and Moin [178] suggested the use of a reaction progress variable \mathcal{Y} enabling the unique identification of all states along the three flamelet branches. Hence, the extended method enables an improved prediction of extinction and reignition events under the constrain that the procedure still employs a steady flamelet solution for an inherently unsteady process.

The FPV model maps the thermo-chemical state onto the two variables Z and \mathcal{Y}

$$\Phi = \Phi(Z, \mathcal{Y}). \quad (3.37)$$

The two-dimensional composition space described by this relation is depicted in Figure 3.12. Instead of solving Equation 3.35 in composition space, all flamelets are calculated in a counterflow flame setup in physical space coordinates, which represents an equivalent configuration for non-premixed flamelets, using an adapted version of Cantera [77]. Since the mixture fraction solution is a monotonic function of the spatial coordinate, the inverse function can be obtained

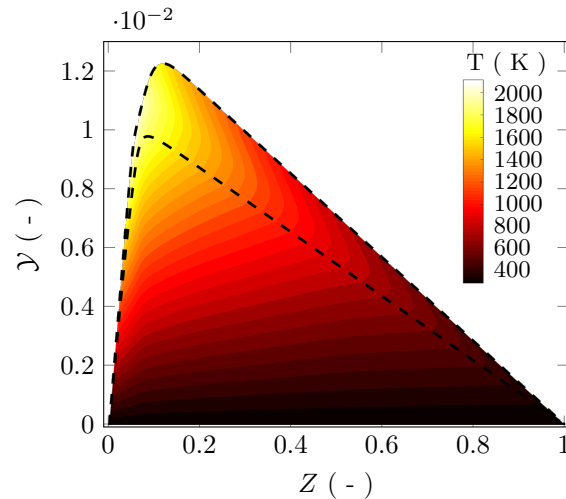


Figure 3.12.: Tabulated flamelet structures of non-premixed flames. Dashed lines indicate solutions from the limits of the stable branch of the S-Curve.

and used to map all of the combustion variables to the mixture fraction. The mixture fraction itself is determined from the element mass fractions.

3.5.2. Extensions for Solid Fuel Combustion

However, these relations are not sufficient to account for the complex processes involved in PCC. First, the interaction of cold particles with the recirculated flue gases leads to substantial heat losses in the gas phase. Moreover, the mixing of multiple fuel streams must be taken into account.

Inclusion of Heat Losses in the FPV Model

A first approach to include radiative heat loss into the FPV model was proposed by Ihme and Pitsch [98]. In their work, the unsteady flamelet equations considering thermal radiation are solved in composition space. Initialized from the steady burning branch without radiation, the flamelet solution for a constant scalar dissipation rate strives against a lower temperature steady burning state. This branch represents the steady solution of the flamelet equations, including thermal radiation. Flamelets along this trajectory are parameterized by the enthalpy and stored as an additional table dimension in the flamelet database.

Considering PCC, the heat losses accounted for by the approach from Ihme and Pitsch might be too small. Therefore, Wollny et al. [268] evaluated a different approach that modifies the energy equation to represent heat losses during flamelet generation. In their work, the energy is lowered by either introducing an artificial radiative source term or by simply rescaling the reaction source term in the energy equation. As outlined in Wollny et al. [268], both approaches result in similar composition spaces. Due to better convergence behavior, the rescaling approach for the reaction source term is applied in this work. In summary, two types of flamelets are computed. First, the enthalpy is raised by increasing the temperature of the oxidizer and fuel stream. In the current work, equal temperatures are used for both streams. For lower enthalpies, the previously introduced rescaling approach is applied. Below the last burning solution, an extrapolation approach proposed by Ketelheun et al. [105] for premixed flames is extended to non-premixed flames. It is assumed that no reaction occurs in the extrapolated region. Therefore, the mixture of the last flamelet is cooled down to the ambient temperature to

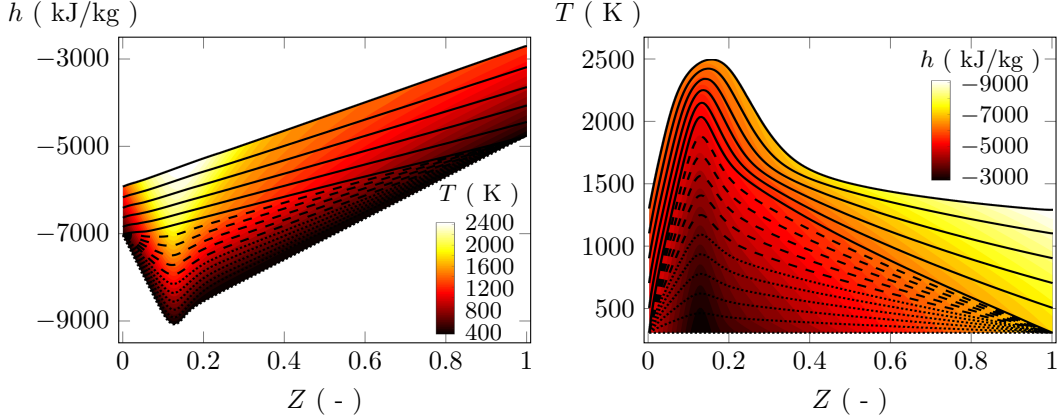


Figure 3.13.: Inclusion of heat-losses in non-premixed flames for constant normalized progress variables. Solid lines: preheated non-premixed flamelets; Dashed lines: non-premixed flamelets with different rescaled energy-source terms; Dotted lines: extrapolated flamelets. Left: flamelet table parameterized by Z and h . Right: flamelet table parameterized by Z and T for the access at boundaries.

fill up the composition space. The full series of flamelets parameterized by enthalpy and mixture fraction for a constant normalized reaction progress variable is depicted in the left-hand side of Figure 3.13.

Similar to the procedure introduced in the FGM method (see Section 3.4.1), an additional table containing the enthalpy as a function of the temperature is generated and used at the domain's boundary. This enables the table access for an arbitrary combination of the other table trajectory variables at walls. The table parameterized by the temperature instead of enthalpy is illustrated on the right side in Figure 3.13.

Multiple Fuel Stream in FPV Model

Additionally, mixing two fuel streams with the surrounding atmospheres needs to be included in the FPV model to simulate PCC. To track the separate evolution of two fuel streams, Hasse and Peters [87] proposed a two mixture fraction model, initially developed in the context of split injection in dual injection diesel engines. However, the method can be further extended to describe coal combustion in the context of tabulated chemistry (e.g., [204; 262]). Considering a three-stream system characterized by two mixture fractions, the (Z_1, Z_2) -space forms a unit triangle in composition space due to the physical constrain that the mixture fraction sum cannot exceed unity. To prevent numerical stability issues and a simplified table interpolation, Hasse and Peters [87] proposed a transformation of the composition space to a unit square as depicted in Figure 3.14. The transformation relations are given by

$$Z = Z_1 + Z_2 \quad Y = \frac{Z_2}{Z_1 + Z_2}. \quad (3.38)$$

In summary, the thermo-chemical state is mapped onto the four trajectory variables Z, Y, \mathcal{Y} , and h , resulting in

$$\Phi = \Phi(Z, Y, \mathcal{Y}, h). \quad (3.39)$$

3.5.3. Presumed Probability Density Function Modeling

Additional modeling is required when tabulated chemistry approaches are coupled to LES since only Favre-filtered scalars are available for the table access. Due to the non-linearities, the direct

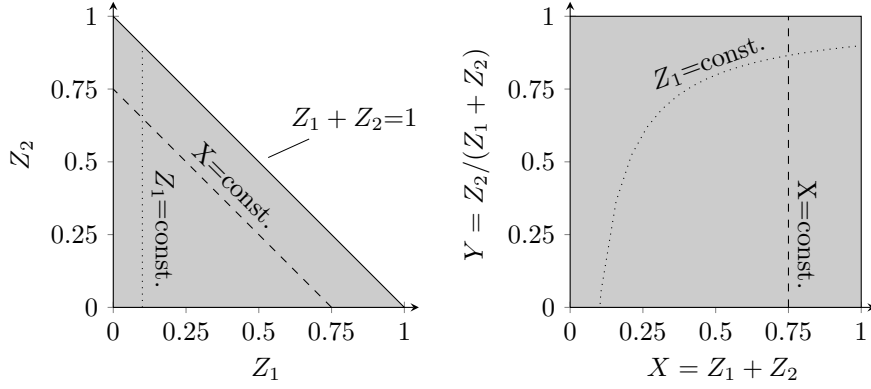


Figure 3.14.: Schematic depiction of composition space for a two fuel stream system. Left: Unit triangle spanned by two mixture fractions. Right: Transformation according to Equation 3.38 to a unit square.

access of the table via Favre-filtered scalars does not result in the Favre-filtered state

$$\tilde{\Phi} \neq \Phi(\tilde{Z}, \tilde{\phi}_1, \tilde{\phi}_2, \dots), \quad (3.40)$$

where \tilde{Z} represents the mixture fraction and $\tilde{\phi}_1, \tilde{\phi}_2, \dots$ are additional scalars parameterizing the thermo-chemical state.

To obtain the filtered quantities for arbitrary nonlinearities, the knowledge of the subgrid filtered/probability density function (FDF/PDF) is required [178]. The filtered quantities can then be obtained through integration of the joint-scalar-PDF in the composition space

$$\tilde{\Psi} = \int \Psi(Z, \phi_1, \phi_2, \dots) \tilde{P}(Z, \phi_1, \phi_2, \dots) dZ d\phi_1 d\phi_2 \dots, \quad (3.41)$$

where the density-weighted PDF \tilde{P} follows from the Favre-averaging procedure given by Equation (2.42). Hence, for evaluating properties in the context of LES, the determination of the subgrid PDF is essential, for which a transport equation can be derived [67; 184]. However, this equation is challenging to solve and two different approaches are commonly used in the literature to obtain the PDF. Either an approximation from eulerian or particle Monte-Carlo methods is employed to solve the PDF transport equation, or the PDF shape is simply prescribed [88]. The first approach has a greater potential for correct PDF estimations; however, computational costs are generally also significantly higher. The latter approach was used in this work to reduce computational costs and is outlined in the following.

In order to represent the joint PDF of multiple scalars in composition space, it is beneficial to represent the PDF as the product of the individual marginal scalar PDFs. First, the statistical independence of the scalars is assumed. Then, all scalars besides the mixture fraction are modeled by a δ -function [204]

$$\tilde{\Psi} = \int \Psi(Z, \phi_1, \phi_2, \dots) \beta(Z, \tilde{Z}, \tilde{Z}''^2) \delta(\phi_1, \tilde{\phi}_1) \delta(\phi_2, \tilde{\phi}_2) \dots dZ d\phi_1 d\phi_2 \dots \quad (3.42)$$

The subgrid PDF of the mixture fraction is approximated by a two-parameter distribution, the so-called β -function, which reads

$$P(Z, \tilde{Z}, \tilde{Z}''^2) = Z^{a-1} (1-Z)^{b-1} \frac{\Gamma(a+b)}{\Gamma(a)\Gamma(b)} \quad (3.43)$$

with

$$a = \tilde{Z} \left[\frac{(1-\tilde{Z})\tilde{Z}}{\tilde{Z}''^2} - 1 \right] \quad \text{and} \quad b = (1-\tilde{Z}) \left[\frac{(1-\tilde{Z})\tilde{Z}}{\tilde{Z}''^2} - 1 \right]. \quad (3.44)$$

For the closure, besides the Favre-filtered mixture fraction, the subgrid variance of the mixture fraction is required. Ways to obtain this quantity are covered in the next paragraph.

The entire flamelet table is pre-integrated using different values of the normalized subgrid-scale variance, resulting in a five-dimensional table that is accessed by the controlling variables

$$\tilde{\phi} = \phi \left(\tilde{Z}_1, \widetilde{Z_1''^2}, \tilde{Z}_2, \tilde{Y}, \tilde{h} \right). \quad (3.45)$$

Modeling of the Variance of a Conserved Scalar

As previously discussed, the reconstruction of the presumed PDF requires the subgrid scalar variance of the mixture fraction. Most single-phase studies rely on an algebraic model for the subgrid-scale variance that can be derived under the assumption of local homogeneity and local equilibrium for the subgrid scales [177; 178]. Based on this assumption, the subgrid-scale variance can be related to the resolved gradient of the conserved scalar, resulting in

$$\overline{\rho Z''^2} = C_Z \overline{\rho} \Delta^2 \left| \frac{\partial \tilde{Z}}{\partial x_i} \right|^2, \quad (3.46)$$

where C_Z is a modeling constant ranging between 0.1-0.2.

However, for multiphase flows, where the particle phase influences the conserved scalar, this algebraic expression might be insufficient. Therefore, Pera et al. [175] derived a transport equation for the subgrid-scale variance of the mixture fraction, taking into account evaporating droplets, which reads

$$\frac{\partial \left(\overline{\rho Z''^2} \right)}{\partial t} + \frac{\partial \left(\overline{\rho \tilde{u}_j Z''^2} \right)}{\partial x_j} = \frac{\partial}{\partial x_j} \left(\left[\frac{\overline{\mu}}{Sc} + \frac{\mu_t}{Sc_t} \right] \frac{\partial \overline{\rho Z''^2}}{\partial x_j} \right) + 2 \frac{\mu_t}{Sc_t} \left| \frac{\partial \tilde{Z}}{\partial x_j} \right|^2 - 2 \overline{S_{\chi Z}} + \overline{S_{\text{prt}}}. \quad (3.47)$$

Besides the gradient approach, additional terms need to be modeled for the transport equation of the unresolved mixture fraction variance. The unresolved scalar dissipation rate (the third term on the RHS) is modeled by

$$\overline{S_{\chi Z}} = C_\chi \frac{\mu_t}{Sc_t} \frac{\overline{\rho Z''^2}}{\Delta^2} \quad (3.48)$$

with the sub-grid scale dissipation rate model constant $C_\chi = 8.0$ [204]. Following Hollmann and Gutheil [93], the effect of the particles on the subgrid mixture fraction variance is modeled by

$$\overline{S_{\text{prt}}} = C_{\text{prt}} \overline{\rho Z''^2} \frac{\overline{S_{\text{prt},Z}}}{\tilde{Z}}. \quad (3.49)$$

Here, C_{prt} is a model constant, which is set to 0.5 as proposed by Tillou et al. [234] for spray combustion and adapted by Rieth et al. [204] for LES of PCC. The determination of the particle source term $\overline{S_{\text{prt},Z}}$ is detailed in Section 4.4.3.

3.5.4. Summary Turbulent Non-Premixed Combustion Modeling

In addition to the standard equations of the FPV model, namely mixture fraction and reaction progress variable transport, the enthalpy and a second mixture fraction are introduced to account for PCC physics. In the context of LES, the unresolved subgrid distribution of the transported scalars is modeled by a commonly employed presumed- β PDF for the mixture fraction sum Z_1 ,

whereas the remaining scalars are modeled by a δ -function. Hence, the entire flamelet table is pre-integrated, resulting in a five-dimensional table that is accessed by the controlling variables

$$\tilde{\phi} = \phi \left(\tilde{Z}, \widetilde{Z''^2}, \tilde{Y}, \tilde{\mathcal{Y}}, \tilde{h} \right). \quad (3.50)$$

For each of these variables, a transport equation is solved in the simulation. Then, the full set of equations is given by the Favre-filtered volatile mixture fraction \tilde{Z}_{vol}

$$\frac{\partial (\bar{\rho} \tilde{Z}_{\text{vol}})}{\partial t} + \frac{\partial (\bar{\rho} \tilde{u}_j \tilde{Z}_{\text{vol}})}{\partial x_j} = \frac{\partial}{\partial x_j} \left(\left[\frac{\bar{\mu}}{Sc} + \frac{\mu_t}{Sc_t} \right] \frac{\partial \tilde{Z}_{\text{vol}}}{\partial x_j} \right) + \bar{S}_{\text{prt}, Z_{\text{vol}}}, \quad (3.51)$$

the Favre-filtered char off-gas mixture fraction \tilde{Z}_{char}

$$\frac{\partial (\bar{\rho} \tilde{Z}_{\text{char}})}{\partial t} + \frac{\partial (\bar{\rho} \tilde{u}_j \tilde{Z}_{\text{char}})}{\partial x_j} = \frac{\partial}{\partial x_j} \left(\left[\frac{\bar{\mu}}{Sc} + \frac{\mu_t}{Sc_t} \right] \frac{\partial \tilde{Z}_{\text{char}}}{\partial x_j} \right) + \bar{S}_{\text{prt}, Z_{\text{char}}}, \quad (3.52)$$

the Favre-filtered reaction progress variable $\tilde{\mathcal{Y}}$

$$\frac{\partial (\bar{\rho} \tilde{\mathcal{Y}})}{\partial t} + \frac{\partial (\bar{\rho} \tilde{u}_j \tilde{\mathcal{Y}})}{\partial x_j} = \frac{\partial}{\partial x_j} \left(\left[\frac{\bar{\mu}}{Sc} + \frac{\mu_t}{Sc_t} \right] \frac{\partial \tilde{\mathcal{Y}}}{\partial x_j} \right) + \bar{\omega}_{\mathcal{Y}} + \bar{S}_{\text{prt}, \mathcal{Y}}, \quad (3.53)$$

the Favre-filtered enthalpy \tilde{h}

$$\frac{\partial (\bar{\rho} \tilde{h})}{\partial t} + \frac{\partial (\bar{\rho} \tilde{u}_j \tilde{h})}{\partial x_j} = \frac{\partial}{\partial x_j} \left(\left[\frac{\bar{\mu}}{Pr} + \frac{\mu_t}{Pr_t} \right] \frac{\partial \tilde{h}}{\partial x_j} \right) + \bar{S}_{\text{prt}, h}, \quad (3.54)$$

and the Favre-filtered subgrid variance of the mixture fraction sum $\widetilde{Z''^2}$

$$\begin{aligned} \frac{\partial (\bar{\rho} \widetilde{Z''^2})}{\partial t} + \frac{\partial (\bar{\rho} \tilde{u}_j \widetilde{Z''^2})}{\partial x_j} &= \frac{\partial}{\partial x_j} \left(\left[\frac{\bar{\mu}}{Sc} + \frac{\mu_t}{Sc_t} \right] \frac{\partial \widetilde{Z''^2}}{\partial x_j} \right) \\ &+ 2 \frac{\mu_t}{Sc_t} \left(\frac{\partial \tilde{Z}}{\partial x_j} \right)^2 - 2 \bar{S}_{\chi Z} + \bar{S}_{\text{prt}}. \end{aligned} \quad (3.55)$$

4. Numerical Treatment of Solid Fuels

This chapter covers the numerical treatment of solid fuel reactions and their coupling to CFD. The first section describes the major features of coal, their standard analyses, and thermochemical properties that are input requirements for CFD simulations. Afterwards, the physical and chemical processes during coal conversion are briefly discussed. This is followed by an overview of employed coal conversion sub-models required for CFD simulations. Thereafter, the developed coupling strategies for these models to the other parts of the holistic CFD model are derived and discussed. In the end, the interaction of solid fuel particles and thermal radiation is addressed, and the applied modeling approach is outlined.

4.1. Characterization of Solid Fuels

Industrial fuels such as residual petroleum fractions or biomass typically do not share features for samples collected at different locations, which prevents simple classifications [166]. In contrast, regardless of the geographical origin, coals share common features facilitating their characterization in a coal rank spectrum. Coals associated with a specific rank share important quantities such as calorific value, volatility, ease of ignition, agglomeration tendencies, and burnout characteristics.

Coal Rank

The simplest way to define a coal rank is to consider the age of a sample since it determines the maturation of the coal. Oxygen and hydrogen are preferentially eliminated during coal aging, resulting in a disordered form of pure carbon. Thus, maturation is the underlying, unifying principle of the coal ranks because it always results in the same product [166].

However, a more general way is required to determine the coal rank. For a simple rank assignment of coal, the so-called van Krevelen diagram is generally preferred [18]. As depicted in Figure 4.1, the atomic ratios of H/C and O/C for samples excluding moisture and ash are utilized to characterize the fuel. The higher the coal rank, the more advanced the development of the graphite structure, resulting in fewer side chains and lower oxygen content. Contrary, low-rank coals have a significant oxygen content; consequently, these have longer side chains and consist of small aromatic structures. Different amounts of energy are required to break such structures, which depends on the particular bond in the polymer network.

In the van Krevelen diagram, biomass is located throughout the upper right quadrant. Coals can be found in a band across the lower left quadrant. Thereby the youngest coals appear in the near-horizontal band. Based on these findings, the following classification for coals is often applied:

- **Lignite/brown coal** is characterized by large moisture content and comparatively high volatile matter.
- **Sub-bituminous coal** has a black color and slightly larger heating values compare to lignite.
- **Bituminous coal** is also black colored but has heating values comparable to anthracite coal.

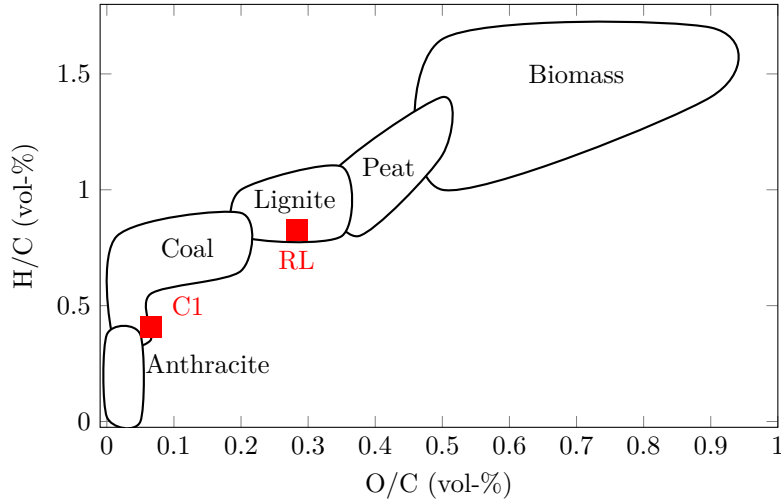


Figure 4.1.: Van Krevelen diagram depicting location of several fuels. Red squares illustrate the position of the fuels considered in this work. Graphic is adapted from [187].

- **Anthracite coal** has the highest rank. Thus, its structure is similar to graphite which is equivalent to having low moisture and volatile content.

Thermophysical Properties of Coal

After this short description of coal characterization, the essential features of coals required to simulate the distinctive behavior of individual coal samples are derived from the standard coal properties. The standard coal properties are given by the so-called proximate and ultimate analyses. A proximate analysis comprises the mass percentages of moisture, ash, volatile matter, and fixed carbon obtained from a series of standardized tests [166]. The proximate volatile matter (PVM) diminishes continuously for coals of progressively higher rank, beginning with 50 weight-% for Lignite coals and nearly vanishing for anthracites. An ultimate analysis determines the mass percentages of the elements C, H, O, N, and S in the combustible portion, excluding moisture and ash (Commonly referred to as dry and ash-free (daf)).

In this work, two different coals, the bituminous Columbian coal Norte and the Rhenish lignite, were used in experimental investigations and thus are also used for modeling. These coals were already predried, and the corresponding proximate and ultimate analysis results are given in Table 4.1.

To correctly predict particle temperature histories, the precise determination of the specific heat capacity is essential. Up to date, the only available self-contained method for predicting the specific heat capacity was reported over 30 years ago by Merrick and Brewster et al. [18; 146]. Hence, using this method remains the only alternative to direct measurements, which, however, is not practical to perform for each considered coal. To apply the correlation, the coal is divided into three parts: combustibles, ash, and moisture. Consequently, the specific heat capacity of the mixture is estimated by

$$c_{p,\text{prt}} = \frac{\text{PVM} + \text{FC}}{100} (1 - Y_{\text{vol}}) c_{p,\text{comb}} + \frac{A}{100} c_{p,\text{ash}} + \frac{M}{100} c_{p,\text{moist}}, \quad (4.1)$$

where the specific heat capacity of the ash is calculated by an empirical correlation $c_{p,\text{ash}} = 539.9 + 0.586T_{\text{prt}}$. The specific heat capacity of the combustibles $c_{p,\text{comb}}$ is calculated as follows

$$c_{p,\text{comb}} = \frac{\mathcal{R}}{W_{\text{comb}}} g_1 \left(\frac{380}{T_{\text{prt}}} \right) + 2g_1 \left(\frac{380}{T_{\text{prt}}} \right) \quad \text{with} \quad g_1(x) = \exp(x) / \left(\frac{\exp(x) - 1}{x} \right)^2, \quad (4.2)$$

Table 4.1.: Coal properties of employed coals determined at *Department of Energy Plant Technology, Ruhr University Bochum* and *Institute of Heat and Mass Transfer, RWTH Aachen*, respectively. 1: as received, 2: dry and ash free basis. Left: Columbian coal Norte (C1). Right: Rhenish lignite (RL)

Proximate Analysis ¹	weight-%	Proximate Analysis ¹	weight-%
Moisture	2.89	Moisture	9.1
Ash	8.45	Ash	5.5
Volatile matter	35.80	Volatile matter	45.0
Fixed carbon	52.86	Fixed carbon	40.4

Ultimate Analysis ²	weight-%	Ultimate Analysis ²	weight-%
Carbon	78.14	Carbon	68.2
Hydrogen	5.22	Hydrogen	4.69
Oxygen	13.55	Oxygen	25.71
Nitrogen	1.96	Nitrogen	0.97
Sulfur	1.13	Sulfur	0.43

where W_{comb} denotes the mean elemental mass of the sample. Besides the direct application of the Merrick correlation, a temperature fit of the specific heat capacity as proposed by Tomeczek et al. [235] is employed.

Bulk (or particle) density describes the density within the external particle surface area, including the internal porosity. The initial bulk density determined from semi-empirical models [233] ranges from 1000 to 1500 kg/m³. Throughout devolatilization, bulk density changes significantly, and the impact is much more significant than the impact of the composition on the actual density of combustibles. Similar to other studies [204], the change of the bulk density is taken into account by fixing the particle diameter during the devolatilization and decreasing the density by the amount of released matter. Following experimental results, the initial density for both studied coals is set to 1200 kg/m³ [108].

Additionally, the particle size might increase due to swelling. Empirical correlations are available in the literature to account for swelling [220; 221]. However, for the considered coals, experiments have shown that the swelling is only moderate [7]. Furthermore, the same study showed the influence of swelling is minor for small particles and non existing for large particles. Therefore, particle swelling was neglected in this work.

4.2. Coal Conversion Process

The overall coal conversion process is generally divided into two conversion steps, which is schematically depicted in Figure 4.2.¹ First, the particle undergoes pyrolysis/devolatilization (grey region in Figure 4.2). Thereby connecting bounds of the coal structure are broken, resulting in the release of light gases and heavy tars to the gas phase. It is a crucial sub-step in coal conversion since it provides the fuel to the gas phase, which facilitates the overall flame stabilization process after ignition. In general, this process occurs first in the coal conversion process. However, at the late stage of devolatilization, the much slower char conversion might overlap.

¹Depending on the literature source, sometimes evaporation is considered as the third conversion phase. However, the comparatively low amounts of moisture in the investigated coals (see Table 4.1) and the significantly increased modeling efforts to separately account for evaporation result in a simplified treatment of moisture. The moisture is released together with the remaining volatiles, which decreases its modeling effort significantly.

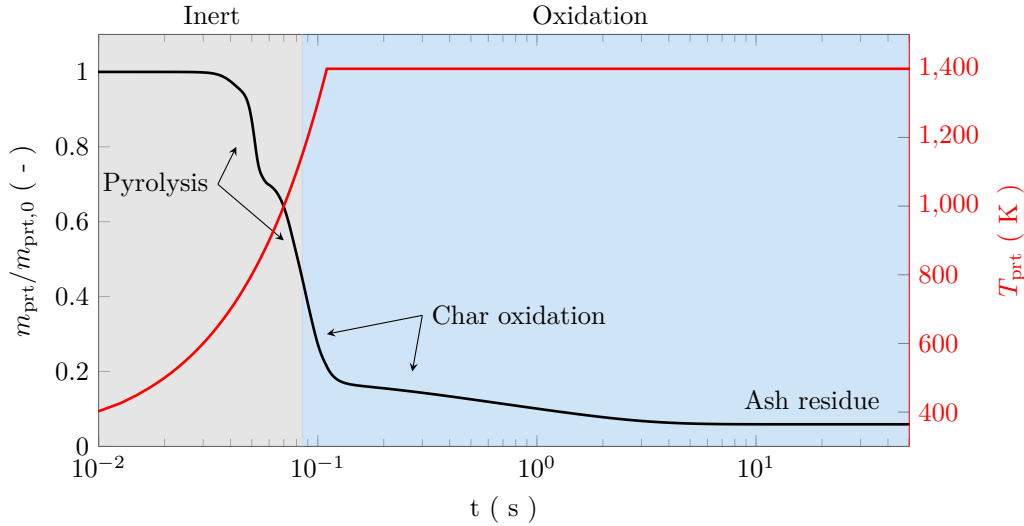


Figure 4.2.: Schematic drawing of the conversion process of a solid fuel particle. Black line corresponds to the normalized particle mass loss. Red line describes the imposed temperature profile. The grey area indicates the pyrolysis process, which can also take place in inert conditions. The Blue area illustrates the slow char reaction, which occurs only in oxidizing atmospheres.

During char conversion, the parent coal matrix, consisting of carbon and ash (mineral matter), reacts with surrounding gases in a heterogeneous surface reaction (blue region in Figure 4.2). Due to the significantly slower conversion rates, the char conversion defines the required time for the full particle burnout. Thus, the correct prediction of this process is important to design industrial applications in which a carbon conversion of more than 99% is necessary from an economic standpoint [95].

In the following two sections, the physical and chemical fundamentals of these processes are briefly outlined as these constitute the foundation for modeling the conversion of the solid. This section follows mostly Hasse et al. [86], some minor details were taken from Niksa [166].

4.2.1. Physical and Chemical Processes: Pyrolysis

During the initial heat-up of the particles, light gases and heavy tars are released from the particle. Considering the coal particle as a macromolecular network structure, pyrolysis describes the breaking of chemical bonds in this structure. During this process, light gases and finite-size fragments are formed. Former leave the particle directly. Depending on their molecular weight, the latter are either vaporized and escape the particle as tars or stay in the coal particle. For increased times inside the particle, the finite-size fragments might also reconnect to the coal matrix. In summary, this pyrolysis process is a multi-step problem, which is strongly influenced by chemistry and the structure of the coal.

Initial Structure

For accurate prediction of the pyrolysis process, detailed knowledge of the initial structure is required [166]. The macromolecular network structure consists of different-sized monomers connect by several bonds. During heat-up, these bonds can break and reform, which depends strongly on the initial properties of the monomers and the bonds. Thus, the rate and yield of released matters can considerably vary for different coals.

Primary Pyrolysis

The primary pyrolysis process is characterized by labile bonds breaking forming molecular fragments, which form light gas and tars. Simultaneously, the formation of stable bonds during this process results in the char matrix. Moreover, in this metaplastic phase, some of the smaller fragments are trapped in the solid. The properties of these trapped fragments determine whether cross-linking reactions occur. Concluding, the overall yields and release rates of gas and tars and the char yield are controlled by primary pyrolysis.

Secondary Pyrolysis

The secondary pyrolysis refers to the gas-phase decomposition of the devolatilization products. Several volatile species are formed, whose composition is significantly influenced by local conditions, such as surrounding atmosphere and temperature.

Char Annealing

Although often modeled separately, the devolatilization and char conversion steps are tightly coupled. After devolatilization, the remaining char can undergo further physico-chemical changes called char thermal annealing or char deactivation. This process takes place at high temperatures [170; 207]. The reorganization of the structure leads to a global loss of reactivity. This loss is caused by the continuous reduction in the specific surface area and the destruction of active sites on the char surface.

4.2.2. Physical and Chemical Processes: Char Conversion

After the devolatilization phase, a highly porous char structure remains, whose actual characteristics strongly depend on preceding conditions. The heterogeneous char surface reaction takes place on the entire intrinsic (inner) surface area. Hence, the char conversion process is determined by surface reactions and transport effects supplying the reactants. Following Smooth and Smith [223], the numerous interacting physics of char conversion can be divided into three main processes:

1. Heterogeneous surface reactions;
2. Intra-particle phenomena, especially pore diffusion;
3. Film diffusion.

Which of these processes depends strongly on the temperature [81; 253]. Retrieved from this observation, the classical *three-zone* theory was developed [223], which is depicted in Figure 4.3.

For low-temperature conditions, the overall char conversion process is solely determined by reaction kinetics. Hence, transport time scales are fast compared to the chemical time scales leading to a uniform concentration profile inside the particle. This regime is called *kinetically controlled* (Zone 1). Higher temperatures result in significantly faster reaction rates, which in turn increases the impact of pore diffusion on the overall conversion. The reaction time scales are same order as the pore diffusion time scales. This second regime is referred to as *pore-diffusion-controlled* (Zone 2). For the last high-temperature regime, reaction rates are significantly faster than the diffusion into the particle, resulting in concentration gradients in the particle's boundary layer. Therefore, particle-flow interactions, which determine the boundary layer thickness, influence the char reaction significantly. Commonly, this zone is denoted as *film-diffusion-controlled regime* (Zone 3).

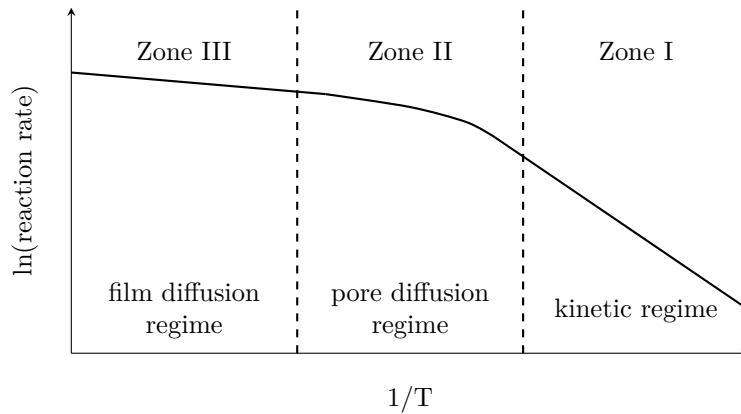


Figure 4.3.: Rate controlling regimes for char reactions adapted from [223]. Black line illustrates the influence of the temperature on the char reaction rate.

4.3. Modeling of Coal Conversion

Based on the previously detailed physical processes of the thermal conversion of coal particles, several model requirements can be derived [86]. For the accurate modeling of pyrolysis, the following aspects should be accounted for:

- Pyrolysis rate and thus also the overall time of the pyrolysis process;
- Yield and composition of the pyrolysis products;
- The transition of the coal structure towards the initial char morphology.

Similarly, the essential aspects for char conversion modeling are given by:

- Correct prediction of the conversion rate to obtain the correct overall time of the process;
- Correct prediction of the formed gas species composition.

In the following, the employed coal conversion models are outlined, and their respective accuracy with respect to the previously given modeling requirements is discussed. Due to the inherently different physics of devolatilization and char conversion, generally, models are developed separately for each process. Thus, the overview of models is likewise split into two parts. One exception is the CRECK-S model proposed by the group from Politecnico di Milano, which provides a seamless description of coal conversion [137; 226]. A separate section is dedicated to this model.

4.3.1. Modeling Pyrolysis

Due to its importance for the initial coal combustion, several models were developed for coal devolatilization, differing significantly in their respective detail levels. A classification of these models was performed in the recent review by Hasse et al. [86].

Generally, pyrolysis models are divided into empirical and network models, where the latter possess higher predictability due to their more complex structure. Contrary, empirical models are less sophisticated and require precise fitting in order to work correctly. However, the computational cost for these models is generally significantly lower, making these models very popular in large-scale simulations. The following two sections summarize the conversion models used in this work.

4.3.1.1. Empirical Pyrolysis Models

Empirical pyrolysis models are characterized by simple Arrhenius-type reaction expressions for describing the complex devolatilization process. Empirical models can be extended by using a distributed activation energy (DAE) [5; 180]. This model, assuming independent parallel reactions with similar activation energies, is combined with single-step and two-step models. However, this model is not used in this work, as the fitting process of the parameters is quite cumbersome. Moreover, the standard integration scheme may lead to significant errors, which require additional treatments [41].

Single first order reaction model (SFOR)

SFOR is the simplest model to describe devolatilization used in this work. It only requires a single rate expression [8]. Thus, the simple conversion mechanism reads



where k is the reaction rate constant given by an Arrhenius law

$$k = AT_{\text{prt}}^b e^{-\frac{E_A}{\mathcal{R}T_{\text{prt}}}}. \quad (4.4)$$

The global release rate is calculated by

$$\frac{dm_{\text{vol}}}{dt} = m_{\text{prt},0} (Y_{\text{vol},0} - Y_{\text{vol}}) k. \quad (4.5)$$

Due to its simplicity, the SFOR model is often applied to simulations. However, not all complex processes that occur during devolatilization are captured by this approach. Although the temperature dependency of pyrolysis is approximately represented, the model has several shortcomings, such as constant volatile yield regardless of the particle history (e.g., heating rate, final temperature).

Multi-step models

These models were developed to overcome the deficits of the simple one-step models. The general idea of this model class is to employ multiple competing or parallel reaction steps during the devolatilization process [5].

In this work, the competing two-step model (C2SM) is used [113]. The reactions mechanism is given by two competing reactions



where k_1 and k_2 denote the reaction rate constant, which is calculated by Arrhenius law similar to (4.4), and α_1 and α_2 are the stoichiometric coefficients for the low and high-temperature conditions, respectively. The stoichiometric coefficients correspond to the final yield of the respective condition and the current volatile content is given by

$$y_{\text{vol}}(t) = \int_0^t (\alpha_1 k_1 + \alpha_2 k_2) \exp\left(-\int_0^t (k_1 + k_2)\right) dt. \quad (4.8)$$

In summary, global pyrolysis models are characterized by one or multiple simple Arrhenius-type reactions. To calibrate such models, either experimental data or data from reference models

are required (see Section 4.4). This calibrating procedure restricts the use of such models to specific operating conditions. Hence, using these simple models for a wide range of operating conditions might lead to inaccurate results. Thus, for predictive simulation, one should ensure that the operating conditions of the application and those of the fitting data are similar.

4.3.1.2. Network Pyrolysis Models

The phenomenological approaches, also named network models, are characterized by significantly more details with respect to the description of the coal structure, resulting in increased flexibility, reliability, and broader application range [86]. However, computational expense generally also rises, making the direct application of such models in CFD more challenging.

The most important network models are:

- The Chemical Percolation Devolatilization (CPD) model [62; 63; 80];
- The Flash-Distillation Chain-Statistics (FLASHCHAIN[®]) model [166];
- The Functional Group-Depolymerization, Vaporization and Crosslinking (FG-DVC) model [224].

All models share similar features, such as a detailed characterization of the coal structure. However, differences concerning the interpretation of the macromolecular structure exist. For more details, the interested reader is referred to Hasse et al. [86].

Out of these models, only the CPD model is distributed by an open-source software license, whereas the other models are only commercially available. Therefore, the CPD model was chosen as a reference model for this work. The implementation in the work bases on the Fortran version available from Brigham Young University (BYU) [64].²

4.3.1.3. Chemical Percolation Devolatilization (CPD) Model

In the following, a brief introduction to the CPD model is given. The model initially proposed by Grant et al. [80] and later significantly extended by Fletcher et al. [62; 63] uses percolation theory to describe the coal lattice. The percolation theory is a statistical method to describe the decomposition of three-dimensional lattices characterized by a coordinate number and the fraction of intact bridges. In the case of CPD, lattice statistics are used to approximate the coal structure [80].

Modeling Pyrolysis by Lattice Statistics

The CPD model calculates the pyrolysis rate by assuming that labile bridges between the aromatic cluster are decomposed. This process forms two types of fragments. The first fragment class mainly consists of large tar precursors featuring high molecular weight and low vapor pressure. In contrast, the second fragment class possesses low molecular weight and thus high vapor pressure. During this process, a viscoelastic fluid called metaplast is formed. It consists of the coal lattice and high molecular weight fragments. All fragments must penetrate this metaplast to reach the surface. Thereby, crosslinking occurs, a process that describes the reattachment of fragments with the coal lattice. This process depends strongly on the heating rate; the faster the particle heating, the lower the likelihood of crosslinking. Therefore, high heating rates result in greater volatile yields. In the CPD model, the complex coal structure is represented by

²Since this version is written in FORTRAN77 and the particle temperature integration was hard-coded in the model, the version served more as a lead example and was employed for code against code verification. The version used in this work has been completely rewritten in free format (FORTRAN90 and newer) and can be flexibly coupled with various particle integration algorithms.

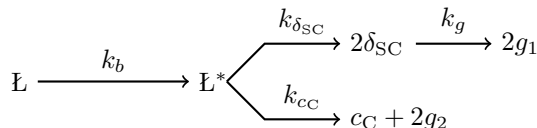


Figure 4.4.: Basic conversion steps of the CPD model. Graphic is adapted from [60].

a reduced lattice network connected by chemical bridges. To describe the conversion of these networks, percolation theory, a mathematical tool for lattice statistics, is applied [61]. Thereby, an infinite cluster represents the unreacted coal matrix, whereas finite clusters constitute tar molecules. More details on the application of lattice statistics for coal are given in [47]. To provide an analytic solution for the lattice decomposition, the percolation theory uses a pseudo lattice, the so-called Bethe lattice. The main feature of the Bethe lattice is that any two sites in a Bethe lattice are only connected by a single path of bridges and sites.

Reaction Mechanism

The standard mechanism of the CPD model is briefly outlined, which describes the breaking of the bonds and the formation of the reacting species. As depicted in Figure 4.4, the mechanism consists of four reactions describing the decomposition of labile bridges leading to the fragmentation of the coal matrix. This fragmentation results in the formation of light non-condensable gases, tar precursors, and the char matrix.

In a first step, the labile bridges \mathbb{L} slowly form a reactive intermediate species \mathbb{L}^* . Two competing parallel reactions follow this process. On the one hand, light non-condensable gas species g_2 are release. Simultaneously, the recombination of the two corresponding sides in the lattice leads to the formation of a char bridge c_C . On the other hand, side chains δ_{SC} form by stabilizing the reactive intermediate species \mathbb{L}^* . These side chains δ_{SC} are converted into light-gases in a subsequent slower reaction. Mathematically this process is described by a series of coupled differential equations. Generally it is assumed that the initially formed reactive species \mathbb{L}^* reacts immediately resulting in a steady state (i.e., $d\mathbb{L}^*/dt = 0$) between production ($k_b\mathbb{L}$) and consumption ($k_{\delta_{SC}}\mathbb{L}^*$ and $k_{c_C}\mathbb{L}^*$). The last reaction steps describe the formation of the light non-condensable gases, which can be either formed by conversion of side chains (g_1) or during the formation of the charred bridges (g_2).

As mentioned previously, not all fragments escape from the particle during devolatilization. Rather some amount of extractable material cross-links back to the char matrix. The mass of the finite fragments not leaving the char is denoted as metaplast mass (m_{meta}). The rate for the reattachment of the metaplast to the char matrix is modeled by a simple first-order law.

All reaction rate constants (e.g., k_b , $k_{\delta_{SC}}$, k_g , k_{c_C} , and k_{cross}) are modeled by an Arrhenius approach with distributed activation energies. These reaction rates are coal independent and are presented elsewhere [60; 86]. Furthermore, coal-dependent structural parameters and composition parameters are required to map the initial coal lattice to the Bethe lattice structure (e.g., the initial fraction of the intact bridges, the initial number of char bridges). These parameters must be determined by solid-state ^{13}C -NMR spectroscopy measurements.

To avoid these expensive and complex measurements, Genetti [71] and Genetti et al. [72] developed a set of correlations for calculation based on ultimate analysis and the PVM content. The recent review by Fletcher [60] indicates that employing these correlations leads to similar results compared to using measured values. Due to the unavailability of measurements, exclusively the Genetti-correlations are used throughout this thesis.

Distribution of the Released Gases

The standard implementation of the CPD model only accounts for the release of tar and gas species. However, their respective composition is not specified by the model. Genetti et al. [72] developed an empirical model, which determines the composition of volatiles based on the triangulation of measured data collected by Solomon et al. [225] and Chen and Niksa [27]. Moreover, Jupudi et al. [102] adapted the approach from the FG-DVC model [224], which solves individual rate equations for each gas species. This approach was further extended by Umemoto et al. [242] for the tar composition.

However, since the CPD model is only coupled to a flamelet description of gas-phase, direct coupling of individually released species is not necessary/possible (see Section 4.4). Only the simple method of Genetti et al. [72] is employed in this thesis to estimate the composition of the final volatile yield.

4.3.2. Modeling Char Conversion

Based on the previously introduced three zones, char conversion is either dominated by chemistry or the transport phenomena. Modeling approaches for char conversion are generally assigned to one of two following categories [86]:

- Global, apparent or observed reaction rates;
- Intrinsic reaction rates.

The apparent reaction rate denotes rates that are measured or observed for a specific condition. Typically all physical effects are reduced to one conversion rate, which depends on the particle temperature, outer surface, and oxidizer concentration at the particle surface. Hence, the model is empirical and only performs well for restricted operating conditions and one coal sample.

In contrast, intrinsic models explicitly account for the internal and external transport by dedicated submodels. Hence, the model accounts for the significantly enlarged inner surface area, where the heterogeneous surface reaction occurs. Moreover, transport limitations leading to non-uniform oxidizer concentrations in the particle are taken into account. However, determining the intrinsic surface area is challenging and generally requires experimental data. Moreover, the intrinsic surface is dynamically changing during the conversion process. In general, physical aspects are treated separately, enabling the application of intrinsic kinetic parameters for the heterogeneous reaction. However, additional models are necessary to describe the remaining processes, such as film diffusion, pore diffusion, and the evolution of the intrinsic surface. The intrinsic rates can be measured directly if the process is kinetically controlled (Zone 1). However, for Zone 2 and Zone 3, the intrinsic reaction rate is significantly larger than the observed reaction rate due to the neglect of transport limitations. Therefore, transport limitations must be explicitly modeled or expressed as an effectiveness factor to counterbalance the reaction rate.

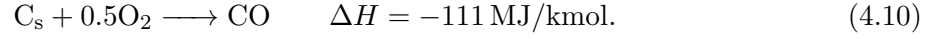
Heterogeneous Surface Reactions

During the heterogeneous surface reaction, both the inner and outer surfaces react with the surrounding atmosphere. Assuming that the particle already released all volatile matter, its main components are carbon and ash, with minor amounts of other elements. Therefore, most models treat char as pure carbon and neglect the reaction of minor components [38].

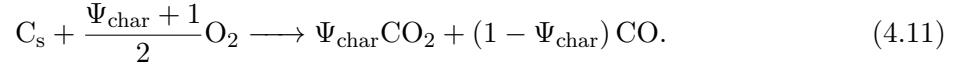
The main reactions occurring during char conversion are generally divided into combustion (oxidation) and gasification reactions [133; 168]. The combustion (oxidation) is orders of magnitude faster than gasification reactions. Therefore, in the first step, only the oxidation reaction

is taken into account in this thesis. Due to the short residence time and overall lean conditions in all configurations studied, oxidation is likely the dominant mechanism for char conversion³.

During oxidation, two competing exothermic reactions occur [86]



To simplify char modeling, both reactions are commonly represented by a single global reaction



Experimental data indicate that CO_2 is mainly formed at low temperature, while CO production becomes dominant at high temperatures. Based on these findings, many modeling studies neglect the CO_2 production entirely and assume that solely CO is formed by char reaction, which might be justifiable by the high reaction temperatures in swirl burners [108; 204].

Baum-Street Model

The simplest approach to describe char conversion in the thesis is the Baum-Street model [10; 57]. In this model, the following equation describes the entire conversion of the char structure

$$\frac{dm_{\text{char}}}{dt} = -\pi D_{\text{prt}}^2 \rho \mathcal{R} T \frac{X_{\text{O}_2}}{W_{\text{O}_2}} \left(R_{\text{diff}}^{-1} + R_{\text{reac}}^{-1} \right)^{-1}. \quad (4.12)$$

Here, D_{prt} is the current particle diameter, X_{O_2} is the oxygen molar fraction and W_{O_2} is the molar mass of oxygen. The diffusion rate coefficient R_{diff} is calculated as follows

$$R_{\text{diff}} = \frac{C_{\text{diff}}}{D_{\text{prt}}} \left(\frac{T_{\text{prt}} + T}{2} \right)^{0.75}. \quad (4.13)$$

The reaction rate R_{reac} coefficient is determined by

$$R_{\text{reac}} = A \varphi_{\text{char}} \exp \left(\frac{-E_a}{\mathcal{R} T_{\text{prt}}} \right). \quad (4.14)$$

The coal-specific coefficients C_{diff} , A , E_a were determined experimentally [79]. To account for the enlarged reactive surface due to porosity, the factor φ_{char} describes the ratio of the reacting surface to the outer sphere surface. φ_{char} was experimentally characterized as

$$\varphi_{\text{char}} = \exp \left(-2.622 - 1.78 \left(1 - \frac{m_{\text{char}}}{m_{\text{char},0}} \right) \right). \quad (4.15)$$

Here, m_{char} and $m_{\text{char},0}$ are the current and the initial char mass, respectively. The experimentally determined model parameters, which are only available for the Rhenish lignite, are given in Table 4.2.

³To investigate the effect of gasification, single-particle simulations in representative conditions were conducted. For all cases, the contributions to the mass loss from gasification reactions were below 1%.

Table 4.2.: Baum-Street model parameters of Rhenish lignite.

Parameter	Value
A	$1.886 \cdot 10^2 \text{ 1/s}$
E_a	$1.286 \cdot 10^5 \text{ J/mol}$
C_{diff}	$7.43 \cdot 10^{-13} \text{ m/sK}^{0.75}$

4.3.3. CRECK-S - Comprehensive Model for Coal Conversion

A recently proposed model, which differs in several aspects compared to previous models, was developed by the CRECK modeling research group at Politecnico di Milano, Italy⁴ [148]. The model is located between the complex network models and the simplified global models with respect to complexity. The main objective of this model is to provide a global description of the entire coal conversion regardless of different compositions and ranks. Thereby, the model employs a set of reference coals used to characterize a given feedstock (see next section). In a first step, this methodology was applied to the pyrolysis process, where a detailed mechanism was derived to predict the coal conversion for various conditions [226]. Subsequently, the method was extended seamlessly also to include char conversion [137].

It is noteworthy that this methodology is already extended to further solid fuels such as plastics [195], and biomass [40; 193; 194]. Therefore, the coupling strategy developed in this work for the solid phase with detailed gas-phase kinetics by means of tabulated chemistry (see Section 4.4) will be readily applicable to other fuels.

Fuel Characterization by Reference Coals

Contrary to network models, which require detailed information on the coal structure, the CRECK-S model only requires the elemental composition to map the coal onto four reference structures typically found in coals:

1. **COAL-1** ($\text{C}_{12}\text{H}_{11}$): This structure represents hydrogen-rich anthracites.
2. **COAL-2** ($\text{C}_{14}\text{H}_{10}\text{O}$): This structure represents bituminous coals similar to other mid-rank coals in terms of composition and structure.
3. **COAL-3** ($\text{C}_{12}\text{H}_{12}\text{O}_5$): This structure represents lignite coals, which have high contents of hydrogen and oxygen.
4. **CHAR-C** (C): This structure represents graphite structures, which consist of pure carbon.

However, not only the composition but also the structure of the respective reference species is specified to provide the composition characteristics and thus determine the reactivity and the released products during the conversion process [226].

In Figure 4.5, a van Krevelen diagram containing all CRECK-S reference species together with the coal samples used throughout this work is depicted. Based on the reference coals, triangular areas are formed. Since the outer triangle restricts the characterization (i.e., CHAR-C, COAL-1, and COAL-3), this area is also referred to as the characterization range. For a coal sample

⁴The CRECK group introduced a systematic nomenclature: CRECK-p-yymm-t, where p denotes the phase, yymm refers to the release date, and t characterizes the fuel type. Since only the solid kinetics for coal are employed in this thesis, the simplified term CRECK-S is used throughout this work.

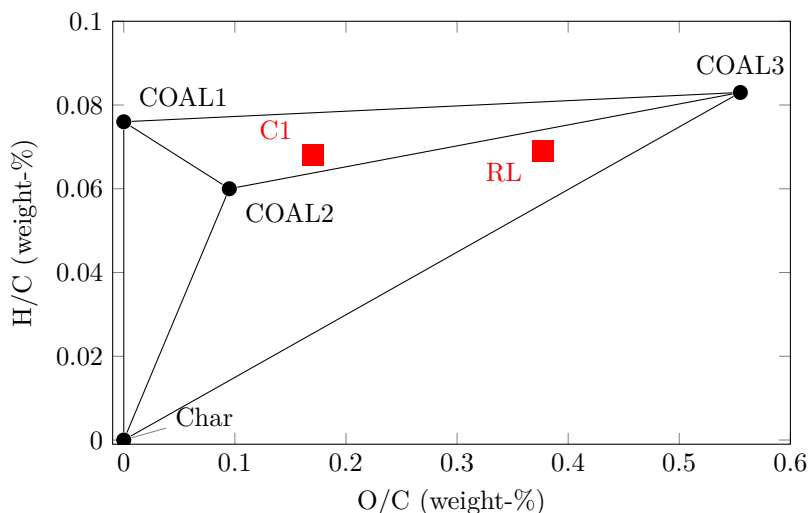


Figure 4.5.: Van Krevelen diagram depicting the location of CRECK-S reference species. Additionally, the locations of the coals employed in this thesis are shown in red.

located in this area, triangulation is performed to characterize it by a linear combination of the three limiting reference coal. Hence, the only information of the fuel required for the CRECK-S model is the ultimate analysis to obtain the fuel's location in the van Krevelen diagram. Moreover, the proximate analysis provides the necessary information about ash and moisture contents. This characterization procedure requires significantly less experimental information than the complex network models, making it attractive for CFD simulations. As an example, the coal samples used in this thesis are also depicted in Figure 4.5. Since both coals are located within the characterization range, these can be characterized by a linear combination of the reference coals as given in Table 5.5.

Table 4.3.: Characterization of the employed coals in the CRECK-S model.

Reference coal	Rhenish lignite	Columbian coal norte
COAL-1	0	0.118
COAL-2	0.21	0.554
COAL-3	0.68	0.243
CHAR-C	0.07	0
ASH	0.04	0.085

Pyrolysis and Char Formation

Each reference coal possesses its independent reaction pathway; thus, the overall coal conversion results from the linear combination of the reference coals. The main mechanism is similar for all coals and schematically depicted in Figure 4.6. In a first step, a metaplastic state is reached in which the coal decomposes into metaplastic gases, metaplastic tars, and char. Subsequently, the metaplastic gases and metaplastic tars are released to the gas phase. Additionally, the metaplastic tars might also reattach to the char matrix by cross-linking.

These processes are modeled by a multi-step kinetic mechanism, which is shown exemplarily for COAL-1 in Table 4.4. The full pyrolysis mechanism is available in the original paper by

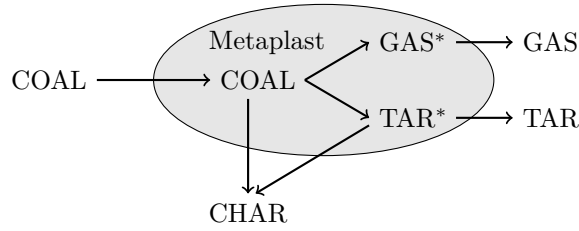


Figure 4.6.: Coal pyrolysis mechanism of CRECK-S model. Graphic is adapted from [226].

Sommariva et al. [226]. The initial decomposition of COAL-1 is modeled by four competing reactions (R1-R4). Thereby two reactions account for low-temperature conditions (R1-R2) and two for high temperatures (R3-R4). For low-temperature conditions, one reaction describes the formation of char and trapped low molecular weight metaplast species (R1), and one reaction the formation of trapped tars (R2). Decomposition (R3) and depolymerization (R4) reactions immediately release volatile species to the gas phase for high-temperature conditions. After the evaporation temperature of the trapped species is reached, these are also released (R5-R6). However, trapped species might also undergo cross-linking, leading to secondary char formation (R7-R8), which, as previously mentioned, determines the overall volatile yield. During pyrolysis and the subsequent char annealing, the three chars CHAR-H, CHAR-C, and CHAR-G, form. Their introduction is required to account for the evolution of the char. First, devolatilization leads to the formation of greater quantities of high reactive CHAR-H. Subsequently, CHAR-H reacts by char annealing to the amorphous CHAR-C (R9), which is less reactive due to lower H contents. The second step is graphitization, which results in a graphitized CHAR-G (R10).

Table 4.4.: Kinetic mechanism of COAL-1 pyrolysis [226] and char annealing in the CRECK-S model [137].

	Reactants		Products	Reaction description
COAL-1 pyrolysis				
R1	COAL-1	→	5 CHAR-H + 0.1 CHAR-C + 0.2 H ₂ + 0.9 CH ₄ + C ₂₋₅ *	} Low-T pyrolysis
R2	COAL-1	→	TAR ₁ *	
R3	COAL-1	→	5 CHAR-H + 0.25 CHAR-C + 0.5 H ₂ + 0.75 CH ₄ + C ₂₋₅	} High-T pyrolysis
R4	COAL-1	→	TAR ₁ *	
R5	TAR ₁ *	→	TAR ₁	} Release of metaplasts
R6	C ₂₋₅ *	→	C ₂₋₅	
R7	TAR ₁ * + CHAR-H	→	5.3 CHAR-H + 3 CHAR-C + 2.55 H ₂ + 0.4 CH ₄	} Cross-Linking
R8	TAR ₁ * + CHAR-C	→	4.3 CHAR-H + 4 CHAR-C + 2.55 H ₂ + 0.4 CH ₄	
CHAR annealing				
R9	CHAR-H	→	2 CHAR-C + 0.5 H ₂	} Annealing
R10	CHAR-C	→	CHAR-G	

The released gas species are also characterized by Sommariva et al. [226]. The consideration of secondary reactions for the released light gases in the gas phase by state-of-the-art reaction mechanisms is straightforward. Contrary, to account for the secondary reactions of the lumped tar species, a de-lumping into real species is required. Nevertheless, this detailed release of individual species is not considered for the coupling of the CRECK-S model with the flamelet model of the gas phase (see next section) and is for brevity omitted here.

All reaction rates are calculated by Arrhenius laws. Thus, the entire solid fuel mechanism is evaluated in a volumetric manner similar to a gas-phase mechanism, which was detailed in Section 2.1.6. A relative density, the so-called partial density, is introduced to obtain the concentration of the solid species. The partial density is calculated as the ratio of species density to the solid density of the particle.

Char Conversion

After pyrolysis and char annealing, the produced chars react with the surrounding gases in heterogeneous surface reactions. This process is modeled in the CRECK-S model by both oxidation and gasification reactions. In this work, only oxidation reactions are considered, as outlined previously.

Table 4.5.: Oxidation mechanism of char oxidation in the CRECK-S model [137].

	Reactants		Products
Oxidation reactions			
R1	CHAR-H + 0.75 O ₂	→	0.5 H ₂ O + CO + CHAR-C
R2	CHAR-C + O ₂	→	CO ₂
R3	CHAR-C + 0.5 O ₂	→	CO
R4	CHAR-G + O ₂	→	CO ₂
R5	CHAR-G + 0.5 O ₂	→	CO

The conversion of the three chars formed during pyrolysis is described by the heterogeneous mechanism developed by Maffei et al. [137], which is outlined in Table 4.5. In this mechanism, the remaining CHAR-H partially oxidizes to CHAR-C, H₂O and CO (R1). Then the competitive oxidation of CHAR-C to either CO or CO₂ (R2-R3) follows. Last, the slow-reacting CHAR-G likewise oxidizes to either CO or CO₂ (R4-R5). All solid species have a reaction order of unity, except for R1, R3, and R5, for which the order was empirically adjusted to 0.78. Combining devolatilization and char oxidation, the overall solid fuel mechanism used in this work consists of 22 solid species and 46 reactions.

The CRECK-S model evaluates the heterogeneous reactions on a volumetric basis. Thus, the kinetic mechanism does not consider changing surface structures, and therefore, mass transfer limitations are neglected. To account for the internal transport, the particle was resolved in the initial approach by Maffei et al. [137]. Due to the large number of particles simulated in this work, this approach might be too expensive to be applied to large-scale LES simulations. Therefore, an effectiveness factor η is introduced in this work to model the transport limitations. The corrected char reaction rate reads

$$r = \eta k_0 \exp\left(-\frac{E_a}{\mathcal{R}T_{\text{prt}}}\right) [\text{CHAR}][\text{O}_2]^\alpha, \quad (4.16)$$

where α denotes the reaction order. Following Senneca et al. [216], the effectiveness factor η is modeled by the Thiele and Biot approach, which is given by

$$\eta = \frac{\frac{3}{\varphi} \left(\frac{1}{\tanh(\varphi)} - \frac{1}{\varphi} \right)}{1 + \frac{\varphi}{Bi_m} \left(\frac{1}{\tanh(\varphi)} - \frac{1}{\varphi} \right)}. \quad (4.17)$$

Here, Bi_m is the mass transfer Biot number defined as

$$Bi_m = \frac{k_g d_{\text{prt}}}{D_e}, \quad (4.18)$$

and φ is the Thiele number given by

$$\varphi = \frac{d_{\text{prt}}}{6} \left(\frac{k_0 \rho_c \mathcal{R} T_{\text{prt}}}{D_e \Psi_{\text{char}}} \right)^{0.5}. \quad (4.19)$$

The required effective diffusivity is calculated by

$$D_e = \frac{D_{\text{mol}} D_k}{D_{\text{mol}} + D_k} \epsilon^2, \quad \text{with} \quad D_k = \frac{2}{3} A_{\text{prt}} r_{\text{pore}} \left(\frac{8 \mathcal{R} T_{\text{prt}}}{\pi W_g} \right)^{0.5}. \quad (4.20)$$

Here, W_g is the molecular weight of the gaseous reactant (O_2) and k_g is the external mass transfer coefficient. The pore radius r_{pore} is assumed to be constant (here: $5 \cdot 10^{-9}$ m), as proposed by Senneca et al. [216]. The molar density of the char is set to 80 kmol/m^3 . The stoichiometric coefficient Ψ_{char} in combustion varies according to the CO/CO_2 production ratio, which depends on temperature, as discussed previously. Further details on the calculations are reported in [211].

4.4. Coupling of Solid Fuel Kinetics to the Gas Phase

Although detailed models for the coal conversion process are widely accessible, most CFD simulations still rely on empirical models. However, in recent times efforts increase to include more advanced models in CFD calculations, as comprehensively discussed by Hasse et al. [86]. With respect to the coupling of the advanced models, two different strategies are employed: 1) Direct coupling; 2) Indirect coupling.

Both approaches have advantages and disadvantages. The direct application of detailed models does not require any *a priori* estimates of the condition that the particle undergoes in the simulation. However, the direct application also involves increased computational costs associated with advanced models.

Before this thesis, the direct application of detailed models was restricted mainly to RANS simulation [47; 101; 121; 236; 274]. For LES or DNS, the application of detailed models has been limited to academic test cases, such as single-particle ignition [52; 78; 239], or to small laboratory-scale experiments that mainly focus on devolatilization [51; 200; 254–256]. To the author's best knowledge, no direct coupling of detailed models to LES of the full burner exists in the literature.

Contrary, indirect approaches bases on a simplified representation of the detailed model. One common approach is fitting the parameters of empirical models (e.g., SFOR or C2SM) using results from the detailed models. Thereby, a proper estimate of the relevant conditions (e.g., particle heating rate, the temperature history, the atmosphere) is mandatory to obtain usable results. Another possibility to obtain the coefficients is the determination from experiments,

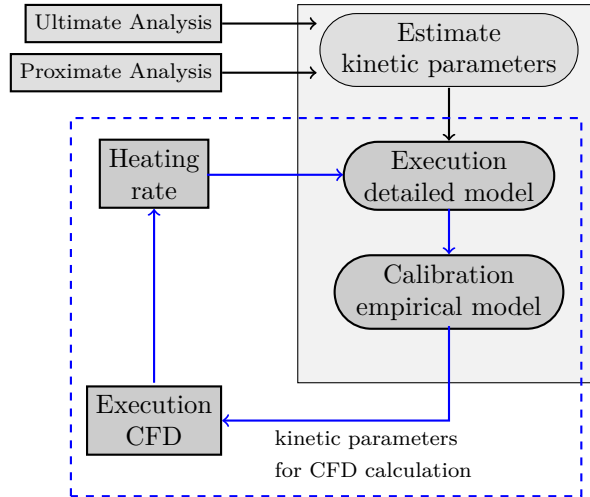


Figure 4.7.: Workflow of the pyrolysis pre-processor. Graphic is adapted from [247].

which is considered the traditional approach. However, the application of these reduced-order models is restricted to conditions similar to the experiments, which is often not the case, as extensively discussed in [166; 167].

In this thesis, both indirect and direct approaches are employed to study pulverized coal combustion. The details of the applied approaches are explained below.

4.4.1. Indirect Coupling by Simplified Kinetics to CFD

In this work, the Pyrolysis Kinetic Preprocessor (PKP), initially developed by Vascellari et al. [247], is used to calibrate the simple empirical models. Thereby, detailed reference solutions (e.g., CPD and CRECK-S) are used to calibrate the simplified models. Employing this strategy, Vascellari et al. [247] found favorable agreement with experimental data.

In summary, the four sub-steps of the overall model, depicted in Figure 4.7 are:

1. Determination of the kinetic parameters of the network pyrolysis models based on the results of proximate and ultimate analyses;
2. Estimation of yields and pyrolysis rates by the network models using the heating rates;
3. Calibration of the empirical model, minimizing the objective function;
4. Execution of the CFD simulation using the kinetic parameters.

Since heating rates must be estimated for the first run of the model, steps 2-4 should be carried out iteratively until a converged solution is reached [247]. However, for LES simulations, several full simulations might be too expensive. Thus, in this thesis, generally, only one to two iterations based on a fraction of the entire simulation time are performed to obtain realistic heating rates.

Simplified devolatilization models do not account for individual species releases as predicted by the detailed models. Instead, surrogate fuels $C_xO_yH_z$ or composition of the final volatile yield is used in the CFD simulation.

4.4.2. Direct Coupling Detailed Kinetics to CFD

As described previously, the CRECK-S solid fuel kinetics provide the unique opportunity to seamlessly model both devolatilization and char oxidation. However, as a flamelet-based de-

scription of the gas phase is adopted, the coupling of the solid kinetics requires additional modeling. A direct coupling would require as many mixture fractions as released species, since each individually released species represents an independent fuel stream. However, using such many mixture fractions would result in an unmanageable amount of table dimensions. Therefore, the coupling function $b_{c,i}$ of the i -th mixture fraction is defined by forming species groups

$$b_{c,i} = \sum_{\alpha=1}^{N_e} \beta_{\alpha,i} \sum_j^{N_{s,\text{prt}}} c_{\alpha,j} \gamma_{i,j} \frac{W_{\alpha}}{W_k} Y_{\text{prt},j} \quad \text{for} \quad i = 1, N_Z, \quad (4.21)$$

where $\gamma_{i,j}$ determines the share of the released species j in the mixture fraction i . The remaining part is similar to the mixture fraction definition in Equation (3.4). Here, N_Z corresponds to the number of employed mixture fractions. To obtain the mixture fraction, the coupling function must be normalized by the fuel since the oxidizer value is zero by definition

$$Z_i = \frac{b_{c,i}}{b_{c,i,f}}. \quad (4.22)$$

Considering $N_Z = N_{s,\text{prt}}$, each species could be associated to one mixture fraction. Thus, the individual release of species would be predicted correctly. By reducing the number of mixture fractions, certain species must be grouped. However, the species grouped can only be released in a fixed ratio.

Of course, the question arises how many mixture fractions are necessary to describe the coal conversion process accurately. Most studies rely on two mixture fractions to describe volatile release and char oxidation reactions separately. However, different studies proposed extensions of the two-mixture fraction model to account for additional physical effects. For example, moisture evaporation could be separated from the release of the remaining volatiles [258], pilot fuel stream could be modeled separately [262], or tars might be treated independently to model soot formation [143].

In this thesis, a two mixture fraction model is employed to avoid significant efforts for extending the already complex five-dimensional flamelet table. Furthermore, this enables a direct comparison with simplified kinetics, which rely on the same number of mixture fractions. Hence, species are grouped into two fuel streams, one representing the volatile species and on the char off-gas species, as it is commonly done for simpler n -step kinetic models [247].

Thus, all gas species formed during particle conversion but not originate from oxidation are combined for the devolatilization process. The volatile composition of this fuel stream is determined from the composition of the volatile yield. A similar procedure was proposed by [200; 255], who coupled the CPD model to a flamelet model. The results of this averaging procedure are depicted in Figure 4.8. Especially in the initial phase of devolatilization, during which predominantly H_2O is released, significant deviations between the averaged and instantaneous composition are visible. However, during later stages of devolatilization, the deviations due to averaging decrease. This assumption seems justifiable considering the short pyrolysis time.

Indeed a recent study to which the author of this thesis contributed showed that neglecting the individual release of species only has a minor influence on global flame characteristics [53]. Similar results have been reported by Wang et al. [256].

An additional possible shortcoming of this approach is the neglect of the heating rate dependency of the species composition. Figure 4.9 depicts the species composition for particles experiencing different heating rates. The most considerable difference is observed for the tar mass fraction due to the lower crosslinking rate at higher particle heating rates. Again, to account for this effect, at least one additional mixture fraction would be required. Compared to the overall model uncertainties, the deviation in the composition of the volatile yield in the

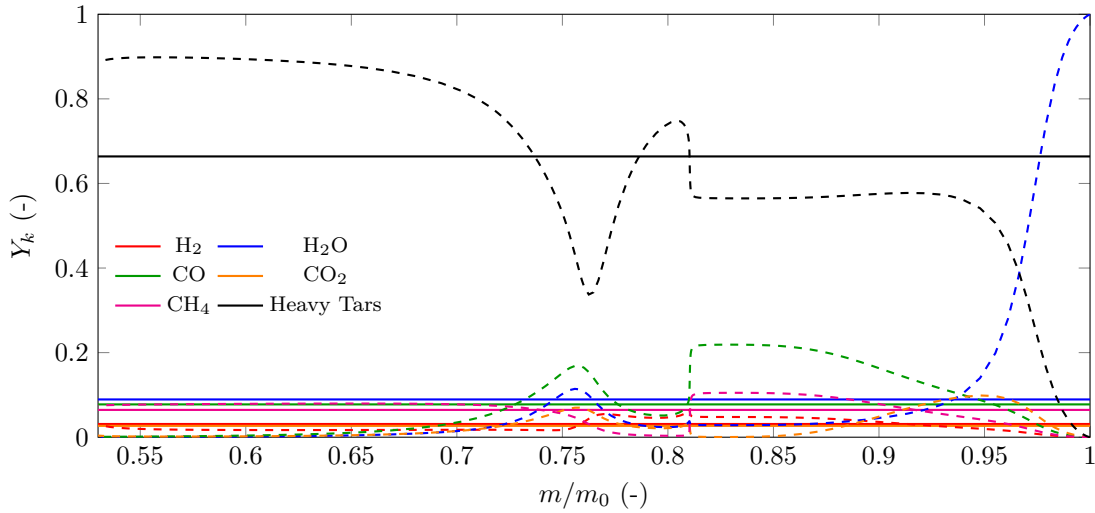


Figure 4.8.: Species release from a single bituminous coal particle which is subjected to a heating rate of 100 K/ms. Dashed lines indicate the dynamic release predicted by the CRECK-S model. Solid lines denote the temporally averaged release.

expected operating range is less than 5%, which is assumed to be neglectable. Therefore, the composition of the volatiles is taken from a detailed single-particle simulation at a representative heating rate. Nevertheless, the heating rate dependency of the volatile yield is still included.

Moreover, in this thesis, the volatile composition predicted by the CRECK-S model is further reduced to match the available gas-phase species (e.g., larger tars are substituted by C_6H_6). The final volatile composition for the employed coals is given in Table 6.12. The same composition is also used for the simplified devolatilization models introduced in Section 4.3.1.1.

Similar to the volatile mixture fraction, the char off-gas mixture fraction requires a fixed composition. From the gas phase point of view, the char conversion must be modeled as one global reaction to obtain a fixed composition. Therefore, the char conversion becomes the reaction of the averaged char composition (C_xH_y) with the surrounding atmosphere ($O_2 + \alpha CO_{2,SFR}$). Here, α denotes the molar ratio of oxidizer to inert species in the atmosphere. The

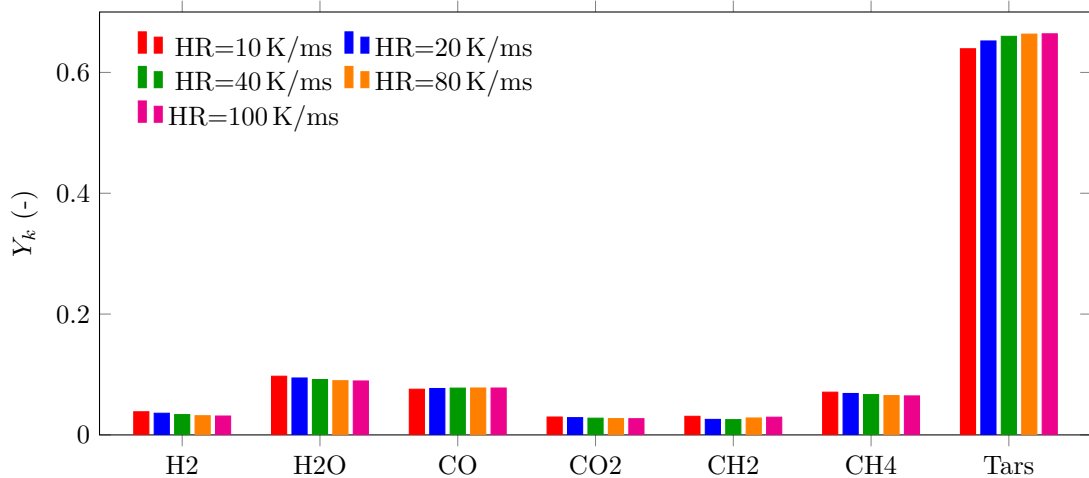
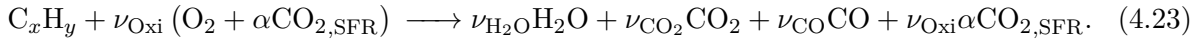


Figure 4.9.: Species composition from single bituminous coal particles subjected to different heating rates ranging from 10 K/ms to 100 K/ms.

Table 4.6.: Composition of the volatile yield for the employed coals.

Coal	H ₂	H ₂ O	CO	CO ₂	CH ₄	C ₆ H ₆
Rhenish lignite	0.134	0.159	0.190	0.093	0.027	0.397
Columbian bituminous coal	0.092	0.072	0.156	0.082	0.059	0.539

composition of char off-gases is determined from the composition of the yield resulting from oxidation. In contrast to the simplified char models (see Equation (4.11)), the CRECK-S model predicts char off-gases consisting of CO, CO₂, and H₂O. Therefore, the global char reaction reads



The stoichiometric coefficients ν_{Oxi} , $\nu_{\text{H}_2\text{O}}$, ν_{CO_2} , ν_{CO} and the averaged composition of the char C_xH_y are calculate prior to the actual simulation using a detailed single-particle simulation representative for the investigated operating point. In this work, a simulation of a single reacting particle at a constant temperature of 1400 K is used to determine the coefficients in Equation (4.23). All parameters are listed in Table 6.13.

Table 4.7.: Stoichiometric coefficients of the global char reaction for a particle oxidized at 1400 K in an atmosphere containing 27 Vol.-% O₂ and 73 Vol.-% CO₂.

α	x	y	$\nu_{\text{H}_2\text{O}}$	ν_{CO_2}	ν_{CO}	ν_{Oxi}
2.703	1.0	0.0175	$8.75 \cdot 10^{-3}$	0.346	0.654	0.677

In summary, the coupling of the CRECK-S model to a flamelet-based description of the gas phase requires the definition of multiple fuel streams. Therefore, an *a priori* knowledge of the species composition is needed to form the species groups. In this study, two fuel streams representing the volatiles and the char off-gases are introduced, as commonly used in the literature for simplified solid fuel kinetics [108; 204]. It should be stressed that both the volatile release rate and char conversion rate are still computed by the full solid fuel kinetics.

4.4.3. Particle Source Terms for the Gas-phase Equation

As outlined in Section 2.3.4, the point-particle interacts with the gas phase via source terms. These source term required the particle's mass release which can be calculated straightforward by summing up the contributions from char reactions and volatile release $\dot{m}_{\text{prt}} = \dot{m}_{\text{vol}} + \dot{m}_{\text{char}}$. Furthermore, source terms are required in the transport equations of the tabulated flamelet models introduced in Sections 3.4.4 and 3.5.4, respectively. Since species that are released from the particle are part of the reaction progress variable \mathcal{Y} , the transport equation of \mathcal{Y} contains the following source term

$$\bar{S}_{\text{prt},\mathcal{Y}} = \frac{1}{V_{CV}} \sum^{N_{\text{prt}}} (\dot{m}_{\text{vol}} \mathcal{Y}_{\text{vol}} + \dot{m}_{\text{char}} \mathcal{Y}_{\text{char}}). \quad (4.24)$$

For the mixture fraction describing the evolution of the volatiles in the gas phase, the source term is given by

$$\bar{S}_{\text{prt},Z_1} = \frac{1}{V_{CV}} \sum^{N_{\text{prt}}} (\dot{m}_{\text{vol}} Z_{1,\text{vol}}). \quad (4.25)$$

For the char conversion, the definition of the source term becomes more complex since the char-off gas mixture fraction includes the released solid mass and the inert part of the atmosphere. Therefore, the source term for Z_2 must be multiplied by a factor γ_{char} describing the ratio of char off-gases to the released solid mass. Then the source term for the char mixture fraction reads

$$\bar{S}_{\text{prt},Z_2} = \frac{1}{V_{CV}} \sum^{N_{\text{prt}}} (\dot{m}_{\text{char}} \gamma_{\text{char}} Z_{2,\text{char}}). \quad (4.26)$$

The factor γ_{char} is derived from the global char reaction and is given by

$$\gamma_{\text{char}} = \frac{W_{\text{CO}} + 0.5\alpha W_{\text{atm}}}{W_{\text{C}}}, \quad \text{and} \quad \gamma_{\text{char}} = \frac{\nu_{\text{CO}} W_{\text{CO}} + \nu_{\text{H}_2\text{O}} W_{\text{H}_2\text{O}} + \nu_{\text{CO}_2} W_{\text{CO}_2} + \nu_{\text{Oxi}} \alpha W_{\text{atm}}}{W_{\text{C}_x\text{H}_y}}, \quad (4.27)$$

for the Baum-Street model and the CRECK-S model, respectively. Here, α describes the molar ratio of the inert species in the atmosphere (i.e., N_2 in air and CO_2 in oxy-fuel) to O_2 . The heat generated by the char reaction is not transferred to the gas phase. Therefore, its contribution is added to the particle heat balance in Equation 2.67.

4.5. Interaction of Radiation with Solid Fuel Particles

In the context of pulverized solid fuel combustion, the complexity of thermal radiation increases significantly compared to pure gaseous radiation since emission, absorption and scattering by particles must be considered. The accurate modeling of the involved processes is challenging and requires complex models, such as Mie theory (which already requires some strong assumptions, e.g., spherical particles). Within this thesis, only the reduced-order models derived from detailed models were applied and are outlined in the following. For detailed information on the derivation of such models, the reader is referred to the Ph.D. thesis of Gronaz [82], who developed the applied models and provided MATLAB[®] routines to evaluate particle properties.

During particle radiation interactions, several effects coincide. Parts of the radiation entering the particle are absorbed and transformed into heat. Another portion changes direction during particle crossing. These effects are quantified by adsorption, scattering, and extinction efficiencies. When parallel radiation encounters a particle with the cross-section C_P , a specific portion is removed from its original direction, as depicted in Figure 4.10. This proportion can be assigned to a virtual projected area C_i . These virtual cross-sections are denoted as scattering, absorption, and extinction cross-sections.

Especially the scattering cross-section C_{sca} is often larger than the cross-section of the particle. The reason is the diffraction of radiation that is not incident on the cross-section of the particle. On the contrary, the absorption cross-section C_{abs} is typically smaller than one. The sum of both scattering and absorption, which corresponds to all radiation that is removed from its original direction, is denoted as extinction. Based on the virtual cross-sections C_i and the cross-section of the particle C_P , the efficiency factors are calculated as

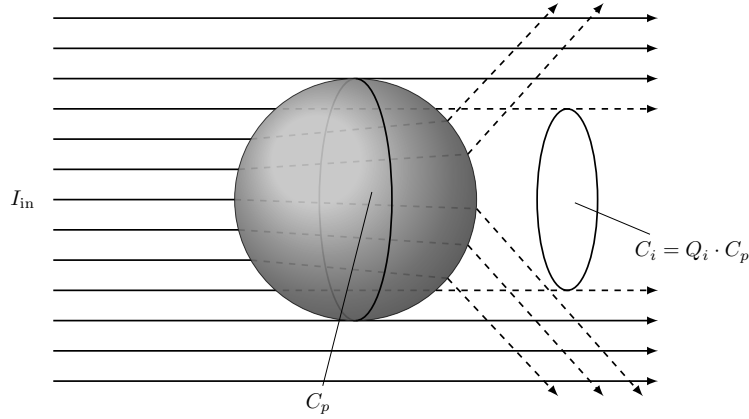


Figure 4.10.: Interaction of parallel radiation with a solid particle. Adapted from Gronanz [82].

$$\text{Scattering :} \quad Q_{\text{sca}} = \frac{C_{\text{sca}}}{C_P}, \quad (4.28)$$

$$\text{Adsorption :} \quad Q_{\text{abs}} = \frac{C_{\text{abs}}}{C_P}, \quad (4.29)$$

$$\text{Extinction :} \quad Q_{\text{ext}} = Q_{\text{sca}} + Q_{\text{abs}}. \quad (4.30)$$

The efficiency factors can be obtained from detailed models, such as Mie theory (see section 4.5.1). To incorporate particle scattering and absorption effects to the RTE, scattering and absorption coefficients are required. These coefficients are calculated from the product of the projected surface area of the particles per volume C_P in each cell multiplied by scattering or absorption efficiency [82]

$$\sigma = \frac{Q_{\text{sca}} C_P}{V_{\text{CV}}}, \quad \kappa = \frac{Q_{\text{abs}} C_P}{V_{\text{CV}}}. \quad (4.31)$$

Using these, the RTE can be extended by additional emission and adsorption from particle radiation interactions. Additional terms arise due to inscattering and outscattering by particles. The final RTE, modeling the spectral dependency with the WSGG model for gas phase and assuming gray particles, yields

$$\begin{aligned} \frac{d\mathbf{I}_j(\mathbf{r}, \mathbf{s})}{ds} = & \underbrace{\kappa_{j,g} a_{j,g} \mathbf{I}_{b,g} + \kappa_{\text{prt}} a_{j,\text{prt}} \mathbf{I}_{b,\text{prt}}}_{\text{Emission}} - \underbrace{(\kappa_{j,g} + \kappa_{\text{prt}}) \mathbf{I}_j(\mathbf{r}, \mathbf{s})}_{\text{Absorption}} \\ & - \underbrace{\sigma_{s,\text{prt}} \mathbf{I}_j(\mathbf{r}, \mathbf{s}) + \frac{\sigma_{s,\text{prt}}}{4\pi} \int_{4\pi} \mathbf{I}_j(\mathbf{r}, \mathbf{s}') \Phi(\mathbf{s}', \mathbf{s}) d\Omega'}_{\text{Scattering}}. \end{aligned} \quad (4.32)$$

4.5.1. Radiative Properties of Particle Clouds

To obtain the coefficients for adsorption and scattering from Mie theory, the complex index of refraction $m_r = n_r + ik_r$ is required, a material property that describes the interaction of electromagnetic waves with a medium. The former real part denotes the refractive index n_r . The absorptive index k_r describes the interaction of a medium with an electromagnetic wave.

For $k = 0$, the wave is transmitted through the medium. In contrast, for $k \geq 0$, parts of the energy of the wave are absorbed and either transformed to heat or emitted as an electromagnetic wave.

The complex index of refraction for ash is calculated based on the data by Goodwin and Mitchner [76], and for coal, the data from Foster and Howarth [66] are used. For the simulation, spectrally averaged radiative properties for particle clouds are determined utilizing a procedure given in Gronaz [82]. Scattering and absorption coefficients are tabulated as a function of particle temperature to avoid repetitive Mie-Theory calculation at runtime. This table is then used to determine the scattering and adsorption coefficients required for solving the RTE using following relation

$$\kappa_{\text{prt}} = \frac{1}{V_{\text{CV}}} \sum_n^{N_{\text{prt}}} Q_{\text{abs},n} A_{\text{prt},n}, \quad (4.33)$$

$$\sigma_{s,\text{prt}} = \frac{1}{V_{\text{CV}}} \sum_n^{N_{\text{prt}}} Q_{\text{sca},n} A_{\text{prt},n}, \quad (4.34)$$

where N_{prt} corresponds to the number of particles within the control volume V_{CV} , $Q_{\text{abs},n}$ and $Q_{\text{sca},n}$ are the absorption and scattering efficiencies associated with the n th particle and $A_{\text{prt},n}$ is the projected area of the n -th particle.

4.5.2. Scattering Phase Function

The interaction of radiation with particles leads to scattering (or redistribution), described by the scattering phase function Φ . This scattering function depends on the solid angle Ω_{S} and is symmetric with respect to polar angle. Hence, the phase function simplifies to $\Phi(\Theta)$. Generally, the dimensionless phase function is normalized leading to

$$\frac{1}{4\pi} \int_{4\pi} \Phi(\Omega_{\text{S}}) d\Omega_{\text{S}} = 1. \quad (4.35)$$

The simplest model is to assume purely forward scattering, which is similar to scattering negligence. Another simplified approximation is the use of an isotropic phase function that is unity for all angular directions. One commonly employed anisotropic phase function is given by the Henyey-Greenstein phase function [90]. This phase function is designed for strongly forward scattering objects. Hence, it should approximate scattering by coal and ash particles well. As

Table 4.8.: Values for parameters a_{HG} and g_{HG} in the modified Henyey-Greenstein phase function [82].

	Coal	Ash
a_{HG}	1.95	2.005
g_{HG}	0.9882	0.9565

outlined by Gronaz [82], fitting the original Henyey-Greenstein phase function to a spectrally averaged scattering phase function are error-prone. Therefore, Gronaz [82] proposed a modified version of the Henyey-Greenstein (HG) phase function specially tailored for the scattering of coal and for ash particles. The modified phase function possesses a new shape parameter a_{HG} , and the denominator exponent is changed to $5/4$, resulting in

$$\Phi_{\text{HGmod}}(\Theta) = \frac{1 - g_{\text{HG}}^{a_{\text{HG}}}}{(1 + g_{\text{HG}}^{a_{\text{HG}}} - 2g_{\text{HG}}\cos\theta)^{5/4}}. \quad (4.36)$$

The parameters of the modified Henyey-Greenstein phase function a_{HG} and g_{HG} for coal and ash are given in Table 4.8.

5. Numerical Implementations and Verifications

In this work, numerical methods are employed to obtain the solution of the governing equations for a given set of initial and boundary conditions. An essential point of this work is the implementation and consistent coupling of the models discussed in previous chapters. Here, the main focus is on embedding all models in the LES framework to enable predictive simulations of pulverized coal combustion at moderate computational costs.

All implementations were conducted in the academic CFD code FASTEST, which was initially developed for constant-density incompressible RANS [46]. The 3D Finite Volume Method (FVM) code uses a SIMPLE pressure-correction scheme [174] and a cell-centered variable arrangement on a non-staggered grid with selective interpolation of the mass fluxes to avoid pressure oscillations [196]. Complex geometries are represented by block-structured, boundary-matched meshes with hexahedral cells. A layer of ghost cells surrounds each block to facilitate connectivity to the surrounding blocks. For multiple core simulations, efficient parallelization is achieved by a Message Passing Interface (MPI).

Based on this foundation, the code was extended for reactive flows by Maltsev [141] and Schneider [213] employing RANS. First developments with respect to combustion LES were performed by Wegner [261]. Thereby, the potential of steady-flamelet and FGM tabulated chemistry simulations was shown. However, stability problems of the implicit Crank-Nicolson method with variable density flows were also reported. In successive works by Hahn [84] and Olbricht [171], significant revisions of the numerical solution procedure were undertaken to allow for more efficient and, most importantly, stable simulations. Thereby, an explicit Runge-Kutta time integration combined with the pressure correction based projection method introduced by Chorin [30] was implemented. Moreover, Hahn [84] and Olbricht [171] developed a scheme that alters the numerical treatment of the scalar transport equations to handle stability problems in regions of strongly varying densities.

Ketelheun [104] and Kuenne [118] provided extensive improvements with respect to chemistry tabulation as well as premixed flame simulations. They developed a methodology that accounts for gas-phase heat losses in the context of tabulated chemistry [104]. Furthermore, the ATF model was implemented to provide an efficient way to simulate turbulent premixed flames within LES [118].

Based on the contributions discussed above, Knappstein [107] and Sacomano [58] extended FASTEST to simulate multi-phase combustion. These developments are the starting point for all implementations carried out in this work.

The numerical methods presented in this chapter are subdivided into four main sections. The first section summarizes the numerical strategy used for the carrier phase. After that, the implementations related to the disperse phase to perform simulations of multi-phase combustion are detailed. This section is followed by a brief discussion of the numerical treatment of radiative heat transfer. Finally, the overall solution procedure illustrates the relationship between these three aforementioned blocks in the last section. Due to this theoretical framework, an extensive range of verification cases were considered to ensure that the numerical code properly represents the physical process. In order to keep within the scope of the work, extensive discussion of the

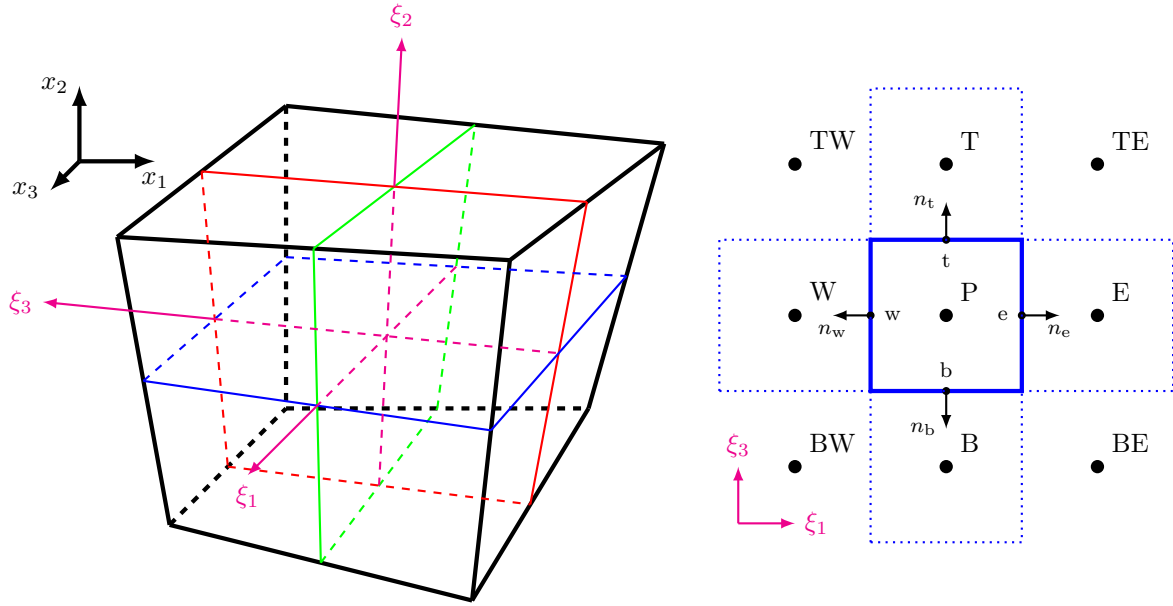


Figure 5.1.: Schematic drawing of the cell coordinates in FASTEST. Left: Control volume indicating both the global coordinate system (x_i) and the local cell-oriented coordinate system (ξ_i). Right: Exemplary two-dimensional depiction of the relation with neighboring cell centers (upper case letters) around the control volume P . Lower case letters indicate the faces connecting the control volumes with their respective normal vectors n_i . This graphic is partly adapted from [118; 171].

cases is omitted here. Verification cases are briefly discussed only when fundamental changes were made (e.g., solid fuel kinetics and carrier phase particle coupling).

5.1. Carrier Phase Treatment

In this section, the numerical approximations used within FASTEST are briefly discussed. The approximation of the solution for coupled PDEs introduced in Chapter 2 is obtained through appropriate interpolation methods based on discrete points in space and time. Both procedures are described in the following. At the end of the section, the treatment at the boundaries is specified.

5.1.1. Finite Volume Discretization of the Transport Equation

The finite volume method (FVM) discretization is illustrated with a generic transport equation for the scalar Φ

$$\frac{\partial}{\partial t}(\rho\Phi) + \frac{\partial}{\partial x_i}(\rho u_i \Phi) = \frac{\partial}{\partial x_i} \left(\Gamma_\Phi \frac{\partial \Phi}{\partial x_i} \right) + \dot{\omega}_\Phi, \quad (5.1)$$

with its diffusion coefficient Γ_Φ and source term $\dot{\omega}_\Phi$. As previously mentioned, the main idea of FVM is to divide the geometry into control volumes. Integrating Equation 5.1 over a control volume yields

$$\int_V \frac{\partial}{\partial t}(\rho\Phi) dV + \int_V \frac{\partial}{\partial x_i}(\rho u_i \Phi) dV = \int_V \frac{\partial}{\partial x_i} \left(\Gamma_\Phi \frac{\partial \Phi}{\partial x_i} \right) dV + \int_V \dot{\omega}_\Phi dV. \quad (5.2)$$

Using the Gauss theorem, the volume integrals of the convective and diffusive flux are transformed to surface integrals

$$\int_V \frac{\partial F_i}{\partial x_i} dV = \int_S F_i n_i dS, \quad (5.3)$$

where n_i denotes the face normal vector component into the i -th direction. Furthermore, for hexahedrons, the surface integral is split up into six surfaces (α =north (n), east (e), south (s), west (w), top (t), bottom (b)). This arrangement is sketched in Figure 5.1. This allows reformulating Equation 5.2 as follows

$$\underbrace{\int_V \frac{\partial}{\partial t} (\rho\Phi) dV}_{\mathcal{T}} + \sum_{\alpha} \underbrace{\int_{S_{\alpha}} \rho u_i \Phi n_i dS_{\alpha}}_{\mathcal{F}_{\alpha}^C} = \sum_{\alpha} \underbrace{\int_{S_{\alpha}} \left(\Gamma_{\Phi} \frac{\partial \Phi}{\partial x_i} \right) n_i dS_{\alpha}}_{\mathcal{F}_{\alpha}^D} + \underbrace{\int_V \dot{\omega}_{\Phi} dV}_{\mathcal{Q}}. \quad (5.4)$$

Here, \mathcal{T} , \mathcal{F}_{α}^C , \mathcal{F}_{α}^D , and \mathcal{Q} denote the transient term, the convective and diffusive fluxes through the face α and the source term, respectively. Up to this point, the equation is still exact since only mathematical transformations were applied. Next, to obtain an algebraic system, all terms are expressed by discrete points. Both surface and volume integrals are approximated by the midpoint rule, resulting in a second-order accuracy, which then read

$$\mathcal{T} = \int_V \frac{\partial}{\partial t} (\rho\Phi) dV \approx \frac{\partial}{\partial t} (\rho\Phi) \Big|_P \delta V \quad (5.5)$$

$$\mathcal{F}_{\alpha}^C = \int_{S_{\alpha}} \rho u_i \Phi n_i dA_{\alpha} \approx \rho u_i \Phi n_i \Big|_{\alpha} \delta S_{\alpha} \quad (5.6)$$

$$\mathcal{F}_{\alpha}^D = \int_{S_{\alpha}} \left(\Gamma_{\Phi} \frac{\partial \Phi}{\partial x_i} \right) n_i dS_{\alpha} \approx \left(\Gamma_{\Phi} \frac{\partial \Phi}{\partial x_i} \right) n_i \Big|_{\alpha} \delta S_{\alpha} \quad (5.7)$$

$$\mathcal{Q} = \int_V \dot{\omega}_{\Phi} dV \approx \dot{\omega}_{\Phi} \Big|_P \delta V. \quad (5.8)$$

The two volume integrals can be directly evaluated since the values at the cell center are known. However, further approximations are required to obtain the cell surface terms, which are detailed in the following.

5.1.2. Approximations of the Convective Flux

To obtain second-order accuracy on distorted grids, FASTEST uses a multi-dimensional Taylor series expansion around the surface point, which was proposed by Lehnhaeuser and Schaefer [127]. The Taylor series expansion under negligence of higher-order terms for the point on the east surface reads

$$\Phi_e \approx \gamma_E \Phi_E + (1 - \gamma_E) \Phi_P + \gamma_{NS} (\Phi_N - \Phi_S) + \gamma_{TB} (\Phi_T - \Phi_B), \quad (5.9)$$

whose weights are given by

$$\begin{aligned}\gamma_E &= \frac{x_{i,P} - x_{i,e}}{\mathcal{J}_e} \psi_e^{1i}, \\ \gamma_{NS} &= \frac{x_{i,P} - x_{i,e}}{\mathcal{J}_e} \psi_e^{2i}, \\ \gamma_{TB} &= \frac{x_{i,P} - x_{i,e}}{\mathcal{J}_e} \psi_e^{3i},\end{aligned}$$

where

$$\begin{aligned}\psi_e^{1i} &= \epsilon_{ikl}[(x_{k,N} - x_{k,S})(x_{l,T} - x_{l,B})] \\ \psi_e^{2i} &= \epsilon_{ikl}[(x_{k,T} - x_{k,B})(x_{l,E} - x_{l,P})] \\ \psi_e^{3i} &= \epsilon_{ikl}[(x_{k,E} - x_{k,P})(x_{l,N} - x_{l,S})] \\ \mathcal{J}_e &= (x_{i,E} - x_{i,P})\psi_e^{1i}.\end{aligned}$$

This interpolation scheme includes fewer nodes for the computation of cell surface values than most other proposed second-order schemes. Compared to the classical central differential scheme (CDS), the computational expense of the method is only slightly increased.

TVD interpolation

To ensure boundedness of the transported scalars, a total variation diminishing (TVD) limiter proposed by Zhou et al. [277] is employed. Thereby, the value of the cell face is computed by its downwind (D), its upwind (U) and its neighboring upwind (UU) nodes, given by

$$\Phi_e = \Phi_U + \frac{|x_{i,e} - x_{i,U}|}{|x_{i,D} - x_{i,U}|} B(r) (\Phi_U - \Phi_{UU}), \quad (5.10)$$

where the limiter function reads

$$B(r) = \begin{cases} \frac{r(3r+1)}{(r+1)^2} & : r > 0 \\ 0 & : r \leq 0. \end{cases} \quad (5.11)$$

Here, r denotes the gradient ratio

$$r = \frac{|x_{i,U} - x_{i,UU}|}{|x_{i,D} - x_{i,U}|} \frac{\Phi_D - \Phi_U}{\Phi_U - \Phi_{UU}}, \quad (5.12)$$

which is close to unity for well-resolved gradients, whereas values of zero or infinity are reached for sharp gradients. For well-resolved gradients, a second-order accuracy is preserved. In contrast, the method switches to pure upwind and, thus, first-order accuracy for sharp gradients.

5.1.3. Approximations of the Diffusive Flux

To facilitate the gradient evaluation required for diffusive fluxes, a formulation in local cell-based coordinates is used. Hence, the transformation between the two bases must be specified to obtain the derivatives in the Cartesian coordinates from the localized coordinate ξ_i (or vice versa). Following Ferziger and Peric [56], the following transformation rule is used

$$\frac{\partial \phi}{\partial x_i} = \frac{\beta^{ij}}{\mathcal{J}} \frac{\partial \phi}{\partial \xi_j}, \quad (5.13)$$

where \mathcal{J} is the Jacobian of the transformation and β^{ij} is the cofactors-matrix, which are specified in [56; 118].

To preserve second-order accuracy for the gradients at the cell face, the interpolation scheme proposed by Lehnhaeuser [126] is used

$$\left(\frac{\partial\Phi}{\partial x_i}\right)_e \approx \frac{\psi_e^{ji}}{\mathcal{J}_e} \Phi_e^j \quad (5.14)$$

with

$$\begin{aligned} \Phi_e^1 &= (\Phi_E - \Phi_P) \\ \Phi_e^2 &= (\Phi_N - \Phi_S + \Phi_{NE} - \Phi_{SE}) \\ \Phi_e^3 &= (\Phi_T - \Phi_B + \Phi_{TE} - \Phi_{BE}) \\ \psi_e^{1i} &= \epsilon_{ikl}[(x_{k,N} - x_{k,S} + x_{k,NE} - x_{k,SE})(x_{l,T} - x_{l,B} + x_{l,TE} - x_{l,BE})] \\ \psi_e^{2i} &= \epsilon_{ikl}[(x_{k,T} - x_{k,B} + x_{k,TE} - x_{k,BE})(x_{l,E} - x_{l,P})] \\ \psi_e^{3i} &= \epsilon_{ikl}[(x_{k,E} - x_{k,P})(x_{l,N} - x_{l,S} + x_{l,NE} - x_{l,SE})] \\ \mathcal{J}_e &= (x_{i,E} - x_{i,P})\psi_e^{1i}. \end{aligned}$$

5.1.4. Time Discretization

The one remaining term in the discretized transport equation is the temporal change of the arbitrary scalar Φ , which is reformulated to

$$\frac{\partial}{\partial t}(\rho\Phi)\Big|_P = \frac{1}{\delta V} \left(\sum_{\alpha} (\mathcal{F}_c^D - \mathcal{F}_c^C) + \mathcal{Q} \right) = \mathcal{R}(\Phi), \quad (5.15)$$

where $\mathcal{R}(\Phi)$ is introduced to summarize all previously introduced numerical approximation on the right-hand side of the equation. For the sake of brevity, the arbitrary variable φ is introduced to represent $\rho\Phi$.

To obtain a numerical approximation of the temporal derivative, FASTEST uses a low-storage Runge-Kutta scheme [267]. To represent a general Runge-Kutta scheme consisting of n stages, the following Butcher table is used

$$\begin{array}{c|c} c & A \\ \hline & b^T \end{array}. \quad (5.16)$$

Here the vector $c = [c_1, c_2, \dots, c_s]^T$ gives the position of the stages within a time step. The i -th staged variable $\varphi^{\text{RK},i}$ is obtained from the preceding stages and the matrix $A = [a_{ij}]$ by

$$\varphi^{\text{RK},i} = \varphi^n + \Delta_t \sum_{j=1}^s a_{ij} \mathcal{R}(\varphi^{\text{RK},j}) \quad (5.17)$$

where φ^n is the value at current time step. The intermediate variables $\varphi^{\text{RK},i}$ are weighted by $b = [b_1, b_2, \dots, b_s]$ to compute the next time step φ^{n+1} by

$$\varphi^{n+1} = \varphi^n + \Delta_t \sum_{i=1}^s b_i \mathcal{R}(\varphi^{\text{RK},i}). \quad (5.18)$$

The Butcher table for the three-stage second-order scheme that is used in FASTEST is depicted in Table 5.1. All intermediate stages and the new time step are computed by only considering

Table 5.1.: Butcher array of the three stage second-order low-storage Runge-Kutta scheme of FASTEST.

0			
1/3	1/3		
1/2	0	1/2	
	0	0	1

the old time step and the previous stage. Hence, only one additional stage needs to be stored, resulting in a low-storage formulation. Although theoretically, the highest achievable order of a Runge-Kutta scheme is equal to the number of stages, the order may be reduced for the sake of higher stability [123].

5.1.5. Pressure Correction

For compressible flows, the momentum and continuity form a system of equations that can be solved and the equation of state is used to obtain the pressure. Likewise, for incompressible flows, the momentum and continuity equations represent a complete system. However, no appropriate equation for the pressure exists.

To overcome this limitation, an iterative pressure correction method is introduced. The first step is to obtain an initial guess for the momentum from the explicit Runge-Kutta stage as introduced in the previous section

$$(\bar{\rho}\tilde{u}_j)^{*,\text{RK},i} = (\bar{\rho}\tilde{u}_j)^n + \alpha_{\text{RK},i}\Delta_t \left(C^{\text{RK},i-1} + D^{\text{RK},i-1} - \frac{\partial \bar{p}^{\text{RK},i-1}}{\partial x_j} \right), \quad (5.19)$$

where C and D denote the convective and diffusive term, respectively. The continuity equation at the new time level $\cdot^{\text{RK},i}$ is not fulfilled by the preliminary momentum. Therefore, the momentum is corrected by a momentum correction $(\bar{\rho}\tilde{u}_j)'$ reading

$$(\bar{\rho}\tilde{u}_j)^{\text{RK},i} = (\bar{\rho}\tilde{u}_j)^{*,\text{RK},i} + (\bar{\rho}\tilde{u}_j)'. \quad (5.20)$$

Together with a corrected pressure

$$\bar{p}^{\text{RK},i} = \bar{p}^{\text{RK},i-1} + \bar{p}', \quad (5.21)$$

continuity is satisfied. Then the corrected momentum can be obtained from

$$(\bar{\rho}\tilde{u}_j)^{\text{RK},i} = (\bar{\rho}\tilde{u}_j)^n + \alpha_{\text{RK},i}\Delta_t \left(C^{\text{RK},i-1} + D^{\text{RK},i-1} - \frac{\partial \bar{p}^{\text{RK},i-1}}{\partial x_j} - \frac{\partial \bar{p}'}{\partial x_j} \right). \quad (5.22)$$

By subtracting Equation (5.19) from Equation (5.22) and using Equation (5.20), the pressure correction is obtained

$$(\bar{\rho}\tilde{u}_j)' = -\alpha_{\text{RK},i}\Delta_t \frac{\partial \bar{p}'}{\partial x_j}. \quad (5.23)$$

By inserting Equation (5.20) into the continuity equation one obtains

$$\frac{\partial \bar{\rho}}{\partial t} + \frac{\partial}{\partial x_j} (\bar{\rho}\tilde{u}_j)^{*,\text{RK},i} + \frac{\partial}{\partial x_j} (\bar{\rho}\tilde{u}_j)' = 0. \quad (5.24)$$

Combining Equations (5.23) and (5.24) yields the final form of the Poisson-equation for the pressure correction

$$\frac{\partial}{\partial x_j} \left(\frac{\partial \bar{p}'}{\partial x_j} \right) = \frac{1}{\alpha_{\text{RK},i} \Delta_t} \left(\frac{\partial \bar{p}}{\partial t} + \frac{\partial}{\partial x_j} (\bar{\rho} \tilde{u}_j)^{*,\text{RK},i} \right) \quad (5.25)$$

which in its discretized form reads as follows

$$\sum_c \left(\frac{\partial \bar{p}'}{\partial x_j} n_i \right) \Big|_c \delta A_c = \frac{1}{\alpha_{\text{RK},i} \Delta_t} \underbrace{\left(\frac{\partial \bar{p}}{\partial t} \Big|_P \delta V + \sum_c \left((\bar{\rho} \tilde{u}_j)^{*,\text{RK},i} n_j \Big|_c \delta A_c \right) \right)}_{\epsilon_{\dot{m}}}. \quad (5.26)$$

This equation gives the relation between the pressure correction and the mass lack $\epsilon_{\dot{m}}$ of a single control volume. From all control volumes, an algebraic system for the pressure correction \bar{p}' is derived. The employed block-structure in FASTEST results in a simplified matrix, where only the diagonals corresponding to the neighboring cells are non-zero. To solve this algebraic system, FASTEST uses an iterative solver, which performs an incomplete lower and upper matrix decomposition (ILU) to take advantage of this structure. The employed procedure is strongly implicit and was proposed by Stone [232] to obtain the decomposition based on seven diagonals. The residuum of this procedure is defined by the mass lack $\epsilon_{\dot{m}}$ normalized by the mass flux. If it falls below a certain limit, convergence is obtained. Otherwise, another loop of inner iterations is performed. For more details on the implementation, the interested reader is referred to [128; 129].

5.1.6. Boundary Conditions

To solve a given set equations an appropriate set of boundary conditions is required. The boundary conditions must be specified at inlets, outlets and walls.

Inlet

A Dirichlet boundary condition determines the inlet values, i.e., the value is directly prescribed. The velocity at the inlet requires special treatments since, in most configurations, inlet velocities are already turbulent. To obtain correct physical results, turbulence must be considered at the inlet. In this work, sufficient upstream geometry is included into the simulation to ensure a developed turbulence profile at the region of interest.

Outlet

To describe the value at the outlet of the computational domain, Von Neumann type conditions are employed by assuming a zero gradient

$$\frac{\partial \varphi}{\partial n} = 0 \quad (5.27)$$

in the boundary normal direction n . Thereby, the skewness of the grid is considered by taking into account additional nodes as outline in Peric [149]. This boundary condition is applied to all variables with exception of the velocity. To avoid instabilities caused by pressure fluctuation at the outlet, Richter et al. [198] suggested to compute the normal velocity component by a convection equation

$$\frac{\partial u_n}{\partial t} + U_c \frac{\partial u_n}{\partial n}, \quad (5.28)$$

where U_c denotes a convection velocity that must be provided. Generally, the estimated bulk velocity is sufficient to obtain stable solutions since additional scaling of the obtained outlet velocity is performed to ensure global mass conservation [118].

Wall / Symmetry

A Dirichlet condition determines the velocities at the wall. The wall normal component is always zero to prevent a mass flux through the wall. In addition, the tangential wall component is set to zero, i.e., a no-slip condition is applied. A similar procedure is adopted for the temperature, which is set to a fixed value at the walls. In contrast, a Von Neumann condition, i.e., a zero-gradient condition, is applied for the species to prevent any species fluxes through the wall. At symmetry planes, Equation (5.27) is applied to all scalars and the symmetry-plane normal velocity.

5.2. Treatment of the Disperse Phase

The temporal evolution of the solid fuel particles is described by the previously introduced Equations (2.57), (2.58), and (2.67). The right-hand side of these equations depends on the time, the state of the disperse element, and the state of the continuous phase at the particle's position. This leads to two numerical challenges: 1) The interpolation of the required gas-phase properties to the particle position. 2) The temporal integration of the particles by an appropriate method. Initial implementations of the disperse phase were performed by Hahn [84] and Knappstein [108]. The inclusion of additional particle properties and detailed solid fuel kinetics required significant changes in the particle framework both in terms of flexibility and efficiency, which are outlined in the following.

5.2.1. Continuous Phase State at the Particle Position

The determination of the carrier phase properties at the particle's position is carried out through trilinear interpolation, i.e., with second-order accuracy. Based on a cell-centered variable ordering, the control volume centers around the particle form a hexahedron. Using the logical coordinates i , this hexahedron can be transformed into a cube with edge lengths of one. Since the basis vectors of the logical coordinate system $e_{\xi,i}$ are independent of each other by definition, the interpolation rule is given by a sequence of interpolations in the direction of the logical coordinates as

$$\begin{aligned}
\varphi(\xi) = & \Delta\xi_3\Delta\xi_2\Delta\xi_1 & \varphi_{i+1,j+1,k+1} + \Delta\xi_3\Delta\xi_2(1 - \Delta\xi_1) & \varphi_{i,j+1,k+1} \\
& + \Delta\xi_3(1 - \Delta\xi_2)\Delta\xi_1 & \varphi_{i+1,j,k+1} + (1 - \Delta\xi_3)\Delta\xi_2\Delta\xi_1 & \varphi_{i+1,j+1,k} \\
& + \Delta\xi_3(1 - \Delta\xi_2)(1 - \Delta\xi_1)\varphi_{i,j,k+1} & + (1 - \Delta\xi_3)\Delta\xi_2(1 - \Delta\xi_1) & \varphi_{i,j+1,k} \\
& + (1 - \Delta\xi_3)(1 - \Delta\xi_2)\Delta\xi_1\varphi_{i+1,j,k} & + (1 - \Delta\xi_3)(1 - \Delta\xi_2)(1 - \Delta\xi_1)\varphi_{i,j,k}. & (5.29)
\end{aligned}$$

Here, ξ is decomposed into an integer part and a fraction part

$$(\xi_1, \xi_2, \xi_3)^T = (i, j, k)^T + (\Delta\xi_1, \Delta\xi_2, \Delta\xi_3)^T. \quad (5.30)$$

By using Equation (5.29), all properties of the continuous phase can be interpolated to the particle position.

5.2.2. Temporal Integration Method

For the temporal integration of the particle phase, several different methods with various orders, either adaptive or non-adaptive, can be found in the literature [212]. In this work, two different methods were implemented: 1) An adaptive six-stage Runge-Kutta method, which automatically adapts the time step based on a numerical error obtained from the comparison of fourth and

Table 5.2.: Butcher array of fifth-order and fourth-order Runge-Kutta scheme [22].

0						
1/5	1/5					
3/10	3/40	9/40				
3/5	3/10	-9/10	6/5			
1	-11/54	5/2	-70/27	35/27		
7/8	1631/55296	175/512	575/13824	44275/110592	253/4096	
5 th -order	37/378	0	250/621	125/594	0	512/1771
4 th -order	2825/27648	0	18575/48384	13525/55296	277/14336	1/4

fifth-order methods; 2) An adaptive second-order predictor-corrector method (Heun’s method). Both methods, together with their respective advantages and disadvantages, are covered in next two paragraphs.

Adaptive Runge-Kutta Scheme

The quality of the solution of the numerical integration method depends on the ratio of the time step size to the smallest relevant time scales. In this context, it is desirable to know the numerical error in order to control its change by adjusting the time step size. Here, an efficient approach based on comparing different numerical methods is used, which goes back to Fehlberg [55]. Within the Runge-Kutta-Fehlberg method, the difference in the solution of simultaneously used Runge-Kutta methods with different orders enables the estimation of numerical errors. The method’s efficiency results from using the same stage for the the lower and higher order method.

The application of the Runge-Kutta procedure, whose coefficients are outlined in Table 5.2, is similar to the procedure outlined in Section 5.1.4. Then the numerical error can be calculated as follows

$$E \equiv y^{n+1} - y^{n+1,*} = \sum_{i=1}^6 (c_i - c_i^*) k_i. \quad (5.31)$$

To include the different order of magnitudes of the solved scalars (e.g., mass $\mathcal{O}(10^{-9})$ versus temperature $\mathcal{O}(10^3)$) in the evaluation, the error of each computed quantity k is normalized. After normalization, the overall error of the time integration is obtained by taking the maximum of all normalized errors

$$\epsilon = \max(E_k^{\text{norm}}) \quad \text{with} \quad E_k^{\text{norm}} = \frac{E_k}{E_k^{\text{scale}}}. \quad (5.32)$$

Based on this error, an optimal time step for the overall procedure is obtained by

$$\Delta_t^{\text{opt}} = \Delta_t \left| \frac{\epsilon}{\epsilon^{\text{krit}}} \right|^{-1/5}, \quad (5.33)$$

where ϵ^{krit} denotes the expected accuracy of the integration. The final time step size is calculated by

$$\Delta_t^{\text{new}} = \begin{cases} S \Delta_t \left| \frac{\epsilon}{\epsilon^{\text{krit}}} \right|^{-1/5} & : \epsilon \leq \epsilon^{\text{krit}} \\ S \Delta_t \left| \frac{\epsilon}{\epsilon^{\text{krit}}} \right|^{-1/4} & : \epsilon > \epsilon^{\text{krit}}, \end{cases} \quad (5.34)$$

where $S = 0.9$ is a safety factor.

Table 5.3.: Butcher array of a second-order predictor corrector method.

0	
1	1
	1/2 1/2

In summary, the scheme presents a robust and accurate way to approximate particle evolution, including efficient time step control. Nevertheless, especially compared to low-order schemes, the main downside of this method is that the right-hand side of the equations must be evaluated six times during one integration step. Thus, if the right-hand side of the particle is costly like for detailed solid fuel kinetics, this method becomes very expensive.

Predictor-Corrector Method

A second newly implemented method to perform particle integration is the Predictor-Corrector method (also called Heun’s method), which can also be classified as a Runge-Kutta method. The Butcher table for the predictor-corrector method is given in Table 5.3. In this method, first, a predictor is constructed from the Euler method (explicit). Subsequently, the predictor is improved by the corrector via the trapezoidal rule (i.e., of second-order accuracy), yielding the next time step value. The time step of the method is adapted based on the maximum gradient of each quantity [64]. More sophisticated methods may be worth elaborating in the future. The most striking difference to the previously discussed method is its lower order of accuracy. Due to the small Euler time step ($\mathcal{O}(10^6)$) required in LES, the most significant particle variations are still captured correctly. Additionally, several other studies (e.g., [44; 58]) have shown that point-particle LES with lower-order methods deliver favorable results, suggesting that the employed particle time-integration scheme is no crucial factor in such simulations.

5.2.3. Determination of the Particle Grid Position

Although Equation (5.29) enables the transformation from logical to physical coordinates, an analytic inversion of this relation to obtain the grid location from the physical particle location is not possible. In fact, the determination of the grid location from physical coordinates would require some iterative searching algorithm [212]. However, a search can be avoided for a block-structured grid, assuming that the particle’s initial position in logical coordinates is known. By taking the temporal derivative of Equation (5.29) (setting $\varphi = x_i$), the relation between the logical and physical velocities is obtained

$$u_{\xi_i} = \mathbf{J}^{-1}(\xi_i)u_i, \quad (5.35)$$

where, \mathbf{J} is the local Jacobi matrix. Based on the velocity, the determination of the particle location in logical coordinates reads

$$\frac{d}{dt}\xi_i = u_{\xi_i}. \quad (5.36)$$

Thus, no search is necessary, but a determination and inversion of the Jacobi matrix are required. Under the assumption that the cells are straight, an analytic approximation of the Jacobian is given in [212]. This procedure requires only one search (at the beginning) to determine the particle’s logical coordinates.

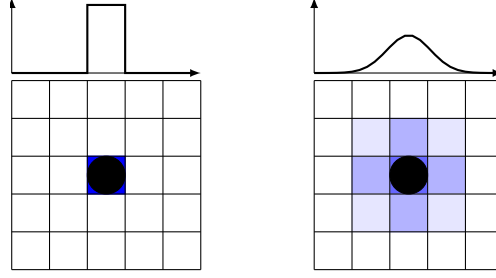


Figure 5.2.: Schematic depiction of the Euler source term without distribution (left) and with Gaussian distribution (right).

5.2.4. Euler Source Term

As previously outlined, the influence of the particles on the gas phase is modeled by source terms in the cell where the particle is located according to the particle in cell method (PSIC) [36]. Within FASTEST, special attention is required for the determination of the scalar transport source terms. For variable density flows, the non-conservative formulation of the transient term in the scalar transport equation is used in FASTEST [171]. Therefore, the convected scalar $\rho\phi$ in the time derivative is split according to the product rule

$$\frac{\partial \rho\phi}{\partial t} = \rho \frac{\partial \phi}{\partial t} + \phi \frac{\partial \rho}{\partial t}. \quad (5.37)$$

Inserting the continuity equation including its particle source term into (5.37) to replace the density derivative yields

$$\frac{\partial \rho\phi}{\partial t} = \rho \frac{\partial \phi}{\partial t} - \phi \frac{\partial \rho u_i}{\partial x_i} + \phi S_{\text{prt},m}. \quad (5.38)$$

Hence, an additional particle source term arises from the splitting of the transient term. The remaining discretization procedure is similar to that outlined in Section 5.1.1 and are thoroughly discussed in [107].

Source Term Distribution

For ignition studies in the context of point particle methods, the ratio of particle to cell size is critical. Too large grid sizes can potentially delay homogeneous ignition around particles due to very dilute mixtures. Therefore, grid widths Δx in the same order of magnitude as the mean particle diameter are generally employed. However, such small grid cells would lead to large source terms.

To overcome these difficulties, several methods are proposed in the literature [275]. One example is the cube averaging method that bases on averaging all quantities inside a fix-sized cube, whose center is located at the particle position. These averaged quantities are then used to compute the evolution of the particle. Similarly, the particle source term is distributed over the entire cube. Another method makes use of two different grid sizes for the gas and particle phase. In this way, both the resolution requirements for the gas phase and the particle can be fulfilled simultaneously.

Differently, in this work, the particle source terms are distributed spatially through convolution with a Gaussian kernel [6], defined as

$$\mathcal{G}(x_i, x_{\text{prt},i}) = \frac{1}{(\sigma\sqrt{2\pi})^3} \exp \left[-\frac{\sum_{k=1}^3 (x_k - x_{\text{prt},k})^2}{2\sigma^2} \right]. \quad (5.39)$$

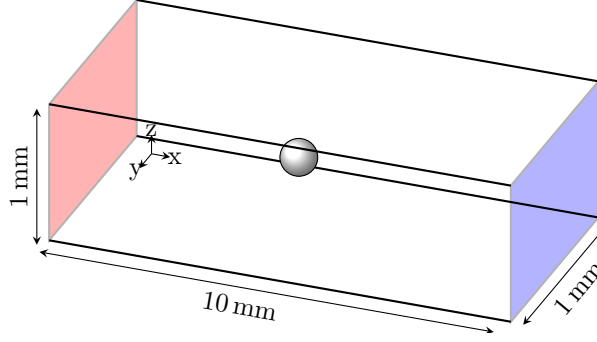


Figure 5.3.: Schematic depiction of the test case. Red: inlet. Blue: outlet.

The characteristic radius σ is set to $2 D_{\text{prt}}$, which is appropriate for single particles and particle groups according to Farazi et al. [51; 52]. In addition, \mathcal{G} is normalized over all participating control volumes to ensure that the particle source term is conserved. The source term distribution is schematically depicted in Figure 5.2 for a two-dimensional grid.

This approach should be seen as a first suggestion and was only applied in the laminar DNS study discussed in Section 6.1. The limiting behavior of particles with the same size as the grid requires significantly more research as no universal solution is available in the literature.

5.2.5. Verification of the Particle-Gas Phase Coupling

The overall model formulation is of significant complexity, involving the definitions of the two mixture fractions, their interaction with the solid fuel particle through source terms and the determination of the thermo-chemical quantities based on sizeable four- or five-dimensional tables. Due to this theoretical framework, an extensive range of verification cases were considered to ensure that the physical process is properly represented by the numerical code, out of which one be presented here. Parts of this section are published in [163]. In this test case, the devolatilization and the char burnout, which describe fundamentally different physics, are investigated individually.

The computational domain, which is depicted in Figure 5.3, is a channel with a length of 10 mm and a square cross-sectional area of 1 mm^2 , which is adapted from [110; 111]. This geometry is discretized with $100 \times 3 \times 3$ cells. In the channel, a particle at a position of $x = 5 \text{ mm}$ is fixed artificially. The surrounding oxy-fuel atmosphere consists of 30 vol % O_2 and 70 vol % CO_2 . The temperature of the two phases is set to 400 K initially to ensure that no heat exchange takes place. Since the temperature is taken from the chemistry table, it can vary inside the domain. This variation is a consequence of numerical errors in solving the transport equations and interpolation errors from reading the chemistry table. Therefore, the temperature profile is a good indicator of the accuracy of the implemented approach. To be able to derive an analytical solution of the outlet composition for the test case, the particle is assumed to have a constant conversion rate instead of using the models introduced in Chapter 4. Hence, the final stationary composition at the end of the simulation area can be determined in advance from the conservation of mass

$$\dot{m}_{\text{inl}} Z_{1,\text{inl}} + \dot{m}_{\text{vol}} Z_{1,\text{prt}} = \dot{m}_{\text{out}} Z_{1,\text{out}} \quad (5.40)$$

$$\dot{m}_{\text{inl}} Z_{2,\text{inl}} + \dot{m}_{\text{char}} \gamma_{\text{char}} Z_{2,\text{prt}} = \dot{m}_{\text{out}} Z_{2,\text{out}}, \quad (5.41)$$

with \dot{m}_{inl} and \dot{m}_{out} are the mass flux through the inlet and outlet, respectively. \dot{m}_{vol} and \dot{m}_{char} defines the fixed mass released from the particle from devolatilization and char oxidation, respectively. γ_{char} gives the ratio of ratio of char off-gases to the released solid mass (see Section

Table 5.4.: Boundary conditions for verification test cases.

	$\dot{m}_{\text{inl}} \left(\frac{\text{kg}}{\text{s}} \right)$	$\dot{m}_{\text{vol}} \left(\frac{\text{kg}}{\text{s}} \right)$	$\dot{m}_{\text{char}} \gamma_{\text{char}} \left(\frac{\text{kg}}{\text{s}} \right)$	$\dot{m}_{\text{out}} \left(\frac{\text{kg}}{\text{s}} \right)$		
Devo.	$4.5e^{-8}$	$0.5e^{-8}$	0	$5.0e^{-8}$		
Char	$4.5e^{-8}$	0	$0.5e^{-8}$	$5.0e^{-8}$		
	$Z_{1,\text{inl}} (-)$	$Z_{1,\text{vol}} (-)$	$Z_{1,\text{out}} (-)$	$Z_{2,\text{inl}} (-)$	$Z_{2,\text{char}} (-)$	$Z_{2,\text{out}} (-)$
Devo.	0.05	1.0	0	0	0	0
Char	0	0	0	0	1.0	1.0

4.4.3). Z_1 and Z_2 describe the first and second mixture fraction, respectively, at the corresponding position.

The boundary conditions for the volatile release and the char conversion test cases can be taken from Table 5.4. Because the particle rates are kept constant, no errors resulting from the devolatilization model or the char model can be investigated. Figure 5.4 depicts the temporal development of the transport quantities of the simulation along the central axis of the channel. These quantities are analyzed to identify sources of error in transport, as well as coupling between the particles and gas phase.

Immediately after the initialization with constant mixture fractions $Z_1 = 0.05$ and $Z_2 = 0$ for the devolatilization and char burnout test, respectively, the fields encounter a drastic increase at the particle position. Convective and diffusive fluxes transport the released mass until the field converges towards a stationary state. In this process, the mass is strictly conserved (for brevity not shown here). Both mixture fractions converge for the particular test case towards the a priori calculated analytical value of $Z_1 = 0.1$ and $Z_2 = 0.1$, respectively, which indicates a correct coupling of the two phases.

The value of the progress variable varies during the mass release. That is to be expected because its value is dependent on both mixture fractions. Since the progress variable contains CO_2 and O_2 , the progress variable becomes non zero for the oxidizer. In contrast, for the volatiles containing in this case only CH_4 , the progress variable is zero. Thus, the progress variable must decrease during the volatile release. In the second case, the products of the char reaction and the atmosphere both contain CO_2 . In addition to CO_2 , the oxy-fuel atmosphere also contains O_2 , which reduces the progress variable. In contrast, the CO from the char reaction increases the progress variable. Thus, the progress variable of the char products has a higher value than that of the atmosphere. Consequently, the mixing process must lead to an increased progress variable, which is reproduced by the model. However, the normalized value of the progress variable used to access the table remains zero. Thus, no chemical reaction takes place, which is correct for the test case.

A similar argumentation holds for the enthalpy. During devolatilization, the enthalpy must rise because the enthalpy of the released gases is higher compared to that of the atmosphere. However, the enthalpy of the char products is lower than that of the atmosphere. Therefore, a lower enthalpy at the outlet is a result of the char conversion. Additionally, the figure depicts the temperature to investigate the heating of the gas phase. The temperature is not a transported quantity but is instead read from the FGM table. Thus, numerical errors for the temperature can arise not only from coupling two phases but also from accessing the table access can arise for the temperature. Overall, the temperature shows minimal deviations from the initial temperature. For both test cases, the final temperature at the outlet of the channel shows a difference of $\approx 1 \text{ K}$ compared to the initial value. These small deviations can be traced back to numerical errors, which are caused by the strict test conditions with very high conversion rates. In real applications, more minor differences should therefore occur.

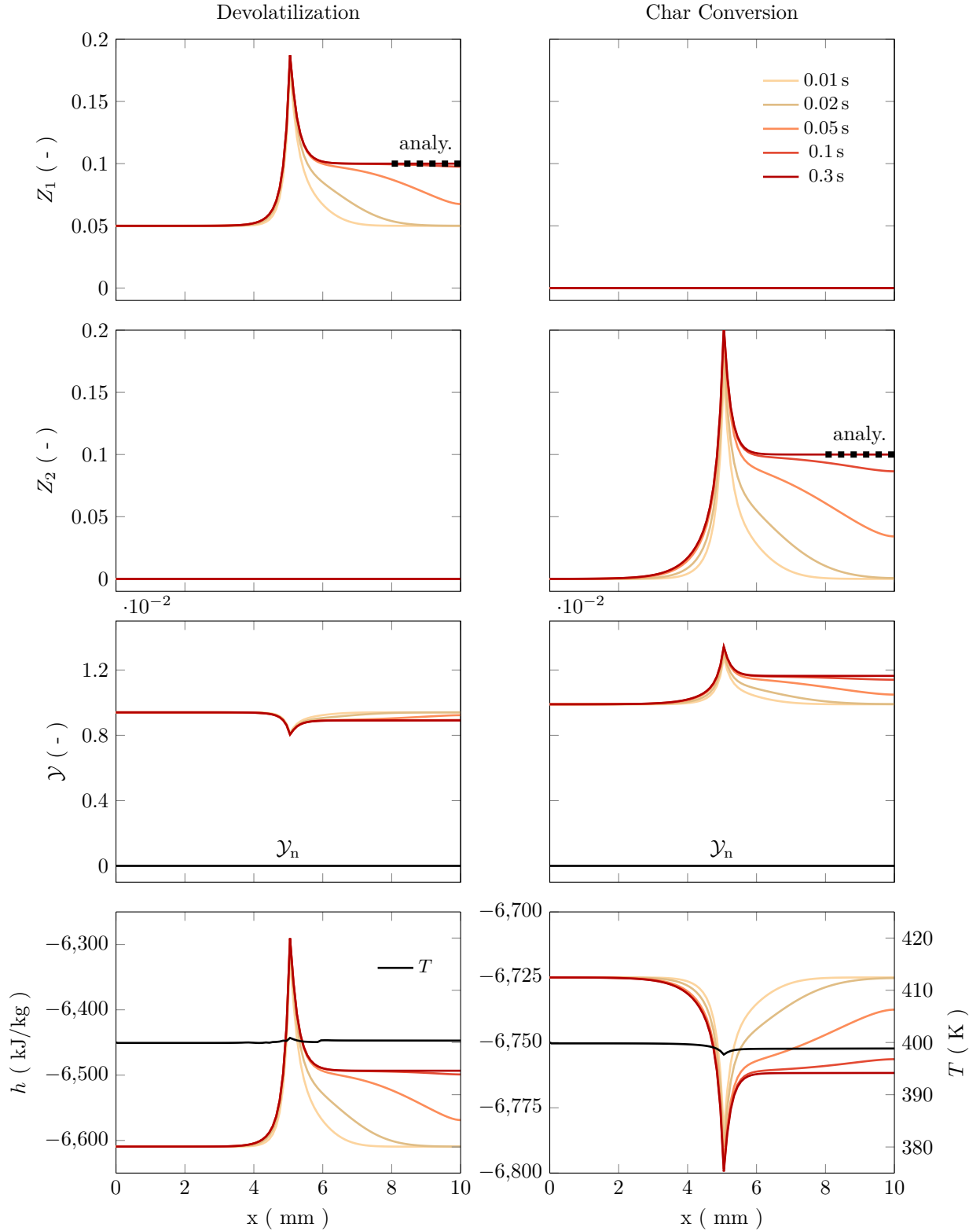


Figure 5.4.: Results for the transported scalars for FGM particle coupling verification test case. Left: Devolatilization of a single particle. Right: Char conversion of a single particle. From top to bottom: The four transported scalars are the: first and second mixture fractions, the reaction progress variable and enthalpy, which are used to access the table. Additionally, the temperature is shown. For the first and second mixture fractions, the analytic reference solution is depicted in black.

Since this variety of phenomenon must be considered, a verification of the coupling constraint is necessary and is successfully performed with the help of the test cases.

5.2.6. Solid Chemistry Treatment

The CRECK-S model (see Section 4.3.3) requires the solution of a stiff system of equations describing the particle conversion. In particular, the different orders of magnitude of the reaction constants are responsible for the stiffness of a differential equation system. As discussed in detail by Meier [144], the direct application of time discretization to complex reaction mechanisms, either solid or gas phase, leads to very small time steps, increasing computational cost substantially. To avoid these small time steps, the source term is generally decoupled from the remaining transport equation and is integrated independently. For the case of solid fuel point particles, the differential equation for the reactants reads

$$\frac{\partial \rho_{\text{prt}} Y_{\text{prt},k}}{\partial t} = W_{\text{prt},k} \frac{\partial c_{\text{prt},k}}{\partial t} = r_k(c_1, \dots, c_{N_{\text{prt},s}}). \quad (5.42)$$

This system of equations is equal to a perfectly stirred reactor. In each time step, the composition of the reactants at $t + \Delta t$ is determined independently as an inner integration of Equation (5.42). The subintegration is performed by an implicit *backward differentiation formulation* (BDF) method, which is available from the solver package LSODE [190].

5.2.7. Verification of Solid Fuel Kinetics

In the following, code-to-code comparisons are carried out to verify the correctness of the implementation. A code-to-code comparison describes the assessment of the output from one code to the output from another code [169]. The reference solutions are obtained using the code provided by the authors of the CRECK-S model (i.e., OpenSMOKE++ framework of the CRECK modeling group [37]).

Integrating detailed solid fuel kinetics in the existing framework involves additional complexity due to the necessity to treat the kinetics separately from the remaining particle phase. Both the integration of the kinetics and the coupling to the surrounding gas phase require verification to ensure the correctness of the results. For the verification of the CRECK-S model, a simplified setup is chosen. The setup consists of a single particle inside a computational cell. The inflow velocity is set very high to ensure short residence times of released gases inside the numerical cell, i.e., the atmosphere around the particle can be considered constant. Two different simulations are conducted: First, a case in an inert atmosphere focusing solely on pyrolysis kinetics is studied. Secondly, the setup is adapted to an atmosphere consisting of 15 weight-% O₂ and 85 weight-% N₂. To focus only on the char conversion, the initial coal composition is also adapted. The initial coals for both cases are summarized in Table 5.5. The particle temperature profile is prescribed by a heating rate of 2.667·10⁵ K/s. After reaching a temperature of 1800 K, the temperature is kept constant.

Devolatilization

The results of the devolatilization case are presented in Figure 5.5. Considering the mass loss denoted by the black line for FASTEST and black dots for OpenSmoke, respectively, excellent agreement between the two codes is observable. Both predict a rapid release of particle mass at around 1 ms, followed by a small decrease of the release rate around 1.5 ms. After 3.75 ms, both codes predict the end of the devolatilization phase with a final mass loss of around 50 weight-%. Comparing the conversion of the initial species also excellent agreement can be

Table 5.5.: Characterization of the coals for the code-to-code comparison of the CRECK-S model.

Reference coal	Case 1: Devolatilization	Case 2: Char oxidation
COAL-1	0.33	0.0
COAL-2	0.5	0.0
COAL-3	0.1	0.0
CHAR-C	0	0.9
ASH	0.05	0.1
Atmosphere		
O ₂	0.0	0.15
N ₂	1.0	0.85

found. The two initial species COAL2 and COAL3 are directly consumed, whereas COAL1 is first produced before its consumption starts. Simultaneously, the CHAR fraction in the coal increases rapidly. The ash fraction of the coal is approximately doubled, which is consistent with the 50% mass loss. Considering the metaplast formation in the bottom of Figure 5.5, both codes show matching results. The formation of metaplast occurs during the main devolatilization phase. Furthermore, most of the metaplast is converted at the end of the devolatilization phase.

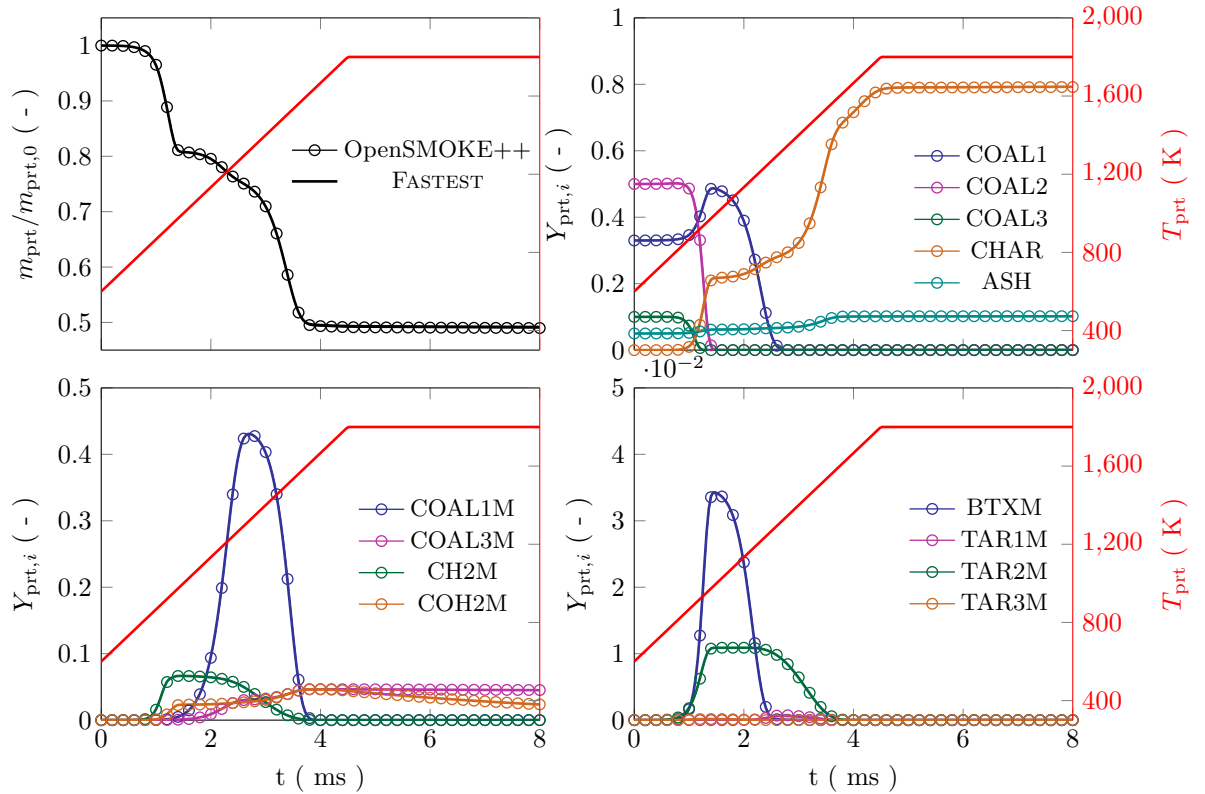


Figure 5.5.: Verification of the solid fuel reaction kinetics for devolatilization in FASTEST (lines) against solution obtained with OpenSmoke (dots). Top left: Normalized mass loss over time. Top right: Mass fraction of the initial species. Bottom left: Formation of the light gas metaplast. Bottom right: Formation of the tar metaplast. Additionally, all plots include the temperature history in red.

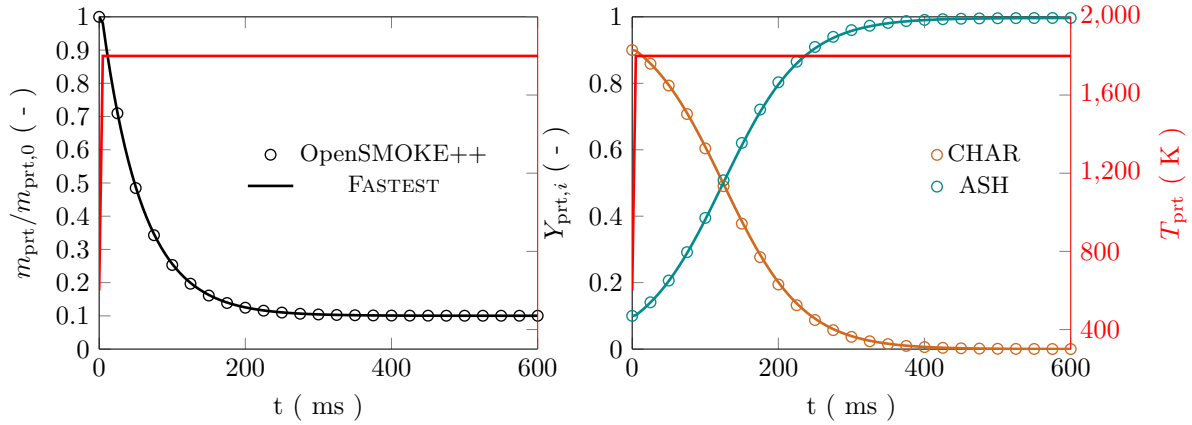


Figure 5.6.: Verification of the solid fuel reaction kinetics for the char oxidation in FASTEST (lines) against solution obtained with OpenSmoke (dots). Top left: Normalized mass loss over time. Top right: Mass fraction of the initial species. Bottom left: Formation of the light gas metaplast.

The remaining metaplast stays nearly constant since no oxygen is available for the metaplast oxidation. Based on the excellent agreement between the two codes, the implementation of the devolatilization part of the CRECK-S model in FASTEST is considered to be verified.

Char

Next, the second test case that deals with the char conversion is investigated in detail. This case possesses an increased complexity compared to devolatilization since the particle conversion depends on the surrounding atmosphere. A particle consisting of 90 weight-% CHAR and 90 weight-% ASH is considered to focus the char conversion solely. Due to the significantly slower reaction of the char, the simulated time is increased to 600 ms. In the first 100 ms, a rapid release of particle mass is observed on the left side of Figure 5.6. Subsequently, the release rate decreases significantly. At around 450 ms full conversion is reached. Comparing both codes, it can be seen that the release rates are the same. Considering the species formation, both the mass fraction of CHAR and ASH exhibit a consistent trend. The char conversion results in a decrease of the CHAR fraction in the particle, which in turn increases the ASH fraction. Complete conversion of the particle is reached when the ASH fraction reaches unity. In summary, the implemented solid fuel kinetics and the coupling of the surrounding atmosphere (i.e., effect of the gas phase on the particle) is verified by means of a code-to-code comparison.

5.3. Radiation

The radiative transfer equation is solved within the finite volume framework of FASTEST. Most implementation and verification of the radiation solver for single-phase flows were carried out by Miranda [150] and Miranda et al. [23]. The core aspects of the solution procedure are briefly summarized next. More details on this topic can be found in [150].

Discretization of the RTE

In the following, all descriptions of the treatment of radiation are given for one gray gas. However, the equation must be solved during the simulations for each gray gas of the WSGG model. Similarly to previous equations, the RTE is integrated over each finite control volume V to obtain a discretized equation. Additionally, an integration over each finite solid angle element

$\Delta\Omega_i$ must be performed

$$\int_{\Delta\Omega_i} \int_V \frac{dI}{ds} dV d\Omega = \int_{\Omega_i} \int_V (aI_b - KI) dV d\Omega + \int_{\Omega_i} \int_V \frac{\sigma_s}{4\pi} \int_{4\pi} \Phi(s', s) I(s') d\Omega' dV d\Omega. \quad (5.43)$$

Using the Gauss theorem, the volume integral is transformed to a surface integral, yielding

$$\sum_k A_k \int_{\Delta\Omega_i} I(s_i \cdot n_k) d\Omega = V \int_{\Omega_i} (aI_b - KI) d\Omega + V \int_{\Omega_i} \frac{\sigma_s}{4\pi} \int_{4\pi} \Phi(s', s) I(s') d\Omega' d\Omega. \quad (5.44)$$

To obtain the surface values of the radiative intensity, a spatial discretization scheme is required. Here, the step scheme is used, a simple but robust first-order method. This method sets the surface intensity equal to the intensity of the volume center. According to Modest, [154], this method, besides its lower order, gives physical results without numerical workarounds. Using

$$D_k = \int_{\Delta\Omega_i} (s_i \cdot n_k) ds \quad (5.45)$$

and assuming constant physical properties in each solid angle, the RTE discretized by finite solid angles reads

$$\sum_k A_k D_k I(s_i \cdot n_k) = V \Omega_i (aI_b - KI) + V \Omega_i \frac{\sigma_s}{4\pi} \int_{4\pi} \Phi(s', s) I(s') d\Omega' d\Omega. \quad (5.46)$$

This equations presents a conservation equation for the radiative intensity in the FVM framework.

For the angular discretization, the FT_n method proposed by Kim and Huh [96] is used. Compared to other FVM methods, a more uniform distribution of the control angles is obtained by the FT_n method. This is achieved by dividing the polar angle into an even number, n_ϕ , and the azimuthal angle uniformly into a number of the sequence 4, 8, .., $2n_\phi, 2n_\phi, .., 8, 4$ in each interval. In this work, the resolution was set to $n_\phi = 8$, leading to a total of $N_{\text{rad}} = 80$ directions.

One remaining difficulty is the treatment of the scattering integral. In the current implementation, the integral is treated by a point-wise integration. As outlined in Gronaz [82], more elaborate methods exist to perform such integrations. However, the method comes with low computational costs, enabling the evaluation of the integral within practically applicable times and reasonable precision. This becomes very important, as all directions of the RTE in Equation (5.46) are coupled. Thus, an iterative solution of the RTE is required, which requires multiple evaluations of the integral¹.

Boundary Conditions of the RTE

By applying the FVM method to discretize for the equation of the diffusely emitting and reflecting wall surfaces boundary condition yields

$$I_w = \epsilon_w I_{b,w} + \frac{1 - \epsilon_w}{\pi} \int_{n_i s_i > 0} I_w n_i s_i d\Omega \approx \epsilon_w I_{b,w} + \frac{1 - \epsilon_w}{\pi} \sum_j^{N_{\text{rad}}} I_w, \quad (5.47)$$

where ϵ_w denotes the emissivity of the wall.

¹Another possibility is to solve all directions simultaneously, allowing to implicitly take care of the dependency between directions. This option requires significantly more memory and is currently not applicable to LES with large numbers of CVs.

Divergence of the Radiative Heat Flux

Similar to the RTE, the divergence of the radiative heat flux is discretized, leading to

$$S_{\text{rad}} = - \left(4\pi\kappa_p I_{b,p} - \sum_j^{N_{\text{rad}}} \kappa_p I_{p,j} \Omega_j \right). \quad (5.48)$$

5.4. Overall Solution Procedure

The complete solution procedure is depicted in Figure 5.7. The procedure starts with the initialization of all fields, either from a initial guess or restart fields. First, the radiative source term is computed from the solution of the RTE. To reduce the computational costs associated with solving the RTE, radiation is computed with a frequency f_{rad} , which is set depending on the configuration. This procedure is similar to many studies found in the literature [75; 150]. Once the radiative source term is computed, the particle integration is performed. In the current implementation, the same MPI splitting as for the Euler phase is applied for the particles. Thus, particles located inside one block are computed by the same processor. After all particles have finished the entire time step, the carrier phase solution is computed using the previously described second-order Runge-Kutta scheme. First, the subgrid-scale variance, all scalars, and the enthalpy are transported. Then, the momentum transport is calculated, followed by the update of all thermodynamics properties and the determination of the chemical reaction. Finally, the pressure correction and correction of the velocities are carried out iteratively until convergence is reached. The procedure for the gaseous phase is repeated three times (three-stage Runge-Kutta). After that, the solution at the next time level $t + \Delta_t$ is obtained in the same manner.

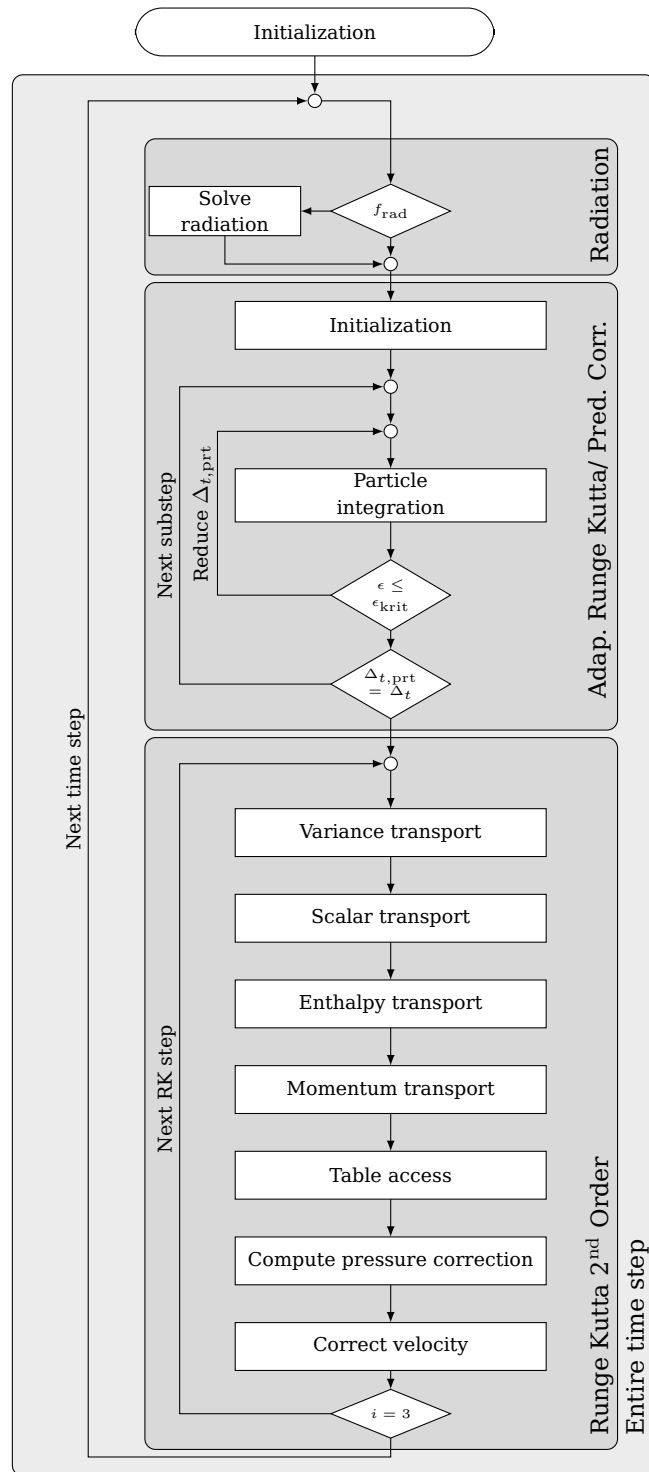


Figure 5.7.: Flow chart of the overall solution procedure employed in this work.

6. Applications

The objective of this chapter is to simulate and analyze both atmospheric and oxy-fuel combustion in chambers of various sizes using the developed simulation methods. Simulating and analyzing chambers at varying scales will provide a more thorough understanding of pulverized solid fuel combustion. To evaluate the interaction of the different models and conclude about the predictive capabilities of the holistic approach, validation against the data from experiments is mandatory. The investigated experimental configurations range from individual particle-scale via laboratory-scale to pilot-scale reactors. Furthermore, an important aspect of this section is that obtained results are analyzed and evaluated concerning numerical models (e.g., model interaction, the accuracy of model reduction) and physical effects (e.g., influence of surrounding atmosphere).

To illustrate the interrelationships of the configurations, Figure 6.1 depicts the results from the studied cases. In the background, the results of the pilot-scale combustion chamber are shown. Here, the focus is on the prediction of the overall process, including all coupled phenomena. However, not only from the simulation side but also from the experimental side, such configurations are challenging to investigate. Due to restricted optical accessibility, measurements are only possible in certain regions and under aggravated conditions. For instance, measurements inside the quarl region, where the flame is stabilized, are not possible.

Hence, smaller laboratory-scale configurations, depicted in the center of Figure 6.1, are required to validate the flame stabilization mechanism. Nevertheless, the adaptations required for these detailed measurements usually lead to compromises concerning practical relevance (e.g., glass walls for the optical access lead to significantly increased heat losses to the surrounding. Thus, only gas-assisted solid fuel combustion is possible.). Therefore, investigations of these facilities focus on regions where deviations from the real reactor are negligible (e.g., regions close to the burner port).

The strong interaction of turbulence with chemistry and particles still results in a significant complexity for such a configuration. Exclusively investigations in laminar environments enable detailed assessments of the interaction of specific submodels, as depicted at the top layer of Figure 6.1. Although the practical relevance of these configurations is limited, such experiments are the only possibility to study the interaction of solid fuel particles with gas-phase chemistry in detail.

This variation of experimental scales ensures a continuous validation of the holistic model. To the best of the author's knowledge, there is no similar systematic scaling study for coal combustion. Such an analysis is key for the advance of the scientific understanding of solid fuel combustion.

The remaining part of this chapter is structured as follows. Starting from the smallest scale, the laminar flow reactor is studied first. In contrast to most studies available in the literature, which focus on single-particle ignition, the ignition and combustion particle groups are investigated here. Thereby, the influence of increasing particle mass flows on the ignition process and flame formation is analyzed in detail. Subsequently, the complexity of the validation case is increased by considering the laboratory-scale burner. Within this examination, the complexity is gradually increased from a non-reacting case via single-phase combustion to gas-assisted solid fuel combustion. Finally, the pilot-scale combustion chamber is investigated, possessing

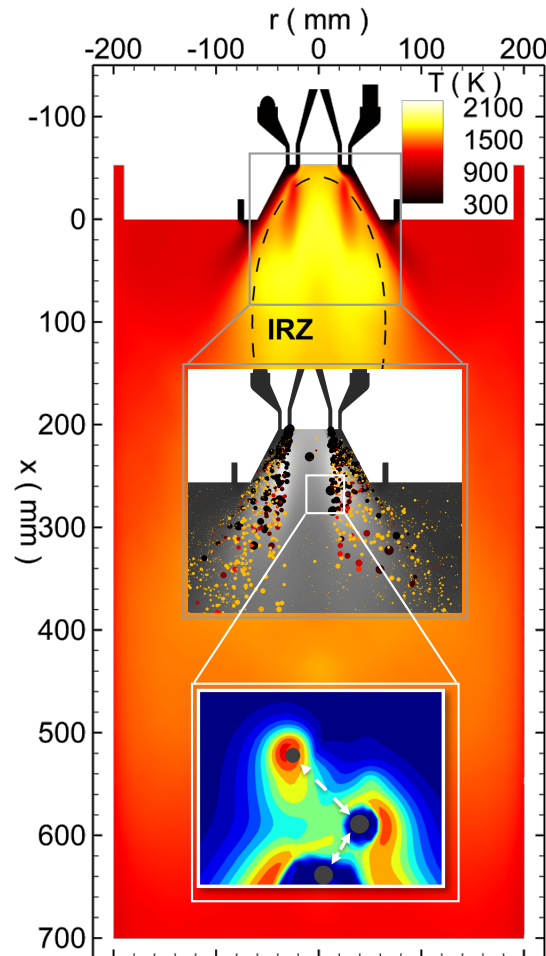


Figure 6.1.: Depiction of different scales involved in PCC is exemplified by the three configurations investigated in this work. Background: Pilot-scale combustion chamber. Middle: Optical accessible laboratory-scale combustion chamber. Foreground: Combustion of particle groups in a flat flame burner.

the highest complexity due to the interaction of all phenomena of practical relevance. First, an investigation devoted to analyzing the effects of oxy-fuel atmospheres on the coal conversion process is presented. Subsequently, a detailed assessment of the interaction of solid fuel conversion sub-models with the overall combustion process is conducted. This is the first time that detailed solid fuel kinetics have been included in the LES of a pilot reactor.

Each section begins with a brief description of the configuration under investigation. After that, to give a more complete and coherent overview, the used modeling strategy for the specific configuration is shortly outlined at the expense of introducing a certain amount of redundancy. Subsequently, the results are outlined and discussed. At the end of each section, the main findings are summarized.

6.1. Laminar Flow Reactor [164]

In this section the results of the simulation of the laminar flow reactor located at the RSM at TU Darmstadt are presented. Parts of this section are published in Nicolai et al. [164].

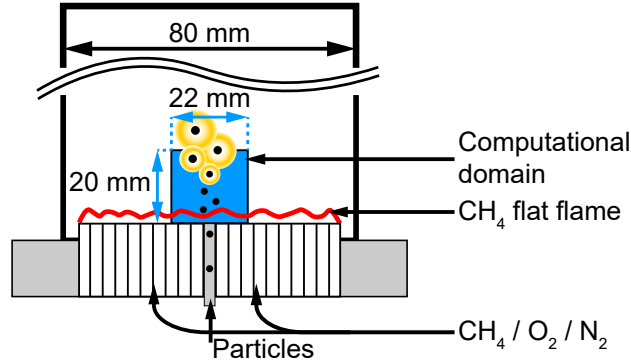


Figure 6.2.: Schematic cross-section of the laminar flow reactor.

6.1.1. Configuration and Boundary Conditions

Figure 6.2 depicts schematically the laminar flow reactor (LFR) [114; 115] used for the novel experiment of particle group combustion. Laminar flow through a quadratic ceramic honeycomb is used to stabilize a laminar premixed flat flame (FF) at ~ 1.8 mm above the honeycomb. The flow through the flat flame has the mixture composition listed in Table 6.1. An inert stream through a 0.8 mm injection pipe transports the particles into the LFR. To avoid disturbances, the burner is enclosed with a quadratic quartz glass chimney. The measurements used in this work to validate the model are published in Li et al. [130].

Table 6.1.: Operating conditions for the LFR.

<i>Inlet</i>	CH ₄	O ₂	N ₂	ϕ	Re
FF (l/min)	5.2	18.1	53.4	0.56	508

This study focuses on the region in which ignition occurs. Therefore, simulations are carried out for the ignition region depicted in Figure 6.2. The domain is discretized with a three-dimensional block-structured mesh, which is locally refined in the inner core to $\Delta x \approx \bar{D}_p$ by an O-grid (For the effect of grid-size on ignition see Appendix A). A laminar flow profile is imposed at the injection pipe and constant velocity for the coflow with a temperature of 313 K has been set to stabilize the premixed flame.

The experiment was carried out with a high-volatile bituminous Colombian coal [109]. The coal properties and the volatile composition are given in [110]. The experimentally determined size distribution of 90-125 μm with a mean diameter \bar{D}_p of 121.6 μm is utilized in the numerical simulation to generate randomly positioned particles at the injection outlet. The initial particle velocities vary randomly between u_{bulk} and $2u_{\text{bulk}}$, following Knappstein et al. [109]. For the simulation, a constant time step $\Delta t = 1 \mu\text{s}$ is used and a total time of approximately 120 ms is simulated after the first particle generation.

6.1.2. Numerical Model

This section presents the specific model combination that was used to study this configuration.

Solid Fuel Kinetics

To compute devolatilization rates, the competing two-step model (C2SM) proposed by Kobayashi et al. [113] is applied. The model parameters listed in Table 6.2 were determined from detailed

CPD simulations for representative heating rates [247]. In addition, the species compositions in the volatile matter are experimentally determined, i.e. CO_2 , CO , CH_4 , C_2H_6 , C_2H_4 , C_2H_2 , C_3H_8 and N_2 with mass fractions $Y_{\text{vol},k}$ of 0.143, 0.281, 0.122, 0.027, 0.111, 0.009, 0.3 and 0.007, respectively [91].

Table 6.2.: Parameters for the Kobayashi C2SM model.

A_1 (s^{-1})	A_2 (s^{-1})	E_1 ($\frac{\text{J}}{\text{mol}}$)	E_2 ($\frac{\text{J}}{\text{mol}}$)	α_1	α_2
1.54e^5	2.31e^7	5.96e^4	1.0e^6	0.41	0.75

Gas-Phase Chemistry

In this study, chemical reactions are represented in the framework of Flamelet Generated Manifolds (FGM). To obtain the FGM table, laminar premixed flames are calculated using the 1D detailed chemistry flame solver Chem1D [26] and the GRI 3.0 mechanism [222] applying a unity Lewis number assumption for all species. The reason for using premixed flames in this configuration, is that burner is operated with a premixed flat flame, which needs to be included to obtain correct particle heating rates due to particle flame interactions [109].

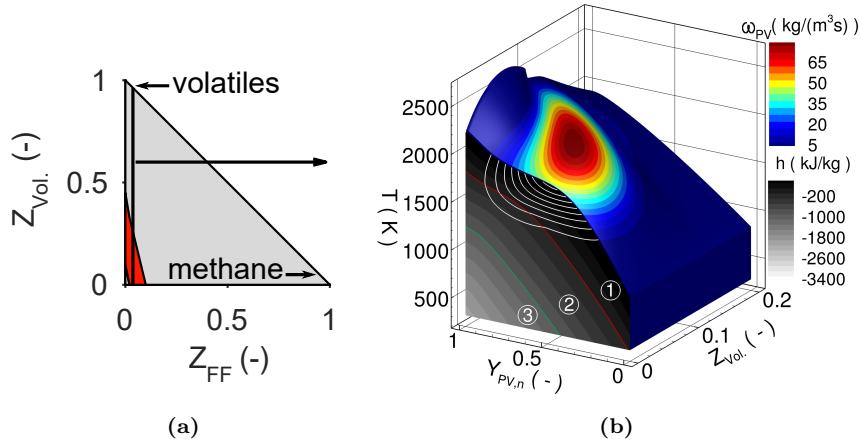


Figure 6.3.: (a): Schematic of the mixing plane spanned by the two fuels and the oxidizer. The red area indicates the flammability range. (b): Section of the chemistry table at $Z_{\text{FF}} = 0.038$. The blue/green/red color scheme depicts the source term of the progress variable, whereas the gray-scale on the slice at $Z_{\text{Vol.}} = 0$ indicates the enthalpy distribution. White iso-lines depict the three-dimensional extent of the source term.

The progress variable Y_{PV} is defined as the CO_2 mass fraction as the best compromise between accuracy and resolution requirements [109]. Since the investigated configuration uses an assisting methane flame to provide heat for particle ignition, two mixture fractions are required to reproduce mixing and reactions correctly. The first mixture fraction Z_{FF} describes the mixing of methane with the oxidizer [109]. The second mixture fraction $Z_{\text{Vol.}} = Z_{\text{C,Vol.}} + Z_{\text{O,Vol.}} + Z_{\text{H,Vol.}} + Z_{\text{N,Vol.}}$, which is defined as the sum of the element fractions of C, O, H and N from volatiles, characterizes the mixing of volatiles with the oxidizer. As depicted in Figure 6.3a), the computations of the flamelets must be repeated for all mixture fractions within the flammability limits. Outside the flammability limits, an interpolation technique described in Knappstein et al. [109] is adopted. To represent interphase heat transfer in the table, the flamelet calculation is repeated for different enthalpy levels. As depicted in Figure 6.3b), two different flamelet types are used to include the heat loss effect. First, in region ①, the enthalpy is varied by adjusting the preheating temperature. In region ②, lower enthalpies are

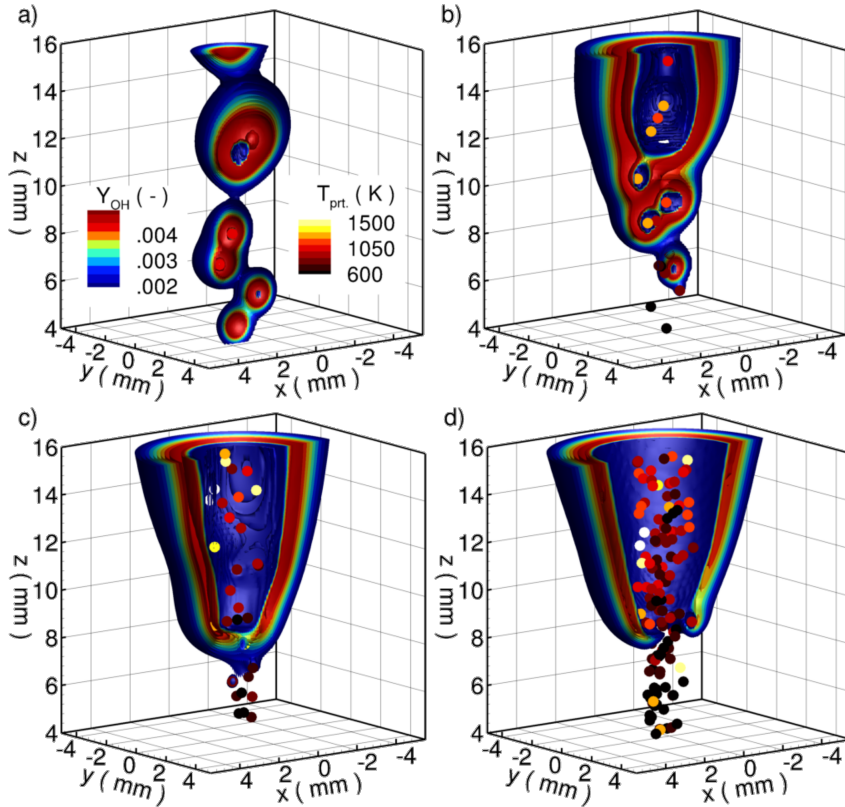


Figure 6.4.: Isocontours of instantaneous OH mass fraction for increasing PNDs at ignition height together with particle temperature. (a) $\text{PND}_{\text{VL}} = 0.15 \text{ 1/mm}^3$, (b) $\text{PND}_{\text{L}} = 0.77 \text{ 1/mm}^3$, (c) $\text{PND}_{\text{M}} = 1.14 \text{ 1/mm}^3$ and (d) $\text{PND}_{\text{H}} = 2.06 \text{ 1/mm}^3$.

obtained by exhaust gas recirculation [246]. Finally in region ③, an extrapolation technique is utilized to complete the thermo-chemical space [109]. The overall table ($101 \times 51 \times 280 \times 91$, $Y_{\text{PV}} \times Z_{\text{FF}} \times Z_{\text{Vol.}} \times h$) is stored on a non-uniform grid using a shared-memory approach [111].

Radiation

Following previous studies of this burner [109], thermal radiation is neglected. The reason is that the heat is solely provided the premixed flame, which itself has non-intensive radiation characteristics. Due to the open configuration and the operating conditions, an effect in the particle energy balance through thermal radiation of the walls is considered negligible. This statement is confirmed by most studies in the literature, where only a minor effect of radiation on single-particle and group-particle ignition are reported. Tulfano et al. [238] tested the impact of the particle heating due to radiative heat transfer for various particle emissivities ($0 < \epsilon_{\text{prt}} < 1$) in similar conditions. They found no significant influence and, therefore, neglected particle heat up by radiation in their study. For the effect of gas-phase radiation, they reported a mild effect.

6.1.3. Results and Discussion

Figure 6.4 gives a first impression of the transition from single particle to group combustion, by depicting instantaneous snapshots of the flame shape visualized by the OH mass fraction for increasing PNDs from a) to d). Significant differences between the formed flames are visible.

For very low PND (PND_{VL}) in Figure 6.4a), separated spherical flames can be detected. Small interactions between spherical flames are visible at the late stage of volatile combustion.

However, overall, the effect of group combustion is limited at this PND. With increasing PND (PND_L) in Figure 6.4b), some individual spherical flames form at the very early stage of ignition. Nevertheless, at later stages, a stronger interaction between the volatile flames leads to richer mixtures in the center, forming a conical flame and only limited reactions are visible inside the flame. Therefore, PND_L can be considered as the transition process from single particle combustion (SPC) to group particle combustion (GP). For the next higher density (PND_M) in Figure 6.4c), non-reactive zones inside the conical flame are observable, indicating a rich mixture exceeding the flammability limit. However, minor wrinkling of the outer flame structure is induced by the remaining spherical structure around individual particles. Furthermore, for the highest PND (PND_H) in Figure 6.4d), no reaction takes place within the conical flame, but no wrinkling of the flame cone is detectable anymore. Moreover, at the flame tip, no reaction can be established. Additionally, when comparing all cases spanning the range from low to high density, a significant increase in ignition height can be found. This qualitative observation corresponds to experimental findings in the literature [134].

6.1.3.1. Validation Against Experiment

After the discussion of the influence of PND on volatile combustion, the results of the simulation will be validated against available measurements, since modeling ignition and combustion of coal particles requires a significant number of physical models and simplifying assumptions. For the LFR, data derived from three-dimensional scanning laser-induced fluorescence of the OH radical (OH-LIF) combined with diffuse back-illumination are available for comparisons. From these measurement techniques, 3D flame structures and PNDs are derived. Since the OH-LIF data provided are non-quantitative, a direct comparison between the OH signal and the mass fraction of OH is not possible. In experiments, a threshold based on the background normalized signal is used to define the flame position [115]. Since the corresponding OH mass fraction is unknown, a range of possible thresholds needs to be taken into account during the comparison [78].

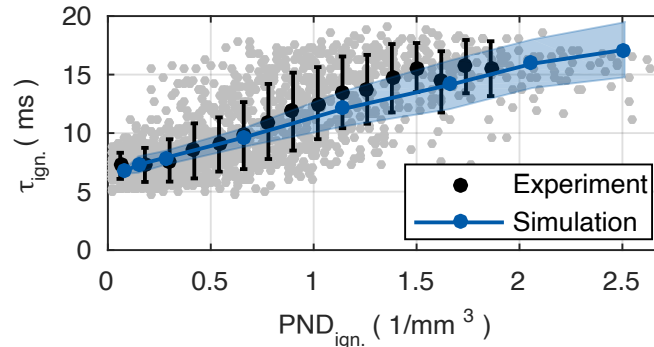


Figure 6.5.: Comparison of ignition delay time $\tau_{ign.}$ between experiments (black dots with errorbars) and numerical simulation (blue line) for different PNDs at ignition height.

First, ignition delay times $\tau_{ign.}$ for different PNDs are compared in Figure 6.5. The model properly captures the trends of higher $\tau_{ign.}$ for higher PNDs. However, compared to the experimental findings, the model predicts a more linear increase in ignition delay and the converging trend of $\tau_{ign.}$ for high PND is not as strong. An explanation for the slight deviation can be found in both measurements and simulations. In the simulation, the coal particles are assumed to be homogeneous spheres releasing volatile matter in all directions homogeneously. In the experiment a two-dimensional measuring technique is used to determine the particle densities. Thus, especially for high PNDs, densities are possibly underestimated due to the line-of-sight super-

position of particles. However, considering the uncertainties both in experiment and simulation, the model provides an overall valid prediction of the correct physical behavior.

After the analysis of the ignition delay time, the structure of different flame shapes will be compared by means of OH mass fraction and OH-LIF signal. In Figure 6.6, the central OH profile of both simulation (a), c), e) and g)) and experimental (b), d), f) and h)) results, respectively, conditioned on their ignition heights are depicted. The same PNDs as used in Figure 6.4 and comparable PNDs from the experiments are selected.

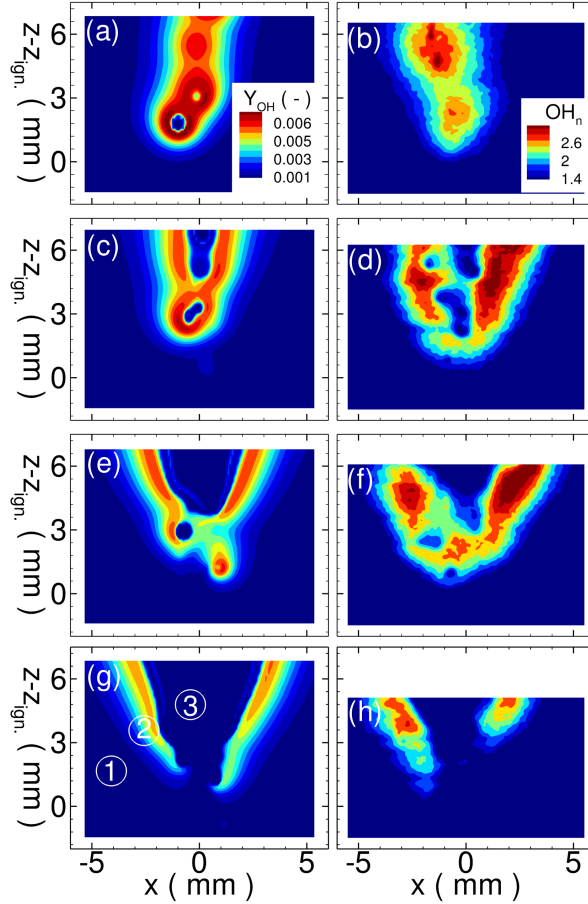


Figure 6.6.: Comparison of flame structures conditioned at similar ignition point for PND_{VL} to PND_H from top to bottom. The experimental results have been chosen to have the same PNDs inside the reaction zone as the corresponding simulation.

For PND_{VL} in Figure 6.6 a) and b), similar structures are observed. As already discussed, for low PNDs, group combustion is rarely observable for both simulation (a)) and experiments (b)). For PND_L, Figure 6.6 c) and d) depict the transition process from single particle to group particle combustion for both experiment and simulation. Although for the experiment, the spherical structures inside the conical flame are somewhat more visible, the actual differences of reaction intensities cannot be compared since the OH signal is not linearly dependent on the mass fraction. In Figure 6.6 e) and f) depicting PND_M, the simulation matches the formation of the conical flame shape. Moreover, the suppression of the reaction by individual particles passing the flame front is also captured in the simulation. For PND_H shown in Figure 6.6 g) and h), the numerical simulation and the experiment both depict a total suppression of the reaction zone at the tip of the conical flame.

Overall, the experiments and simulations show the comparable flame shapes for different

PNDs. The formation of the main reaction zone, as well as particle flame interactions, are in good agreement between simulation and experiment.

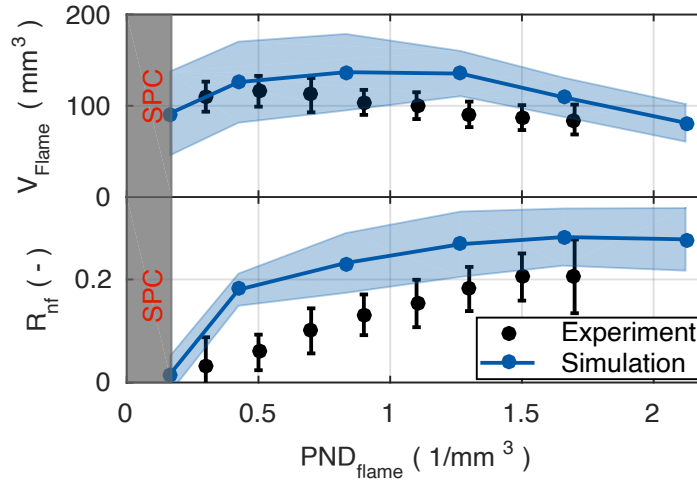


Figure 6.7.: Comparison of flame volume (top) and the ratio of the volume of non-flammability to the volume of the flame (bottom) between simulation (blue line) and experiments (black dots with errorbars) for different PNDs inside the flame. For very low particle densities, this ratio is not defined due to single particle combustion (grey area).

To establish a quantitative comparison between simulation and experiments, flame volume and the ratio of the volume of non-flammability (region ③) compared to the volume of the flame (region ② + ③) is analyzed in Figure 6.7. This ratio is only accessible for group combustion, and therefore only PNDs higher than 0.18 are analyzed. Within the uncertainties of the experiments, the trend of lower flame volumes V_{Flame} for higher PND is correctly reproduced by the model. As expected, the non-flammability ratio R_{nf} increases significantly from low PND to moderate PND. For high PND, the ratio converges towards a constant value of $R_{nf} \approx 0.29$ for the simulation and $R_{nf} \approx 0.21$ for experiments. Considering the uncertainties both in experiment and simulation, it can be concluded that the tabulated flamelet model is capable of predicting the reaction upwards of the ignition point, which is in accordance with the a priori DNS analysis of Wen et al. [264].

6.1.3.2. Analysis of Heat Transfer Mechanisms

To analyze the mechanism for the larger ignition delay and the formation of the different types of flames, Figure 6.8 depicts the gas temperatures combined with the particle temperatures for PND_L and PND_H , respectively. Additionally, the flame position is marked in black and red dotted isolines indicate the region of volatile matter. For PND_L behind the flat flame, a small region of low heat losses due to the rapid particle heating is indicated by the 1700 K isoline. In contrast, a large region with significant heat losses forms in the center of the domain for PND_H . Therefore, very low temperatures occur at the tip of the flame, suppressing the chemical reaction, even though the mixture is within the flammability limits. Also, a somewhat lower heating rate can be detected, resulting in a slower release of volatile matter. Concluding from this discussion, the heat loss in the gas phase due to particle heat up has a significant influence on the flame formation and its stabilization.

The top of Figure 6.9 depicts the temporal evolution of the gas-phase temperature T_{gas} at particle positions and particle temperatures T_{prt} , respectively, for PND_{VL} to PND_H . Vertical lines indicate the ignition delay time.

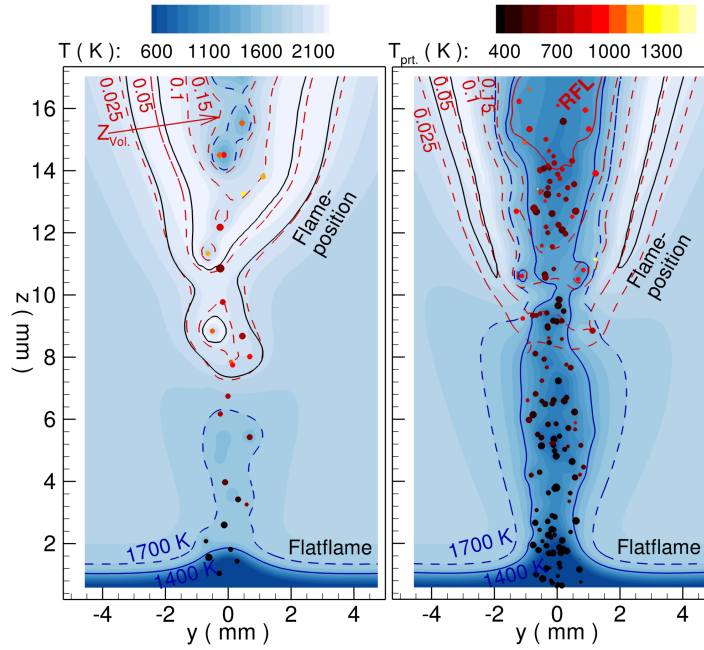


Figure 6.8.: Instantaneous gas field temperature with particles colored in their respective temperature. A black isoline at $Y_{OH} = 0.004$ indicates the flame position. Additionally, the four representative red dotted isolines of $Z_{Vol.}$ indicate regions of volatile matter.

As the particles pass the flat flame, a steep increase in both temperatures can be detected. The slope and the final value of the temperatures are strongly influenced by the PND. After the first increase, the gas-phase temperature remains constant until the volatile ignition leads to a second smaller increase. After volatile combustion, a small decrease in the gas-phase temperature is visible due to further heating of the particles. In contrast, the particle temperatures increase constant for the investigated time series, but with a temperature difference of about 800 K at the final observed point in time between PND_{VL} and PND_H . Therefore, the heating rate varies between 65 K/ms for PND_{VL} , which is in accordance with the heating rate of single particles in this configuration [109], and 20 K/ms for PND_H .

Additionally, the bottom of Figure 6.9b) depicts the mean volatile content of particles. The initial release of the volatiles starts at a particle temperature of around 600 K. Due to further heating of the particles after ignition, particles continue to release volatiles. Again, the mass of released volatiles is very dependent on the PND. For PND_{VL} , nearly all volatile matter is released within the investigated 20 ms. In contrast, for PND_H , only small parts of the volatile matter of each particle are released. However, as depicted in Figure 6.8, the overall amount of volatiles in the gas phase, is higher for PND_H than for the cases with lower PNDs. This can be explained by the significantly higher number of particles inside the flame.

6.1.4. Model Sensitivities for Predicting Ignition Delay Times

As outlined at the beginning of the section, the previously presented results were simulated with the C2SM model and a fixed particle heat capacity of $c_{p,prt} = 1200 \text{ J}/(\text{kg K})$. To show the sensitivities of these assumptions, additional simulations are performed using different model combinations. With respect to the particle heat capacity, in addition to the constant heat capacity previously used, the temperature-dependency of $c_{p,prt}$ is considered by using a polynomial fit of the Merrick Brewster model for the coal under investigation [18; 146; 235]. To investigate

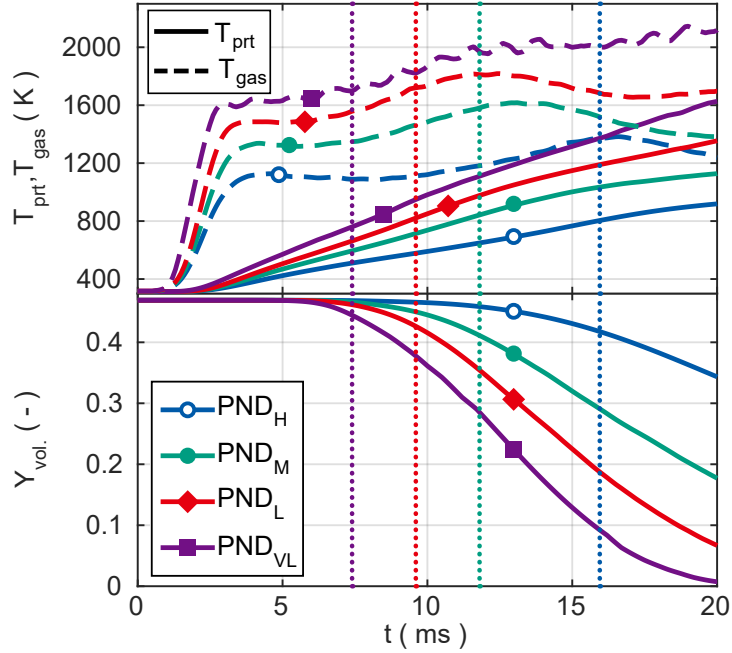


Figure 6.9.: Averaged particle histories for different particle densities over time. a): Averaged particle temperature (solid lines) and gas-phase temperature (dashed lines). b): Averaged particle volatile content. For each case, ignition time is marked with a vertical dotted line.

the influence of the devolatilization modeling, three additional models are considered. As a representative of the detailed network models, the CPD model is used as a reference solution. Furthermore, the CRECK-S model is used as an intermediate model between the network models and simplified kinetics. Finally, the SFOR model is used as the most simple model. The SFOR model was fitted prior to this study by experimental data [109].

The results for all model combinations are depicted in Figure 6.10. Note that the particle injection rate quantifies the particle load instead of the particle density at the ignition position. The main reason is that the model comparison becomes more straightforward since the previously used particle number density is part of the solution. For the change of the particle heat capacity, the ignition delay increases for all model combinations. This effect is mainly observed at high particle loads, while the influence almost disappears at low rates. Since the heat capacity directly influences particle heating and thus the heat transfer to the gas phase, the deviations are expected to increase at high particle loads. The reason for this is the increased importance of heat transfer at high particle densities, as outlined previously. Hence, assuming constant heat transfer for a single particle does not influence the ignition process. However, at higher particle loads, the constant heat capacity influences the transient behavior of particle heating.

Concerning the different devolatilization models, a significant scatter in the results for the ignition delay is apparent. Independent of the heat capacity treatment, the SFOR model predicts the fastest ignition, followed by the CRECK-S model. The CPD model predicts similar ignition delay times to the CRECK-S for low injection rates, whereas a slower ignition is observed for high injection rates. For all cases, the C2SM predicts the slowest ignition. For single-particle ignition and low injection rate group particle ignition, all models are suitable for predicting the ignition process. However, at higher loads, results are influenced by the devolatilization treatment. It is interesting to note that CPD, the most complex model, underpredicts the ignition significantly at the last particle rate. One reason might be that the Gennetti correlation was used to estimate the initial coal structure (see Section 4.3.1.3). Using detailed solid-state ^{13}C -NMR

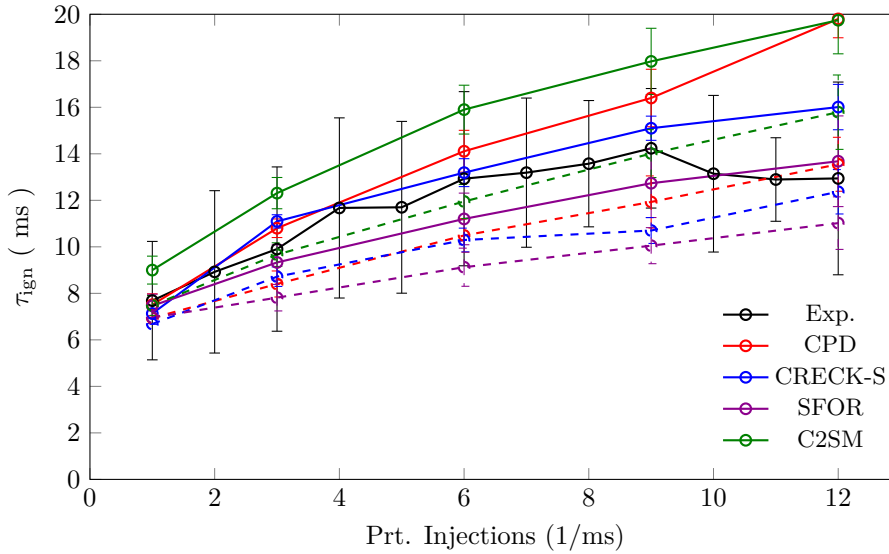


Figure 6.10.: Comparison of ignition delay time τ_{ign} between experiments (black dots with errorbars) and simulations (solid line and dashed lines) for different particle injection rates. Solid lines denote model combinations with a temperature-dependent particle heat capacity. Dashed lines denote models with a constant particle heat capacity of $c_{p,prt} = 1200 \text{ J}/(\text{kg K})$. Colors indicate the devolatilization model.

spectroscopy measurements to obtain the initial coal structure might improve the prediction for low-heating rate conditions. However, such data were not available for the coal under investigation. Furthermore, the simplest model in combination with a temperature-dependent $c_{p,prt}$ matches the data at high particle loads best (However, the remaining data are overpredicted). One reason for this might be the challenging measurements at high particle injections [130]. Another interesting thing to note is the clear underprediction of the ignition delay for the C2SM model in combination with a temperature-dependent heat capacity. This can be explained by the fitting procedure used in [164]. The coefficients were fitted by the CPD model considering a tight heating rate range extracted from this configuration employing a constant heat capacity. From the above discussion, it can be concluded that switching to a temperature-dependent heat capacity results in lower heating rates because the ignition is delayed. Since the C2SM blends between low and high heating rates, the heating rate shift towards lower heating rates results in the primary use of the low heating rate conditions, which underpredict the ignition process. This shows that the conditions used to fit the model coefficients are critical to obtaining correct devolatilization.

The flame formation was found to be similar for all investigated model combinations. Besides the different lift of heights due to the different ignition delays, the transition from single-particle combustion to particle group combustion is predicted correctly. For the sake of brevity, this is not shown here again. Detailed results on the influence of the devolatilization modeling on the flame formation were presented in a joint publication [53], where a reduced setup (e.g., flat flame particle interaction was neglected) was investigated.

6.1.5. Section Summary

Group particle ignition and combustion have been simulated in a laminar flow reactor applying a C2SM model for devolatilization coupled with FGM tabulated chemistry within an Euler-Lagrange framework. An extension of the FGM approach was necessary to account for the complex mixture of gases being released during devolatilization. Several different PNDs have

been simulated, and the results were validated against a series of experiments.

The ignition delay time shows good agreement with the experimental findings. Moreover, the global trend of increasing ignition delay times for higher densities is predicted correctly. The evolution of the volatile flame in the transition process from single particle to group particle combustion is analyzed and explained. Reasonable agreement in terms of reaction zone and flame particle interaction were found for the change from spherical flames around single particles towards a conical flame shape with a suppressed reaction at the tip at high PNDs. The flame volume and formation of zones exceeding the flammability limits inside the conical flame shape is slightly over predicted by the model, but the global trend is captured correctly.

Coal particle group ignition and combustion were found to be significantly delayed compared to single particle combustion due to ample heat losses in the gas phase for heating multiple particles. Because of the slower particle heat up the release of volatiles becomes slower, too. However, due to the higher number of particles, the overall content of volatile matter in the gas phase is larger for high PNDs compared to low PNDs. Overall, the PND has substantial effects on mixture and flame formation, which could be well reproduced and explained by the applied modeling approach for the investigated condition.

A sensitivity analysis of different model combinations revealed that constant particle heat capacities for single-particle ignition might be justifiable. In contrast, effects on ignition delay predictions are apparent for increased particle loads. With respect to the devolatilization modeling, one main conclusion is that the simplified models can correctly predict the ignition delay. However, the heating rates used to determine the model coefficients are critical to account for the devolatilization process properly.

6.2. Laboratory-Scale Gas-Assisted Oxy-Coal Swirl-Combustor [163]

In this section, the overall model is validated in an optically accessible gas-assisted pulverized coal combustion chamber operated under oxy-fuel atmospheres. Parts of this section are published in [163]. First, the construction of the combustion chamber and the operating conditions are briefly described. After that, the employed modeling strategy is outlined. This is followed by the discussion of the results. In the end the main findings are summarized.

6.2.1. Configuration and Boundary Conditions

The investigated combustion chamber is a generic test rig which is operated with a 20 kW_{th} methane flame and varying coal mass flows depending on the operating point [11; 12]. The geometry of the combustion chamber is similar to that of a self-sustaining swirl-stabilized coal combustion chamber [236] with the following modifications. The length of the combustion chamber is significantly reduced. In order to have better optical access to the combustion chamber, all walls consist of quartz glass. Figure 6.21 shows a schematic sketch of the combustion chamber. There are three annular inlets into the chamber, and an annular gap serves as an outlet from the chamber. The inner inlet of the quartz works as the primary flow through which the coal particles and methane-oxidizer mixture enter the combustion chamber. As can be seen from the nozzle excerpt (top right of Figure 6.21), the secondary flow is divided into eight different channels upstream. All channels bring oxidizer into the combustion chamber. Moreover, four of the eight channels are inclined to create a swirl in the flow. The swirled flow then enters the quartz and stabilizes the flame. The tertiary flow serves to bring fresh oxidizer into the chamber for the char burnout that occurs further downstream. The outlet of the chamber was designed

as an annular gap to prevent backflow into the combustion chamber.

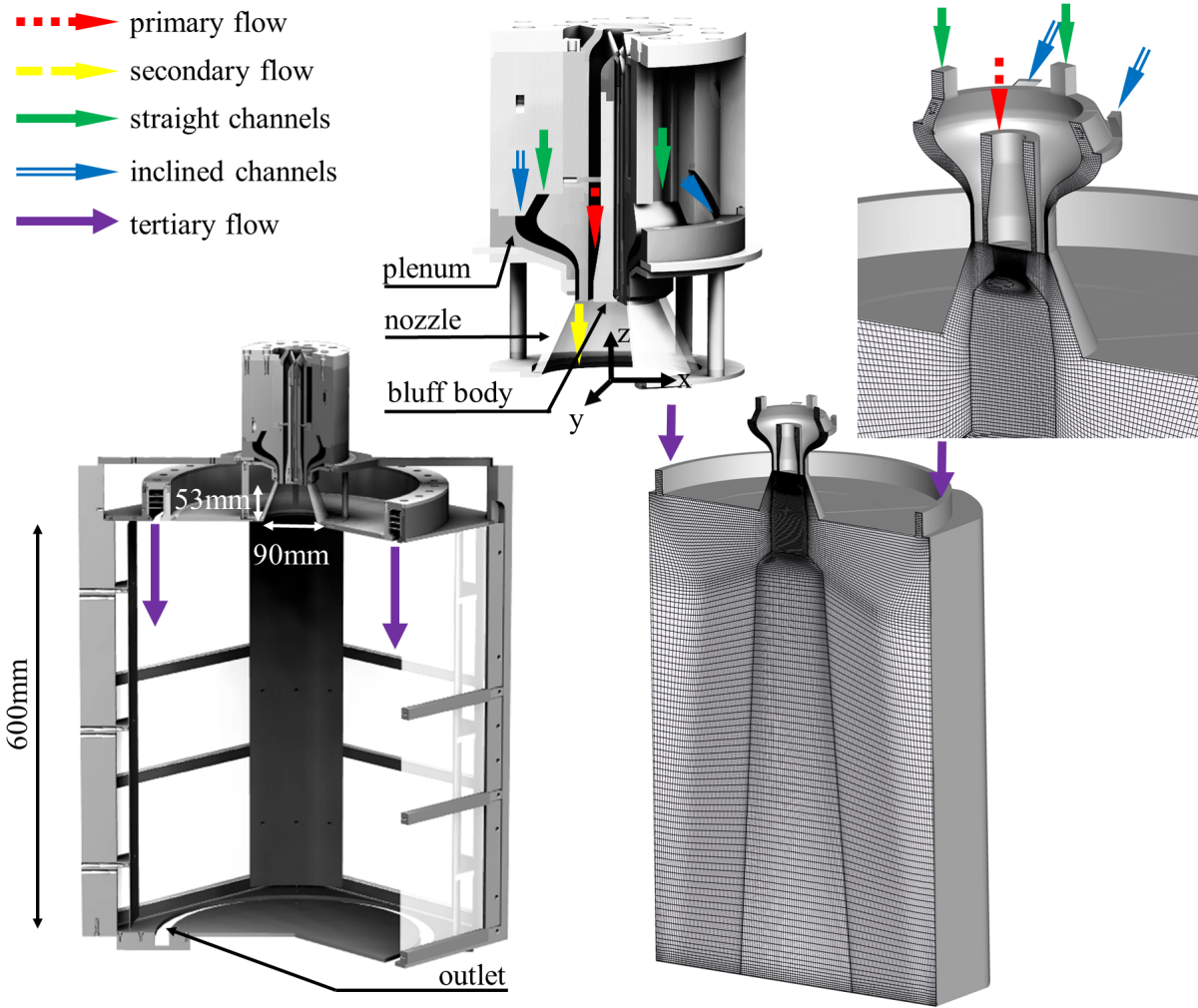


Figure 6.11.: Schematic drawing of the combustion chamber. Left: Full chamber together with a closer view of the burner head. Right: Computational domain and numerical grid of the burner together with a closer view of the burner head.

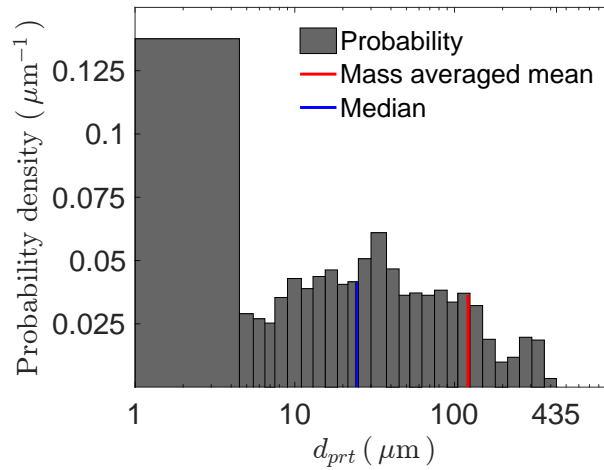
In the following, four different operating points are analyzed. First, a non-reactive single-phase operating point (SPNR) is simulated to evaluate whether LES can predict the swirl in the burner correctly. Second, a partially-premixed methane flame in an oxy-fuel atmosphere, consisting of 30 vol % O_2 and 70 vol % CO_2 , is investigated to validate the newly developed FGM table in a single-phase reactive (SPR) environment. Subsequently, complexity is increased by adding coal particles to the methane flame. In particular, two different coal mass flows with 7 kW (TPR7) and 20 kW (TPR20) thermal power, respectively, are investigated. For both operating conditions, the assisting methane flame possesses a thermal power of 20 kW. Table 6.5 lists the complete operating conditions. The coal used is Rhenish lignite. The proximate and ultimate analysis of the coal were given in Section 4.1 in Table 4.1.

During the simulation, particles are initialized using a random process, reproducing the size distribution depicted in Figure 6.12. All operating conditions use the same numerical grid. It has a resolution of $\Delta_x = 0.5$ mm in the quarl and is coarsened to $\Delta_x = 1 - 3$ mm below the quarl. In total, the grid consists of approximately 2.5 million cells. Wall temperatures were obtained from radiation thermometer measurements and are locally dependent in the range of 320 K-500 K.

Table 6.3.: Parameters of the four operating points. I: Primary flow. II: Secondary flow. III: Tertiary flow.

	Single Phase Non-Reactive (SPNR)	Single Phase Reactive (SPR)	Two Phase Reactive 7 kW Coal (TPR7)	Two Phase Reactive 20 kW Coal (TPR20)
I Mass flow of gas (g/s)	4.13	3.85	3.85	3.85
I Mass flow of coal particles (kg/h)	–	–	1.12	3.25
II Mass flow of gas, straight channels (g/s)	1.91	1.89	1.89	1.89
II Mass flow of gas, inclined channels (g/s)	3.68	3.67	3.67	3.67
III Mass flow of gas (g/s)	21.57	21.45	21.45	21.45
Equivalence ratio Φ_I (only gas phase)	–	1.97	1.97	1.97
Equivalence ratio Φ_{I+II} (only gas phase)	–	0.75	0.75	0.75
Theoretic total equivalence ratio $\Phi_{Gas+Coal}$	–	0.22	0.31	0.45
Thermal power P_{th} from methane (kW)	–	20	20	20
Thermal power P_{th} from coal (kW)	–	–	7	20

During the simulation, a time step of $5 \cdot 10^{-6}$ s was selected to ensure stability. Depending on the operating point, the simulation time was chosen to achieve sufficient convergence of the statistics in the investigated areas.

**Figure 6.12.:** Particle size distribution of Rhenish lignite measured by laser diffraction [108].

6.2.2. Numerical Model

Solid Fuel Kinetics

The devolatilization process is described with a Single First-Order Reaction (SFOR) model proposed by Badzioch and Hawksley [8]. The parameters of this model are coal-specific and were taken from calculations using the CPD (Chemical Percolation and Devolatilization) model

[60]. The char conversion is calculated utilizing the model developed by Baum and Street [10; 57]. The coal-specific coefficients were determined experimentally [79] and are given in Section 4.3.2.

Gas-phase Combustion Modeling

In this section the extended FGM model introduced in Section 3.4.1. Two mixture fractions \tilde{Z}_1 and \tilde{Z}_2 are required to describe the mixing of oxidizer, volatiles and char products. Additionally, the chemical reaction is described by a reaction progress variable $\tilde{\mathcal{Y}}$. In order to take heat losses into account, enthalpy \tilde{h} is transported.

To build the chemistry table, one-dimensional premixed flames are calculated with the help of the detailed chemistry solver Chem1D [26] and the GRI 3.0 mechanism [222] assuming unity Lewis numbers for all species. The flamelet is then mapped to a progress variable and stored in a table. In this section, a combination of the massfractions of Y_{CO_2} , Y_{CO} and Y_{O_2} is used (see Section 3.1.1).

Since both volatile release and char burnout occur in the current configuration, each mixture fraction is assigned to one of these fuel streams. The volatiles are described using a first mixture fraction $Z_1 = Z_{\text{C,CH}_4} + Z_{\text{H,CH}_4}$ where $Z_{\text{C,CH}_4}$ and $Z_{\text{H,CH}_4}$ denote the element mass fractions of C and H, respectively, originating from CH_4 . So that the complexity of the devolatilization process can be modeled within the four-dimensional table, CH_4 is assumed to be a surrogate for the volatiles. Its reaction can be described within the framework of the GRI 3.0 mechanism used [222]. As shown in Knappstein et al. [109], the influence of this assumption in the overall model is small. The second fuel is described by a second mixture fraction $Z_2 = Z_{\text{C,CO}} + Z_{\text{O,CO}} + Z_{\text{CO}_2,\text{SFR}}$. Similarly to the first mixture fraction, $Z_{\text{C,CO}}$ and $Z_{\text{O,CO}}$ denote the element mass fractions of C and O, respectively, originating from char products. $Z_{\text{CO}_2,\text{SFR}}$ represents the element mass fraction of CO_2 , which participates in the surface reaction (SFR).

Radiation

The dominant radiative transport mechanism for oxy-fuel combustion, despite the increased partial pressure of CO_2 , is still particle radiation, as shown by Andersson et al. [3]. Compared to their study, the investigated setup has lower particle densities and due to the surrounding walls being made out of quartz glass significantly lowers the overall temperatures. Therefore, the influence of thermal radiation can be considered minor compared to convective and diffusive heat transfer in the investigated combustion chamber and is neglected in the current study.

6.2.3. Results and Discussion

In the following sections, the results of operating points with increasing complexity are discussed. In the beginning, a single-phase non-reactive case is briefly discussed. This is followed by a discussion of a single-phase reactive case. In the end, two two-phase cases with different thermal loads are discussed.

6.2.3.1. Single-Phase Non-Reactive Case (SPNR)

For the single-phase non-reactive flow, the mass flows of the SPNR operating point are used according to Table 6.5. All flows - primary, secondary and tertiary - consist of an oxy-fuel atmosphere (30 vol-% O_2 and 70 vol-% CO_2) and have a temperature of 300 K. A physical time of 2.5 s was simulated to obtain sufficiently convergent statistics in the studied region. As indicated in Figure 6.21, large parts of the nozzle geometry were included in the computational domain to allow the turbulent flow to develop. The SPNR operating point is mainly studied to evaluate the adequacy of the boundary conditions and to characterize the velocity field. It

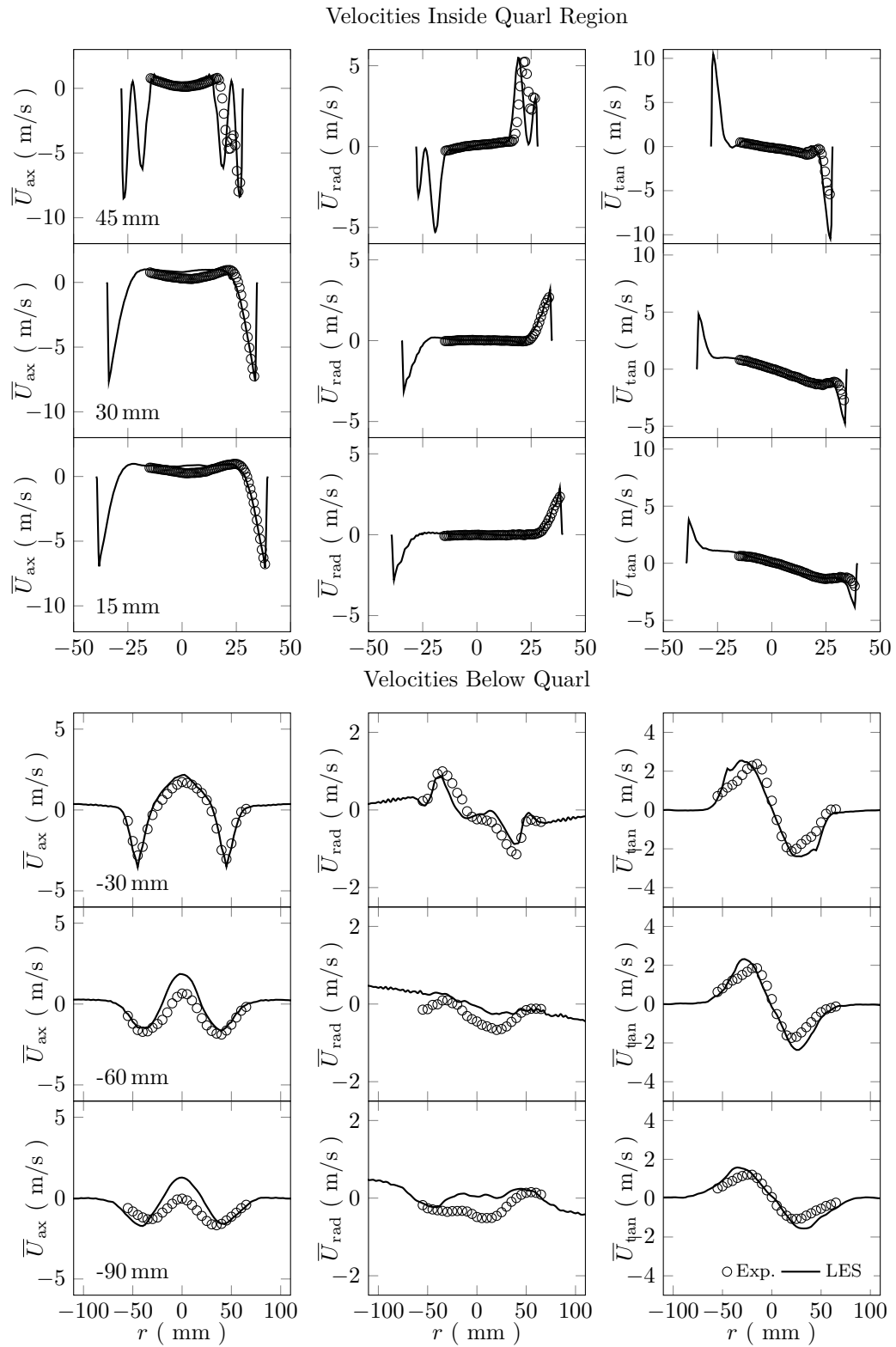


Figure 6.13.: Comparison of single-phase non-reactive experimental (dots) and numerical (lines) mean velocity data. Left: axial velocity component. Middle: radial velocity component. Right: tangential velocity component. Upper three rows: velocity inside quarl. Lower three rows: velocity below quarl.

is essential to ensure that the tangential component of the secondary flow velocity immediately after leaving the opening corresponds to experiments since it determines the swirling strength. A low tangential velocity would be an indicator of excessive numerical diffusion within the narrow nozzle channels.

Both numerical results and experimental data for the three velocity components are depicted in Figure 6.13. In general, good agreements between the experiment and the simulation are observed concerning the main flow properties. The two streams exiting the inlets are displaced by the internal recirculation zone and form a swirled flow at the quarl walls. Considering the region close to the annular orifices where primary and secondary streams are mixed (particularly at $z = 45$ mm), the simulation predicts a somewhat slower merging of the streams. However, these differences do not affect the flow at the outlet of the quarl. One possible reason for these deviations might be an inaccurate mapping of the experimental flow field in that region [11]. In the quarl, the tangential velocity representing swirling motion is approximately the same magnitude as the axial component. Since the maximum swirl velocity is located very close to the wall, the correct measurement of this out-of-plane component by using stereoscopic PIV becomes challenging [11]. Considering the experimental uncertainties, the tangential component in the quarl is well reproduced by the simulation. These results do not indicate any underestimations due to numerical dissipation in the channels of the burner head. Hence, the boundary conditions are set appropriately.

For the flow field below the quarl, the axial and tangential components show good agreement with the experiments. Hence, both the extent and strength of the inner recirculation zone are predicted correctly by the simulation. Although the radial component exhibits some quantitative deviations, the main characteristics are qualitatively correct. Due to the small magnitude of the radial velocity, the impact of these deviations is considered small. Furthermore, the slight asymmetry also indicates challenging measurements in the complex. According to the experimental study [11], the asymmetry might be the consequence of a not perfectly aligned bluff body in the center of the burner head.

A similar good agreement exists for the RMS values of the velocity, which for brevity is not shown here but in the Appendix B.

6.2.3.2. Single-Phase Reactive Case (SPR)

Figure 6.14 shows the averaged fields of the equivalence ratio and temperature as well as streamlines of the velocity fields for the SPR operating point corresponding to Table 6.5. The contour depicts a rich mixture of methane passing through the primary inlet into the quarl. The mixing of the primary and secondary flow in the diffuser results in a lean mixture. The addition of further oxidizer from the tertiary inlet below the quarl causes an even leaner mixture. The streamlines on the right-hand side of Figure 6.14 show a strong recirculation inside the diffuser, induced by the swirled secondary stream. This recirculation zone serves as a stabilizer for the flame, which can be identified by the strong temperature gradient. Within the quarl, very high temperatures can be ascertained, due to the recirculation of the flue gas. In contrast, there is a cold mixture of primary and secondary flow directly at the wall. Between these two flows, there is a strong temperature gradient, which indicates the primary reaction zone in the combustion chamber, as already mentioned.

After this introductory analysis of the physical effects that occur, the validation of the overall model will follow. For this purpose, PIV measurements for the velocity fields and OH-PLIF data for the flame position are available. For further details about the measurement methods used, see Becker et al. [11].

Figure 6.15 illustrates the numerically obtained mean OH mass fraction fields, as well as the

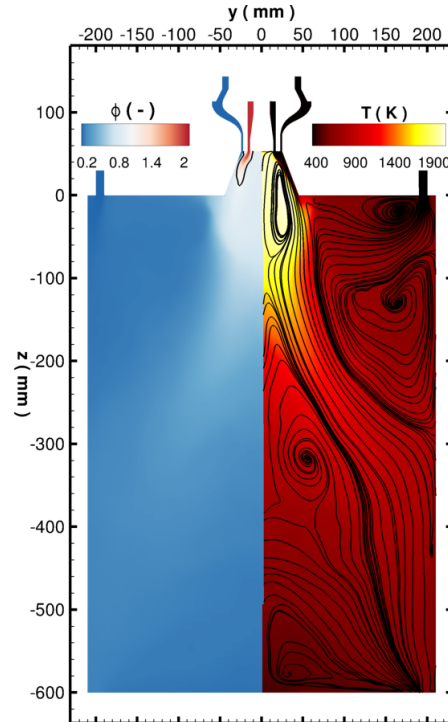


Figure 6.14.: Mean contour of single-phase reactive operating points. Left: Equivalence ratio with an isoline of $\phi = 1$. Right: Streamline of velocity together with contour plot of temperature in the background.

mean laser-induced OH fluorescence signal from the experiment, inside and below the quarl. It should be noted that optical access is not available at the end of the quarl, therefore no experimental results could be obtained in this small area. When the results are compared, symmetric fields can be observed inside the diffusor for the experiments and the simulation. The only difference is that the reaction zone exhibited by the OH signal of the experiment is slightly narrower and longer than that of the simulation. Overall, as an indicator of the reaction zone, the OH exhibits a similar maximum profile within the quarl in both the experiment and the simulation. Below the quarl, the experimental OH signal is no longer symmetric. One reason for this is the absorption along the laser path [11]. Since the laser enters the chamber

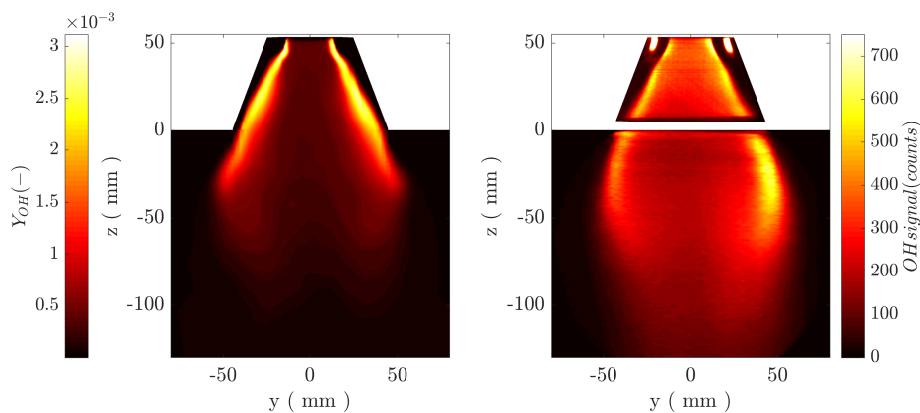


Figure 6.15.: Results of OH at the central plain. Left: OH mass fraction of the LES simulation. Right: Experimentally obtained mean OH fluorescence signal.

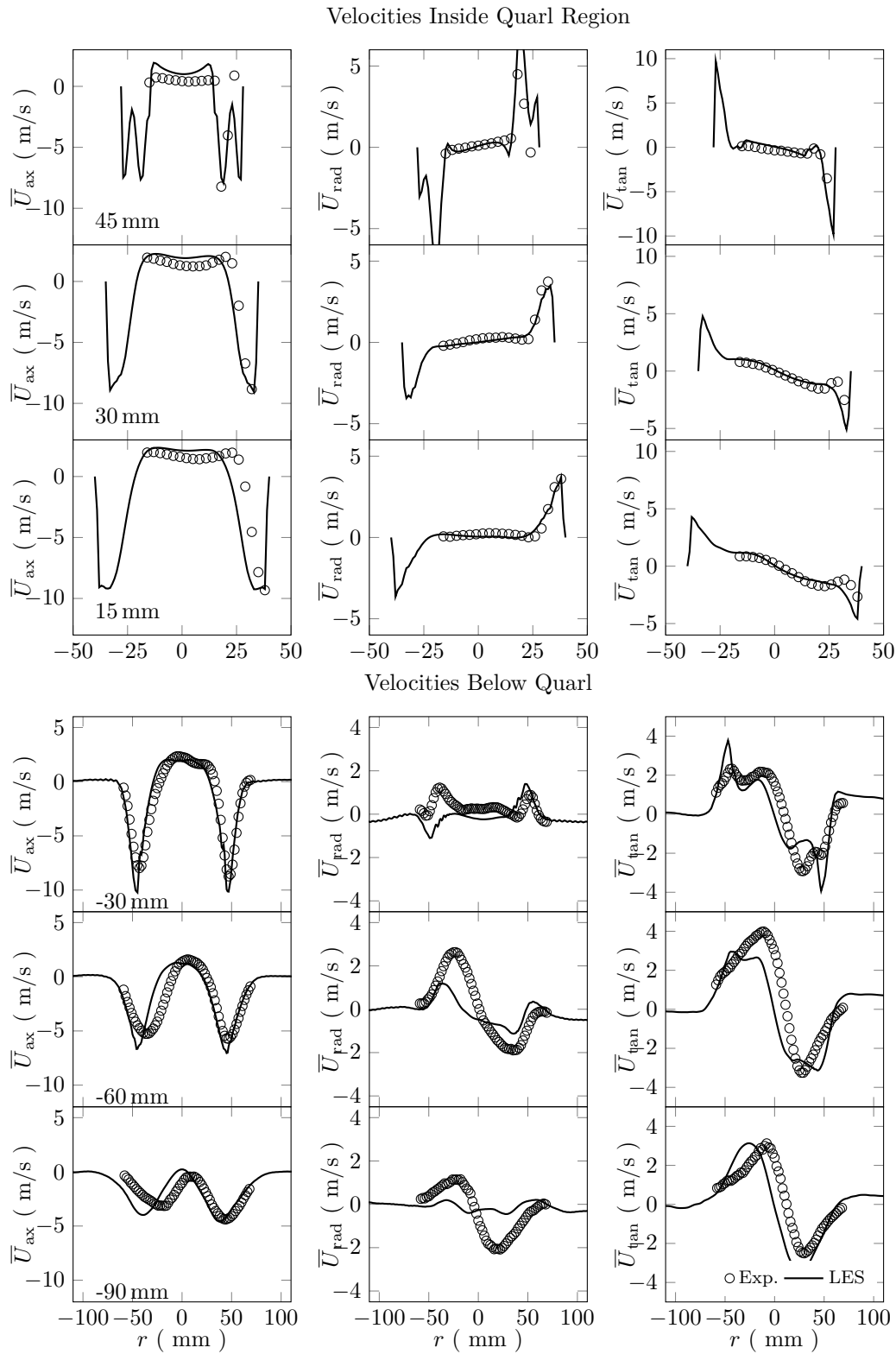


Figure 6.16.: Comparison of single-phase reactive experimental (dots) and numerical (lines) mean velocity data. Left: axial velocity component. Middle: radial velocity component. Right: tangential velocity component. Upper three rows: velocity inside quarl. Upper three rows: velocity below quarl.

from the right-hand side, the signal on the left side is weaker. The mass fraction of OH from the simulation has a symmetrical shape. When the simulation is compared with the experiment, it is noticeable that the reaction zone in the experiment seems somewhat longer and, at the same time, a stronger signal is recorded inside the recirculation zone. However, one should consider that in the present setup laser-induced OH fluorescence produces only a non-quantitative signal, therefore quantitative comparison with the OH mass fraction is not possible. A final difference is noticeable directly at the burner head. For the experimental field, a small side-flame is observed between the primary and secondary slot that was not ignited in the numerical simulation. It seems that this side flame is strongly influenced by the local conditions (e.g. flow characteristics, thermal wall, ignition conditions). Nevertheless, comparing the main flame structure inside the quarl, only a small difference between the experiments and the simulation can be detected. Therefore, the influence of the side flame on the main flame structure seems to be minor.

The next step is to compare the velocity fields of the experiment with those of the simulation. Figure 6.19 depicts the velocity components of the single-phase reactive operating point inside and below the quarl for different heights, respectively. Two negative velocity peaks in the axial speed can be identified near the burner head. The primary and secondary inlets cause these peaks. At the second height, one large velocity peak near the wall can be observed. At the same time, the recirculation zone forms in the middle of the quarl. This profile can also be identified below the quarl in the Figure 6.19. Downstream, the intensity of the recirculation zone decreases. At the lowest height, the recirculation zone has almost vanished.

Overall, the simulation is able to reproduce the velocity profiles measured by PIV. Some small deviations occur at the lowest position of the quarl and below the quarl. However, especially below the quarl, the PIV measurements are asymmetric, leading to a constant shift between the simulation and experiments. Inside the quarl, there is good agreement between the velocities of the simulation and the measurement results, although the simulation cannot reproduce the side flame. Thus, the side flame does not have any significant influence on the flame stabilization, which mainly takes place by recirculation. Even though no measurements of scalar data are available, the combustion has a considerable influence on the velocity field due to the strong density change and the good agreement, and therefore, suggests that the reaction zone is correctly predicted.

A similar good agreement exists for the RMS data of the velocity, which for brevity is not shown here but in the Appendix B.

6.2.3.3. Two-Phase Reactive Cases

In the following, the two-phase operating points TPR7 and TPR20 described in Table 6.5 are examined. In the simulations, coal particles with the size distribution given in Figure 6.12 are initialized using a random process. In both simulations, a time of 2s with a time step of $\Delta t = 5e^{-6}$ s is calculated before the actual averaging process of 0.5s is started. After that time, the statistics in the examined regions are fully converged.

The following paragraph introduces the physical processes inside the combustion chamber and compares the two operating points. The focus is on the quarl area, where flame stabilization takes place. To provide information about these, Figure 6.22 compares the temperature, progress variable source term, and first and second mixture fraction of the two operating points. In addition, particles are added to Figure 6.22, to give an overview of the main particle paths and their corresponding thermo-chemical states. The particle distribution shows that the particles move differently through the quarl, depending on their size. Large particles are mainly driven by gravitational forces and therefore do not follow the flow closely. In contrast, the small particles follow the flow first towards the wall and then into the recirculation zone. In addition, the larger

particles heat up much more slowly than smaller particles due to their higher thermal inertia. As a result, large particles start the devolatilization process much further downstream. It can also be seen that the large particles hardly pass over into char burnout. In contrast, the small particles devolatilize immediately when they enter the hot zones of the combustion chamber.

Comparing the two operating points, several significant differences are revealed. Whereas operating point TPR7 shows no evident changes compared to the single-phase case, the fields of TPR20 are substantially different. For the temperature, the increased coal mass flow leads the reaction zone to shift downstream. The mixture formation explains this downstream shift. Comparing the first mixture fraction, one can identify a richer mixture in the TPR20 case. An explanation for the richer mixture is the higher proportion of volatile gases from the solid phase. The flame stabilization within the quarl has also changed for TPR20 compared to TPR7. In the TPR7 case, a flame stabilizes itself close to the wall at the exit of the quarl. Compared to the single-phase case, the flame burns much further below the burner inlet. On the other hand, the TPR20 case is characterized by low chemical reactions inside the quarl. However, an increase can be seen in the chemical reaction rates with increasing distance from the quarl. Due to continuous mixing with oxygen and volatile matter, the region of chemical reactions is considerably larger, which represents the contribution of the increased thermal power of the coal.

Due to the experimental design (short chamber) and the resulting short residence times, the char conversion is significantly lower than in real geometries. However, when the two operating points are compared, the second mixture fraction indicates a considerably higher amount of char gases for TPR20. The reason for this is the significantly higher number of particles within the combustion chamber, which lead to a substantially larger reaction zone in the TPR20 case compared to the TPR7 case. This larger zone at high temperatures results in a longer particle residence time in the hot gases, which increases the char reaction. At this point, however, it should also be noted that stoichiometry is affected by the assumption of methane as volatiles. Thus a slightly higher oxygen concentration in the area of the quarl might possibly support the char conversion. However, this effect is not dominant since the char conversion correlates very strongly with the regions of high temperature in the combustion chamber. Therefore, the high temperature in this combustion chamber seems to be the driving factor for the char conversion. This implication appears to be credible because the char conversion is limited to the hot gas zones, although the tertiary stream provides sufficient amounts of oxygen.

To verify this statement, the left side of figure 6.18 depicts the averaged O_2 mass fraction. On the right side of figure 6.18 are the average particle temperature, volatile and char content for both operating points, respectively, over the axial position. Inside the quarl, a strong heat-up of the particles leads to nearly full devolatilization of the particles for both operating points. Nearly no char reactions happen inside the quarl. This can be attributed to the overall low oxygen content inside the quarl. Below the quarl, a more significant char reaction occurs where average char content is lower for the TPR7 case. At the end of the combustion chamber, the char content of the particles increases for both operating points. This can be attributed to large particles that do not follow the flow well. These particles cluster at the cold bottom of the chamber and move slowly outwards towards the outlet.

After this introduction to the coal's influence on combustion and flame stabilization based on the numerical simulations, the results are validated. PIV measurement data from Becker et al. [12] are available for this purpose. Instead of tracer particles in the flow, coal particles were used directly as tracers. In a post-processing step, the small particles were separated from the large ones using a separation algorithm. For further information on the procedure in the experiments, see [12]. Figure 6.19 depicts a comparison of the numerical and experimental results. It should

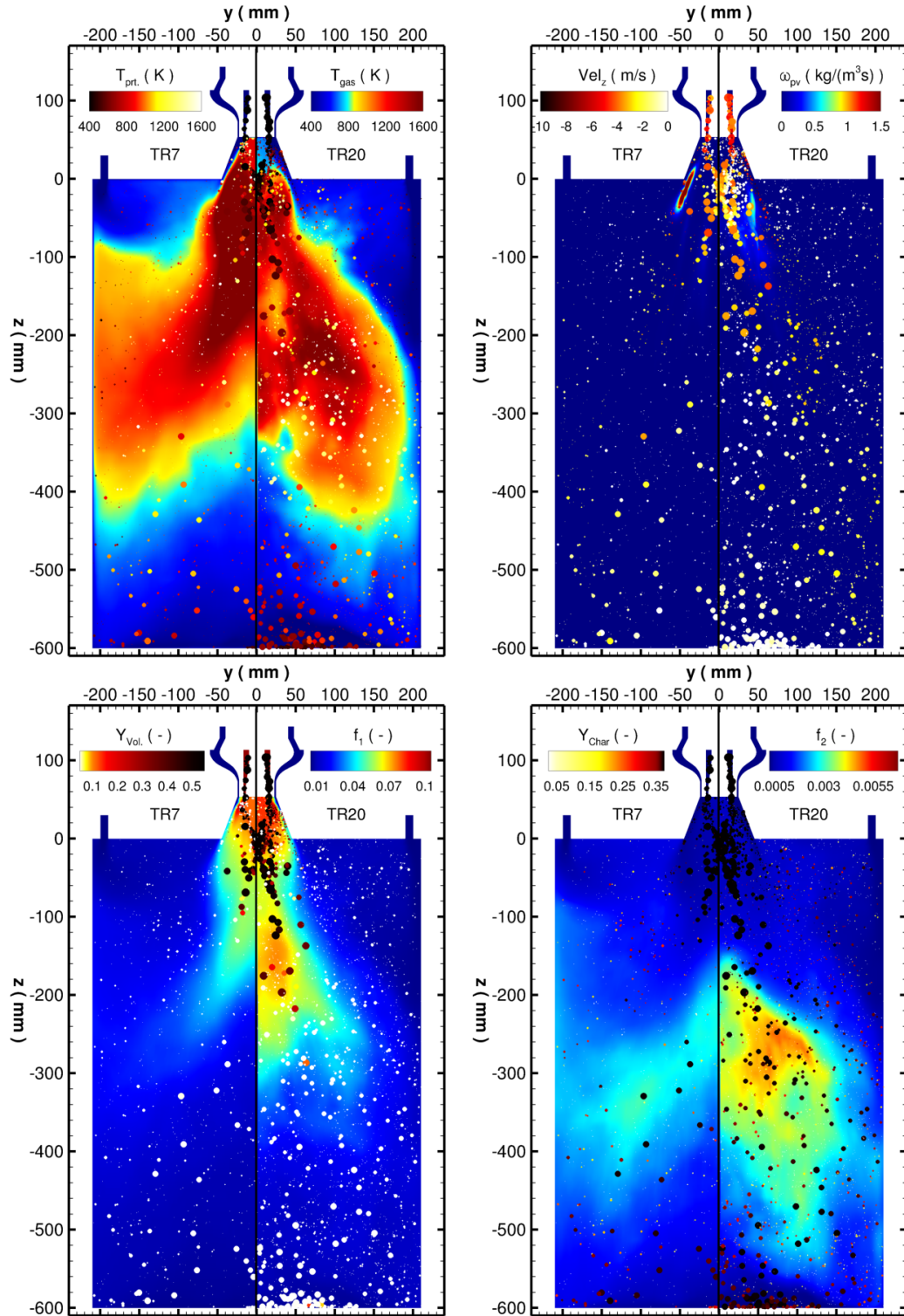


Figure 6.17.: Mean images of Euler fields at the y - z plane with an instantaneous snapshot of the particle phase between $x = 0$ and $x = 1$ mm are depicted for both operating points. Top row: particle temperature and gas-phase temperature on the left side and velocity in z direction and progress variable source term on the right side. Bottom row: particle volatile content and first mixture fraction on the left side, and particle char content and second mixture fraction on the right side.

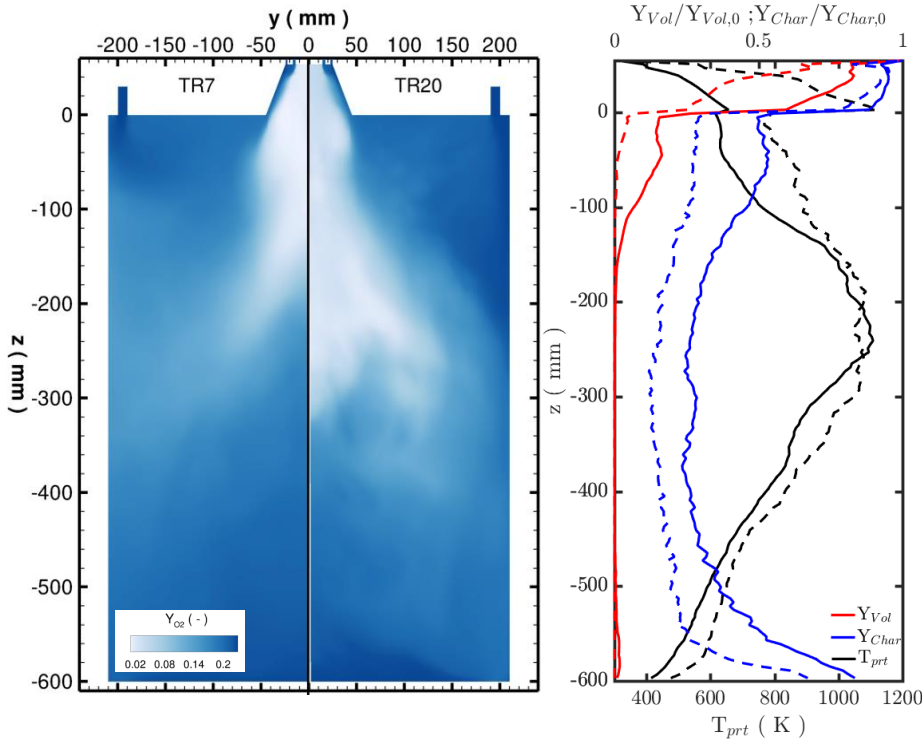


Figure 6.18.: Left: Averaged O₂ massfraction inside the combustion chamber. Right: Averaged particle temperatures T_{prt} , averaged normalized massfraction of volatile content $Y_{Vol.}/Y_{Vol.,0}$, averaged normalized massfraction of char content $Y_{Char.}/Y_{Char.,0}$ over the axial position z . Dashed lines represent TPR7 and solid lines represent TPR20.

be mentioned that for the TPR20 case, no measurements inside the quarl were possible, as argued by Becker et al. [12]. Moreover, in the current measurement setup, the out-of-plane component of the velocity, which in this case is the tangential velocity, could not be measured. When the simulation and measurements are compared, good agreement can be found for both cases, taking into account the complexity of the investigated phenomena. A more significant deviation occurs in the areas of high particle densities. In particular, high particle densities occur at the burner inlet and the walls of the quarl. When the measured data are compared at these positions, however, the fact should be considered that the high particle densities represent a major challenge for the separation mechanism. A comparison of the two operating points shows a slightly higher axial velocity in the case of the TPR7 operating point. In particular, this effect can be observed in the center of the quarl at 15 mm and 30 mm and for the peak velocities downstream of the quarl. The reason for this is the low particle density. Since the particles extract heat from the gas phase while they are heated, a higher particle density reduces the thermal expansion in the gas phase, leading to lower velocities. Concluding, the different velocities of both operating points correlate with the different temperature fields in Figure 6.22. In the regions with similar temperatures (e.g., close to the wall of the quarl), the velocities are similar between both operating points. This effect is reproduced correctly by the simulation. A similar good agreement exists for the RMS data of the velocity, which for brevity is not shown here but in the Appendix B.

After this validation of the gas phase velocities, the particle phase will be analyzed in the following. Since the particles behave very differently depending on their size, particle groups of different sizes will be investigated. The selected particle classes are summarized in Table 6.4.

The transient behavior of the particles is analyzed utilizing particle trajectories depicted in

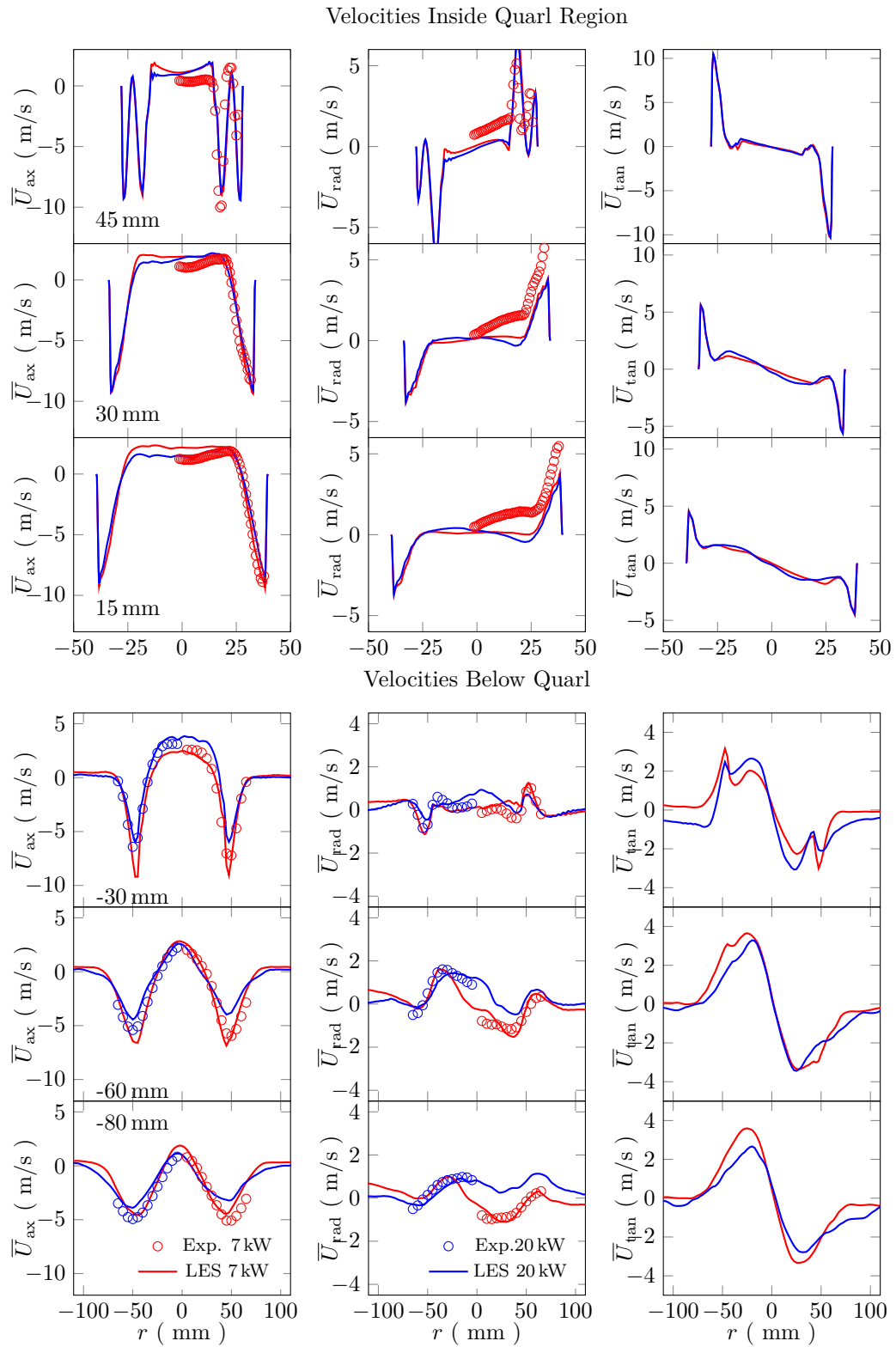


Figure 6.19.: Comparison of two-phase reactive experimental (dots) and numerical (lines) mean velocity data. Left: axial velocity component. Middle: radial velocity component. Right: tangential velocity component. Upper three rows: velocity inside quarl. Upper three rows: velocity below quarl.

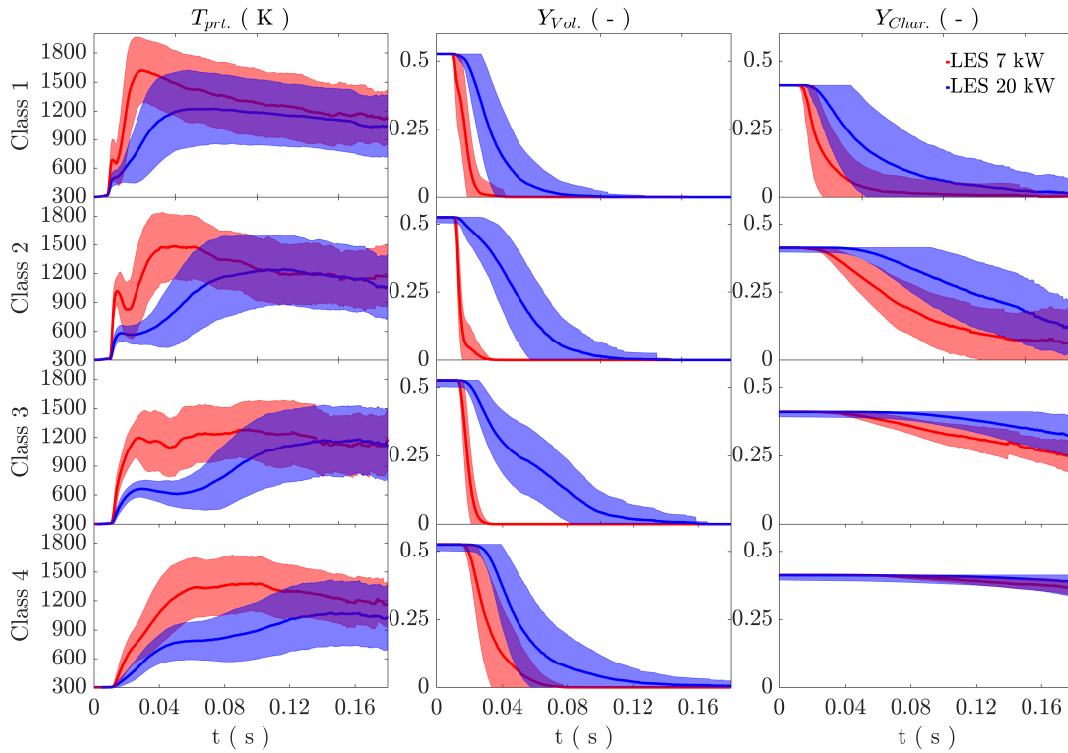


Figure 6.20.: Particle histories divided into particle size classes as defined in Table 6.4 for the particle temperature, volatile content and char content, respectively.

Figure 6.20. For the creation of the particle trajectories, the particles have been classified using the sizes distribution shown in Table 6.4. For each particle class, 1000 particles out of the total 550000 particles for TPR20 and the total 160000 particles for TPR7, respectively, were tracked to obtain converged statistics. As expected, the smaller particles are heated much faster than the larger particles, due to their lower thermal inertia. Consequently, the volatiles of the smaller particles are released much faster. After all volatiles are released, the much slower char conversion follows. Due to their short residence time in the hot zone, the largest particles hardly reach char conversion, as also seen in Figure 6.22.

Another effect occurs when the trajectories of different size classes are compared for the TPR7 case. Particles in Classes 2 and 3 exhibit a steeper temperature increase with lower variance than those in the first class. The higher variance can be attributed to the shorter relaxation time of the first class, which allows them to follow the turbulent motions better. The steeper temperature increase can be ascribed to the different particle trajectories within the quarl. Due to the different particle dynamics, Class 2 and Class 3 particles are carried into the reaction zone directly, leading to a rapid heat up. In contrast, the small particles follow the cold flow along the wall. Knappstein et al. [108] made similar observations.

A comparison of the two operating points reveals apparent differences in the trajectories. In the TPR7 case, a much faster temperature rise can be seen, which consequently leads to much faster devolatilization. The reason for this is also the lower particulate mass, which leads to less heat removal from the gas phase, which was already discussed in the context of Figure 6.22. A more pronounced char reaction can also be detected for the small particle classes. However, the effect is negligible for the large classes, also due to the overall low char conversion.

Table 6.4.: Division of particles into different classes according to their size for post-processing.

Class	Particle size
1	$D_{\text{prt}} \leq 25 \mu\text{m}$
2	$25 \mu\text{m} < D_{\text{prt}} \leq 50 \mu\text{m}$
3	$50 \mu\text{m} < D_{\text{prt}} \leq 100 \mu\text{m}$
4	$100 \mu\text{m} < D_{\text{prt}}$

6.2.4. Section Summary

In this section, a four-dimensional FGM modeling approach coupled with ATF was applied in a LES of a laboratory-scale gas-assisted coal combustion chamber. Thereby, operating points with successively increased complexity were investigated. First, a non-reacting single phase operating point was investigated to show the potential of LES to predict the flow field in complex burner geometries. Subsequent, a $20 \text{ kW}_{\text{th}}$ methane flame inside the combustion chamber was investigated to show the model's potential to reproduce single-phase flames under oxy-fuel atmospheres. Good agreement was found regarding the velocity field. It was also possible to reproduce the mean flame shape, and the flame stabilization mechanism, could be reproduced. For the two-phase reactive operating point, Rhenish lignite was added to the methane flame. Two different thermal loads of 7 kW and 20 kW , respectively, were investigated. For the $20 \text{ kW}_{\text{th}}$ operating point, the coal delivers nominally the same amount of power as the assisting gas flame. Meanwhile for the 7 kW operating point, only approximately one-quarter of the nominal thermal power is supplied by the solid phase. Due to the different amounts of coal, two different flame shapes are formed. At a low particle density, the combustion process changes near the combustion inlet. Further downstream, the assisted methane flame remains the dominant stabilizer. In contrast, at the operating point with 20 kW thermal power from the coal, a much wider reaction zone forms below the quarl. In general, the developed model reproduced the essential flow characteristics of both operating points. However, in regions of high particle density, deviations occur which can be attributed to the challenging evaluation of the PIV data.

The analysis of particle histories revealed a rapid heat-up that caused devolatilization, followed by the slower char reaction. For different particle sizes, the maximum temperature changed, as did the heating rates. The explanation for that is the different Stokes numbers and different thermal inertia. The temporal progression of the particles exhibits apparent differences between the two investigated operating points. Overall, the heating rates at the operating point with 7 kW thermal power from coal are significantly higher than at the operating point with 20 kW thermal power from coal. The explanation for this is the lower heat extraction of the solid phase due to the lower particle densities.

In summary, the analysis of the particle trajectories shows significant differences between the two operating points. At operating point TPR7, the methane flame seems to be the dominant stabilizer, and the coal particles have hardly any influence on the gas phase. In contrast, at operating point TPR20, the effects are significantly different. Instead of a stabilizing methane flame, a much wider reaction zone forms below the quarl, which is closer to that of a real coal flame.

Overall, the extended model produced consistent results for complex physical processes inside the laboratory-scaled gas-assisted coal combustion chamber under oxy-fuel atmospheres.

6.3. Self-Sustained Oxy-Coal Swirl-Combustor [165]

In this section, the overall model is validated in a self-sustained pulverized coal combustion chamber operated under different conditions. Parts of this section are published in [165]. First, the combustion chamber and the operating conditions are briefly described. This is followed by the presentation and discussion of the results. In the end, the main findings of this section are summarized.

6.3.1. Configuration and Boundary Conditions

The experiments were carried out at the WSA-RWTH Aachen University combustion test furnace. A schematic cross section of the down-fired combustion chamber, which has an internal diameter of 400 mm and a maximal height of 4200 mm, is depicted in Figure 6.21 a). The top of the combustion chamber is composed of a ceramic burner port with the burner mounted in the center. This burner port can be accurately traversed along the axis of the combustion chamber. Three radial observations ports, located at the half-length of the combustion chamber, are available for probe and optical measurements.

The traversable burner, which was specifically designed to ensure stable combustion of pulverized coal in oxy-fuel and atmospheric conditions [236], consists of two concentric annular orifices. The central annular orifice, named the primary nozzle, is built around a central bluff body and provides the coal particles, carried in an oxidizer stream. The adjacent annular orifice, named the secondary nozzle, provides a swirled oxidizer stream. Both jets issuing from the these two orifices, mix rapidly in the conical quarl. The level where the gases leave the quarl (dump plane) is coincident with the burner port. Two additional annular orifices, the tertiary stream and the staging stream, provide additional oxidizer to stage the flame. The former is located between the quarl and the burner port. The latter is located at the gap between the burner port and the walls of the chamber. The inner walls of the combustion chamber consist of three layers of ceramic insulation with electric heating elements inserted in the outermost layer. The combination of both ceramic material and electric heating minimizes heat losses, which allows the unit to operate at uniform wall temperatures in various operating conditions.

Experimental characterization of different flames under air and oxy-fuel conditions have been recently conducted in the chamber. Measurements were done employing intrusive and non-intrusive measurement techniques. Zabrodiec et al. [271] compared Laser Doppler Velocimetry (LDV) and Particle Image Velocimetry (PIV) to obtain the velocity field inside the burner. Moreover, Zabrodiec et al. [272] used an intrusive cold-background optical probe to collect and evaluate the radiation from single and small particle clouds in air and oxy-fuel conditions. In addition, Hees et al. [89] performed parametric studies on the fuel-to-oxidizer ratios and different oxidizer compositions to assess the general behavior of oxy-fuel combustion. This was done by means of OH* radical visualization in the flame and analyzing the local fuel gas concentration by means of sampling probe measurements.

Figures 6.21 b) and c) depict the simulation domain, which includes the burner port with the mixing chambers where the swirled flow is generated. Below the dump plane, the domain size of the simulation is 700 mm, representing a reduced domain length compared to the whole furnace length. The numerical grid has a resolution of $x = 0.5$ mm in the quarl and is coarsened to $x = 1-3$ mm below the quarl using O-grids. In total, the grid consists of approximately 1.8 million cells.

Three different sets of operating conditions (two oxy-fuel cases and one conventional air-fired reference case) were chosen to study the effects of different atmospheres upon the flame and flow fields. Table 6.5 shows all relevant parameters for the operating conditions studied. In

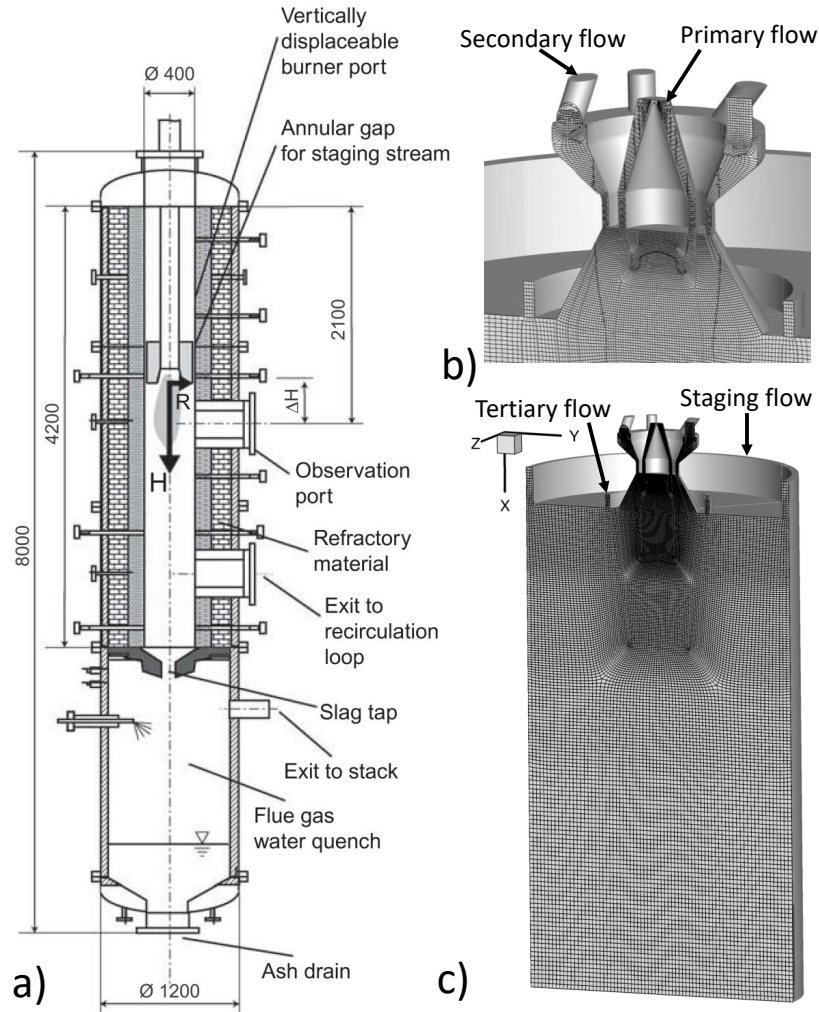


Figure 6.21.: Schematic drawing of the combustion chamber. Left: Cross section of the combustion chamber. Right: Computational domain and the numerical grid of the burner together with a closer view of the burner head.

all studied conditions, the thermal output of the flame was kept constant at 60 kW. In order not to vary the particle injection velocity, the volume flow rate for the primary stream was also kept constant between all cases. The oxidizer composition was modified between a conventional atmospheric reference case (AIR) and the two oxy-fuel cases, with 21 vol-% O₂ and 79 vol-% CO₂ (OXY21) and with 25 vol-% O₂ and 75 vol-% CO₂ (OXY25), respectively. In addition, the flame stoichiometry is kept constant for all cases. The investigated operating conditions provide an overall lean mixture in the chamber with a fuel-rich zone close to the burner. The fuel used in this study was Rhenish Lignite (RBK). The corresponding coal composition and heating values obtained from the ultimate analysis are given in Table 4.1. The particle size distribution (PSD), which is used to generate the coal particles at the inlet, was measured by laser diffraction and is given in [272]. The estimated volume based diameters are $D_{10} = 5.61 \mu\text{m}$, $D_{50} = 29.67 \mu\text{m}$, and $D_{90} = 132.62 \mu\text{m}$.

Table 6.5.: Parameters of the three operating conditions. I: Primary stream. II: Secondary stream. III: Tertiary stream. IV: Staging stream.

	AIR	OXY21	OXY25
I Coal mass flow (kg/h)	9.8	9.8	9.8
I Volume flow, primary stream ^a (m ³ /h)	9.4	9.4	9.4
I Temperature, primary stream (K)	300	300	300
II Volume flow, secondary stream ^a (m ³ /h)	28.8	28.8	23.8
II Temperature, secondary stream (K)	313	313	313
III Volume flow, tertiary stream ^a (m ³ /h)	5.1	5.1	4.2
III Temperature, tertiary stream (K)	313	313	313
IV Volume flow, staging stream ^b (m ³ /h)	26.5	26.5	26.5
IV Temperature, staging stream (K)	1125	1125	1125
Global oxygen-fuel ratio ^c λ_{global} (-)	1.3	1.3	1.3
Local oxygen-fuel ratio ^c λ_{local} (-)	0.8	0.8	0.8
Thermal power P_{th} from coal (kW)	60	60	60

Table 6.6.: Devolatilization kinetic parameters for the SFOR model of Rhenish lignite.

Y_0	A	b	E
0.5494	29,058 1/s	0	42,879 J/mol

6.3.2. Numerical Model

Solid Fuel Kinetics

To describe particle devolatilization, the CPD model was used to adjust kinetic parameters for simplified and widely used SFOR model. The Arrhenius parameters (pre-exponential factor A , temperature exponent b and activation energy E), which are coal specific and have been determined prior to this study [108; 163] are listed in Table 6.6. The char conversion process is modeled using the Baum and Street model [10; 57]. In this model, the following equation describes the entire conversion of the char structure. The experimentally determined model parameters for the coal in use are given in Table 4.2 in Section 4.3.2.

Gas-Phase Chemistry Modeling

In this section the FGM approach is used for the gas-phase description, where two mixture fractions (Z_1, Z_2), the enthalpy h and a reaction progress variable \mathcal{Y} are taken to build a four-dimensional manifold. The two-mixture-fraction approach describes the mixing of volatiles and char oxidation products with the oxidizer, respectively. Including the enthalpy and a reaction progress variable accounts for non-adiabatic physics and finite rate chemistry effects are accounted for, respectively. The 4-D FGM table is generated from a series of one-dimensional premixed flamelets. The flamelets are calculated in physical space using the detailed chemistry

solver Chem1D [26] and the GRI 3.0 mechanism [222], applying unity Lewis numbers for all species. To store the flamelet in the table, the complete thermo-chemical state is mapped on the progress variable \mathcal{Y} , which is defined as $\mathcal{Y} = Y_{\text{CO}_2}/M_{\text{CO}_2} + Y_{\text{CO}}/M_{\text{CO}} + Y_{\text{H}_2\text{O}}/M_{\text{H}_2\text{O}}$, where Y_i and M_i are the mass fraction and molecular mass of the species, respectively. This choice is appropriate for both air and oxy-fuel combustion [163]. The release of the volatiles is described by the first mixture fraction $Z_1 = Z_{\text{C,Vol}} + Z_{\text{H,Vol}} + Z_{\text{O,Vol}}$, where $Z_{\text{C,Vol}}$, $Z_{\text{H,Vol}}$, $Z_{\text{O,Vol}}$ and $Z_{\text{N,Vol}}$ denote the element mass fractions of C, H, O and N, respectively, originating from the volatiles. Contrary to the previous works [163] presented in Section 6.2, the volatiles are represented by a complex composition, instead of using a surrogate species. The volatile composition used, which was measured with a technique described in [91], is composed of CO_2 , CO , CH_4 , C_2H_6 , C_2H_4 , C_2H_2 , C_3H_8 and N_2 with mass fractions $Y_{\text{vol},k}$ of 0.143, 0.281, 0.122, 0.027, 0.111, 0.009, 0.3 and 0.007, respectively. Since the GRI 3.0 [222] mechanism is adopted for the gas-phase chemistry in this work, tar must be modeled by lighter gases (e.g., C_2H_4 , C_2H_2 , and C_3H_8), this follows the procedure successfully used in previous work [110; 204]. The split in composition is performed such that it does not change the elemental composition and the heating value of the coal significantly. The effect of this assumption was assessed in the recent study of Farazi et al. [51] revealing that modeling tars by lighter gases change the ignition process only slightly.

The second fuel is described by a second mixture fraction $Z_2 = Z_{\text{C,CO}} + Z_{\text{O,CO}} + Z_{\text{Oxi.,SFR}}$ [111]. Similarly to the first mixture fraction, $Z_{\text{C,CO}}$ and $Z_{\text{O,CO}}$ denote the element mass fractions of C and O, respectively, originating from char products. $Z_{\text{Oxi.,SFR}}$ represents the element mass fraction of N_2 and CO_2 for atmospheric and oxy-fuel atmospheres, respectively, which participates in the surface reaction (SFR).

Radiation

In this section, the radiation model introduced in Sections 2.4 and 4.5 is applied. A total of 80 directions is used to discretize the radiative transport equation. For the gas phase, the weighted sum of gray gases (WSGG) method is used for the spectral behavior. The absorption coefficients and weighting factor are taken from Dorigon et al. [43] for air atmospheres and Bordbar et al. [16] for oxy-fuel atmospheres. The particle phase is assumed to be gray, i.e., its radiative properties are constant over the spectrum.

6.3.3. Results and Discussion

Results from simulations, shown in Figure 6.22, depicts the averaged axial velocity (U_{ax}) and averaged gas temperature fields (T) for all three investigated operating conditions.

On the left-hand side of Figure 6.22 a)-c), a swirl-induced main internal recirculation zone (IRZ) is visible in the center of the chamber. This recirculation zone with significant negative axial velocity stabilizes the flame. Besides the IRZ, two additional smaller external recirculation zones (ERZ) are visible in Figure 6.22. One is located directly below the dump plane and is enclosed by the tertiary and staging streams. The second ERZ is located directly below the staging stream.

The IRZ transports hot flue gas back to the burner inlet, where fresh coal particles are injected. This mechanism is visible when the gas phase temperature is considered on the right-hand side of Figure 6.22 a)-c). Increased gas phase temperatures reveal a main reaction region below the quarl. Due to the high gas temperature, cold fresh particles are heated up and devolatilize. The released volatile matter mixes with the surrounding atmosphere and is ignited when the flammability limit is reached. The reacted hot flue gas is then recirculated again. A region with lower temperatures can be clearly identified inside the quarl, below the primary inlet. In this region, mostly large particles enter the recirculation zone, as their inertia is too large for them

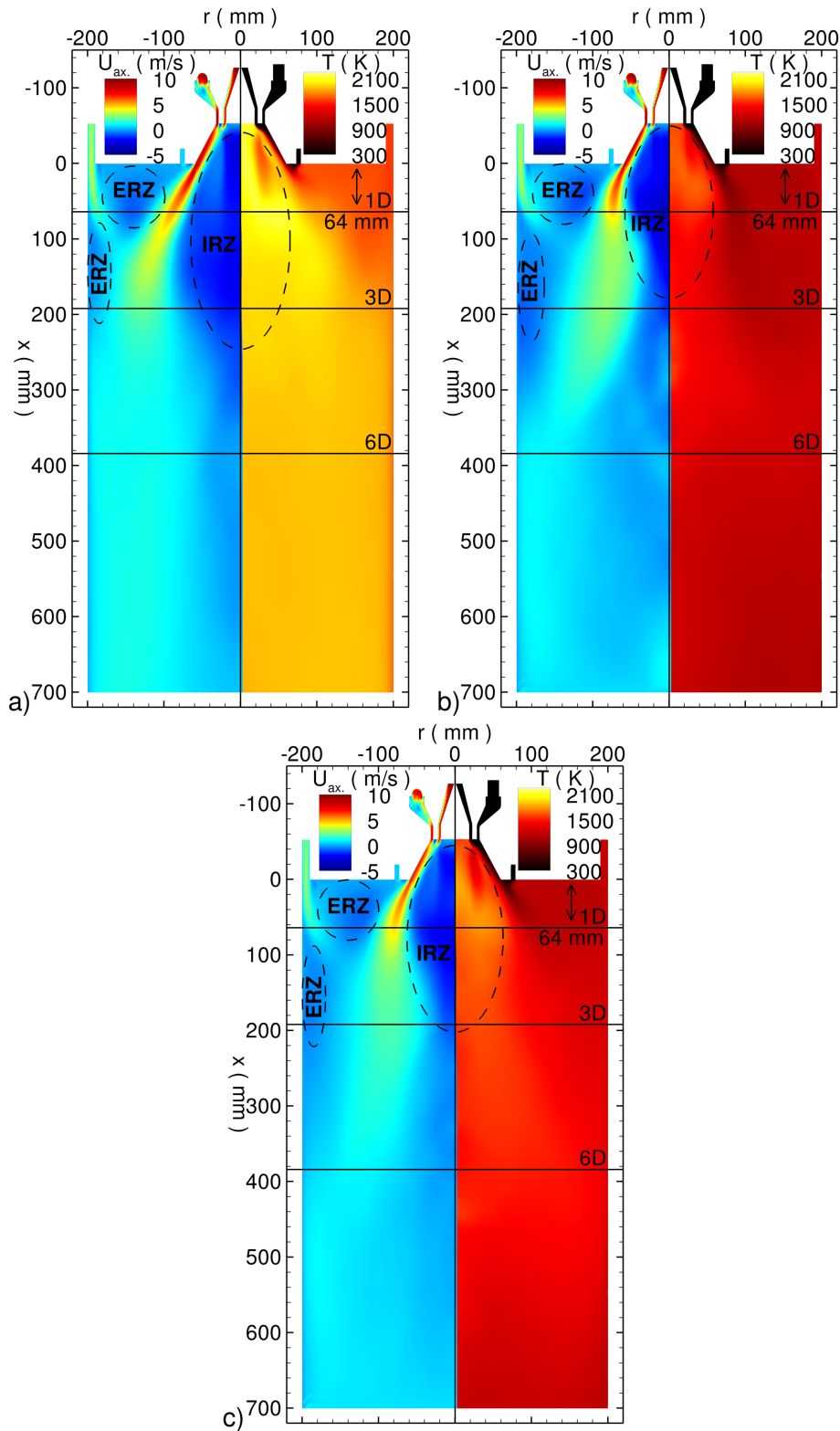


Figure 6.22.: Averaged results of Eulerian-fields in the r - x plane: (a) AIR, b) OXY21 and c) OXY25). Left: axial velocity. Right: gas temperature. As a reference, the locations of experimental measurements are depicted for different axial distances below the dump plane for all operating points. The regions IRZ and ERZ indicate the internal and external recirculation zones.

to follow the cold flow towards the wall directly. These particles extract heat from the gas phase as they heat up.

Qualitatively similar flow fields are observed when the axial velocity fields of all three investigated atmospheres are compared. However, the OXY21 and AIR cases exhibit slightly higher velocities in the quarl region. This can be explained by the increased initial momentum flux compared to the OXY25 case, needed to retain comparable stoichiometries for all cases. Furthermore, a somewhat more extended recirculation zone is visible in the AIR case, which indicates a weaker swirl. This observation agrees with the observed qualitative results of the PIV measurements [272].

Contrary to the velocity field, the temperature fields exhibits noticeable quantitative differences between the operating conditions. The temperature of the AIR case is significantly higher compared to the two oxy-fuel operating conditions. Although the OXY25 case has a higher oxygen content compared to the AIR case, the different heat capacities of N_2 and CO_2 yield lower adiabatic flame temperatures. Compared to the OXY25 case, the OXY21 case exhibits even lower temperatures, which can be attributed to the lower oxygen content in this atmosphere.

In order to identify the central release zones of volatile gases and char products, Figure 6.23 depicts the values of the first (f_1) and second (f_2) mixture fractions for all investigated operating conditions. Additionally, particles, which are colored by their volatile ($Y_{Vol.}$) and char content (Y_{Char}), respectively, are shown. Despite the strong recirculation, the figure depicts the clear spatial separation of volatile gases and char off-gases for all three atmospheres. High contents of volatile gases mostly occur very close to the burner port, where particles are rapidly heated up. Due to the local flow field, the volatile gases are recirculated and thus stabilize the flame. By contrast, char off-gases are mainly formed below the quarl. In this region, fresh air from the tertiary and staging flows is mixed with the volatile flue gases. Char conversion is particularly strong in regions with high temperatures and available oxygen. This clear separation of the volatile release and char reaction can also be seen for the particles. While nearly all volatile matter is released within the quarl, the char content of the particles starts to decrease about 100 mm below the quarl. Only small ash particles are recirculated inside the recirculation zone.

In all cases, a high volatile content, i.e. a large first mixture fraction, is observed inside the quarl. A significant amount of char gases is visible about 100 mm below the dump plane. It is interesting to note that the main char formation zone shifts slightly from the wall (AIR and OXY25) and towards the center (OXY21) of the combustion chamber. This observation can be explained by the different flow fields, which influence the particle pathways through the combustion chamber. These different particle pathways also lead to a broader distribution of the larger particles in the OXY21 case. Due to the more substantial recirculation zone in the OXY21 case, larger particles are steered further into the center of the chamber, while in the OXY25 and AIR case, large particles move towards the furnace walls.

After this introductory comparison of the simulation results, the overall model will be extensively evaluated against the available measurement data for the gas phase velocities, particle temperatures and species compositions. First, Figure 6.24 presents radial profiles of experimental and numerical mean axial ($\overline{U}_{ax.}$) and tangential velocities ($\overline{U}_{tan.}$) at different axial positions D (as multiples of $D = 64$ mm, corresponding to the radius of the secondary annular nozzle (For reference see Figure 6.22)). For the radial velocity component, no measurement data are available.

The measurements and simulations show a similar profile for the closest location below the burner ($0.5D$). In the center of the chamber, the inner recirculation zone can be identified by negative axial velocities. At around $r = 80$ mm the maximum axial velocities occur. Compared to the measurements, the simulation shows a slightly lower maximal velocity and a small shift in

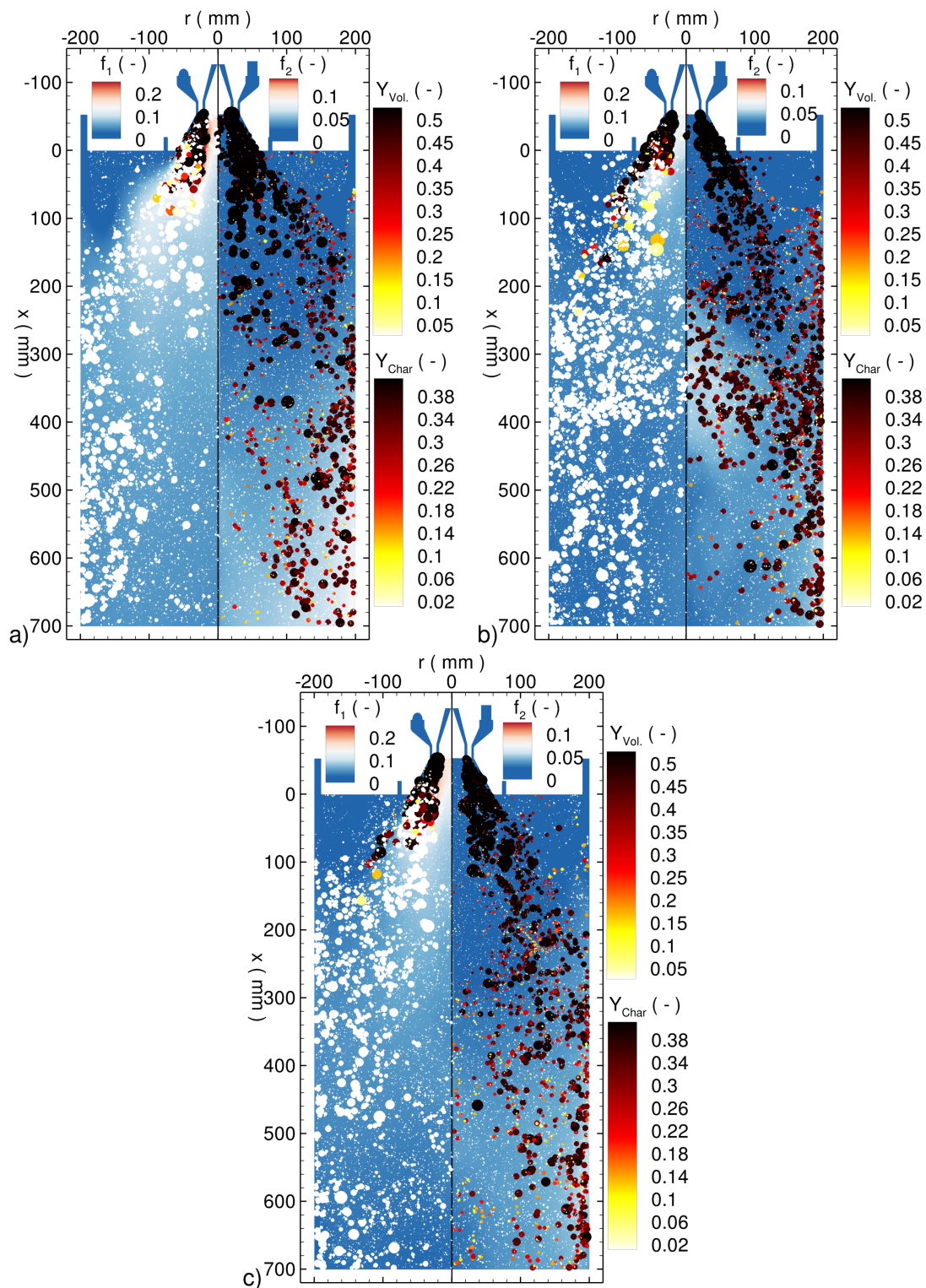


Figure 6.23.: Mean images of Eulerian-fields in the r - x plane together with instantaneous distribution of particles scaled by diameter for the different atmospheres: (a) AIR, b) OXY21 and c) OXY25). Left: Mixture fraction for the volatiles and particles colored by volatile content. Right: Mixture fraction for the char reaction products and particles colored by char content.

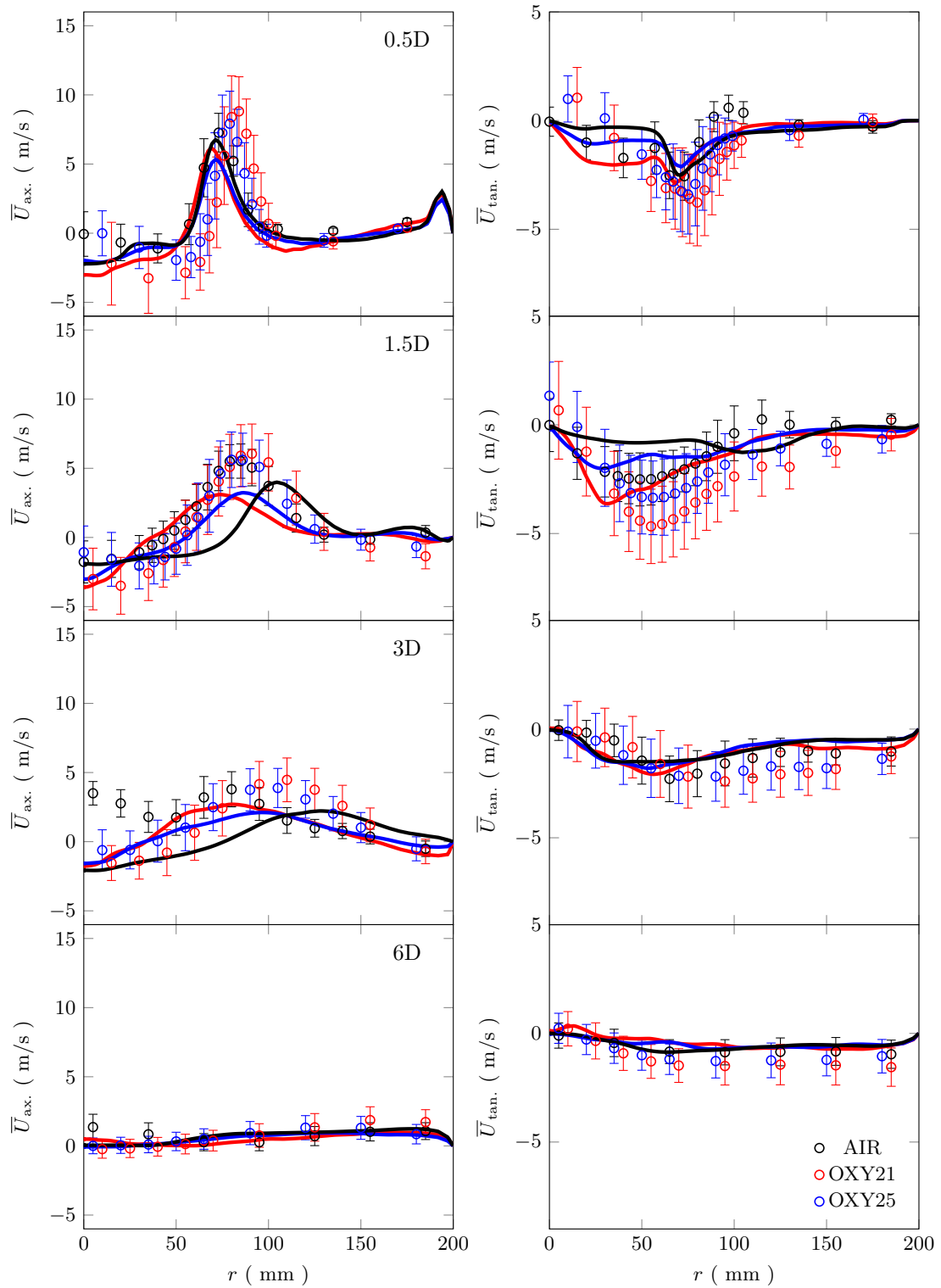


Figure 6.24.: Comparison of experimental (symbols with error bars) and simulation (lines) mean axial velocity (left) and mean tangential velocity (right) profiles below the quarl for different axial heights.

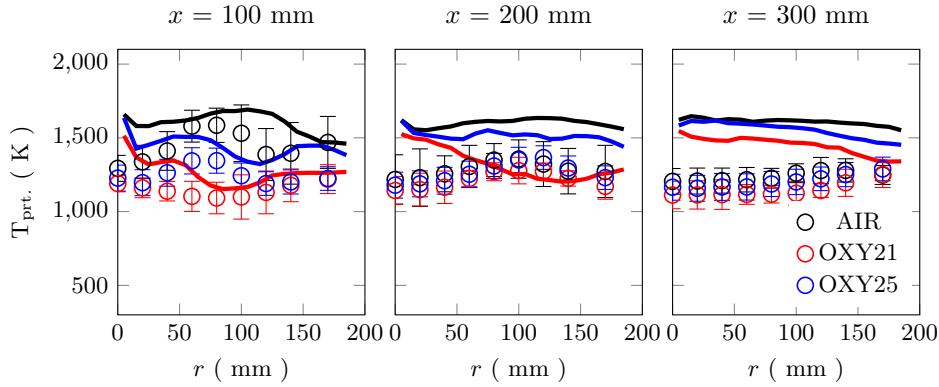


Figure 6.25.: Comparison of particle temperatures between experiments (symbols with error bars) and simulations (lines) for different axial distances below the dump plane.

the velocity peak towards the center of the chamber. This could be attributed to slip velocities between the gas phase and the particles. As mentioned in [272], velocity measurements can be biased by the presence of large coal particles in the flow. Since the velocity determination in the experiments is based on particles, especially at locations with significant amounts of large particles or strong velocity gradients or both, deviations between the measurements and simulations are expected. For all simulations, a small velocity increase at $r = 190$ mm delineates the location of the staging flow. This cannot be reproduced by the measurements, because the coal particles are used as tracers. Since the staging flow is not loaded, no particles are available to determine the velocity. For the tangential velocities, the trend of increasing velocities from AIR (lowest velocities), to OXY25 up to OXY21 (highest velocities) is captured well. Again, the peak position is slightly shifted inwards for the simulation. However, as the tangential velocity does not become zero in the center for the LDV measurements, a slight outwards shift is very likely for all measurements, which would also explain the deviation in the axial velocity peak. A similar trend is visible at $1.5D$ below the dump plane. For the simulation, a shift of the axial velocity, which is following the different tangential velocities, is apparent. This shift is not visible in the measurements. However, the correct trend for the tangential velocities is still preserved. At $3D$, strongly reduced peak velocities can be seen in the measurements and are reproduced well by the simulation. The deviation between measurements and simulation seen in the AIR case near the center is likely to be associated with larger particles influencing the velocity measurements. Given the high temperatures in these regions, measurements are challenging to obtain. At the last location ($6D$), a more uniform velocity field is depicted by the measurements and is well reproduced by the simulation for all investigated conditions.

Considering the uncertainties in both the simulation and the experiment, the model used is capable of correctly predicting the velocities inside the combustion chamber. Moreover, differences between the studied atmospheres can be described in a qualitative way.

Following, particle temperatures from simulations are compared to measurement data at three representative locations depicted in Figure 6.25. For the first location 100 mm below the dump plane, average particle temperatures from experiments (dots with error bars) show a noticeable difference between the atmospheres. In overall, the AIR case exhibits significantly higher particle temperatures compared to both oxy-fuel atmospheres. This agrees well with the observed gas phase temperature difference in Figure 6.22. These different gas temperatures depending on the operating conditions directly affect particle heating. Hence, the different thermodynamic properties of CO_2 compared to N_2 have a substantial influence on the particle phase. Comparing the experiment and simulation for the first location 100 mm below the dump plane, reasonable

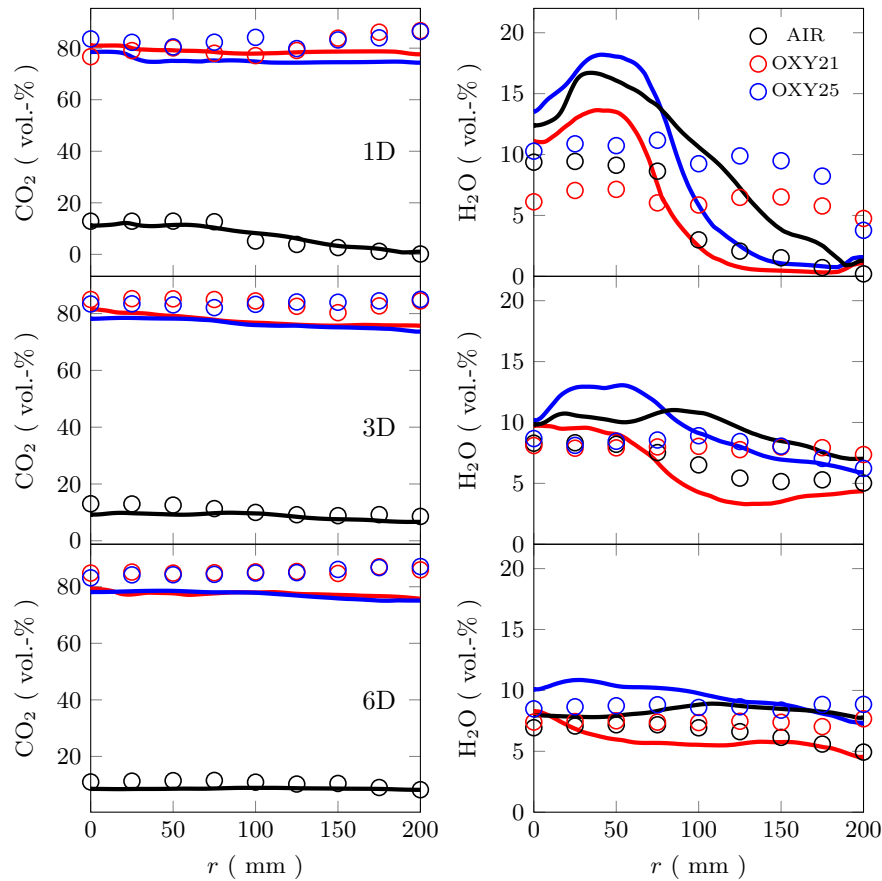


Figure 6.26.: Comparison of of CO_2 and H_2O molar fraction between experiments (symbols) and simulations (lines) for different axial distances below the dump plane.

agreement can be observed close to the furnace wall. In contrast, small differences are visible in the burner center. In the center of the combustion chamber, the particle temperature is overpredicted by the simulation. However, the trend of OXY21 having the lowest temperature, followed by OXY25, with the highest temperatures for the AIR case, is predicted correctly. At the locations 200 mm and 300 mm below the dump plane, the experimentally determined particle temperatures depict a particle temperature which rapidly approaches uniformity for all cases. To a lesser extent, the simulations show similar trends. However, for all three operating conditions, the particle temperature is overpredicted by the simulation.

The overall deviation can be attributed to both the simulation and measurements. In the measurements, a cooled background probe is used to determine the particle temperatures [271]. Due to the technique's invasive character, a significant influence on the thermo-physical state at the measured location cannot be eliminated. Especially at high temperatures and low velocities, which is the main characteristic observed for the recirculation zones, an influence of the measurement technique can be expected. In the simulation, the assumption of homogenous spherical particles could potentially lead to a false prediction of the heating behavior.

Figure 6.26 shows the profiles for the molar fractions of CO_2 and H_2O . For CO_2 , good agreement can be observed close to the burner, while the LES predicts somewhat lower values. The trend of there being a higher CO_2 concentration close to the burner center is predicted well. Furthermore, the trend of a similar CO_2 concentration in the oxy-fuel cases for larger axial distances is correctly predicted. A high H_2O molar fraction can be observed at the center of the

chamber close to the quarl exit. The rich volatile gas mixture can explain these values. Further downstream, a more uniform H_2O molar fraction can be observed, with good agreement between the simulation and experiment.

The mean global error of each validated quantity is included in Table 6.7. All integrated errors are normalized by their respective reference value. To avoid dividing by zero, the maximum range of the occurring velocities was used to normalize the velocities as proposed by Ries et al. [199]. For all three investigated operating conditions, the global error is similar. This is another confirmation that the developed model can provide reliable results in both air and oxy-fuel conditions.

Table 6.7.: Global errors between simulation and experiment for gas phase velocities, particle temperature and species concentrations

	AIR	OXY21	OXY25
$\frac{\text{abs}(U_{\text{ax.}} - U_{\text{ax.,exp}})}{d(U)}$ (%)	14.04	10.11	7.93
$\frac{\text{abs}(U_{\text{tan.}} - U_{\text{tan.,exp}})}{d(U)}$ (%)	16.11	14.81	15.29
$\frac{\text{abs}(T_{\text{prt.}} - T_{\text{prt.,exp}})}{T_{\text{prt.,exp}}}$ (%)	21.42	15.84	21.01
$\frac{\text{abs}(H_2O - H_2O_{\text{exp}})}{H_2O_{\text{exp}}}$ (%)	21.58	21.74	20.85
$\frac{\text{abs}(CO_2 - CO_{2,\text{exp}})}{CO_{2,\text{exp}}}$ (%)	16.53	6.94	7.6

Following the validation of the gas phase velocities, particle temperature and species concentrations, the effect of the oxidizer atmosphere on the particle phase will be analyzed in more detail below. Figure 6.27 depicts scatterplots of one in every five-hundred particles randomly selected out of approximately 3 million particles. Particles consisting of more than 99% ash are not included in the scatterplots.

In Figure 6.27 a),c) and e) (left column), the velocity slip between the gas phase and particles is analyzed for all operating conditions. As expected, larger particles generally tend to possess larger slip velocities, which can be identified by the deviation from the angle bisector. This holds true for all three operating conditions. In addition, only small particles reach very high velocities. This can be explained by the lower inertia of the small particles, which leads to different particle trajectories through the combustion chamber. Because the small particles follow the flow much better to the wall of the quarl, where the highest velocities occur, as seen in the Figure 6.22, these particles have much higher velocities than the large particles falling through the recirculation zone. In addition, the absolute and slip velocities decrease with increasing temperature. This effect can be explained either by small particles, which are trapped inside the recirculation zone or by the fact that larger particles are located below the recirculation, where overall lower velocity gradients occur. It is interesting to note that although very different particle temperatures can be seen between the different operating points, the absolute and slip velocities are not strongly affected by the change in the atmosphere. In addition, this analysis reveals that the LDV data quality, which is influenced by the particle velocity slip, is independent of the atmosphere.

In Figure 6.27 b),d) and f) (right column), the temperature differences between the gas phase and particle are shown for all operating conditions. Additionally, the particles are colored based on their burnout value. These values indicate the conversion status of the particle, where zero means fully unreacted and one means pure ash. Generally, unreacted particles have a lower temperature than the gas phase because the surrounding hot gases heat these particles. This heat-up process leads to an increase in the particle burnout due to the release of volatiles and char off-gases. For some particles with intermediate to high burnout, however, noticeably higher particle temperatures than the surrounding gas can be detected. There are two reasons for

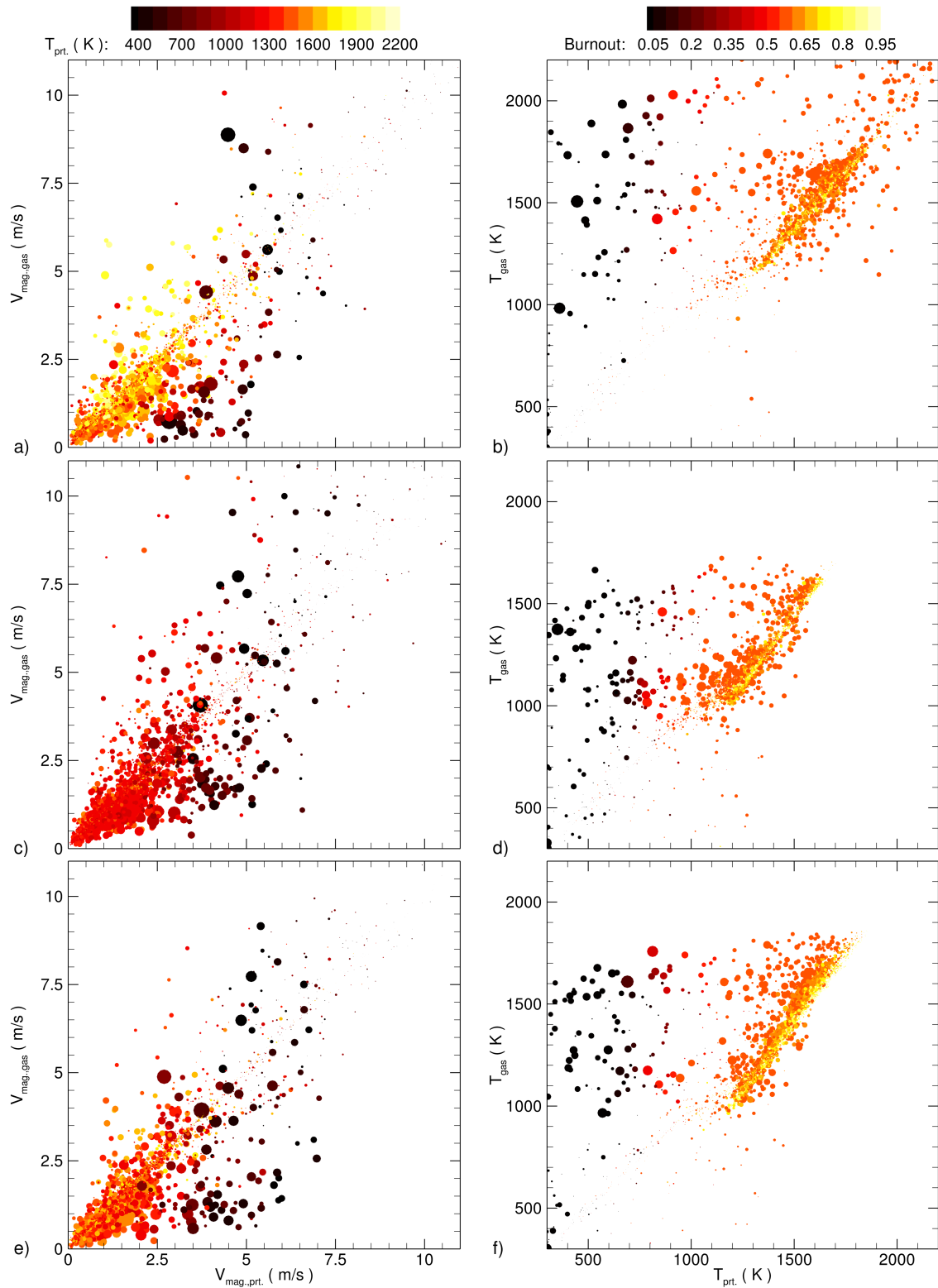


Figure 6.27.: Representative instantaneous scatterplots of particles in the combustion chamber. Left: Particle velocity over gas velocity with the temperature of individual particles indicated by color. Right: Particle temperature over gas temperature with burnout state indicated by color. Top row: AIR. Middle row: OXY21. Bottom row: OXY25.

this temperature slip. On the one hand, particles may be entrained in the colder flow stream before completing the conversion process. On the other hand, the heat of the char reaction may raise the particle temperature above the level of the surrounding gas. Most particles close to full burnout have a negligible thermal slip and are therefore close to thermal equilibrium. Similar observations have been reported in several other studies for different configurations [163; 172; 204].

The most significant difference between the investigated cases is, again, the different temperature levels. For the AIR case, the dominant particle conversion process happens in the region between 1200 K and 1600 K. Moreover, some particles with significantly higher temperatures occur for the AIR case. In contrast, the temperature where the particle conversion takes place is less widespread but lower overall in oxy-fuel atmospheres. This result agrees with the observations in Figure 6.22. For the AIR case, the flame with high temperatures leads to some very high particle temperatures. For the oxy-fuel conditions, an overall region with a higher, more homogeneous temperature distribution forms, which in turn leads to more uniform particle heating.

Following, the conversion of particles in air and oxy-fuel conditions will be investigated in more detail. Since the conversion process is strongly dependent on particle temperature and local oxygen content, these two parameters are shown in Figure 6.28. Figure 6.28 a)-c) (left) depicts particles in the combustion chamber in a horizontal plane of 2 mm thickness. A qualitatively similar particle behavior is found for all three operating conditions. First, particles are heated up rapidly. Due to the strongly swirled flow, particles, especially small ones, are pushed towards the quartz walls. Some small particles are recirculated inside the main recirculation zone and advected back towards the burner inlet. However, only a small number of particles can be found at the center of the main recirculation zone. One explanation for this observation is that the recirculation is not strong enough to overcome the particle inertia. Similar observations have been made both numerically [204] and experimentally [12] for different swirl-stabilized PCC flames.

The right-hand side of Figure 6.28 a)-c) depicts the averaged O_2 mass fraction. Inside the quartz, as expected, the oxygen is fully consumed by the reaction of the volatiles. In the center of the combustion chamber, an overall content of oxygen remains low because the hot particles directly consume the fresh oxidizer from the tertiary and staging flows in the heterogeneous char surface reaction. A large oxygen fraction can only be observed in the external recirculation zone between the tertiary and staging flows. Here, only small numbers of ash particles recirculate, therefore no or very little oxygen is consumed. Further downstream from the burner, an increase in oxygen mass fraction is visible. In these regions, most of the small particles are fully converted, and only large particles, with high thermal inertia, still react.

Table 6.8.: Particle classified into different size classes for particle histories.

Class	Particle size
1	$D_{\text{prt}} \leq 25 \mu\text{m}$
2	$25 \mu\text{m} < D_{\text{prt}} \leq 50 \mu\text{m}$
3	$50 \mu\text{m} < D_{\text{prt}} \leq 100 \mu\text{m}$
4	$100 \mu\text{m} < D_{\text{prt}}$

To investigate the transient particle behavior, Figure 6.29 depicts particle histories for the particle temperature, the volatile content and the char content. For this, particles have been

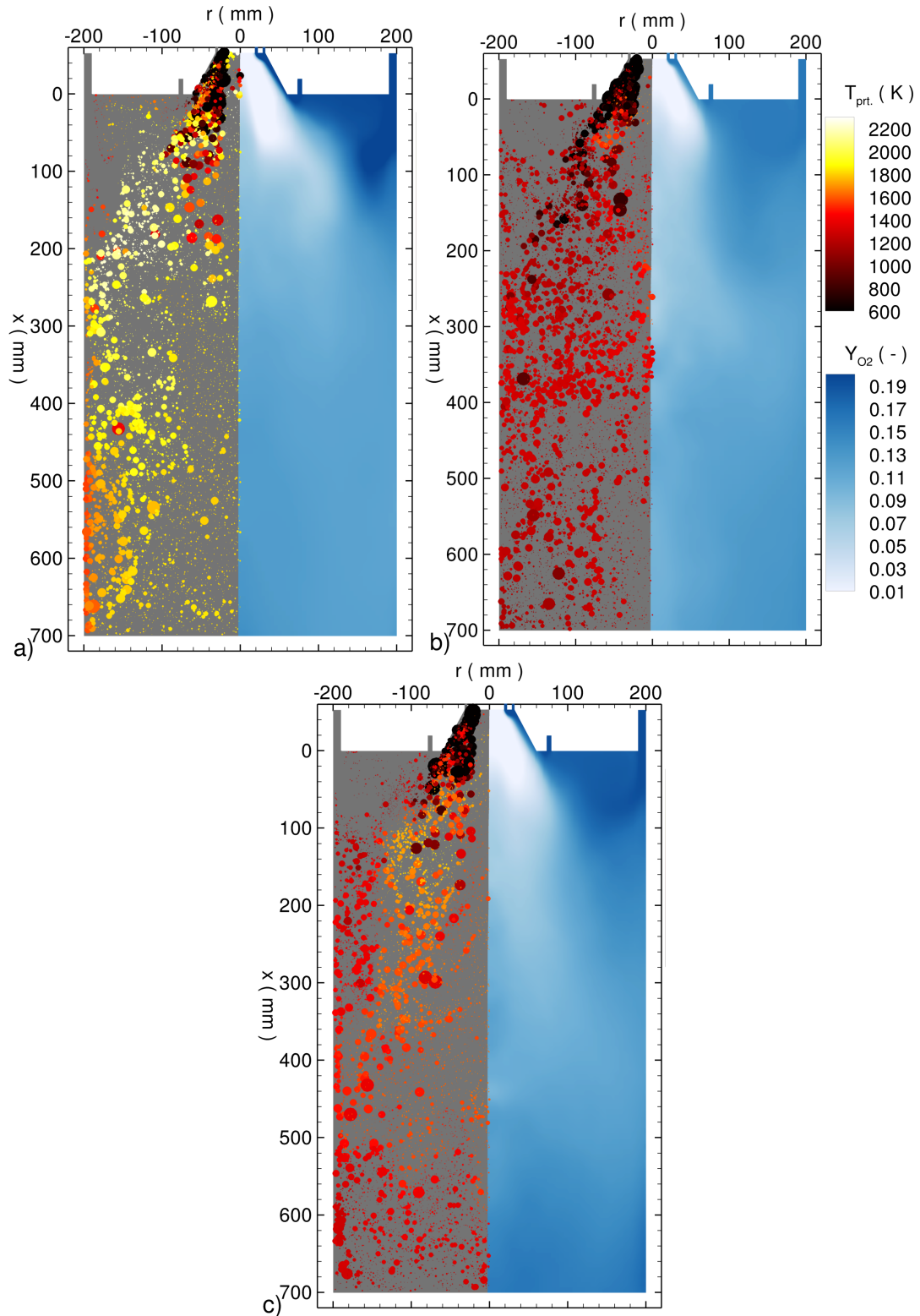


Figure 6.28.: Particles scaled with the diameter and colored based on their temperature (left-hand side of each plot) and averaged oxygen mass fraction (right-hand side of each plot) for AIR (a), OXY21 (b) and OXY25 (c).

split up into four different classes as shown in Table 6.8, to include the effect of different particle sizes. In order to achieve sufficient statistics, each particle class is represented by 1000 particle histories.

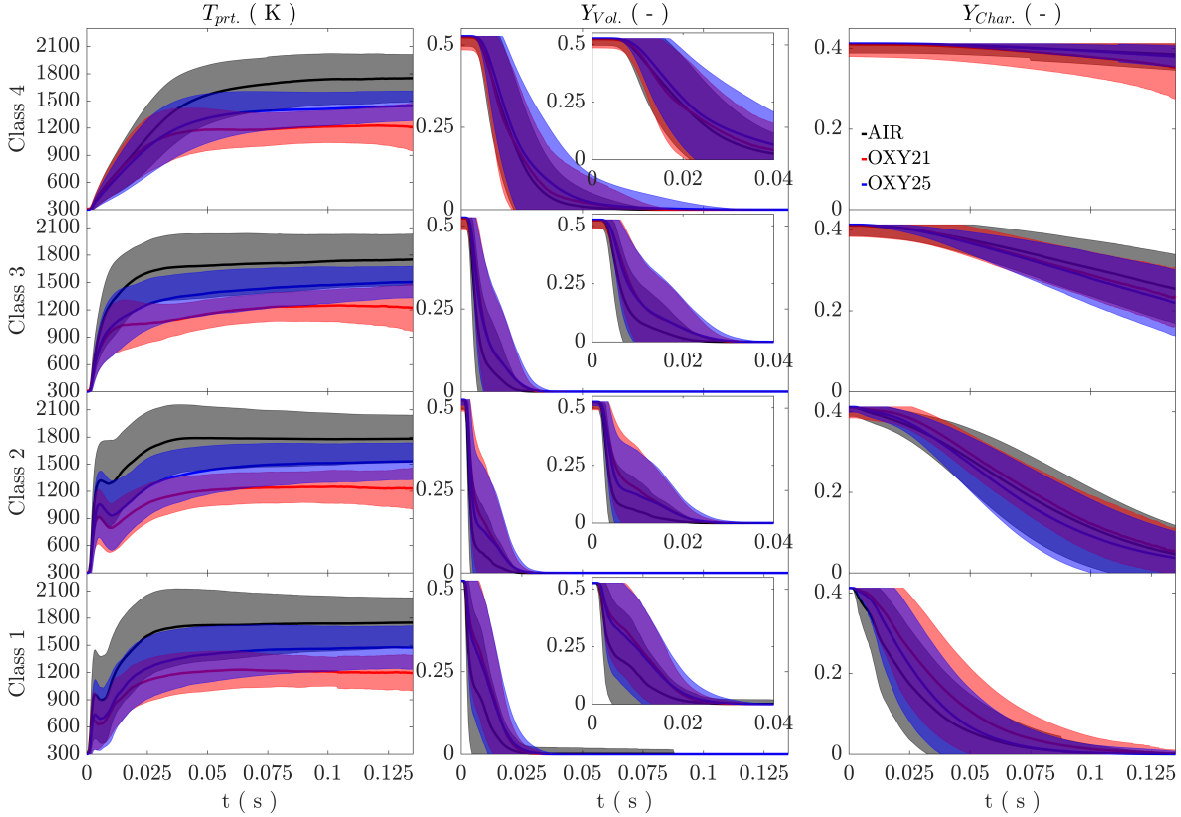


Figure 6.29.: Particle histories over time for particle size classes as defined in Table 6.8. Left: Particle temperature. Center: Volatile content. Right: Char content. Solid lines represent the mean values and shaded areas represent the standard deviation.

In general, the same temporal development can be seen for all operating conditions. During the first few milliseconds, a rapid heat-up leads the volatiles to be released. The time in which the gases are released corresponds to the time of heating. After the heating and volatile release, the heterogeneous char conversion follows. When comparing the trajectories of different particle classes, a significant influence of particle size is seen. Due to the lower thermal inertia, smaller particles exhibit a steeper temperature increase compared to larger particles. The faster temperature increase correlates with a faster release of volatiles. For the char conversion, a significantly faster conversion is visible for the smaller particles, which reach full burnout at around 0.125 s. By contrast, Class 4 particles only start char conversion after 0.125 s. When comparing between the different operating conditions, the aforementioned different particle temperatures between the different conditions are visible again. For all trajectories, the AIR case involves significantly higher particle temperatures, followed by the OXY25 case. The lowest temperatures occur for the OXY21 case. The volatile release correlates with different temperature trajectories. Interestingly, for some short periods, the particle temperatures of the OXY21 case exceed the temperatures with OXY25. Local differences in the respective flow fields affect the particle movement and therefore the particle heat-up. It is interesting to note that the char conver-

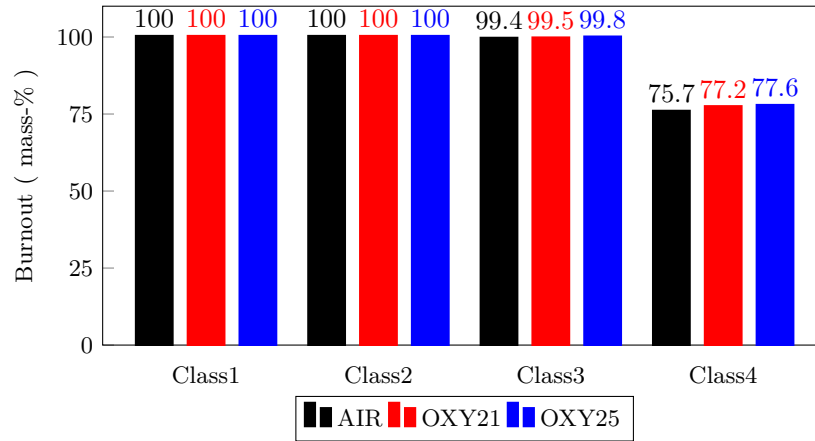


Figure 6.30.: Particle burnout for particle size classes as defined in Table 6.8 at the outlet of the simulation domain (700 mm below the dump plane).

sion process seems to have a similar reaction rate for all investigated operating points. Small discrepancies exist in the start time of the char reaction process. However, these differences can be attributed to the different end times of volatile release, which determine when the char conversion process begins. The slopes of char conversion, however, are very similar. The very different particle temperatures might be expected to influence the char conversion. However, due to the very similar oxygen content below the volatile flame, as identified in Figure 6.28, the amount of available oxygen is the limiting factor for char conversion.

The conclusion drawn from Figure 6.29 is that both the particle dynamics and the thermal inertia influence the particle conversion process significantly, the former especially during the heat-up and devolatilization process and the latter when it comes to reaching the final temperature and the resulting char conversion.

From Figure 6.29, it can be concluded that not all particles are completely converted inside the simulation domain. For this reason, the mean final burnout of the different particle classes is shown in Figure 6.30. The final particle burnout is sampled at the end of the simulation domain at 700 mm for each particle size class below the dump plane for all three operating points. All particles in Classes 1 and 2 reach full burnout, while near full burnout is reached for Class 3 particles. Only in the case of Class 4 particles does a substantial amount of coal remain. Comparing the three operating points, interestingly, there is no significant difference, although the particle temperatures differ significantly. Therefore, the conversion process of the large particles seems to be controlled by the partial pressure of oxygen, which is similar in all three cases. Hence, the AIR case does not achieve the highest conversion even though the particle temperatures are significantly higher. The AIR case even achieves a slightly lower conversion rate for the largest particles. This can be explained by the slightly lower residence time of the particles in the AIR case caused by the slightly higher axial gas velocities.

6.3.4. Section Summary

A LES study of self-sustained pulverized coal combustion under atmospheric and oxy-fuel conditions was performed utilizing 4D-FGM-tabulated chemistry coupled with ATF embedded in an Euler-Lagrange framework and detailed radiation modeling. The tabulated chemistry model was extended to account for the complex mixture of volatile gases being released. The model was applied to the test furnace at WSA-RWTH Aachen. Two oxy-fuel atmospheres (21 vol-% and 25 vol-% oxygen) and one conventional air-fired case were studied. Good agreement between

simulations and experiments was found for the available velocity fields. Particle temperatures tend to better agree at locations close to the burner, while an over-prediction was found for locations further downstream in the chamber. For the H₂O concentration profiles, overall good agreement was obtained, with some deviations in the quarl region. For the AIR condition the CO₂ matches the experimental values well. However, for the oxy-fuel conditions a lower concentration is observed in the simulation compared with the experimental value. No significant differences are revealed when comparing the instantaneous slip velocity under the three operating conditions, while temperature scatter plots show that higher gas phase temperature has a significant influence on particle heating. The particle trajectories exhibit differences at the beginning of the conversion phase, which can be explained by the different surrounding temperatures and local flow fields. Interestingly, at the end of the chamber, the overall conversion of the particles is similar, although the particle temperatures vary significantly between the different atmospheres. This observation can be explained by the similar low partial pressure of oxygen in all investigated cases.

Overall, the numerical model provided consistent results for the complex coupled physical process inside self-sustained pulverized coal combustion chambers for both air and oxy-fuel atmospheres.

6.4. Adapted Self-Sustained Oxy-Coal Swirl-Combustor [162]

In this section, the model is validated in a self-sustained pulverized coal combustion chamber operated under oxy-fuel conditions. Parts of this section are published in [162]. The combustion chamber is the same as in the previous Section 6.3. However, the burner head is replaced by the same one used in the laboratory-scale gas-assisted chamber introduced in Section 6.2. First, the operating conditions are briefly described. This is followed by the presentation and discussion of the results. In the end, the main findings of this section are summarized.

6.4.1. Configuration and Boundary Conditions

The experiments were carried out again at the WSA-RWTH Aachen University combustion test furnace [236]. Since the overall construction is similar to the one presented in Section 6.3.1, it is not repeated here for the sake of brevity.

Experimental characterization in different oxy-fuel conditions has been recently conducted in the chamber [273]. Laser Doppler Velocimetry (LDV) was used to obtain the velocity field inside the burner. An intrusive cold-background optical probe was used to collect and evaluate the radiation from single particles and small particle clouds to obtain particle temperatures.

In this study, an operating condition with 27 vol-% O₂ is investigated (Table 6.9). The coal mass flow supplied leads to a theoretical thermal output of 40 KW_{th}. Rhenish lignite was employed as a fuel for the study. The particle size analysis determined by Laser diffraction has a median particle diameter of D50 = 29 μm, with D10 = 5 μm and D90 = 132 μm. The measured size distribution is used to initialize particles in the simulation.

Table 6.9.: Summary of the operating condition with a 27 vol.-% O₂ and 73 vol.-% CO₂ atmosphere [273].

Parameter	
Coal mass flow rate [kg/h]	6.7
Volume flow rate of primary stream [m ³ /h]	9.4
Temperature of primary stream [K]	300
Volume flow rate of secondary stream [m ³ /h]	8.8
Temperature of secondary stream [K]	300
Volume flow rate of staging stream [m ³ /h]	23.1
Temperature of staging stream [K]	1173
Local / global stoichiometric ratio (λ_L/λ_L)	0.6/1.4

Two grids with roughly 3 and 1 mio. cells were used for the simulation. Below the dump plane, the domain size of the simulation is 750 mm, representing a reduced domain length compared to the whole furnace length similar to previous studies [68; 165]. The resolution of $x \approx 0.75$ mm and $x \approx 1$ mm in the quarl is coarsened to $x = 10$ mm and $x = 15$ mm below the quarl using O-grids, respectively. All simulations were run up to 3.5 s of physical time. The last second of each run was used to obtain the statistics.

6.4.2. Numerical Model

Solid fuel kinetics

The reference simulation in this section is performed using the CRECK-S conversion model. Hence, both devolatilization and char reaction are seamlessly modeled. Additionally, two simulations employing the standard conversion models, i.e., the SFOR model coupled to the Baum-Street model and the C2SM model coupled to the Baum-Street model, are also performed. The coal-specific coefficients of the devolatilization models are fitted using the CRECK-S model.

For the SFOR model, the coefficients are fitted by one particle history with a heating rate of 80 K/ms and a final temperature of 1400 K. For the C2SM, multiple particles with heating rates ranging from 10 to 200 K/ms were considered. A summary of all coal-specific coefficients is given in Table 6.10. For the Baum-Street model, parameters are fitted by measurement data as described in Section 4.3.2.

Table 6.10.: Coefficients of the simplified devolatilization models for Rhenish Lignite.

	Y_i (-)	A_i (s ⁻¹)	E_i ($\frac{J}{mol}$)
SFOR	0.54	$1.29 \cdot 10^6$	$5.99 \cdot 10^4$
C2SM	0.484	$1.65 \cdot 10^5$	$4.900 \cdot 10^4$
	0.752	$4.31 \cdot 10^8$	$1.324 \cdot 10^5$

A summary of all simulation parameters for both studied grids is given in Table 6.11. Considering the simulation cost on the fine grid, one can see that the simulation becomes approximately five times more expensive when detailed solid fuel kinetics are used. Comparing the simulation cost from the fine grid with the coarse grid simulation, the simulation cost for the simplified kinetics reduces by a factor of 3.5. In contrast, the simulation cost for the detailed simulation reduces by a factor of less than two. The reason being, even though the cell count is significantly reduced, the particle number stays approximately constant for both grids. Hence, the computation of the particles becomes the dominant share of the simulation cost on the coarse grid.

Table 6.11.: Summary of the simulation parameters for all simulation.

		physical time (s)	cores	core hours
CRECK-S	coarse	3.5	96	105000
	fine		192	182700
SFOR-BS	coarse	3.5	48	10000
	fine		96	35000
C2SM-BS	coarse	3.5	48	10000
	fine		96	35000

Gas-phase chemistry

To describe the turbulent reacting gas phase, the multi-stream FPV model introduced in Section 3.5.4 is applied. The flamelet table is generated from counterflow-diffusion flamelets, which are solved in physical coordinates using Cantera [77] assuming unity Lewis number for all species. Gas-phase kinetics are described by a mechanism developed by Cai et al. [21], which is validated for both air and oxy-fuel atmospheres. The reaction progress variable in the FPV context [178] is defined as

$$\mathcal{Y} = \frac{Y_{CO_2}}{W_{CO_2}} + \frac{Y_{CO}}{W_{CO}} - \frac{Y_{O_2}}{W_{O_2}}. \quad (6.1)$$

The inclusion of additional physical effects into the table (e.g., heat losses, multiple mixture fractions) follows the procedure introduced in Section 3.5.2.

All gas species released by the CRECK-S model but not resulting from oxidation are summarized to devolatilization products. The volatile composition of the fuel is determined by the overall volatile yield composition, as discussed in Section 4.4.2. Moreover, the volatile composition predicted by the CRECK-S model is further reduced to match the available gas-phase

species (e.g., larger tars are substituted by C_6H_6). The final volatile composition is given in Table 6.12. The same composition is also used for the simplified devolatilization models.

Table 6.12.: Composition of the overall volatile yield for a lignite particle under a heating rate of 80 K/ms.

H_2	H_2O	CO	CO_2	CH_4	C_6H_6
0.134	0.159	0.190	0.093	0.027	0.397

Following the procedure introduced for obtaining the volatile composition, a similar procedure was derived for char oxidation (see Section 4.4.2). The char conversion must be modeled as one global reaction to obtain a fixed composition from the gas phase's perspective. The stoichiometric coefficients $\nu_{O_{xi}}$, ν_{H_2O} , ν_{CO_2} and ν_{CO} for the released char off-gas species and the composition of the char itself C_xH_y are calculate prior to the actual simulation by using a detailed single-particle simulation representative for the investigated operating point. For this study, a simulation of a single reacting particle at a constant temperature of 1400 K has been used to determine the coefficients in Equation (4.23). All parameters are listed in Table 6.13. It follows that the char-off gas stream consist of 16 weight-% CO, 0.1 weight-% H_2O and 83.9 weight-% CO_2 .

Table 6.13.: Stoichiometric coefficients of the global char reaction for a particle oxidized at 1400 K in an atmosphere containing 27 Vol.-% O_2 and 73 Vol.-% CO_2 .

α	x	y	ν_{H_2O}	ν_{CO_2}	ν_{CO}	$\nu_{O_{xi}}$
2.703	1.0	0.0175	$8.75 \cdot 10^{-3}$	0.346	0.654	0.677

For the Baum-Street model, the released species are considered to be solely CO [163; 204]. Then, the char off-gas stream is composed of 32 weight-% CO and 68 weight-% CO_2 . Hence, a second table with a slightly different composition (i.e., no H_2O and CO_2 from the char reaction.) of the char fuel stream is generated for the simplified models.

Radiation

In this section, the radiation model introduced in Sections 2.4 and 4.5 is applied. A total of 80 directions is used to discretize the radiative transport equation. For the gas phase, the weighted sum of gray gases (WSGG) method is used for the spectral behavior. The absorption coefficients and weighting factor are taken Bordbar et al. [16]. The particle phase is assumed to be gray, i.e., its radiative properties are constant over the spectrum. The effects of radiation are presented in Appendix D. Overall, up to 200 K higher gas-phase temperatures are predicted when radiation is neglected.

6.4.3. Results and Discussion

Before an in-depth comparison of the various approaches previously discussed is provided, the main characteristics for the investigated operating point is discussed using mean and instantaneous contour plots. These are depicted in Figure 6.31 for the axial velocity, temperature, and both mixture fractions for the CRECK-S model on the fine grid. The axial velocity indicates the main features of the flow field inside the combustion chamber. The turbulent swirled flow

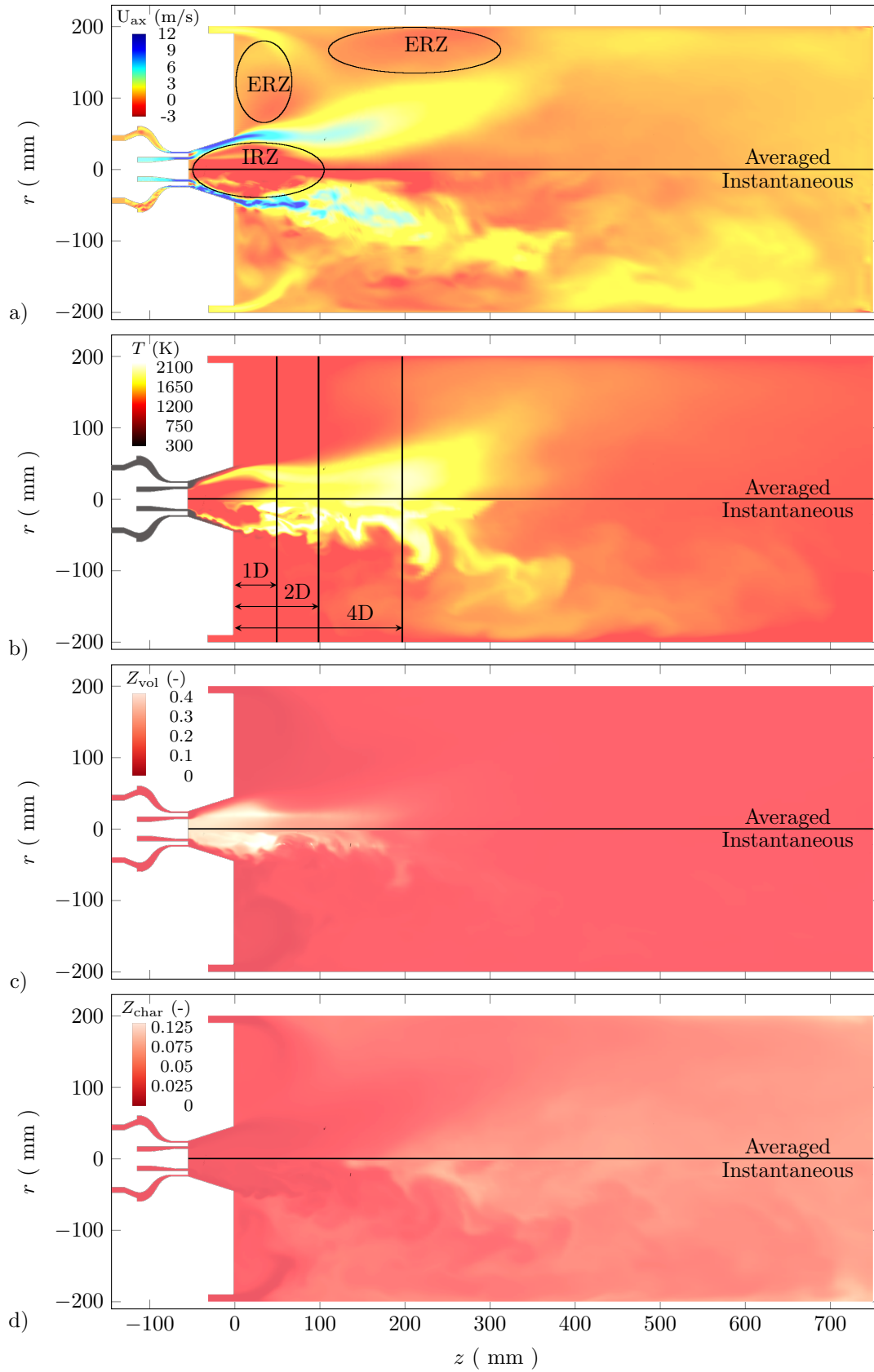


Figure 6.31.: Averaged (top) and instantaneous (bottom) gas-phase results for the CRECK-S simulation on the fine grid. Top to bottom: a) axial velocity and recirculation zones indicated by circles, b) temperature and measurement locations, c) volatile mixture fraction, and d) char off-gas mixture fraction.

of the secondary inlet forces both the primary and secondary flows towards the quarl walls, resulting in a large inner recirculation zone (IRZ) inside the quarl. Small turbulent structures can be identified in the shear layer between the fresh gases at the quarl wall and the recirculated flue gases. Further downstream, only larger structures are present. Furthermore, the velocity contours indicate two additional external recirculation zones (ERZs). One ERZ is located below the dump plane, surrounded by the flow issuing from the staging inlet and the main flow exiting the quarl. The second ERZ is situated at the wall below the staging stream. Compared to the other main flow structures, the ERZs exhibit a lower turbulence level.

The gas-phase temperature field indicates temperatures of up to 2000 K in the shear layer inside the quarl. In these regions, the oxidizer stream carrying the coal particles interacts with the hot recirculated flue gases. The turbulence in this region interacts with the reaction zone, as indicated by the strongly wrinkled flame front. Inside the IRZ, the temperature varies from 1100 K directly below the bluff body of the quarl to 1600 K at the quarl outlet.

This temperature profile results from the interaction of large particles with the hot recirculating flue gases. This observation is directly linked to the higher inertia of these larger particles, which means they do not follow the flow towards the quarl walls. A large reaction zone can be seen at the end of the IRZ, characterized by high temperatures in the center of the chamber. This is a result of the increased volatile release, facilitating the fuel supply to the flame. As a result, a temperature of approximately 2000 K is reached. Further downstream, the temperature field homogenizes, indicating the transition to the char reaction. Similar homogeneous temperature contours are present in the ERZs, suggesting that flue gases have long residence times.

Due to the recirculation of the released volatiles, the volatile mixture fraction reveals a fuel-rich mixture inside the IRZ. Within one quarl length downstream of the dump plane, the volatile mixture fraction decreases due to the mixing with the fresh oxidizer. After a sufficient oxygen level is reached inside the hot environment, the char surface reactions become more pronounced. This is evident from the char off-gas mixture fraction, which steadily increases downstream of the IRZ. Overall, the mixture fraction contours suggest that there is a distinct separation between the volatile reaction and char reaction. Comparing the influence of turbulence on the formation of the mixture fraction fields, one sees different structures depending on the location. The strong effect of turbulence on mixing inside the quarl for the volatile mixture fraction becomes apparent in the instantaneous field. On the other hand, interactions with the larger turbulent scales downstream of the IRZ are noticeable for the char mixture fraction. Furthermore, the mixture fractions suggest that the gas in the ERZs mostly consists of the oxidizer from the coflow. Hence, only few flue gases are transported to this region.

6.4.3.1. Validation

The averaged gas phase velocities from the simulations for all three model combinations are compared against the available measurements in Figure 6.32. Although coal particles are used as flow tracers, the comparison is carried out with the gas phase velocities. Only minor deviations in regions of large velocity gradients or locations with predominantly large particles occur between particle and gas-phase velocities for the given particle size distribution. Therefore, the use of gas-phase velocities is justifiable for the validation. The flow structures discussed previously are apparent. High axial and tangential velocities at the first measurement location illustrate the strongly swirled flow issuing from the quarl. Moreover, the recirculation zone indicated by negative axial velocities is visible in the center. Further downstream, the initially high velocities decrease significantly, indicating the end of the IRZ.

At the first location of 0.5D, both the strongly swirled flow and the central recirculation

are apparent in both simulations and experiments. However, slight discrepancies are visible at the axial velocity peak. An inside shift in the experimental axial velocity peak is noticeable. A slight asymmetry of the measurement can explain this deviation. Following the estimation of the experimental paper [272], a conservative estimation of the LDA measurement uncertainty is in the order of 7% of the measured velocity. Although flow fields are assumed to be axisymmetric, the experimental data revealed slight asymmetries, which amount to a maximum difference of up to 10% measured at symmetrically opposite points. The reasons for the asymmetry in such complex systems cannot be readily determined since several effects and their superposition can lead to deviations from axisymmetric profiles. For example, the sticking of hot particles to walls might locally influence the stabilization mechanisms, or a not perfectly located bluff body in the

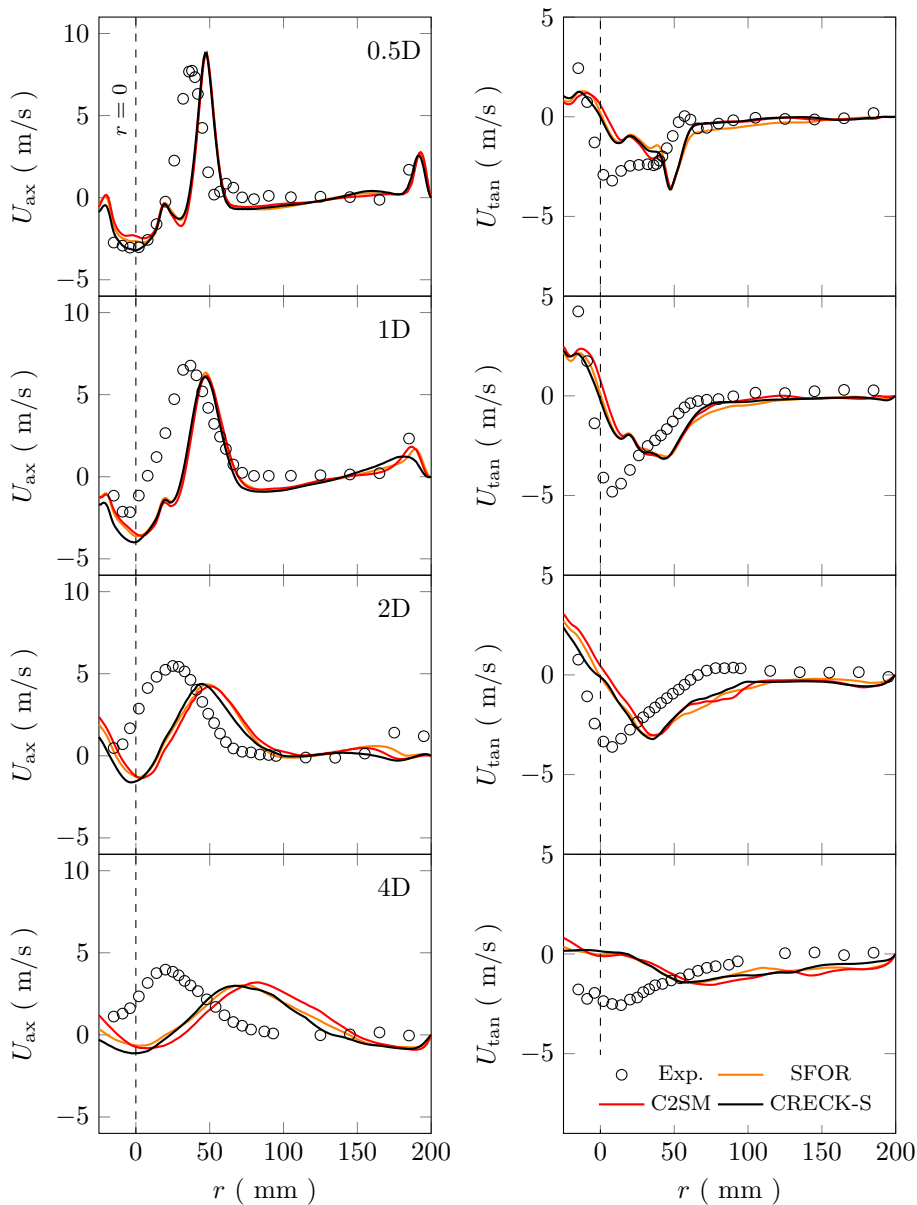


Figure 6.32.: Comparison of mean axial velocity (left) and mean tangential velocity (right) profiles determined by experiment (symbols) and simulation (lines) below the quarl for different axial heights. The vertical dashed line indicates the location of the center line ($r = 0$ mm).

quarl region leads to slightly different inflow conditions. Such effects are not represented by the LES and their inclusion is very challenging. The axial velocity amplitude matches well for the IRZ but shows signs of a slight over-prediction. Since coal particles are used as tracers, a slight slip between the particles and gas phase in these locations caused by large velocity gradients might explain these deviations. With respect to the swirling velocity, again taking into account the not perfectly axisymmetric measurements (indicated by the non-zero swirling velocity in the center), reasonable agreement with the simulations is found. For increasing axial distances, the simulations correctly predict the collapse of the IRZ. However, the previously discussed shift in the experiments towards the domain center remains. Furthermore, the experiments indicate that the axial velocity peak shifts slightly towards the center, whereas the simulation predicts an outward shift.

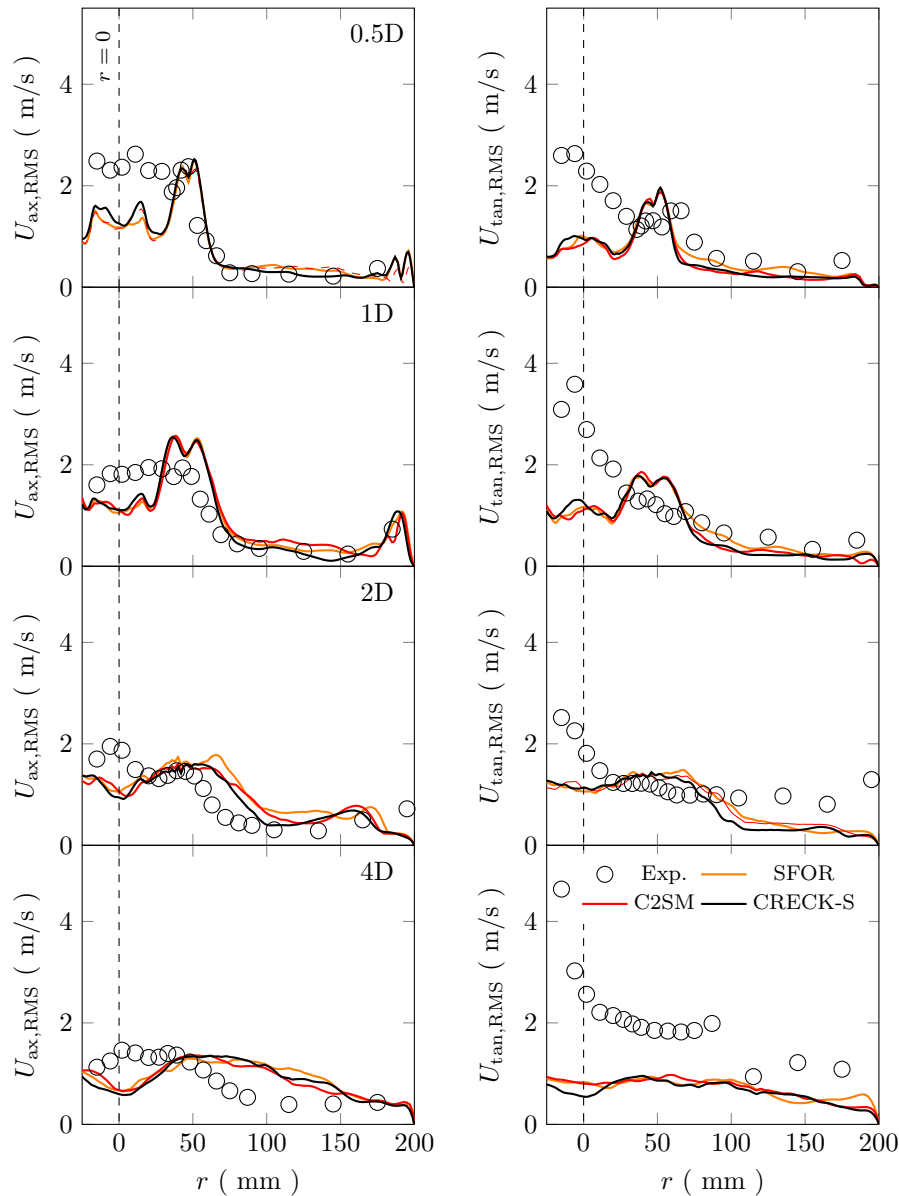


Figure 6.33.: Comparison of mean axial velocity RMS profiles (left) and mean tangential velocity RMS profiles (right) profiles determined experimentally (symbols) and by simulation (lines) below the quarl for different axial heights. The vertical dashed line indicates the location of the center line ($r = 0$ mm).

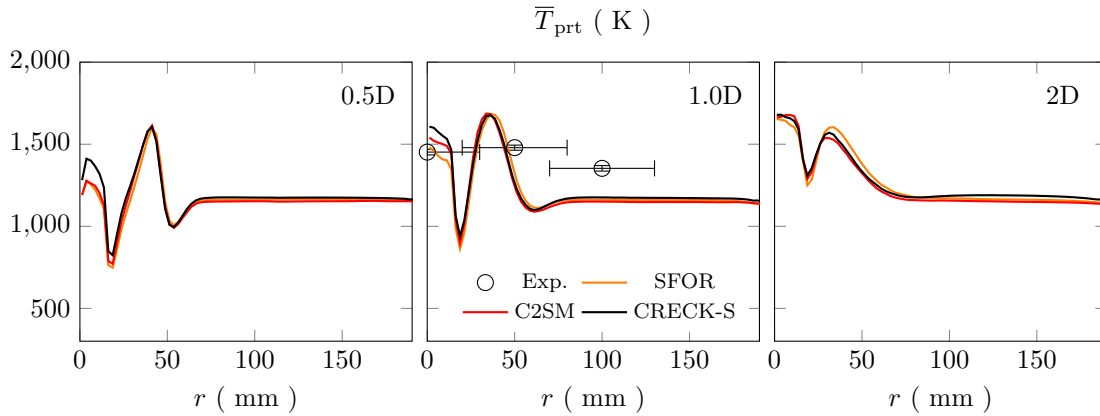


Figure 6.34.: Comparison of particle temperatures found in experiments (symbols with error bars) and simulations (lines) for different axial distances below the dump plane.

Considering these difficulties in measuring and the resulting experimental uncertainties (7% LDA measurement uncertainty + 10% shift due to asymmetry), the agreement between experimental data and simulations is favorable. Overall, the most considerable deviations result from the non-axisymmetric measurements.

No significant differences are found when comparing the three different model combinations. Hence, the solid fuel kinetics model has a minor influence on the velocity in complex swirl flows. This result agrees with the observations reported by Rieth et al. [200] for devolatilization kinetics in turbulent jet flows. Similar trends hold for the coarse grid, which, for the sake of brevity, are not shown here (See Appendix C).

Figure 6.33 illustrates the comparison of the predicted RMS velocities and the experimental values. For all axial locations, the amplitude of maximum fluctuations is similar and the simulation only underestimates the tangential fluctuations for increased axial distance from the burner. In the domain center especially, the simulations underpredict the RMS values for the axial and tangential velocity. However, for increased axial distances, an inward shift of the peak fluctuations of the experiments is apparent. As discussed in the previous section, these deviations between the experiments and simulations are likely caused by the non-axisymmetric data determined in the measurement. Again, the different solid fuel models do not show a significant difference in terms of velocity RMS profiles.

Local particle temperatures measured by a cooled background probe are depicted in Figure 6.34. Similar temperature levels for the simulation and the experiment are visible inside of the IRZ. For the measurement point outside of the IRZ, the simulations underpredict the particle temperature. The simulation indicates two temperature peaks. One is located in the center of the domain, where the hot recirculated flue gases provide heat for the particles. The second peak further from the center indicates the flame position. At 0.5 D and 1 D, two negative temperature lows are apparent. The outer low is caused by the cold particle stream entering the combustion chamber without interacting with the flame, whereas the low inside of the IRZ is induced by massive particles with large thermal inertia. Note that this low might be overpredicted by the point-particle method employed, since only averaged particle temperatures are calculated. In contrast, the measurements provide particle surface temperatures. Due to the measurements' large probe volume, the substantial temperature variations are not resolvable in the experiment. All the solid fuel kinetics used show similar results, indicating that the particle temperature evolution close to the burner is not significantly influenced by solid fuel kinetics.

Figure 6.35 shows the profiles for the mol fractions of O_2 and H_2O . For the comparison,

only measurements for H_2O are available. A high H_2O molar fraction can be observed at the center of the chamber, close to the quartz exit. The rich volatile gas mixture inside the IRZ zone causes such high values of this kind. Further downstream, a more uniform H_2O molar fraction can be observed, with good agreement between the simulation and experiment. With respect to H_2O , slight deviations between the different models can be perceived. In the case of the O_2 molar fraction, more considerable differences are apparent. For regions close to the burner head, both simplified models (SFOR-BS, C2SM-BS) predict somewhat lower oxygen fractions. At the downstream locations with more homogenous O_2 profiles, differences can also be observed over large radial segments, indicating that the solid fuel kinetics influence the overall conversion process. In the following section, the differences between the models are analyzed in detail.

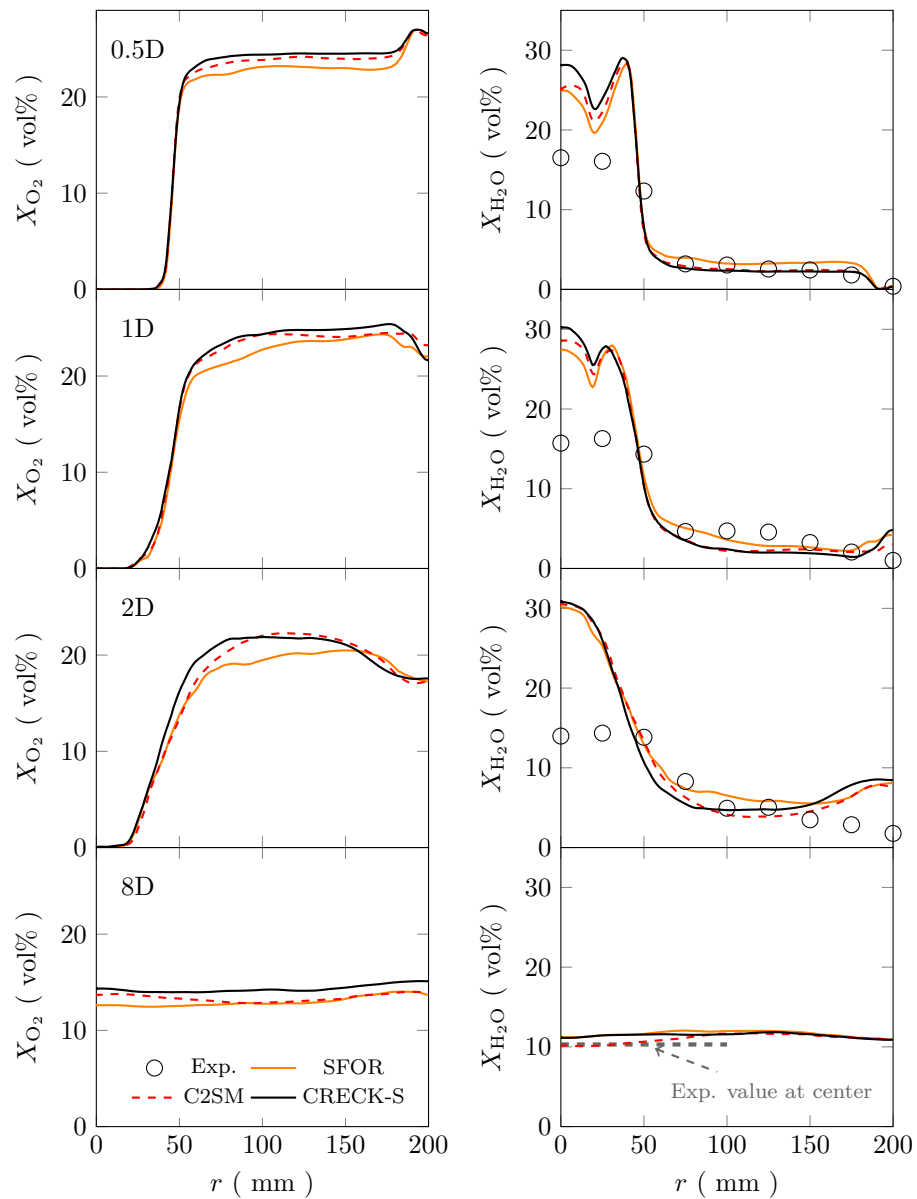


Figure 6.35.: Comparison of species molar fraction of O_2 and H_2O found in experiments (symbols only H_2O) and simulations (lines) for different axial distances below the dump plane.

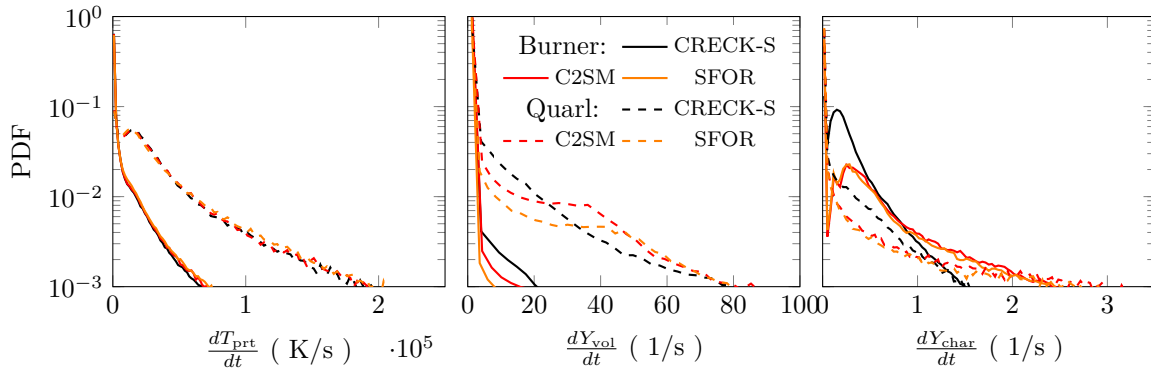


Figure 6.36.: PDFs of particle heating rates (left), volatile release rates (middle), and char release rates (right) inside the full burner (solid lines) and the quarl region (dashed lines).

6.4.3.2. Assessment of the Effects of Solid Fuel Kinetics

To compare the effect of solid fuel kinetic modeling, Figure 6.36 illustrates the PDF of the particle heating rate, devolatilization rate, and char conversion rate. To differentiate between the solid fuel kinetics inside the quarl region and those in the entire combustion chamber, the PDF is calculated by conditioning the particles extracted on the corresponding regions. Significant differences can be seen when comparing the heating rates inside the quarl and the combustion chamber. Inside the quarl, a broad distribution of rates of up to $2 \cdot 10^5$ K/s is apparent. Examining the entire combustion chamber, a narrower distribution is seen since most particles have reached equilibrium with the surrounding gas phase. Comparing the different models, the heating rate PDF exhibits only a marginal difference. This is interesting to note, particularly since the devolatilization rates exhibit some deviations. Inside the quarl, the devolatilization rate PDF width is similar for all models. However, the CRECK-S model reports higher counts at low devolatilization rates, whereas this trend shifts at higher rates. For the devolatilization rate PDF throughout the entire combustion chamber, the CRECK-S model shows a broader distribution of the heating rates, indicating a somewhat slower release. The most striking difference between the models is seen for the char release rate. The CRECK-S model predicts a significantly narrower PDF with a higher peak at low rates compared to the simplified models. This observation holds for both the entire chamber and the quarl region. Due to the minor influence of char in the quarl region, as evident from the char mixture fraction contour in Figure 6.31, the influence of these differences can be considered negligible. On the other hand, the difference may influence the gas phase for the entire chamber, a possibility which will be further analyzed below.

The observed differences are further evaluated in Figure 6.37 by means of scatter plots. Here, the devolatilization process is separated from the subsequent char reaction, i.e., only particles that have not undergone any char conversion are seen. When comparing the three models, apparent differences can be seen in the scattering behavior. For the CRECK-S model, a narrow distribution up to a release of 30% of the volatiles is observable. At approximately 35% released volatiles, a broad scattering indicates a slower volatile release, i.e., particles stay for a prolonged time in this state, increasing the time of interaction with the flow. Subsequently, a second release phase follows until the total volatile yield is released. This type of two-stage volatile release is well known in the literature [51; 256]. However, this release profile is challenging to capture with simplified models. Therefore, Wang et al. [256] very recently proposed an extension of the C2SM model to capture these effects better. Comparing CRECK-S to the simplified devolatilization models, striking differences are apparent. Both show a relatively broad distribution at the

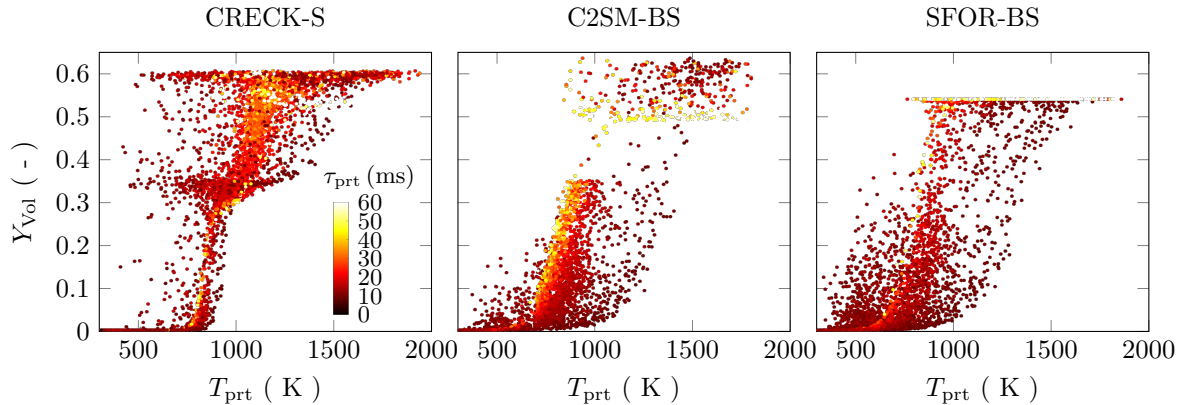


Figure 6.37.: Scatter plot of the particle phase: volatile yield vs. particle temperature with colors representing particle residence time. Left: CRECK-S. Middle: C2SM-BS. Right: SFOR-BS.

beginning of the devolatilization phase, indicating a slow release. This is followed by a rapid release of volatiles, which can be identified by the low number of scatter points in the upper half of the plots. In the end, both models reach the maximum yield. However, the SFOR model cannot take into account the possibility of varying volatile yields resulting in the same volatile yield independent of the particle history. Comparing the final volatile yield between CRECK-S and C2SM, the C2SM shows a somewhat larger yield distribution. In terms of the particle residence time, it is seen that long particle residence times, i.e., low heating rates, result in a low volatile yield. This effect is caused by the increased time for crosslinking reactions. The differences between the models result from a slight overprediction of the heating rate dependency of the C2SM model. Overall, the correlation between the particle temperature and volatile yield is much higher for the CRECK-S than for C2SM and SFOR. In the SFOR, the particle temperature is the only input parameter that can be used to obtain the devolatilization rate. Hence, a large scatter in volatile yield can be observed for a specific temperature that the particle has reached. The volatile release for CRECK-S bases on a multi-step reaction mechanism, which also incorporates the composition of the particle. The particles heating history and the current temperature are also taken into account, which apparently results in particles behaving more alike in volatile yield-temperature space. Similar observations were made by Rieth et al. [200].

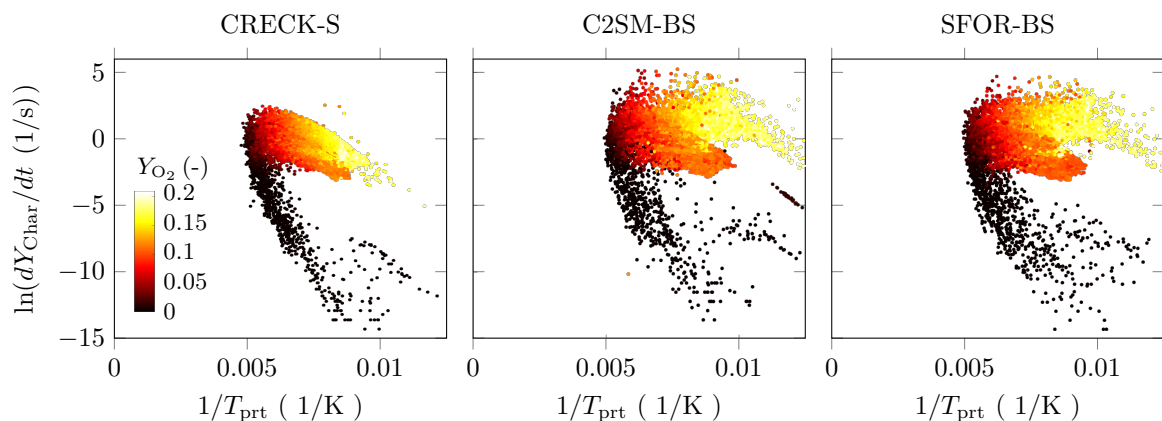


Figure 6.38.: Scatter plot of the particle phase: char reaction rate vs. inverse temperature colored by the oxygen fraction at the particle position. Left: CRECK-S. Middle: C2SM-BS. Right: SFOR-BS.

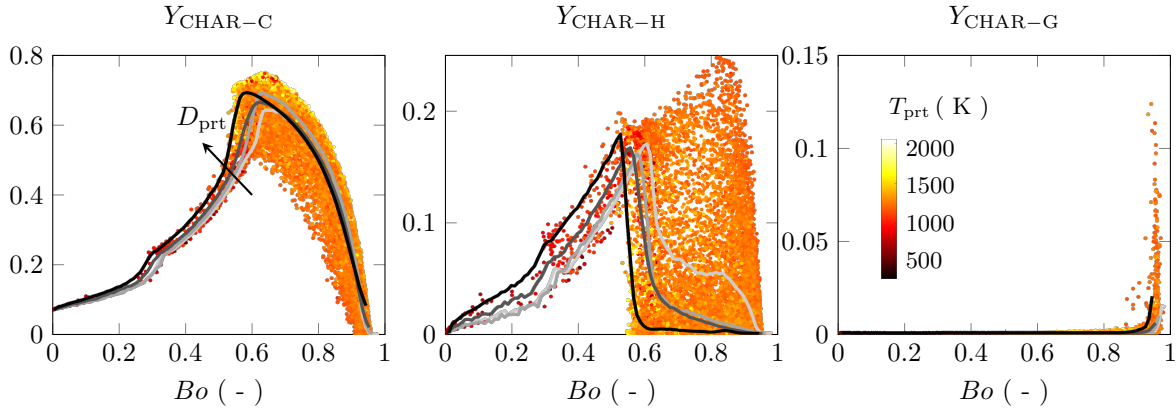


Figure 6.39.: Scatter plot for the particle char fractions vs. particle burnout for the CRECK-S simulation. Left: CHAR-C. Center: fast-reacting CHAR-H. Right: slow-reacting CHAR-G. Lines illustrate the averaged fraction for the particle groups in Table 6.14. From light grey representing class 1 to black representing class 4.

Next, the model effect on the char conversion is analyzed by the scatter plots illustrated in Figure 6.38. For the CRECK-S model, the scattering forms a curved shape, which is, however, different from the standard curve of the char regime diagram [86]. The main reason for these deviations is the strongly varying oxygen content in the burner, as indicated by the color code. As expected, the initial increase of the particle temperature leads to a linear increase in the conversion rate. However, the surrounding oxygen partial pressure decreases rapidly in the real chamber, resulting in a decline in the char conversion rate. Comparing the three models, especially under oxygen-rich conditions, significantly different rates are observed. In accordance with Figure 6.36, the CRECK-S model predicts lower conversion rates compared to the simplified Baum–Street model. Furthermore, the reaction starts at slightly higher temperatures (note that the inverse temperature is used). With respect to the scattering range, the simplified model exhibits a more substantial variation than the CRECK-S model.

Table 6.14.: Particle classified into different size classes for particle histories.

Class	Particle size
1	$D_{\text{prt}} \leq 25 \mu\text{m}$
2	$25 \mu\text{m} < D_{\text{prt}} \leq 50 \mu\text{m}$
3	$50 \mu\text{m} < D_{\text{prt}} \leq 100 \mu\text{m}$
4	$100 \mu\text{m} < D_{\text{prt}}$

Particles are grouped as in Table 6.14 to study the effect of the solid fuel modeling for different particle sizes. The different behavior concerning the char conversion of the models can be attributed to two possible reasons. The first reason could be that the char structure predicted by the CRECK-S model is strongly affected by the preceding devolatilization step (see thermal annealing in Section 4.2.1), which is not accounted for by the simple model. The second reason might be that the conditions of the experimental setup used to fit the parameters of the Baum–Street model are not representative of the investigated conditions. To investigate the former effect, Figure 6.39 depicts scatterplots of the different CRECK-S chars (e.g., highly reactive CHAR-H, initial char CHAR-C, and less reactive CHAR-G) over the particle burnout Bo . Additionally, the lines indicated the different particle classes. CHAR-C represents the

initial char (as evident from the initial fraction at zero burnout). During devolatilization, the CHAR-C fraction inside the particle increases by formation due to devolatilization reactions and the overall mass loss. During devolatilization, also notable amounts of the highly reactive CHAR-H are formed. However, as indicated by averaged lines for the particle classes, most of the CHAR-H is directly oxidized, and only a few particles retain significant amounts until complete burnout. Only small amounts of the less reactive CHAR-G, the main product of char annealing, are formed throughout the particle conversion period. The reason for this is most likely the too low particle temperature during the devolatilization process. Hence, char annealing does not affect the char conversion in the CRECK-S model.

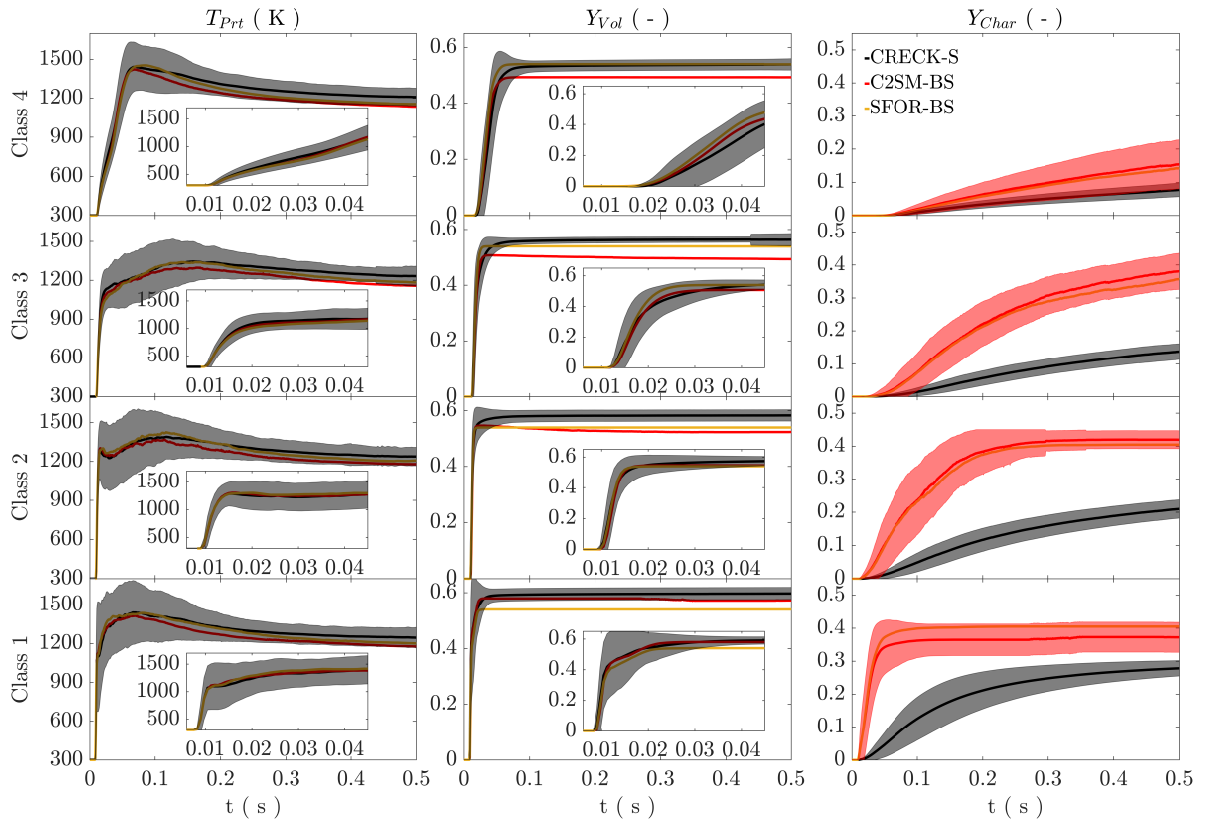


Figure 6.40.: Particle histories with respect to particle temperature (left), particle volatile yield (center) and particle char yield (right). Each row of the figure corresponds to one particle class specified in Table 6.14. The lines indicate the mean values. The variation represented by one standard deviation is depicted by the gray shading (for a better overview, the variation is only shown for the CRECK-S model if there is an overlap exist).

Figure 6.40 depicts the averaged particle histories of temperature, volatile yield, and char yield for each particle class. For the averaging process, 1000 individual particle histories are employed to obtain a statistically independent result. All particles, regardless of their size, experience a rapid heat up when entering the combustion chamber. However, concerning the slope of the temperature increase, slight differences are apparent. Due to their large thermal inertia, Class 4 particles heat up more slowly than the other particle classes. Although Class 4 particles have the lowest heating rate, these particles reach the highest temperature. The reason is that the particles do not follow the flow well, resulting in direct interaction with the recirculated flue gases and the main flame below the quarl. After traveling past the volatile reaction zone, all particles

strive towards a homogeneous temperature of approximately 1300 K. The volatile release follows the temperature well, which is in accordance with Figure 6.37. All models predict a similar profile for the volatile yield for the high heating rate conditions in Classes 1 and 2. However, SFOR, as discussed previously, cannot predict the final volatile yield correctly. Interestingly, the C2SM underpredicts the volatile yield for lower heating rates (Class 2-4). Thus, only some of the complex physical phenomena and their interactions determining the overall yield can be predicted correctly by the C2SM model. Furthermore, both simplified models overpredict the volatile release rate for Class 4 particles. The history of the char release again shows the most striking differences. While the Baum–Street model only slightly overestimates the conversion of large particles, all other classes are predicted to release almost twice as fast. One reason for these discrepancies is that the model coefficients adopted from an experiment always apply only to a specific operating range. However, the wide range of conditions to which a particle is exposed in the combustion chamber can lead to significant deviations from the conditions used in the experiment, resulting in deviating release rates.

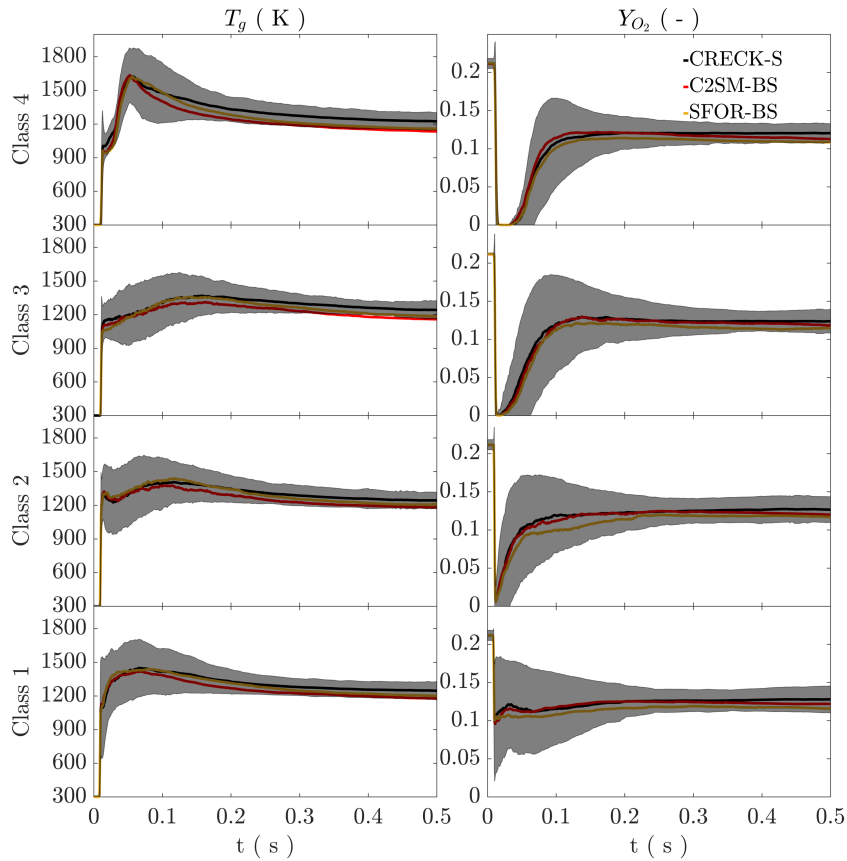


Figure 6.41.: Surrounding conditions the particles are exposed to on their path with regard to gas phase temperature and O_2 mass fraction. Each row of the figure corresponds to one particle class specified in Table 6.14. The lines indicate the mean values. The variation represented by one standard deviation is depicted by the gray shading (for a better overview, this is only shown for CRECK-S).

Figure 6.41 depicts the gas phase temperature and the oxygen mass fraction at the particle location. These two properties determine the particle conversion. For Classes 1, 2, and 3, the gas-phase temperature follows a similar course. After a rapid increase at the beginning, the temperature reaches a constant level of approximately 1300 K. The level is similar for Class 4; however, the maximum temperature at the particle location is significantly higher than for

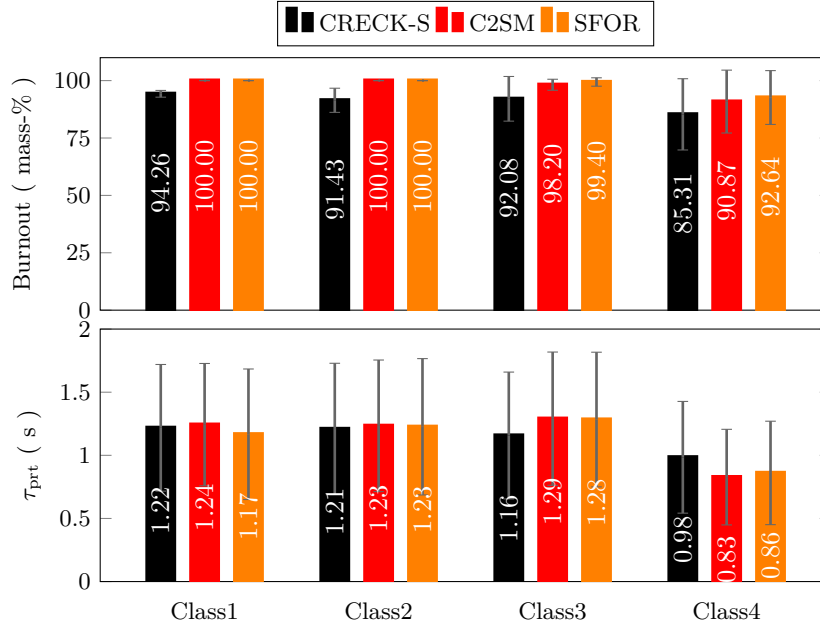


Figure 6.42.: Bar plot of particle properties at the outlet of the domain. The classes are specified in Table 6.14. Top: particle burnout Bo . Bottom: total residence time τ_{prt} . The bars indicate the standard deviation for each class.

other classes. This can be explained by the different particle trajectories, as discussed previously. With regard to the oxygen mass fraction at the particle position, Classes 2, 3, and 4 show a similar trend. The particles partially enter IRZ directly after entering the chamber, where the oxygen fraction approaches zero. Downstream of the quarl, where the staging stream supplies additional oxygen, the oxygen partial pressure reaches a constant value. The smallest particles behave differently. Due to their trajectory, which follows the flow directly towards the wall, these particles are primarily in oxygen-rich regions. The differences between the modeling approaches are not significant. Hence, the different predicted particle conversions previously discussed have a limited influence on the local gas phase.

Figure 6.42 illustrates the particle burnout (Bo) and particle residence time (τ_{prt}) at the outlet of the domain 750 mm below the quarl. Similarly to previous observations, in the CRECK-S model shows a lower char conversion at the outlet. While the Baum–Street model predicts complete conversion for the first two classes, some char is left in the case of CRECK-S model. Since the residence times of the particles are very similar in all cases, the different conversion mechanisms are the main reason for these deviations. For Classes 3 and 4, the Baum–Street model also predict that the coal is not fully converted. However, particle burnout is more advanced than for the CRECK-S model.

To investigate how the particles affect the gas phase, Figure 6.43 depicts instantaneous scatter plots of gas-phase data (every 10th cell value randomly selected from the total of around 3 M). The top row of Figure 6.43 shows the mixture fraction sum Z_1 vs. the gas-phase temperature colored by the mixture fraction ratio Z_2 for all three model combinations. The maximum temperature of approximately 1900 K corresponds to the maximum flame temperature, which is located at the stoichiometric mixture fraction of the volatiles (≈ 0.1) and is similar for all cases. For rich volatile mixtures, temperatures around 1200 K can be seen for all cases. However, the maximum value of the mixture fraction sum is higher for both simplified models, indicating a more rapid devolatilization rate, which is consistent with the observations made in Figure

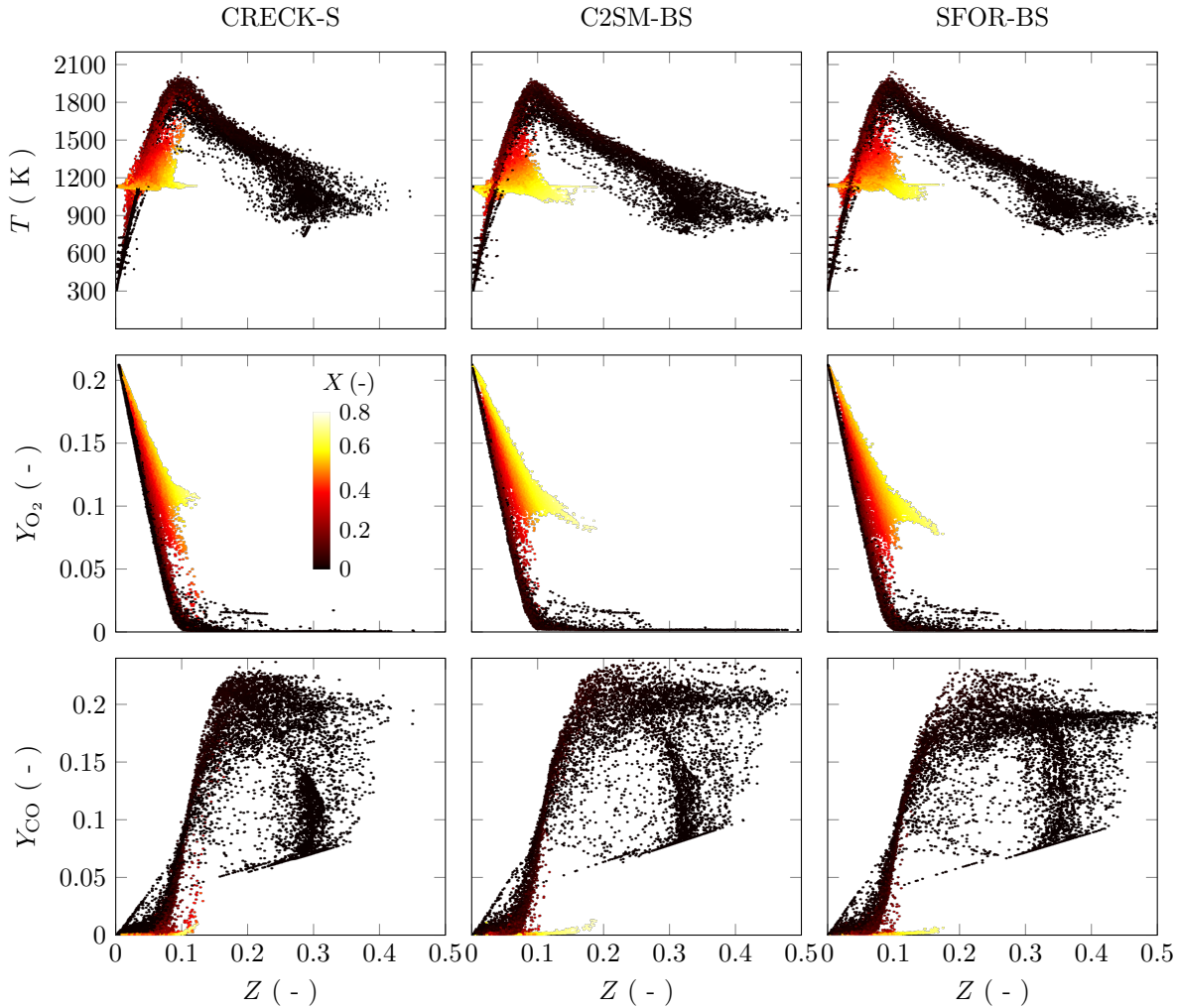


Figure 6.43.: Instantaneous scatter plots from Eulerian data. Top: gas temperature vs. mixture fraction sum Z_1 colored by mixture fraction ratio Z_2 . Middle: oxygen mass fraction Y_{O_2} vs. mixture fraction sum Z_1 colored by mixture fraction ratio Z_2 . Bottom: Y_{CO} vs. mixture fraction sum Z_1 colored by mixture fraction ratio Z_2 .

6.36. Similarly, compositions rich in the char off-gas mixture fraction are characterized by temperatures around 1500 K. Since volatile and char combustion are consecutive processes, as indicated in Figure 6.40, the rich volatile flame ($Z_1 > 0.3$) is first diluted in the staging oxidizer before char oxidation takes place. In this process, the mixture is slowly enriched again to the final state with $Z \approx 0.15$ and $Z_2 \approx 0.6$. Comparing the models, differences are observed in this region. The previously discussed increased char reaction rate of the Baum–Street model results in a slight increase in the mixture fraction sum at high mixture fraction ratios.

For the oxygen mass fraction at the particle position in the middle row of Figure 6.43, increasing Z_1 leads to a rapid decrease in oxygen until no oxygen is present at $Z_1 > 0.1$. Comparing the oxygen decrease of volatile reaction ($Z_2 \approx 0$) and char reactions ($Z_2 > 0.6$), a more substantial oxygen decrease is apparent for the volatile reaction. The reason for this is the higher stoichiometric oxygen demand of the volatile gas. Furthermore, compositions consisting primarily of char are mostly lean and contain oxygen. The higher char conversion rate predicted by the simplified models results in a higher sum of mixture fractions with lower oxygen fractions.

The bottom row of Figure 6.43 shows the CO mass fraction vs. the mixture fraction sum Z_1 .

For the volatile flame, high CO fractions are apparent. By contrast, mixtures with a high char off-gas content generally feature low CO mass fractions. Although the char off-gas has a high CO content (in the case of the Baum–Street model, it consists solely of CO), the CO directly reacts with the surrounding oxygen.

6.4.4. Section Summary

A LES study of self-sustained pulverized coal combustion under oxy-fuel conditions was performed using directly coupled solid fuel kinetics embedded in an Euler–Lagrange framework. For the description of the turbulent reacting gas phase, a five-dimensional FPV model was used. The five parameters take into account the volatile and char off-gas mixing, reaction progress, heat losses, and subgrid-scale turbulence chemistry interaction. The model was applied to the adapted test furnace at WSA-RWTH Aachen, where an oxy-fuel atmosphere (27 vol% oxygen) was studied. Good agreement between the simulations and experiments was found for the available velocity fields, which tend to agree better at locations close to the burner. In contrast, an outward shift in the velocity peaks was found for locations further downstream in the chamber. In addition, the available particle temperature measurements showed good agreement with the simulations.

Additional simulations are performed to assess the sensitivity of the state-of-the-art simplified particle conversion models. With regards to mean velocities and particle temperatures, only minor differences were found. In terms of the particle conversion, small differences are apparent for devolatilization and significant differences with respect to char conversion. Detailed analysis reveals that taking char kinetics from experiments with non-representative conditions might lead to wrong conversion behavior. Nevertheless, the gas-phase properties were found not to be strongly affected. This holds both for the ambient conditions at the particle position averaged over several particle histories and for the instantaneous composition space.

Overall, all model combinations provided consistent results for the complex coupled physical processes in a self-sustained pulverized coal combustion chamber operated at oxy-fuel conditions. Hence, simplified kinetics might produce correct results under the constraint that the correct conditions are used to fit their coefficients. However, this constraint does not apply to the directly coupled CRECK-S flamelet model and thus improves the predictive capabilities of the overall modeling framework.

To assess the modeling framework further, it should be applied to different operating conditions in future works, including different oxygen partial pressures and coals from different ranks. Since also simplified models showed potential to predict PCC accurately, the uncertainty associated with their modeling parameters requires quantification in future research to ensure the predictive capabilities of such approaches.

7. Summary and Outlook

This work addresses LES of solid fuel combustion in oxy-fuel atmospheres. At this, one of the main aspects was the development of a holistic modeling framework, with a focus on the combustion process. First of all, suited modeling approaches were elaborated. The strategy chosen combines the flamelet-based chemistry tabulation and multi-step kinetics for the solid fuel conversion and detailed radiation modeling, which are individually established.

Two different flamelet-based models were further developed to perform LES for pulverized coal combustion under oxy-fuel conditions. An extension of the FGM approach, which bases on premixed flame structures, was necessary to account for the complex processes involved in solid fuel combustion. Eventually, a four-dimensional manifold was proposed to account for finite rate chemistry, mixing of volatiles and char products, and heat losses in the gas phase. Moreover, the FGM modeling approach was coupled with an artificially thickened flame approach to resolve the premixed flame structure on the numerical grid. For the description of the turbulent reacting flows with a dominating non-premixed flame structure, a five-dimension FPV model was developed. Here, four of the five parameters account for the volatile and char off-gas mixing, reaction progress, heat losses in the gas phase. The last dimension represents subgrid turbulence chemistry interactions, for which a presumed PDF model is used. The required subgrid variance in the context of solid fuel combustion is obtained from an additional transport equation.

Besides using simplified kinetics to describe the solid fuel conversion process, particular emphasis was put on including more detailed solid fuel kinetics into larger-scale simulations. For this purpose, a recently introduced seamless model for devolatilization and char oxidation was extended for the application in an Euler-Lagrange point-particle framework. Subsequently, the extended solid fuel model was coupled to the tabulated chemistry description of the gas phase. The developed modeling strategies were applied to various configurations ranging from single-particle and particle group combustion up to a pilot-scale combustion chamber. This enables a seamless validation of the modeling framework.

First, the transition from single-particle to particle group ignition and combustion was simulated in a laminar flow reactor operated with a premixed flame. This configuration allows investigations of devolatilization and ignition of solid fuel particles under realistic heating rates. The trend of increased ignition delay times for higher particle densities showed good agreement with the experimental findings. Furthermore, the evolution of the volatile flame from spherical flames around single particles towards a conical flame shape with a suppressed reaction at the tip for high particle densities was validated with experimental data. Overall, the mixture and flame formation was well reproduced and explained by the applied modeling approach.

Next, the complexity level was increased by considering an optical accessible laboratory-scale chamber, in which solid fuel combustion is stabilized and assisted by a swirled methane flame. Within this configuration, different operating points with successively increasing complexity were investigated. First, in a single-phase non-reactive operating point, the appropriateness of boundary conditions to reproduce the main characteristics of the turbulent flow were demonstrated. Subsequently, the complexity was increased by adding a flammable methane mixture to show the model's potential to reproduce single-phase flames under oxy-fuel atmospheres. For the single-phase reactive operating point, both the main reaction zone and the velocity fields

were in good agreement with experimental results. Finally, two-phase reactive cases were considered, where coal particles were added to the assisting methane flame. Two different thermal loads, one where the thermal power from coal equals the assisting gas flame and one where the solid phase supplies approximately one-quarter of the nominal thermal power, were investigated. The methane flame remained the dominant stabilizer for low particle loads, whereas the reaction zone was significantly broader for higher loads. The model reproduced the essential flow characteristics of both operating points well, with minor deviations in regions of high particle density, which were partially attributed to the challenging evaluation of the measurement data.

The final configuration considered was a self-sustaining pulverized coal combustion chamber that was operated under atmospheric and oxy-fuel conditions. At this configuration, the full complexity of the model was required. Reasonable agreement between simulations and experiments was found for the available velocity fields. Comparing the three investigated operating conditions, no significant differences were revealed in velocities, while the different gas-phase temperatures significantly influenced particle heating. Hence, particle trajectories exhibited differences at the beginning of the conversion phase. Interestingly, at the end of the chamber, the overall conversion of the particles was similar, although the particle temperatures varied substantially between the different atmospheres. This observation was explained by the similar low partial pressure of oxygen in all investigated cases.

Finally, the model was extended by detailed solid fuel kinetics and applied to a slightly adapted combustion chamber under an oxy-fuel atmosphere. Good agreement between simulations and experiments was found for the available velocity fields, which tend to better agree at locations close to the burner. In contrast, an outward shift of the velocity peaks was found for locations further downstream in the chamber. The available particle temperatures agreed well. Furthermore, the accuracy of the state-of-the-art simplified particle conversion models was assessed using the detailed reference simulation. With regards to mean velocities and particle temperatures, only minor differences were apparent. The particle conversion showed minor differences for devolatilization but significant differences with respect to char conversion. Detailed analysis revealed that taking char kinetics from experiments with non-representative conditions might lead to wrong conversion behavior. Nevertheless, the gas-phase properties were found to be not strongly affected. In this study, coupling detailed gas-phase kinetics by means of flamelet-based tabulation approaches with detailed solid fuel kinetics for the entire particle conversion process in a LES framework was performed for the first time to the authors' knowledge.

Overall, the coupled numerical models provided consistent results for the complex physical process in pulverized coal combustion configurations of various sizes for air and oxy-fuel atmospheres. One of the key findings of this work was that large-eddy simulation, in conjunction with flamelet-based tabulated chemistry, detailed solid fuel kinetics, and radiation modeling, enables the prediction of the combustion of pulverized solid fuels under oxy-fuel conditions at various scales.

In future works, the overall framework might be extended by other models accounting for additional physical effects. From a particle perspective, two additional phenomena might occur during pulverized solid fuel combustion. Firstly, the consideration of particle fragmentation might increase the predictive capacity even further. Secondly, the interaction of particles with walls may lead to slagging, influencing the heat transfer to the walls. However, only highly empirical correlations are available for both effects, indicating the necessity of further research for predictive models. Furthermore, pollutants and soot formation might be of interest for the burner design. Concerning the former, research is currently being carried out, particularly on the treatment of pollutants by the flamelet-model [263]. However, the influence of detailed solid fuel kinetics for predicting pollutants in CFD is still an open issue. In particular, the interaction

between solid fuel kinetics and gas-phase kinetics should be investigated in the future. With respect to soot formation, only simplified models are available. However, due to the severe effect of soot on the heat transfer in combustion chambers, more precise models are desirable. Since soot is mainly formed during the secondary pyrolysis of tars, the influence of detailed solid fuel kinetics on soot formation requires further research.

This work showed that the proposed models possess a high fidelity. However, computational costs are also increased. Therefore, possible reduction strategies should be evaluated. Among these, machine learning based approaches have a high potential for including detailed solid fuel kinetics into CFD simulation [39]. Reactor network models are a different possibility to include the more detailed kinetics for both gas phase and particle chemistry into the simulations. These models rely on a very simplified description of the flow field by employing simple 0D and 1D reactors. Hence, these models can be seen as a complementary tool for expensive LES to analyze certain chemical effects such as pollutant formation in more detail. However, up to date, these models are only available for single-phase combustion [237].

In addition, further solid fuels should be considered in the future. In the context of oxy-fuel combustion, biomass is an attractive alternative solid fuel due to its potential for negative CO₂ emission. The extension of the proposed modeling strategy to incorporate biomass should be straightforward. However, a similar seamless validation as performed in this thesis should be conducted for the even more complex fuel biomass to ensure the predictive capabilities of the modeling framework. As an alternative carbon-free chemical energy carrier for renewable energy, iron oxidation and reduction are currently actively researched. The developed methodology for heterogeneous surface reaction could also be applicable to iron particles, which could be investigated in the future.

Bibliography

- [1] A. H. Al-Abbas, J. Naser, and D. Dodds. CFD modelling of air-fired and oxy-fuel combustion of lignite in a 100 KW furnace. *Fuel*, 90(5):1778–1795, 2011.
- [2] J. Anderson. *Fundamentals of Aerodynamics*. McGraw-Hill, New York, USA, 2007.
- [3] K. Andersson, R. Johansson, F. Johnsson, and B. Leckner. Radiation Intensity of Propane-Fired Oxy-Fuel Flames: Implications for Soot Formation. *Energy & Fuels*, 22(3):1535–1541, 2008.
- [4] C. Angelberger, D. Veynante, F. Egolfopoulos, and T. Poinso. Large eddy simulations of combustion instabilities in premixed flames. In *Proceedings of the Summer Program 1998, Center for Turbulence Research*, pages 61–82, 1998.
- [5] D. B. Anthony and J. B. Howard. Coal devolatilization and hydrogastification, 1976.
- [6] S. V. Apte, K. Mahesh, and T. Lundgren. Accounting for finite-size effects in simulations of disperse particle-laden flows. *International Journal of Multiphase Flow*, 34(3):260–271, 2008.
- [7] A. Attili, P. Farmand, C. Schumann, S. Farazi, B. Böhm, T. Li, C. Geschwindner, J. Köser, A. Dreizler, and H. Pitsch. Numerical Simulations and Experiments of Ignition of Solid Particles in a Laminar Burner: Effects of Slip Velocity and Particle Swelling. *Flow, Turbulence and Combustion*, 106(2):515–531, 2021.
- [8] S. Badzioch and P. G. W. Hawksley. Kinetics of Thermal Decomposition of Pulverized Coal Particles. *Industrial & Engineering Chemistry Process Design and Development*, 9.4:521–530, 1970.
- [9] R. S. Barlow. Laser diagnostics and their interplay with computations to understand turbulent combustion. *Proceedings of the Combustion Institute*, 31(1):49–75, 2007.
- [10] M. M. Baum and P. J. Street. Predicting the Combustion Behaviour of Coal Particles. *Combustion Science and Technology*, 3(5):231–243, 1971.
- [11] L. G. Becker, H. Kosaka, B. Böhm, S. Doost, R. Knappstein, M. Habermehl, R. Kneer, J. Janicka, and A. Dreizler. Experimental investigation of flame stabilization inside the quarl of an oxyfuel swirl burner. *Fuel*, 201:124–135, 2017.
- [12] L. G. Becker, S. Pielsticker, B. Böhm, R. Kneer, and A. Dreizler. Particle dynamics in a gas assisted coal combustion chamber using advanced laser diagnostics. *Fuel*, 269:117188, 2020.
- [13] J. Bellan and K. Harstad. The details of the convective evaporation of dense and dilute clusters of drops. *International Journal of Heat and Mass Transfer*, 30(6):1083–1093, 1987.
- [14] A. A. Bhuiyan and J. Naser. Numerical modelling of oxy fuel combustion, the effect of radiative and convective heat transfer and burnout. *Fuel*, 139:268–284, 2015.

Bibliography

- [15] B. R. Bird, W. E. Stewart, and E. N. Lightfoot. *Transport Phenomena*. Wiley, New York, 2006.
- [16] M. H. Bordbar, G. Weceł, and T. Hyppänen. A line by line based weighted sum of gray gases model for inhomogeneous CO₂-H₂O mixture in oxy-fired combustion. *Combustion and Flame*, 161(9):2435–2445, 2014.
- [17] B. P. BP. Economics BP energy. In *P Energy Outlook*, 2020.
- [18] B. S. Brewster, L. L. Baxter, and L. D. Smoot. Treatment of coal devolatilization in comprehensive combustion modeling. *Energy and Fuels*, 2(4):362–370, 1988.
- [19] T. D. Butler and P. J. O'Rourke. A numerical method for two dimensional unsteady reacting flows. *Symposium (International) on Combustion*, 16(1):1503–1515, 1977.
- [20] D. Butz, S. Hartl, S. Popp, S. Walther, R. S. Barlow, C. Hasse, A. Dreizler, and D. Geyer. Local flame structure analysis in turbulent CH₄/air flames with multi-regime characteristics. *Combustion and Flame*, 210:426–438, 2019.
- [21] L. Cai, S. Kruse, D. Felsmann, and H. Pitsch. A Methane Mechanism for Oxy-Fuel Combustion: Extinction Experiments, Model Validation, and Kinetic Analysis. *Flow, Turbulence and Combustion*, 106(2):499–514, 2021.
- [22] J. R. Cash and A. H. Karp. A Variable Order Runge-Kutta Method for Initial Value Problems with Rapidly Varying Right-Hand Sides. *ACM Transactions on Mathematical Software (TOMS)*, 16.3:201–222, 1990.
- [23] F. Cavalcanti Miranda, F. di Mare, A. Sadiki, and J. Janicka. PERFORMANCE ANALYSIS OF DIFFERENT SOLVERS FOR COMPUTING THE RADIATIVE TRANSFER EQUATION IN COMPLEX GEOMETRIES USING FINITE VOLUME METHOD AND BLOCK STRUCTURED GRIDS. *Computational Thermal Sciences: An International Journal*, 9(3):269–282, 2017.
- [24] CBC. Workshop on Measurement and Simulation of Coal and Biomass Conversion. In *Proceedings*, 2019.
- [25] F. Charlette, C. Meneveau, and D. Veynante. A power-law flame wrinkling model for LES of premixed turbulent combustion Part I: non-dynamic formulation and initial tests. *Combustion and Flame*, 131(1-2):159–180, 2002.
- [26] CHEM1D. A one-dimensional laminar flame code, developed at Eindhoven University of Technology.
- [27] J. C. Chen and S. Niksa. Coal devolatilization during rapid transient heating. 1. Primary devolatilization. *Energy & Fuels*, 6(3):254–264, 1992.
- [28] L. Chen and A. F. Ghoniem. Simulation of Oxy-Coal Combustion in a 100 kWth Test Facility Using RANS and LES: A Validation Study. *Energy and Fuels*, 26(8):4783–4798, 2012.
- [29] L. Chen, S. Z. Yong, and A. F. Ghoniem. Oxy-fuel combustion of pulverized coal: Characterization, fundamentals, stabilization and CFD modeling. *Progress in Energy and Combustion Science*, 38(2):156–214, 2012.

- [30] A. J. Chorin. Numerical solution of the Navier-Stokes equations. *Mathematics of Computation*, 22(104):745–745, 1968.
- [31] K. A. Cliffe and D. A. Lever. Isothermal flow past a blowing sphere. *International Journal for Numerical Methods in Fluids*, 5(8):709–725, 1985.
- [32] P. J. Coelho. Detailed numerical simulation of radiative transfer in a nonluminous turbulent jet diffusion flame. *Combustion and Flame*, 136(4):481–492, 2004.
- [33] P. J. Coelho. Numerical simulation of the interaction between turbulence and radiation in reactive flows, 2007.
- [34] O. Colin, F. Ducros, D. Veynante, and T. Poinso. A thickened flame model for large eddy simulations of turbulent premixed combustion. *Physics of Fluids*, 12(7):1843, 2000.
- [35] C. T. Crowe, J. D. Schwarzkopf, M. Sommerfeld, and Y. Tsuji. *Multiphase Flows with Droplets and Particles*. Crc Press Inc, 2011.
- [36] C. T. Crowe, M. P. Sharma, and D. E. Stock. The Particle-Source-In Cell (PSI-CELL) Model for Gas-Droplet Flows. *Journal of Fluids Engineering*, 99(2):325–332, 1977.
- [37] A. Cuoci, A. Frassoldati, T. Faravelli, and E. Ranzi. OpenSMOKE++: An object-oriented framework for the numerical modeling of reactive systems with detailed kinetic mechanisms. *Computer Physics Communications*, 192:237–264, 2015.
- [38] P. Debiagi, G. Gentile, A. Cuoci, A. Frassoldati, E. Ranzi, and T. Faravelli. A predictive model of biochar formation and characterization. *Journal of Analytical and Applied Pyrolysis*, 134:326–335, sep 2018.
- [39] P. Debiagi, H. Nicolai, W. Han, J. Janicka, and C. Hasse. Machine learning for predictive coal combustion CFD simulations From detailed kinetics to HDMR Reduced-Order models. *Fuel*, 274:117720, 2020.
- [40] P. E. A. Debiagi, C. Pecchi, G. Gentile, A. Frassoldati, A. Cuoci, T. Faravelli, and E. Ranzi. Extractives Extend the Applicability of Multistep Kinetic Scheme of Biomass Pyrolysis. *Energy & Fuels*, 29(10):6544–6555, 2015.
- [41] E. Donskoi and D. L. McElwain. Optimization of coal pyrolysis modeling. *Combustion and Flame*, 122(3):359–367, 2000.
- [42] A. Doost, F. Ries, L. Becker, S. Bürkle, S. Wagner, V. Ebert, A. Dreizler, F. di Mare, A. Sadiki, and J. Janicka. Residence time calculations for complex swirling flow in a combustion chamber using large-eddy simulations. *Chemical Engineering Science*, 156:97–114, 2016.
- [43] L. J. Dorigon, G. Duciak, R. Brittes, F. Cassol, M. Galarça, and F. H. França. WSGG correlations based on HITEMP2010 for computation of thermal radiation in non-isothermal, non-homogeneous H₂O/CO₂ mixtures. *International Journal of Heat and Mass Transfer*, 64:863–873, 2013.
- [44] L. Dressler, F. L. S. Filho, F. Ries, H. Nicolai, J. Janicka, and A. Sadiki. Numerical Prediction of Turbulent Spray Flame Characteristics Using the Filtered Eulerian Stochastic Field Approach Coupled to Tabulated Chemistry. *Fluids 2021, Vol. 6, Page 50*, 6(2):50, 2021.

Bibliography

- [45] L. Durand and W. Polifke. Implementation of the Thickened Flame Model for Large Eddy Simulation of Turbulent Premixed Combustion in a Commercial Solver. In *Volume 2: Turbo Expo 2007*, pages 869–878. ASMEEDC, 2007.
- [46] F. Durst and M. Schaefer. A Parallel Block-Structured Multigrid Method For the Prediction of Incompressible Flows. *International Journal for Numerical Methods in Fluids*, 22:996, 1996.
- [47] A. M. Eaton, L. D. Smoot, S. C. Hill, and C. N. Eatough. Components, formulations, solutions, evaluation, and application of comprehensive combustion models. *Progress in Energy and Combustion Science*, 25:387–436, 1999.
- [48] P. Edge, S. R. Gubba, L. Ma, R. Porter, M. Pourkashanian, and A. Williams. LES modelling of air and oxy-fuel pulverised coal combustion impact on flame properties. *Proceedings of the Combustion Institute*, 33(2):2709–2716, 2011.
- [49] D. Edwards. Molecular gas band radiation. In *Advances in heat transfer*, pages 115–193. Elsevier, 1976.
- [50] B. Epple, R. Leithner, W. Linzer, and H. Walter, editors. *Simulation von Kraftwerken und Feuerungen*. Springer Vienna, Vienna, 2012.
- [51] S. Farazi, A. Attili, S. Kang, and H. Pitsch. Numerical study of coal particle ignition in air and oxy-atmosphere. *Proceedings of the Combustion Institute*, 37:2867–2874, 2019.
- [52] S. Farazi, J. Hinrichs, M. Davidovic, T. Falkenstein, M. Bode, S. Kang, A. Attili, and H. Pitsch. Numerical investigation of coal particle stream ignition in oxy-atmosphere. *Fuel*, 241:477–487, 2019.
- [53] P. Farmand, H. Nicolai, C. Schumann, A. Attili, L. Berger, T. Li, C. Geschwindner, F. di Mare, C. Hasse, B. Böhm, J. Janicka, and H. Pitsch. Numerical investigation and assessment of flamelet-based models for the prediction of pulverized solid fuel homogeneous ignition and combustion. *Combustion and Flame*, 235:111693, 2022.
- [54] A. Favre. Statistical equations of turbulent gases. *Problems of hydrodynamics and continuum mechanics*, pages 231–66, 1969.
- [55] E. Fehlberg. Klassische Runge-Kutta-Formeln fünfter und siebenter Ordnung mit Schrittweiten-Kontrolle 1. *Computing*, 4:93–106, 1969.
- [56] J. H. Ferziger and M. Peric. Computational methods for fluid dynamics. *Springer*, 2002.
- [57] M. A. Field, D. W. Gill, B. B. Morgan, and P. G. W. Hawksley. Combustion of Pulverized Coal. *The British Coal Utilization Research Association*, 1967.
- [58] F. L. S. Filho. Novel approach toward the consistent simulation of turbulent spray flames using tabulated chemistry. *Ph.D. thesis, TU Darmstadt, Darmstadt*, 2017.
- [59] B. Fiorina, R. Baron, O. Gicquel, D. Thevenin, S. Carpentier, and N. Darabiha. Modelling non-adiabatic partially premixed flames using flame-prolongation of ILDM. *Combustion Theory and Modelling*, 7(3):449–470, 2003.
- [60] T. H. Fletcher. Review of 30 Years of Research Using the Chemical Percolation Devolatilization Model. *Energy & Fuels*, 33:12123–13153, 2019.

- [61] T. H. Fletcher, A. R. Kerstein, R. Pugmire, R. J. Pugmire, M. Solum, and D. M. Grant. A Chemical Percolation Model for Devolatilization: Summary. *Brigham Young University*, 1992.
- [62] T. H. Fletcher, A. R. Kerstein, R. J. Pugmire, and D. M. Grant. Chemical Percolation Model for Devolatilization. 2. Temperature and Heating Rate Effects on Product Yieldst. *54 Energy & Fuels*, 4:54–60, 1990.
- [63] T. H. Fletcher, A. R. Kerstein, R. J. Pugmire, M. S. Solum, and D. M. Grant'. Chemical Percolation Model for Devolatilization. 3. Direct Use of ^{13}C NMR Data To Predict Effects of Coal Type. *Energy & Fuels*, 6:414–431, 1992.
- [64] T. H. Fletcher and R. J. Pugmire. Chemical Percolation Model for Coal Devolatilization Retrieved from <https://www.et.byu.edu/~tom/cpd/cpdcodes.html>, 2021.
- [65] D. V. Flores and T. H. Fletcher. The Use of Two Mixture Fractions to Treat Coal Combustion Products in Turbulent Pulverized-Coal Flames. *Combustion Science and Technology*, 150(1):1–26, 2000.
- [66] P. Foster and C. Howarth. Optical constants of carbons and coals in the infrared. *Carbon*, 6(5):719–729, 1968.
- [67] R. O. Fox. *Computational Models for Turbulent Reacting Flows*. Cambridge University Press, 2003.
- [68] B. Franchetti, F. Cavallo Marincola, S. Navarro-Martinez, and A. Kempf. Large Eddy Simulation of a 100 kWth swirling oxy-coal furnace. *Fuel*, 181:491–502, 2016.
- [69] B. M. Franchetti, F. Cavallo Marincola, S. Navarro-Martinez, and A. M. Kempf. Large Eddy simulation of a pulverised coal jet flame. *Proceedings of the Combustion Institute*, 34(2):2419–2426, 2013.
- [70] K. Fröhlich, M. Meinke, and W. Schröder. Correlations for inclined prolates based on highly resolved simulations. *Journal of Fluid Mechanics*, 901:5–5, 2020.
- [71] D. Genetti. An Advanced Model of Coal Devolatilization Based on Chemical Structure. *PhD thesis Brigham Young University*, 1999.
- [72] D. Genetti, T. H. Fletcher, and R. J. Pugmire. Development and Application of a Correlation of ^{13}C NMR Chemical Structural Analyses of Coal Based on Elemental Composition and Volatile Matter Content. *Energy & Fuels*, 13(1):60–68, 1999.
- [73] M. Germano, U. Piomelli, P. Moin, and W. H. Cabot. A dynamic subgrid-scale eddy viscosity model. *Physics of Fluids A*, 3(7):1760–1765, 1991.
- [74] O. Gicquel, N. Darabiha, and D. Thévenin. Liminar premixed hydrogen/air counterflow flame simulations using flame prolongation of ILDM with differential diffusion. *Proceedings of the Combustion Institute*, 28(2):1901–1908, 2000.
- [75] R. Gonçalves, D. Santos, S. Ducruix, O. Gicquel, and D. Veynate. A study of three-dimensional LES of turbulent combustion with radiative heat transfer. *Journal of the Brazilian Society of Mechanical Sciences and Engineering*, 38:33–48, 2016.

Bibliography

- [76] D. Goodwin and M. Mitchner. Flyash radiative properties and effects on radiative heat transfer in coal-fired systems. *International Journal of Heat and Mass Transfer*, 32(4):627–638, 1989.
- [77] D. G. Goodwin, R. L. Speth, H. K. Moffat, and B. W. Weber. Cantera: An object-oriented software toolkit for chemical kinetics, thermodynamics, and transport processes. <https://www.cantera.org>. *Version 2.5.1.*, 2021.
- [78] B. Goshayeshi and J. C. Sutherland. A comparison of various models in predicting ignition delay in single-particle coal combustion. *Combustion and Flame*, 161:1900–1910, 2014.
- [79] B. Gövert, S. Pielsticker, T. Kreitzberg, M. Habermehl, O. Hatzfeld, and R. Kneer. Measurement of reaction rates for pulverized fuel combustion in air and oxyfuel atmosphere using a novel fluidized bed reactor setup. *Fuel*, 201:81–92, 2017.
- [80] D. M. Grant, R. J. Pugmire, T. H. Fletcher, and A. R. Kerstein. Chemical Model of Coal Devolatilization Using Percolation Lattice Statistics. *Energy & Fuels*, 3:175–186, 1989.
- [81] D. Gray, J. G. Cogoli, and R. H. Essenhigh. Problems in Pulverized Coal and Char Combustion. *Adv Chem Ser*, 13:72–91, 1974.
- [82] T. Gronaz. Modeling of Particle-Radiation-Interaction for the Numerical Simulation of Coal Combustion. *PhD thesis RWTH Aachen*, 2017.
- [83] F. Hahn. Zur Vorhersage technischer Verbrennungssysteme im Hinblick auf flüssige Brennstoffe. *Ph.D. thesis, TU-Darmstadt, Darmstadt*, 2008.
- [84] F. Hahn. Zur Vorhersage technischer Verbrennungssysteme im Hinblick auf flüssige Brennstoffe. *Ph.D. thesis, TU Darmstadt, Darmstadt*, 2009.
- [85] T. Hara, M. Muto, T. Kitano, R. Kurose, and S. Komori. Direct numerical simulation of a pulverized coal jet flame employing a global volatile matter reaction scheme based on detailed reaction mechanism. *Combustion and Flame*, 162(12):4391–4407, 2015.
- [86] C. Hasse, P. Debiagi, X. Wen, K. Hildebrandt, M. Vascellari, and T. Faravelli. Advanced modeling approaches for CFD simulations of coal combustion and gasification. *Progress in Energy and Combustion Science*, 86:100938, 2021.
- [87] C. Hasse and N. Peters. A two mixture fraction flamelet model applied to split injections in a DI Diesel engine. *Proceedings of the Combustion Institute*, 30(2):2755–2762, 2005.
- [88] D. C. Haworth. Progress in probability density function methods for turbulent reacting flows. *Progress in Energy and Combustion Science*, 36(2):168–259, 2010.
- [89] J. Hees, D. Zabrodiec, A. Massmeyer, S. Pielsticker, B. Gövert, M. Habermehl, O. Hatzfeld, and R. Kneer. Detailed analyzes of pulverized coal swirl flames in oxy-fuel atmospheres. *Combustion and Flame*, 172:289–301, 2016.
- [90] L. G. Henyey and J. L. Greenstein. Diffuse radiation in the galaxy. *The Astrophysical Journal*, 93:70–83, 1941.
- [91] S. Heuer, O. Senneca, A. Wütscher, H. Düdder, M. Schiemann, M. Muhler, and V. Scherer. Effects of oxy-fuel conditions on the products of pyrolysis in a drop tube reactor. *Fuel Processing Technology*, 150:41–49, 2016.

- [92] J. O. Hirschfelder, C. F. Curtis, and R. B. Bird. *Molecular Theory of Gases and Liquids*. Wiley, New York, 1964.
- [93] C. Hollmann and E. Gutheil. Modeling of turbulent spray diffusion flames including detailed chemistry. *Symposium (International) on Combustion*, 26(1):1731–1738, 1996.
- [94] H. Hottel and A. Sarofim. *Radiative Transfer*. McGraw-Hill, New York, USA, 1967.
- [95] R. Hurt, J. K. Sun, and M. Lunden. A kinetic model of carbon burnout in pulverized coal combustion. *Combustion and Flame*, 113(1-2):181–197, 1998.
- [96] S. Hyun Kim and K. Y. Huh. A new angular discretization scheme of the finite volume method for 3-D radiative heat transfer in absorbing, emitting and anisotropically scattering media. *International Journal of Heat and Mass Transfer*, 43:1233–1242, 2000.
- [97] IEA. Global Energy Review. *IEA. Paris*, 2020.
- [98] M. Ihme and H. Pitsch. Modeling of radiation and nitric oxide formation in turbulent nonpremixed flames using a flamelet/progress variable formulation. *Physics of Fluids*, 20(5):055110, 2008.
- [99] IPCC. Global Warming of 1.5°C. An IPCC Special Report on the impacts of global warming of 1.5°C above pre-industrial levels and related global greenhouse gas emission pathways, in the context of strengthening the global response to the threat of climate change,. In *Special Report*, 2018.
- [100] J. Janicka and A. Sadiki. Large eddy simulation of turbulent combustion systems. *Proceedings of the Combustion Institute*, 30:537–547, 2005.
- [101] R. Jovanovic, A. Milewska, B. Swiatkowski, A. Goanta, and H. Spliethoff. Sensitivity analysis of different devolatilisation models on predicting ignition point position during pulverized coal combustion in O₂/N₂ and O₂/CO₂ atmospheres. *Fuel*, 101:23–37, 2012.
- [102] R. S. Jupudi, V. Zamansky, and T. H. Fletcher. Prediction of Light Gas Composition in Coal Devolatilization. *Energy & Fuels*, 23(6):3063–3067, 2009.
- [103] V. P. Kabashnikov and G. I. Myasnikova. Thermal radiation in turbulent flowstemperature and concentration fluctuations. *eat Transfer-Soviet Research*, 17.6:116–125, 1985.
- [104] A. Ketelheun. Development of Tabulated Chemistry Methods for the Accurate Simulation of Turbulent Combustion Systems. *Ph.D. thesis, TU Darmstadt, Darmstadt*, 2014.
- [105] A. Ketelheun, G. Kuenne, J. Janicka, A. Ketelheun, · · G. Kuenne, · · J. Janicka, and J. Janicka. Heat Transfer Modeling in the Context of Large Eddy Simulation of Premixed Combustion with Tabulated Chemistry. *Flow Turbulence Combust*, 91:867–893, 2013.
- [106] A. Ketelheun, C. Olbricht, F. Hahn, and J. Janicka. Premixed Generated Manifolds for the Computation of Technical Combustion Systems. *Proceedings of the ASME Turbo Expo*, 2:695–705, 2010.
- [107] R. Knapstein. Large Eddy Simulation of Pulverized Coal Combustion in the Context of Tabulated Chemistry. *Ph.D. thesis, TU-Darmstadt, Darmstadt*, 2018.

Bibliography

- [108] R. Knappstein, G. Kuenne, L. G. Becker, F. di Mare, A. Sadiki, A. Dreizler, and J. Janicka. Large Eddy Simulation of a Novel Gas-Assisted Coal Combustion Chamber. *Flow, Turbulence and Combustion*, 101(3):895–926, 2018.
- [109] R. Knappstein, G. Kuenne, A. Ketelheun, J. Köser, L. Becker, S. Heuer, M. Schiemann, V. Scherer, A. Dreizler, A. Sadiki, and J. Janicka. Devolatilization and volatiles reaction of individual coal particles in the context of FGM tabulated chemistry. *Combustion and Flame*, 169:72–84, 2016.
- [110] R. Knappstein, G. Kuenne, T. Meier, A. Sadiki, and J. Janicka. Evaluation of coal particle volatiles reaction by using detailed kinetics and FGM tabulated chemistry. *Fuel*, 201:39–52, 2017.
- [111] R. Knappstein, G. Kuenne, H. Nicolai, F. di Mare, A. Sadiki, and J. Janicka. Description of the char conversion process in coal combustion based on premixed FGM chemistry. *Fuel*, 236:124–134, 2019.
- [112] E. Knudsen and H. Pitsch. Combustion and Flame A general flamelet transformation useful for distinguishing between premixed and non-premixed modes of combustion. *Combustion and Flame*, 156:678–696, 2009.
- [113] H. Kobayashi, J. B. Howard, and A. F. Sarofim. Coal devolatilization at high temperatures. *Symposium (International) on Combustion*, 16(1):411–425, 1977.
- [114] J. Köser, L. G. Becker, A.-K. Goßmann, B. Böhm, and A. Dreizler. Investigation of ignition and volatile combustion of single coal particles within oxygen-enriched atmospheres using high-speed OH-PLIF. *Proceedings of the Combustion Institute*, 36(2):2103–2111, 2017.
- [115] J. Köser, T. Li, N. Vorobiev, A. Dreizler, M. Schiemann, and B. Böhm. Multi-parameter diagnostics for high-resolution in-situ measurements of single coal particle combustion. *Proceedings of the Combustion Institute*, 37(3):2893–2900, 2019.
- [116] G. Kuenne. Large eddy simulation of premixed combustion using artificial flame thickening coupled with tabulated chemistry. *Optimus-Verlag*, 2012.
- [117] G. Kuenne, A. Avdić, and J. Janicka. Assessment of subgrid interpolation for the source term evaluation within premixed combustion simulations. *Combustion and Flame*, 178:225–256, 2017.
- [118] G. Kuenne, A. Ketelheun, and J. Janicka. LES modeling of premixed combustion using a thickened flame approach coupled with FGM tabulated chemistry. *Combustion and Flame*, 158(9):1750–1767, 2011.
- [119] G. Kuenne, F. Seffrin, F. Fuest, T. Stahler, A. Ketelheun, D. Geyer, J. Janicka, and A. Dreizler. Experimental and numerical analysis of a lean premixed stratified burner using 1D Raman/Rayleigh scattering and large eddy simulation. *Combustion and Flame*, 159(8):2669–2689, 2012.
- [120] M. Kumar and A. F. Ghoniem. Multiphysics Simulations of Entrained Flow Gasification. Part I: Validating the Nonreacting Flow Solver and the Particle Turbulent Dispersion Model. *Energy & fuels*, 26.1:451–463, 2012.

- [121] M. Kumar and A. F. Ghoniem. Multiphysics Simulations of Entrained Flow Gasification. Part II: Constructing and Validating the Overall Model. *Energy & Fuels*, 26.1:464–479, 2012.
- [122] R. Kurose and H. Makino. Large eddy simulation of a solid-fuel jet flame. *Combustion and Flame*, 135(1-2):1–16, 2003.
- [123] J. Lambert. Numerical Methods for Ordinary Differential Systems: The Initial Value Problem. *John Wiley & Sons, Inc, Hoboken, USA*, 1991.
- [124] B. Launder and D. Spalding. The Numerical Computation of Turbulent Flows. In *Numerical Prediction of Flow, Heat Transfer, Turbulence and Combustion*, pages 96–116. Elsevier, 1983.
- [125] J. P. Legier, T. Poinso, and D. Veynante. Dynamically thickened flame LES model for premixed and non-premixed turbulent combustion. In *Center for Turbulence Research Proceedings of the Summer Program*, 2000.
- [126] T. Lehnhaeuser. Eine effiziente numerische Methode zur Gestaltoptimierung von Strömungsgebieten. *Ph.D. thesis, TU Darmstadt, Darmstadt*, 2004.
- [127] T. Lehnhaeuser and M. Schäfer. Improved linear interpolation practice for finite-volume schemes on complex grids. *International Journal for Numerical Methods in Fluids*, 38(7):625–645, 2002.
- [128] H. Leister. Stone1968. *Ph.D. thesis, University Erlangen-Nuernberg, Erlangen*, 1994.
- [129] H. J. Leister and M. Perić. Vectorized strongly implicit solving procedure for a seven-diagonal coefficient matrix. *International Journal of Numerical Methods for Heat & Fluid Flow*, 4(2):159–172, 1994.
- [130] T. Li, C. Geschwindner, J. Köser, M. Schiemann, A. Dreizler, and B. Böhm. Investigation of the transition from single to group coal particle combustion using high-speed scanning OH-LIF and diffuse backlight-illumination. *Proceedings of the Combustion Institute*, 38(3):4101–4109, 2021.
- [131] D. K. Lilly. A proposed modification of the Germano subgrid-scale closure method. *Physics of Fluids A*, 4(3):633–635, 1992.
- [132] A. Liñán. The asymptotic structure of counterflow diffusion flames for large activation energies. *Acta Astronautica*, 1(7-8):1007–1039, 1974.
- [133] G.-S. Liu and S. Niksa. Coal conversion submodels for design applications at elevated pressures. Part II. Char gasification. *Progress in Energy and Combustion Science*, 30(6):679–717, 2004.
- [134] Y. Liu, M. Geier, A. Molina, and C. R. Shaddix. Pulverized coal stream ignition delay under conventional and oxy-fuel combustion conditions. *International Journal of Greenhouse Gas Control*, 5:S36–S46, 2011.
- [135] K. Luo, H. Wang, J. Fan, and F. Yi. Direct Numerical Simulation of Pulverized Coal Combustion in a Hot Vitiated Co-flow. *Energy & Fuels*, 26(10):6128–6136, 2012.

Bibliography

- [136] U. Maas and S. Pope. Laminar flame calculations using simplified chemical kinetics based on intrinsic low-dimensional manifolds. *Symposium (International) on Combustion*, 25(1):1349–1356, 1994.
- [137] T. Maffei, R. Khatami, S. Pierucci, T. Faravelli, E. Ranzi, and Y. A. Levendis. Experimental and modeling study of single coal particle combustion in O₂/N₂ and Oxy-fuel (O₂/CO₂) atmospheres. *Combustion and Flame*, 160(11):2559–2572, 2013.
- [138] B. Magnussen and B. Hjertager. On mathematical modeling of turbulent combustion with special emphasis on soot formation and combustion. *Symposium (International) on Combustion*, 16(1):719–729, 1977.
- [139] B. F. Magnussen. THE EDDY DISSIPATION CONCEPT A BRIDGE BETWEEN SCIENCE AND TECHNOLOGY. *ECCOMAS Thematic Conference on Computational Combustion*, 21, 2005.
- [140] A. Majda and J. Sethian. The derivation and numerical solution of the equations for zero mach number combustion. *Combustion Science and Technology*, 42(3-4):185–205, 1985.
- [141] A. Maltsev. Towards the Development and Assessment of Complete CFD Models for the Simulation of Stationary Gas Turbine Combustion Processes. *Ph.D. thesis, TU Darmstadt, Darmstadt*, 2003.
- [142] B. Mayr, R. Prieler, M. Demuth, M. Potesser, and C. Hochenauer. CFD and experimental analysis of a 115 kW natural gas fired lab-scale furnace under oxy-fuel and airfuel conditions. *Fuel*, 159:864–875, 2015.
- [143] J. McConnell and J. C. Sutherland. Assessment of various tar and soot treatment methods and a priori analysis of the steady laminar flamelet model for use in coal combustion simulation. *Fuel*, 265:116775, apr 2020.
- [144] T. Meier. Entwicklung numerischer Methoden zur Anwendung detaillierter Chemie in komplexen Verbrennungssystemen. *TU Darmstadt; TUprints*, 2016.
- [145] C. Meneveau and T. Poinso. Stretching and quenching of flamelets in premixed turbulent combustion. *Combustion and Flame*, 86(4):311–332, 1991.
- [146] D. Merrick. Mathematical models of the thermal decomposition of coal. 2. Specific heats and heats of reaction. *Fuel*, 62(5):540–546, 1983.
- [147] D. Messig, M. Vascellari, and C. Hasse. Flame structure analysis and flamelet progress variable modelling of strained coal flames. *Combustion Theory and Modelling*, 21(4):700–721, 2017.
- [148] G. Migliavacca, E. Parodi, L. Bonfanti, T. Faravelli, S. Pierucci, and E. Ranzi. A general mathematical model of solid fuels pyrolysis. *Energy*, 30(8 SPEC. ISS.):1453–1468, 2005.
- [149] Milovan Peric. Three-Dimensional Fluid Flow in Complex Ducts. *Ph.D. thesis, Empirical College London, London*, M(August), 1985.
- [150] F. C. Miranda. Large Eddy Simulation of Turbulent Reacting Flows With Radiation Heat Transfer Dem. *Ph.D. thesis, TU-Darmstadt, Darmstadt*, 2018.

- [151] F. C. Miranda, P. J. Coelho, F. di Mare, and J. Janicka. Study of turbulence-radiation interactions in large-eddy simulation of scaled Sandia flame D. *Journal of Quantitative Spectroscopy and Radiative Transfer*, 228:47–56, 2019.
- [152] F. C. Miranda, P. J. Coelho, J. Ströhle, and J. Janicka. Large-eddy simulation of a bluff-body stabilised nonpremixed flame with radiation heat transfer. *Combustion Theory and Modelling*, 24(4):632–649, 2020.
- [153] M. F. Modest. The weighted-sum-of-gray-gases model for arbitrary solution methods in radiative transfer. *Journal of Heat Transfer*, 113(3):650–656, 1991.
- [154] M. F. Modest. *Radiative heat transfer, 2nd edition*. Elsevier Inc., 2003.
- [155] M. F. Modest and D. C. Haworth. *Radiative Heat Transfer in Turbulent Combustion Systems: Theory and Applications*. Springer, 2016.
- [156] P. Moin and K. Mahesh. DIRECT NUMERICAL SIMULATION: A Tool in Turbulence Research. *Annual Review of Fluid Mechanics*, 30(1):539–578, 1998.
- [157] A. Molina and C. R. Shaddix. Ignition and devolatilization of pulverized bituminous coal particles during oxygen/carbon dioxide coal combustion. *Proceedings of the Combustion Institute*, 31:1905–1912, 2007.
- [158] S. A. Morsi and A. J. Alexander. An investigation of particle trajectories in two-phase flow systems. *Journal of Fluid Mechanics*, 55(2):193–208, 1972.
- [159] N. G. C. o. E. National Academy of Engineering. Develop Carbon Sequestration Methods, 2021.
- [160] P.-D. Nguyen, L. Vervisch, V. Subramanian, and P. Domingo. Multidimensional flamelet-generated manifolds for partially premixed combustion. *Combustion and Flame*, 157(1):43–61, 2010.
- [161] H. Nicolai. Overview of fundamental effects of pulverized solid fuel conversion in a swirled laboratory combustion chamber. <https://tudatalib.ulb.tu-darmstadt.de/handle/tudatalib/3410>, 2022.
- [162] H. Nicolai, P. Debiagi, X. Wen, L. Dressler, A. Massmeyer, J. Janicka, and C. Hasse. Flamelet LES of swirl-stabilized oxy-fuel flames using directly coupled multi-step solid fuel kinetics. *Combustion and Flame*, 241:112062, 2022.
- [163] H. Nicolai, G. Kuenne, R. Knappstein, H. Schneider, L. Becker, C. Hasse, F. di Mare, A. Dreizler, and J. Janicka. Large Eddy Simulation of a laboratory-scale gas-assisted pulverized coal combustion chamber under oxy-fuel atmospheres using tabulated chemistry. *Fuel*, 272:117683, 2020.
- [164] H. Nicolai, T. Li, C. Geschwindner, F. di Mare, C. Hasse, B. Böhm, and J. Janicka. Numerical investigation of pulverized coal particle group combustion using tabulated chemistry. *Proceedings of the Combustion Institute*, 38(3):4033–4041, 2021.
- [165] H. Nicolai, X. Wen, F. Miranda, D. Zabrodiec, A. Massmeyer, F. di Mare, A. Dreizler, C. Hasse, R. Kneer, and J. Janicka. Numerical investigation of swirl-stabilized pulverized coal flames in air and oxy-fuel atmospheres by means of large eddy simulation coupled with tabulated chemistry. *Fuel*, 287:119429, 2021.

Bibliography

- [166] S. Niksa. *Process chemistry of coal utilization: impacts of coal quality and operating conditions*. Woodhead Publishing, 2019.
- [167] S. Niksa and C.-W. Lau. Global rates of devolatilization for various coal types. *Combustion and Flame*, 94(3):293–307, 1993.
- [168] S. Niksa, G.-s. Liu, and R. H. Hurt. Coal conversion submodels for design applications at elevated pressures. Part I. devolatilization and char oxidation. *Progress in Energy and Combustion Science*, 29(5):425–477, jan 2003.
- [169] W. L. Oberkampf and C. J. Roy. *Verification and validation in scientific computing*. Cambridge University Press, 2010.
- [170] A. Oberlin and M. Oberlin. Graphitizability of carbonaceous materials as studied by TEM and Xray diffraction. *Journal of Microscopy*, 132(3):353–363, 1983.
- [171] C. Olbricht. Numerische Berechnung technischer Verbrennungssysteme. *Ph.D. thesis, TU Darmstadt, Darmstadt*, 2009.
- [172] G. Olenik, O. T. Stein, and A. Kronenburg. LES of swirl-stabilised pulverised coal combustion in IFRF furnace No. 1. *Proceedings of the Combustion Institute*, 35:2819–2828, 2015.
- [173] P. J. O’Rourke and F. V. Bracco. Two scaling transformations for the numerical computation of multidimensional unsteady laminar flames. *Journal of Computational Physics*, 33(2):185–203, 1979.
- [174] S. Patankar and D. Spalding. A CALCULATION PROCEDURE FOR HEAT, MASS AND MOMENTUM TRANSFER IN THREE-DIMENSIONAL PARABOLIC FLOWS. In *Numerical Prediction of Flow, Heat Transfer, Turbulence and Combustion*, pages 54–73. Elsevier, 1983.
- [175] C. Pera, J. Réveillon, L. Vervisch, and P. Domingo. Modeling subgrid scale mixture fraction variance in LES of evaporating spray. *Combustion and Flame*, 146(4):635–648, 2006.
- [176] N. Peters. Laminar diffusion flamelet models in non-premixed turbulent combustion. *Progress in Energy and Combustion Science*, 10(3):319–339, 1984.
- [177] C. D. Pierce and P. Moin. A dynamic model for subgrid-scale variance and dissipation rate of a conserved scalar. *Physics of Fluids*, 10(12):3041, 1998.
- [178] C. D. Pierce and P. Moin. Progress-variable approach for large-eddy simulation of non-premixed turbulent combustion. *J. Fluid Mech*, 504:73–97, 2004.
- [179] H. Pitsch. Large-Eddy Simulation of Turbulent Combustion. *Annual Review of Fluid Mechanics*, 38:453–482, 2006.
- [180] G. J. Pitt. The kinetic of the evolution of volatile products from coal. *Fuel*, 41:267–274, 1962.
- [181] T. Poinsot and D. Veynante. *Theoretical and Numerical Combustion*. RT Edwards, Inc., 2012.

- [182] T. Poinso, D. Veynante, and S. Candel. Quenching processes and premixed turbulent combustion diagrams. *Journal of Fluid Mechanics Digital Archive*, 228:561, 1991.
- [183] S. Pope. PDF methods for turbulent reactive flows. *Progress in Energy and Combustion Science*, 11(2):119–192, 1985.
- [184] S. Pope. *Turbulent flows*. Cambridge University Press, 2011.
- [185] S. Popp, S. Hartl, D. Butz, D. Geyer, A. Dreizler, L. Vervisch, and C. Hasse. Assessing multi-regime combustion in a novel burner configuration with large eddy simulations using tabulated chemistry. *Proceedings of the Combustion Institute*, 38(2):2551–2558, 2021.
- [186] L. Prantl. Ueber die ausgebildete turbulenz. *ZAMM* 5, pages 136–139, 1925.
- [187] M. J. Prins, K. J. Ptasinski, and F. J. Janssen. From coal to biomass gasification: Comparison of thermodynamic efficiency. *Energy*, 32(7):1248–1259, 2007.
- [188] F. Proch and A. M. Kempf. Numerical analysis of the Cambridge stratified flame series using artificial thickened flame LES with tabulated premixed flame chemistry. *Combustion and Flame*, 161(10):2627–2646, 2014.
- [189] M. Rabaçal, B. M. Franchetti, F. C. Marincola, F. Proch, M. Costa, C. Hasse, and A. M. Kempf. Large Eddy Simulation of coal combustion in a large-scale laboratory furnace. *Proceedings of the Combustion Institute*, 35(3):3609–3617, 2015.
- [190] K. Radhakrishnan and A. C. Hindmarsh. Description and use of LSODE, the Livermore solver for ordinary differential equations. Technical report, Lawrence Livermore National Laboratory, 1993.
- [191] W. F. Ranz and W. R. Marshall. Evaporation from drops: I. *Chemical Engineering Progress*, 48:141–146, 1952.
- [192] W. F. Ranz and W. R. Marshall. Evaporation from drops: II. *Chemical Engineering Progress*, 48:173–180, 1952.
- [193] E. Ranzi, P. E. A. Debiagi, and A. Frassoldati. Mathematical Modeling of Fast Biomass Pyrolysis and Bio-Oil Formation. Note I: Kinetic Mechanism of Biomass Pyrolysis. *ACS Sustainable Chemistry & Engineering*, 5(4):2867–2881, 2017.
- [194] E. Ranzi, P. E. A. Debiagi, and A. Frassoldati. Mathematical Modeling of Fast Biomass Pyrolysis and Bio-Oil Formation. Note II: Secondary Gas-Phase Reactions and Bio-Oil Formation. *ACS Sustainable Chemistry & Engineering*, 5(4):2882–2896, 2017.
- [195] E. Ranzi, T. Faravelli, and F. Manenti. Pyrolysis, Gasification, and Combustion of Solid Fuels. In *Advances in Chemical Engineering*, chapter one, pages 1–94. Academic Press, 2016.
- [196] C. M. Rhie and W. L. Chow. Numerical study of the turbulent flow past an airfoil with trailing edge separation. *AIAA Journal*, 21(11):1525–1532, 1983.
- [197] L. F. Richardson. *Weather prediction by numerical process*. Cambridge university press, 2007.

Bibliography

- [198] K. Richter, R. Friedrich, and L. Schmitt. Large-eddy simulation of turbulent wall boundary layers with pressure gradient. In *6th Symposium on Turbulent Shear Flows*, pages 2231–2237, 1987.
- [199] F. Ries, K. Nishad, L. Dressler, J. Janicka, and A. Sadiki. Evaluating large eddy simulation results based on error analysis. *Theoretical and Computational Fluid Dynamics*, 32(6):733–752, 2018.
- [200] M. Rieth, A. G. Clements, M. Rabaçal, F. Proch, O. T. Stein, and A. M. Kempf. Flamelet LES modeling of coal combustion with detailed devolatilization by directly coupled CPD. *Proceedings of the Combustion Institute*, 36:2181–2189, 2017.
- [201] M. Rieth, A. Kempf, A. Kronenburg, and O. Stein. Carrier-phase DNS of pulverized coal particle ignition and volatile burning in a turbulent mixing layer. *Fuel*, 212:364–374, 2018.
- [202] M. Rieth, A. M. Kempf, O. T. Stein, A. Kronenburg, C. Hasse, and M. Vascellari. Evaluation of a flamelet/progress variable approach for pulverized coal combustion in a turbulent mixing layer. *Proceedings of the Combustion Institute*, 37(3):2927–2934, 2019.
- [203] M. Rieth, F. Proch, A. G. Clements, M. Rabaçal, and A. M. Kempf. Highly resolved flamelet les of a semi-industrial scale coal furnace. *Proceedings of the Combustion Institute*, 36(3):3371–3379, 2017.
- [204] M. Rieth, F. Proch, M. Rabaçal, B. M. Franchetti, F. Cavallo Marincola, and A. M. Kempf. Flamelet LES of a semi-industrial pulverized coal furnace. *Combustion and Flame*, 173:39–56, 2016.
- [205] L. S. Rothman, I. E. Gordon, A. Barbe, D. C. Benner, P. F. Bernath, M. Birk, V. Boudon, L. R. Brown, A. Campargue, J. P. Champion, K. Chance, L. H. Coudert, V. Dana, V. M. Devi, S. Fally, J. M. Flaud, R. R. Gamache, A. Goldman, D. Jacquemart, I. Kleiner, N. Lacome, W. J. Lafferty, J. Y. Mandin, S. T. Massie, S. N. Mikhailenko, C. E. Miller, N. Moazzen-Ahmadi, O. V. Naumenko, A. V. Nikitin, J. Orphal, V. I. Perevalov, A. Perrin, A. Predoi-Cross, C. P. Rinsland, M. Rotger, M. Šimečková, M. A. Smith, K. Sung, S. A. Tashkun, J. Tennyson, R. A. Toth, A. C. Vandaele, and J. Vander Auwera. The HITRAN 2008 molecular spectroscopic database. *Journal of Quantitative Spectroscopy and Radiative Transfer*, 110(9-10):533–572, 2009.
- [206] L. S. Rothman, I. E. Gordon, R. J. Barber, H. Dothe, R. R. Gamache, A. Goldman, V. I. Perevalov, S. A. Tashkun, and J. Tennyson. HITEMP, the high-temperature molecular spectroscopic database. *Journal of Quantitative Spectroscopy and Radiative Transfer*, 111(15):2139–2150, 2010.
- [207] J. N. Rouzaud and A. Oberlin. Structure, microtexture, and optical properties of anthracene and saccharose-based carbons. *Carbon*, 27(4):517–529, 1989.
- [208] F. L. Sacomano Filho, G. Kuenne, M. Chrigui, A. Sadiki, and J. Janicka. A consistent Artificially Thickened Flame approach for spray combustion using LES and the FGM chemistry reduction method: Validation in Lean Partially Pre-vaporized flames. *Combustion and Flame*, 184:68–89, 2017.
- [209] A. Sadiki, S. Agrebi, M. Chrigui, A. Doost, R. Knappstein, F. Di Mare, J. Janicka, A. Massmeyer, D. Zabrodiec, J. Hees, and R. Kneer. Analyzing the effects of turbulence

- and multiphase treatments on oxy-coal combustion process predictions using LES and RANS. *Chemical Engineering Science*, 166:283–302, 2017.
- [210] P. Sagaut. *Large Eddy Simulation for Incompressible Flows*. Springer Science & Business Media, 2006.
- [211] P. Salatino, O. Senneca, and S. Masi. Gasification of a coal char by oxygen and carbon dioxide. *Carbon*, 36(4):443–452, 1998.
- [212] F. Schäfer and M. Breuer. Comparison of c-space and p-space particle tracing schemes on high-performance computers: accuracy and performance. *International Journal for Numerical Methods in Fluids*, 39(4):277–299, 2002.
- [213] E. Schneider. Numerische Simulation turbulenter vorgemischter Verbrennungssysteme: Entwicklung und Anwendung eines RANS-basierten Gesamtmodells. *Ph.D. thesis, TU Darmstadt, Darmstadt*, 2005.
- [214] L. Schneiders, C. Günther, M. Meinke, and W. Schröder. An efficient conservative cut-cell method for rigid bodies interacting with viscous compressible flows. *Journal of Computational Physics*, 311:62–86, 2016.
- [215] A. Scholtissek, S. Popp, S. Hartl, H. Olguin, P. Domingo, L. Vervisch, and C. Hasse. Derivation and analysis of two-dimensional composition space equations for multi-regime combustion using orthogonal coordinates. *Combustion and Flame*, 218:205–217, 2020.
- [216] O. Senneca, N. Vorobiev, A. Wütscher, F. Cerciello, S. Heuer, C. Wedler, R. Span, M. Schiemann, M. Muhler, and V. Scherer. Assessment of combustion rates of coal chars for oxy-combustion applications. *Fuel*, 238:173–185, 2019.
- [217] H. Seung Min, R. Kurose, F. Akamatsu, H. Tsuji, H. Makino, and M. Katsuki. Application of Optical Diagnostics Techniques to a Laboratory-Scale Turbulent Pulverized Coal Flame. *Energy and Fuels*, 19(2):382–392, 2005.
- [218] C. R. Shaddix and A. Molina. Particle imaging of ignition and devolatilization of pulverized coal during oxy-fuel combustion. *Proceedings of the Combustion Institute*, 32:2091–2098, 2009.
- [219] A. Shamooni, P. Debiagi, B. Wang, T. D. Luu, O. T. Stein, A. Kronenburg, G. Bagheri, A. Stagni, A. Frassoldati, T. Faravelli, A. M. Kempf, X. Wen, and C. Hasse. Carrier-phase DNS of detailed NO_x formation in early-stage pulverized coal combustion with fuel-bound nitrogen. *Fuel*, 291:119998, 2021.
- [220] R. C. Shurtz, J. W. Hogge, K. C. Fowers, G. S. Sorensen, and T. H. Fletcher. Coal swelling model for pressurized high particle heating rate pyrolysis applications. In *Energy and Fuels*, volume 26, pages 3612–3627. American Chemical Society, 2012.
- [221] R. C. Shurtz, K. K. Kolste, and T. H. Fletcher. Coal swelling model for high heating rate pyrolysis applications. *Energy and Fuels*, 25(5):2163–2173, 2011.
- [222] G. P. Smith, D. M. Golden, M. Frenklach, N. W. Moriarty, B. Eiteneer, M. Goldenberg, C. T. Bowman, R. K. Hanson, S. Song, W. C. Gardiner, V. V. L. Jr., and Z. Qin. GRI-Mech 3.0.

Bibliography

- [223] L. D. Smoot and P. J. Smith. *Coal Combustion and Gasification*. Springer Science & Business Media, 1985.
- [224] P. R. Solomon, D. G. Hamblen, R. M. Carangelo, M. A. Serio, and G. V. Deshpande. General Model of Coal Devolatilization. *Energy & Fuels*, 2:405–422, 1988.
- [225] M. S. Solum, R. J. Pugmire, and D. M. Grant. Carbon-13 solid-state NMR of Argonne-premium coals. *Energy & Fuels*, 3(2):187–193, 1989.
- [226] S. Sommariva, T. Maffei, G. Migliavacca, T. Faravelli, and E. Ranzi. A predictive multi-step kinetic model of coal devolatilization. *Fuel*, 89(2):318–328, 2010.
- [227] T. H. Song and R. Viskantaj. Interaction of Radiation with Turbulence: Application to a Combustion System. *Journal of Thermophysics*, 1(1), 1986.
- [228] J. Spurk and N. Aksel. *Fluid Mechanics*. Springer, 2008.
- [229] O. T. Stein, G. Olenik, A. Kronenburg, F. Cavallo Marincola, B. M. Franchetti, A. M. Kempf, M. Ghiani, M. Vascellari, C. Hasse, F. Cavallo Marincola, M. Ghiani, and A. M. Kempf. Towards Comprehensive Coal Combustion Modelling for LES. *Flow Turbulence Combust*, 90:859–884, 2013.
- [230] M. Stöllinger, B. Naud, D. Roekaerts, N. Beishuizen, and S. Heinz. PDF modeling and simulations of pulverized coal combustion Part 1: Theory and modeling. *Combustion and Flame*, 160(2):384–395, feb 2013.
- [231] M. Stöllinger, B. Naud, D. Roekaerts, N. Beishuizen, and S. Heinz. PDF modeling and simulations of pulverized coal combustion Part 2: Application. *Combustion and Flame*, 160(2):396–410, 2013.
- [232] H. L. Stone. Iterative Solution of Implicit Approximations of Multidimensional Partial Differential Equations. *SIAM Journal on Numerical Analysis*, 5:530–558, 1968.
- [233] A. Strugała. Empirical formulae for calculation of real density and total pore volume of hard coals. *Fuel*, 73(11):1781–1785, 1994.
- [234] J. Tillou, J. B. Michel, C. Angelberger, and D. Veynante. Assessing LES models based on tabulated chemistry for the simulation of Diesel spray combustion. *Combustion and Flame*, 161(2):525–540, 2014.
- [235] J. Tomeczek and H. Palugniok. Specific heat capacity and enthalpy of coal pyrolysis at elevated temperatures. *Fuel*, 75(9):1089–1093, 1996.
- [236] D. Toporov, P. Bocian, P. Heil, A. Kellermann, H. Stadler, S. Tschunko, M. Förster, and R. Kneer. Detailed investigation of a pulverized fuel swirl flame in CO₂/O₂ atmosphere. *Combustion and Flame*, 155(4):605–618, 2008.
- [237] S. Trespi, H. Nicolai, P. Debiagi, J. Janicka, A. Dreizler, C. Hasse, and T. Faravelli. Development and Application of an Efficient Chemical Reactor Network Model for Oxy-fuel Combustion. *Energy & Fuels*, 35(9):7121–7132, 2021.
- [238] G. L. Tufano, O. T. Stein, A. Kronenburg, A. Frassoldati, T. Faravelli, L. Deng, A. M. Kempf, M. Vascellari, and C. Hasse. Resolved flow simulation of pulverized coal particle devolatilization and ignition in air- and O₂/CO₂-atmospheres. *Fuel*, 186:285–292, 2016.

- [239] G. L. Tufano, O. T. Stein, A. Kronenburg, G. Gentile, A. Stagni, A. Frassoldati, T. Faravelli, A. M. Kempf, M. Vascellari, and C. Hasse. Fully-resolved simulations of coal particle combustion using a detailed multi-step approach for heterogeneous kinetics. *Fuel*, 240:75–83, 2019.
- [240] G. L. Tufano, O. T. Stein, B. Wang, A. Kronenburg, M. Rieth, and A. M. Kempf. Coal particle volatile combustion and flame interaction. Part I: Characterization of transient and group effects. *Fuel*, 229:262–269, 2018.
- [241] G. L. Tufano, O. T. Stein, B. Wang, A. Kronenburg, M. Rieth, and A. M. Kempf. Coal particle volatile combustion and flame interaction. Part II: Effects of particle Reynolds number and turbulence. *Fuel*, 234:723–731, 2018.
- [242] S. Umemoto, S. Kajitani, K. Miura, H. Watanabe, and M. Kawase. Extension of the chemical percolation devolatilization model for predicting formation of tar compounds as soot precursor in coal gasification. *Fuel Processing Technology*, 159:256–265, 2017.
- [243] United Nations Treaty Collection. Paris Agreement. Technical report, UNFCCC, 2015.
- [244] J. van Oijen and L. de Goey. Modelling of Premixed Laminar Flames using Flamelet-Generated Manifolds. *Combustion Science and Technology*, 161:113–137, 2000.
- [245] J. A. van Oijen, A. Donini, R. J. Bastiaans, J. H. ten Thijsse Boonkkamp, and L. P. de Goey. State-of-the-art in premixed combustion modeling using flamelet generated manifolds. *Progress in Energy and Combustion Science*, 57:30–74, 2016.
- [246] J. A. Van Oijen, F. A. Lammers, and L. P. De Goey. Modeling of complex premixed burner systems by using flamelet-generated manifolds. *Combustion and Flame*, 127(3):2124–2134, 2001.
- [247] M. Vascellari, R. Arora, M. Pollack, and C. Hasse. Simulation of entrained flow gasification with advanced coal conversion submodels. Part 1: Pyrolysis. *Fuel*, 113:654–669, 2013.
- [248] M. Vascellari, D. Messig, A. Scholtissek, C. Hasse, M. Xia, B. Fiorina, and N. Darabiha. Experimental and numerical investigation of a stagnation pulverised coal flame. *Proceedings of the Combustion Institute*, 37(3):2857–2866, 2019.
- [249] M. Vascellari, G. L. Tufano, O. T. Stein, A. Kronenburg, A. M. Kempf, A. Scholtissek, and C. Hasse. A flamelet/progress variable approach for modeling coal particle ignition. *Fuel*, 201:29–38, 2017.
- [250] M. Vascellari, H. Xu, and C. Hasse. Flamelet modeling of coal particle ignition. *Proceedings of the Combustion Institute*, 34:2445–2452, 2013.
- [251] D. Veynante and L. Vervisch. Turbulent combustion modeling. *Progress in Energy and Combustion Science*, 28(3):193–266, 2002.
- [252] A. W. Vreman, B. A. Albrecht, J. A. van Oijen, L. P. de Goey, and R. J. Bastiaans. Premixed and nonpremixed generated manifolds in large-eddy simulation of Sandia flame D and F. *Combustion and Flame*, 153(3):394–416, 2008.
- [253] P. L. Walker, F. Rusinko, and L. G. Austin. Gas Reactions of Carbon. *Advances in Catalysis*, 11(C):133–221, 1959.

Bibliography

- [254] K. Wan, L. Vervisch, J. Xia, P. Domingo, Z. Wang, Y. Liu, and K. Cen. Alkali metal emissions in an early-stage pulverized-coal flame: DNS analysis of reacting layers and chemistry tabulation. *Proceedings of the Combustion Institute*, 37:2791–2799, 2019.
- [255] K. Wan, J. Xia, Z. Wang, L. C. Wrobel, and K. Cen. Online-CPD-Coupled Large-Eddy Simulation of Pulverized-Coal Pyrolysis in a Hot Turbulent Nitrogen Jet. *Combustion Science and Technology*, 189(1):103–131, 2017.
- [256] B. Wang, A. Shamooni, O. T. Stein, A. Kronenburg, A. M. Kempf, P. Debiagi, and C. Hasse. Investigation of Turbulent Pulverized Solid Fuel Combustion with Detailed Homogeneous and Heterogeneous Kinetics. *Energy & Fuels*, 35(9):7077–7091, 2021.
- [257] H. Watanabe, R. Kurose, and S. Komori. Large-Eddy Simulation of Swirling Flows in a Pulverized Coal Combustion Furnace with a Complex Burner. *Journal of Environment and Engineering*, 4(1):1–11, 2009.
- [258] J. Watanabe, T. Okazaki, K. Yamamoto, K. Kuramashi, and A. Baba. Large-eddy simulation of pulverized coal combustion using flamelet model. *Proceedings of the Combustion Institute*, 36(2):2155–2163, 2017.
- [259] J. Watanabe and K. Yamamoto. Flamelet model for pulverized coal combustion. *Proceedings of the Combustion Institute*, 35(2):2315–2322, 2015.
- [260] R. Weber and M. Mancini. On scaling and mathematical modelling of large scale industrial flames. *Journal of the Energy Institute*, 93(1):43–51, 2020.
- [261] B. Wegner. A Large-Eddy Simulation Technique for the Prediction of Flow, Mixing and Combustion in Gas Turbine Combustors. *Ph.D. thesis, TU Darmstadt, Darmstadt*, 2006.
- [262] X. Wen, Y. Luo, H. Wang, K. Luo, H. Jin, and J. Fan. A three mixture fraction flamelet model for multi-stream laminar pulverized coal combustion. *Proceedings of the Combustion Institute*, 37(3):2901–2910, 2019.
- [263] X. Wen, H. Nicolai, O. T. Stein, J. Janicka, A. Kronenburg, and C. Hasse. Effects of air and oxy-fuel atmospheres on flamelet modeling of pollutant formation in laminar counterflow solid fuel flames. *Fuel*, 285:119079, 2021.
- [264] X. Wen, M. Rieth, A. Scholtissek, O. T. Stein, H. Wang, K. Luo, A. M. Kempf, A. Kronenburg, J. Fan, and C. Hasse. A comprehensive study of flamelet tabulation methods for pulverized coal combustion in a turbulent mixing layer Part I: A priori and budget analyses. *Combustion and Flame*, 216:439–452, 2020.
- [265] X. Wen, M. Rieth, A. Scholtissek, O. T. Stein, H. Wang, K. Luo, A. Kronenburg, J. Fan, and C. Hasse. A comprehensive study of flamelet tabulation methods for pulverized coal combustion in a turbulent mixing layer Part II: Strong heat losses and multi-mode combustion. *Combustion and Flame*, 216:453–467, 2020.
- [266] D. C. Wilcox. *Turbulence Modeling for CFD*. DCW Industries, Inc., 1994.
- [267] J. H. Williamson. Low-storage Runge-Kutta schemes. *Journal of Computational Physics*, 35(1):48–56, 1980.

- [268] P. Wollny, B. Rogg, and A. Kempf. Modelling heat loss effects in high temperature oxy-fuel flames with an efficient and robust non-premixed flamelet approach. *Fuel*, 216:44–52, 2018.
- [269] K. Yamamoto, T. Murota, T. Okazaki, and M. Taniguchi. Large eddy simulation of a pulverized coal jet flame ignited by a preheated gas flow. *Proceedings of the Combustion Institute*, 33(2):1771–1778, 2011.
- [270] C. F. You and X. C. Xu. Coal combustion and its pollution control in China. *Energy*, 35:4467–4472, 2010.
- [271] D. Zabrodiec, L. Becker, J. Hees, A. Maßmeyer, M. Habermehl, O. Hatzfeld, A. Dreizler, and R. Kneer. Detailed Analysis of the Velocity Fields from 60 kW Swirl-Stabilized Coal Flames in CO₂/O₂- and N₂/O₂-Atmospheres by Means of Laser Doppler Velocimetry and Particle Image Velocimetry. *Combustion Science and Technology*, 189(10):1751–1775, 2017.
- [272] D. Zabrodiec, J. Hees, A. Massmeyer, F. vom Lehn, M. Habermehl, O. Hatzfeld, and R. Kneer. Experimental investigation of pulverized coal flames in CO₂/O₂- and N₂/O₂-atmospheres: Comparison of solid particle radiative characteristics. *Fuel*, 201:136–147, 2017.
- [273] D. Zabrodiec, J. Hees, G. Möller, O. Hatzfeld, and R. Kneer. Pulverized coal swirl flames in oxy-fuel conditions: Effects of oxidizer O₂ concentration on flow field and local gas composition. *Proceedings of the Combustion Institute*, 37(4):4471–4478, 2019.
- [274] C. Zhang. Numerical Modeling of Coal Gasification in an Entrained-Flow Gasifier. *Proceedings of the ASME 2012 International Mechanical Engineering Congress & Exposition*, 45226:1193–1203, 2012.
- [275] J. Zhang, T. Li, H. Ström, and T. Løvås. Grid-independent Eulerian-Lagrangian approaches for simulations of solid fuel particle combustion. *Chemical Engineering Journal*, 387:123964, 2020.
- [276] X. Y. Zhao and D. C. Haworth. Transported PDF modeling of pulverized coal jet flames. *Combustion and Flame*, 161(7):1866–1882, 2014.
- [277] G. Zhou, L. Davidson, and E. Olsson. Transonic inviscid/turbulent airfoil flow simulations using a pressure based method with high order schemes. In *Fourteenth International Conference on Numerical Methods in Fluid Dynamics*, pages 372–378. Springer Berlin Heidelberg, Berlin, Heidelberg, 1995.

List of Figures

1.1.	Schematic representation of the physical processes inside a solid fuel combustion chamber [161].	2
2.1.	Schematic distribution of the TKE onto different sizes as proposed by the energy cascade of turbulent flows.	14
2.2.	Schematic comparison of the three turbulence modeling approach with respect to the energy spectrum.	15
2.3.	Electromagnetic spectrum indicating the important spectral range of thermal radiation. Adapted from [154].	24
2.4.	Schematics of the solid angles, adapted from [82].	25
3.1.	Schematic representation of a premixed flame in a flat flame configuration (left) and a non-premixed flame in a counterflow configuration (right). The characteristic transport of fuel and oxidizer towards the reaction zone is depicted (fuel in green and oxidizer in blue).	31
3.2.	Exemplary premixed flame structure for a stoichiometric methane oxy-fuel mixture. Left: Physical coordinates. Right: Composition space coordinates.	32
3.3.	Comparison of monotonicity for the temperature over different progress variables for several equivalence ratios. Non-monotonic parts are marked red.	33
3.4.	Definitions of flame thicknesses. Left side: Definition based on the maximum gradient of an arbitrary scalar φ . Right side: Definition by means of the source term of the scalar φ	34
3.5.	Exemplary non-premixed flame structure for methane reacting in an oxy-fuel atmosphere. Left: Physical coordinates. Right: Composition space coordinates.	35
3.6.	Manifold of premixed flamelets with different equivalence ratios parameterized by mixture fraction Z . The solid line denotes stoichiometry and dashed lines represent lean flammability limit (lfl) and rich flammability limit (rfl), respectively. Left: Temperature; Right: Source term of the reaction progress variable.	40
3.7.	Manifold of premixed flamelets with different enthalpy levels. Solid lines: pre-heated flamelets. Dashed lines: flamelets with exhaust gas recirculation. Dotted lines: extrapolated "flamelets". Left: temperature contour as a function of enthalpy and progress variable. Right: enthalpy contour as a function of temperature and progress variable for the table access at the boundaries.	41
3.8.	Schematic depiction of composition space spanned by two mixture fractions for a two fuel stream system.	41
3.9.	Schematic representation of the transformation of the ATF model for a laminar flame for a thickening factor of $\mathcal{F}=2$. Graphic is adapted from [118].	43
3.10.	Left: Source term of the reaction progress variable over normalized progress variable for a representative methane flamelet in an oxy-fuel atmosphere. The absolute normalized curvature of the source term is also depicted. Right: Numerically defined flame sensor based on the curvature of the source term. In addition, the error that results from a linear interpolation is presented.	44

3.11. Maximum temperature profile for a complete set of flamelet solutions including the unstable branch, parameterized by the scalar dissipation rate at stoichiometry.	47
3.12. Tabulated flamelet structures of non-premixed flames. Dashed lines indicate solutions from the limits of the stable branch of the S-Curve.	48
3.13. Inclusion of heat-losses in non-premixed flames for constant normalized progress variables. Solid lines: preheated non-premixed flamelets; Dashed lines: non-premixed flamelets with different rescaled energy-source terms; Dotted lines: extrapolated flamelets. Left: flamelet table parameterized by Z and h . Right: flamelet table parameterized by Z and T for the access at boundaries.	49
3.14. Schematic depiction of composition space for a two fuel stream system. Left: Unit triangle spanned by two mixture fractions. Right: Transformation according to Equation 3.38 to a unit square.	50
4.1. Van Krevelen diagram depicting location of several fuels. Red squares illustrate the position of the fuels considered in this work. Graphic is adapted from [187].	54
4.2. Schematic drawing of the conversion process of a solid fuel particle. Black line corresponds to the normalized particle mass loss. Red line describes the imposed temperature profile. The grey area indicates the pyrolysis process, which can also take place in inert conditions. The Blue area illustrates the slow char reaction, which occurs only in oxidizing atmospheres.	56
4.3. Rate controlling regimes for char reactions adapted from [223]. Black line illustrates the influence of the temperature on the char reaction rate.	58
4.4. Basic conversion steps of the CPD model. Graphic is adapted from [60].	61
4.5. Van Krevelen diagram depicting the location of CRECK-S reference species. Additionally, the locations of the coals employed in this thesis are shown in red.	65
4.6. Coal pyrolysis mechanism of CRECK-S model. Graphic is adapted from [226].	66
4.7. Workflow of the pyrolysis pre-processor. Graphic is adapted from [247].	69
4.8. Species release from a single bituminous coal particle which is subjected to a heating rate of 100 K/ms. Dashed lines indicate the dynamic release predicted by the CRECK-S model. Solid lines denote the temporally averaged release.	71
4.9. Species composition from single bituminous coal particles subjected to different heating rates ranging from 10 K/ms to 100 K/ms.	71
4.10. Interaction of parallel radiation with a solid particle. Adapted from Gronanz [82].	74
5.1. Schematic drawing of the cell coordinates in FASTEST. Left: Control volume indicating both the global coordinate system (x_i) and the local cell-oriented coordinate system (ξ_i). Right: Exemplary two-dimensional depiction of the relation with neighboring cell centers (upper case letters) around the control volume P . Lower case letters indicate the faces connecting the control volumes with their respective normal vectors n_i . This graphic is partly adapted from [118; 171].	77
5.2. Schematic depiction of the Euler source term without distribution (left) and with Gaussian distribution (right).	86
5.3. Schematic depiction of the test case. Red: inlet. Blue: outlet.	87
5.4. Results for the transported scalars for FGM particle coupling verification test case. Left: Devolatilization of a single particle. Right: Char conversion of a single particle. From top to bottom: The four transported scalars are the: first and second mixture fractions, the reaction progress variable and enthalpy, which are used to access the table. Additionally, the temperature is shown. For the first and second mixture fractions, the analytic reference solution is depicted in black.	89

List of Figures

5.5.	Verification of the solid fuel reaction kinetics for devolatilization in FASTEST (lines) against solution obtained with OpenSmoke (dots). Top left: Normalized mass loss over time. Top right: Mass fraction of the initial species. Bottom left: Formation of the light gas metaplast. Bottom right: Formation of the tar metaplast. Additionally, all plots include the temperature history in red.	91
5.6.	Verification of the solid fuel reaction kinetics for the char oxidation in FASTEST (lines) against solution obtained with OpenSmoke (dots). Top left: Normalized mass loss over time. Top right: Mass fraction of the initial species. Bottom left: Formation of the light gas metaplast.	92
5.7.	Flow chart of the overall solution procedure employed in this work.	95
6.1.	Depiction of different scales involved in PCC is exemplified by the three configurations investigated in this work. Background: Pilot-scale combustion chamber. Middle: Optical accessible laboratory-scale combustion chamber. Foreground: Combustion of particle groups in a flat flame burner.	97
6.2.	Schematic cross-section of the laminar flow reactor.	98
6.3.	(a): Schematic of the mixing plane spanned by the two fuels and the oxidizer. The red area indicates the flammability range. (b): Section of the chemistry table at $Z_{FF} = 0.038$. The blue/green/red color scheme depicts the source term of the progress variable, whereas the gray-scale on the slice at $Z_{Vol.} = 0$ indicates the enthalpy distribution. White iso-lines depict the threedimensional extent of the source term.	99
6.4.	Isocontours of instantaneous OH mass fraction for increasing PNDs at ignition height together with particle temperature. (a) $PND_{VL} = 0.15 \text{ 1/mm}^3$, (b) $PND_L = 0.77 \text{ 1/mm}^3$, (c) $PND_M = 1.14 \text{ 1/mm}^3$ and (d) $PND_H = 2.06 \text{ 1/mm}^3$	100
6.5.	Comparison of ignition delay time $\tau_{ign.}$ between experiments (black dots with errorbars) and numerical simulation (blue line) for different PNDs at ignition height.	101
6.6.	Comparison of flame structures conditioned at similar ignition point for PND_{VL} to PND_H from top to bottom. The experimental results have been chosen to have the same PNDs inside the reaction zone as the corresponding simulation.	102
6.7.	Comparison of flame volume (top) and the ratio of the volume of non-flammability to the volume of the flame (bottom) between simulation (blue line) and experiments (black dots with errorbars) for different PNDs inside the flame. For very low particle densities, this ratio is not defined due to single particle combustion (grey area).	103
6.8.	Instantaneous gas field temperature with particles colored in their respective temperature. A black isoline at $Y_{OH} = 0.004$ indicates the flame position. Additionally, the four representative red dotted isolines of $Z_{Vol.}$ indicate regions of volatile matter.	104
6.9.	Averaged particle histories for different particle densities over time. a): Averaged particle temperature (solid lines) and gas-phase temperature (dashed lines). b): Averaged particle volatile content. For each case, ignition time is marked with a vertical dotted line.	105
6.10.	Comparison of ignition delay time $\tau_{ign.}$ between experiments (black dots with errorbars) and simulations (solid line and dashed lines) for different particle injection rates. Solid lines denote model combinations with a temperature-dependent particle heat capacity. Dashed lines denote models with a constant particle heat capacity of $c_{p,prt} = 1200 \text{ J/(kg K)}$. Colors indicate the devolatilization model.	106

6.11. Schematic drawing of the combustion chamber. Left: Full chamber together with a closer view of the burner head. Right: Computational domain and numerical grid of the burner together with a closer view of the burner head.	108
6.12. Particle size distribution of Rhenish lignite measured by laser diffraction [108].	109
6.13. Comparison of single-phase non-reactive experimental (dots) and numerical (lines) mean velocity data. Left: axial velocity component. Middle: radial velocity component. Right: tangential velocity component. Upper three rows: velocity inside quarl. Upper three rows: velocity below quarl.	111
6.14. Mean contour of single-phase reactive operating points. Left: Equivalence ratio with an isoline of $\phi = 1$. Right: Streamline of velocity together with contour plot of temperature in the background.	113
6.15. Results of OH at the central plain. Left: OH mass fraction of the LES simulation. Right: Experimentally obtained mean OH fluorescence signal.	113
6.16. Comparison of single-phase reactive experimental (dots) and numerical (lines) mean velocity data. Left: axial velocity component. Middle: radial velocity component. Right: tangential velocity component. Upper three rows: velocity inside quarl. Upper three rows: velocity below quarl.	114
6.17. Mean images of Euler fields at the y - z plane with an instantaneous snapshot of the particle phase between $x = 0$ and $x = 1$ mm are depicted for both operating points. Top row: particle temperature and gas-phase temperature on the left side and velocity in z direction and progress variable source term on the right side. Bottom row: particle volatile content and first mixture fraction on the left side, and particle char content and second mixture fraction on the right side.	117
6.18. Left: Averaged O_2 massfraction inside the combustion chamber. Right: Averaged particle temperatures T_{prt} , averaged normalized massfraction of volatile content $Y_{Vol.}/Y_{Vol.,0}$, averaged normalized massfraction of char content $Y_{Char.}/Y_{Char.,0}$ over the axial position z . Dashed lines represent TPR7 and solid lines represent TPR20.	118
6.19. Comparison of two-phase reactive experimental (dots) and numerical (lines) mean velocity data. Left: axial velocity component. Middle: radial velocity component. Right: tangential velocity component. Upper three rows: velocity inside quarl. Upper three rows: velocity below quarl.	119
6.20. Particle histories divided into particle size classes as defined in Table 6.4 for the particle temperature, volatile content and char content, respectively.	120
6.21. Schematic drawing of the combustion chamber. Left: Cross section of the combustion chamber. Right: Computational domain and the numerical grid of the burner together with a closer view of the burner head.	123
6.22. Averaged results of Eulerian-fields in the r - x plane: (a) AIR, b) OXY21 and c) OXY25). Left: axial velocity. Right: gas temperature. As a reference, the locations of experimental measurements are depicted for different axial distances below the dump plane for all operating points. The regions IRZ and ERZ indicate the internal and external recirculation zones.	126
6.23. Mean images of Eulerian-fields in the r - x plane together with instantaneous distribution of particles scaled by diameter for the different atmospheres: (a) AIR, b) OXY21 and c) OXY25). Left: Mixture fraction for the volatiles and particles colored by volatile content. Right: Mixture fraction for the char reaction products and particles colored by char content.	128

List of Figures

6.24. Comparison of experimental (symbols with error bars) and simulation (lines) mean axial velocity (left) and mean tangential velocity (right) profiles below the quarl for different axial heights.	129
6.25. Comparison of particle temperatures between experiments (symbols with error bars) and simulations (lines) for different axial distances below the dump plane. .	130
6.26. Comparison of of CO ₂ and H ₂ O molar fraction between experiments (symbols) and simulations (lines) for different axial distances below the dump plane.	131
6.27. Representative instantaneous scatterplots of particles in the combustion chamber. Left: Particle velocity over gas velocity with the temperature of individual particles indicated by color. Right: Particle temperature over gas temperature with burnout state indicated by color. Top row: AIR. Middle row: OXY21. Bottom row: OXY25.	133
6.28. Particles scaled with the diameter and colored based on their temperature (left-hand side of each plot) and averaged oxygen mass fraction (right-hand side of each plot) for AIR (a)), OXY21 (b)) and OXY25 (c)).	135
6.29. Particle histories over time for particle size classes as defined in Table 6.8. Left: Particle temperature. Center: Volatile content. Right: Char content. Solid lines represent the mean values and shaded areas represent the standard deviation. . .	136
6.30. Particle burnout for particle size classes as defined in Table 6.8 at the outlet of the simulation domain (700 mm below the dump plane).	137
6.31. Averaged (top) and instantaneous (bottom) gas-phase results for the CRECK-S simulation on the fine grid. Top to bottom: a) axial velocity and recirculation zones indicated by circles, b) temperature and measurement locations, c) volatile mixture fraction, and d) char off-gas mixture fraction.	142
6.32. Comparison of mean axial velocity (left) and mean tangential velocity (right) profiles determined by experiment (symbols) and simulation (lines) below the quarl for different axial heights. The vertical dashed line indicates the location of the center line ($r = 0$ mm).	144
6.33. Comparison of mean axial velocity RMS profiles (left) and mean tangential velocity RMS profiles (right) profiles determined experimentally (symbols) and by simulation (lines) below the quarl for different axial heights. The vertical dashed line indicates the location of the center line ($r = 0$ mm).	145
6.34. Comparison of particle temperatures found in experiments (symbols with error bars) and simulations (lines) for different axial distances below the dump plane. .	146
6.35. Comparison of species molar fraction of O ₂ and H ₂ O found in experiments (symbols only H ₂ O) and simulations (lines) for different axial distances below the dump plane.	147
6.36. PDFs of particle heating rates (left), volatile release rates (middle), and char release rates (right) inside the full burner (solid lines) and the quarl region (dashed lines).	148
6.37. Scatter plot of the particle phase: volatile yield vs. particle temperature with colors representing particle residence time. Left: CRECK-S. Middle: C2SM-BS. Right: SFOR-BS.	149
6.38. Scatter plot of the particle phase: char reaction rate vs. inverse temperature colored by the oxygen fraction at the particle position. Left: CRECK-S. Middle: C2SM-BS. Right: SFOR-BS.	149

6.39.	Scatter plot for the particle char fractions vs. particle burnout for the CRECK-S simulation. Left: CHAR-C. Center: fast-reacting CHAR-H. Right: slow-reacting CHAR-G. Lines illustrate the averaged fraction for the particle groups in Table 6.14. From light grey representing class 1 to black representing class 4.	150
6.40.	Particle histories with respect to particle temperature (left), particle volatile yield (center) and particle char yield (right). Each row of the figure corresponds to one particle class specified in Table 6.14. The lines indicate the mean values. The variation represented by one standard deviation is depicted by the gray shading (for a better overview, the variation is only shown for the CRECK-S model if there is an overlap exist).	151
6.41.	Surrounding conditions the particles are exposed to on their path with regard to gas phase temperature and O_2 mass fraction. Each row of the figure corresponds to one particle class specified in Table 6.14. The lines indicate the mean values. The variation represented by one standard deviation is depicted by the gray shading (for a better overview, this is only shown for CRECK-S).	152
6.42.	Bar plot of particle properties at the outlet of the domain. The classes are specified in Table 6.14. Top: particle burnout Bo . Bottom: total residence time τ_{prt} . The bars indicate the standard deviation for each class.	153
6.43.	Instantaneous scatter plots from Eulerian data. Top: gas temperature vs. mixture fraction sum Z_1 colored by mixture fraction ratio Z_2 . Middle: oxygen mass fraction Y_{O_2} vs. mixture fraction sum Z_1 colored by mixture fraction ratio Z_2 . Bottom: Y_{CO} vs. mixture fraction sum Z_1 colored by mixture fraction ratio Z_2	154
A.1.	Grid dependency study for different particle number densities.	186
B.1.	Comparison of single-phase non-reactive experimental (dots) and numerical (lines) RMS velocity data. Left: axial velocity component. Middle: radial velocity component. Right: tangential velocity component. Upper three rows: velocity inside quarl. Upper three rows: velocity below quarl.	188
B.2.	Comparison of single-phase reactive experimental (dots) and numerical (lines) RMS velocity data. Left: axial velocity component. Middle: radial velocity component. Right: tangential velocity component. Upper three rows: velocity inside quarl. Upper three rows: velocity below quarl.	189
B.3.	Comparison of two-phase reactive experimental (dots) and numerical (lines) RMS velocity data. Left: axial velocity component. Middle: radial velocity component. Right: tangential velocity component. Upper three rows: velocity inside quarl. Upper three rows: velocity below quarl.	190
C.1.	Comparison of the mean axial velocity (left) and the mean tangential velocity (right) with experimental data. Solid lines represent the fine grid results, whereas dashed lines indicate the coarse grid results. Different axial locations with increasing distance from the burner port from top to bottom. The vertical dashed line indicates the centerline of the burner.	191
D.1.	Comparison of the mean gas-phase temperature (left) and the mean particle temperature (right) over radius with (solid) and without (dashed) thermal radiation. Different axial locations with increasing distance from the burner port from top to bottom.	192

List of Tables

3.1.	Literature overview of flamlet models applied to PCC.	38
4.1.	Coal properties of employed coals determined at <i>Department of Energy Plant Technology, Ruhr University Bochum</i> and <i>Institute of Heat and Mass Transfer, RWTH Aachen</i> , respectively. 1: as received, 2: dry and ash free basis. Left: Columbian coal Norte (C1). Right: Rhenish lignite (RL)	55
4.2.	Baum-Street model parameters of Rhenish lignite.	64
4.3.	Characterization of the employed coals in the CRECK-S model.	65
4.4.	Kinetic mechanism of COAL-1 pyrolysis [226] and char annealing in the CRECK-S model [137].	66
4.5.	Oxidation mechanism of char oxidation in the CRECK-S model [137].	67
4.6.	Composition of the volatile yield for the employed coals.	72
4.7.	Stoichiometric coefficients of the global char reaction for a particle oxidized at 1400 K in an atmosphere containing 27 Vol.-% O ₂ and 73 Vol.-% CO ₂	72
4.8.	Values for parameters a_{HG} and g_{HG} in the modified Henyey-Greenstein phase function [82].	75
5.1.	Butcher array of the three stage second-order low-storage Runge-Kutta scheme of FASTEST.	81
5.2.	Butcher array of fifth-order and fourth-order Runge-Kutta scheme [22].	84
5.3.	Butcher array of a second-order predictor corrector method.	85
5.4.	Boundary conditions for verification test cases.	88
5.5.	Characterization of the coals for the code-to-code comparison of the CRECK-S model.	91
6.1.	Operating conditions for the LFR.	98
6.2.	Parameters for the Kobayashi C2SM model.	99
6.3.	Parameters of the four operating points. I: Primary flow. II: Secondary flow. III: Tertiary flow.	109
6.4.	Division of particles into different classes according to their size for post-processing.	121
6.5.	Parameters of the three operating conditions. I: Primary stream. II: Secondary stream. III: Tertiary stream. IV: Staging stream.	124
6.6.	Devolatilization kinetic parameters for the SFOR model of Rhenish lignite.	124
6.7.	Global errors between simulation and experiment for gas phase velocities, particle temperature and species concentrations	132
6.8.	Particle classified into different size classes for particle histories.	134
6.9.	Summary of the operating condition with a 27 vol.-% O ₂ and 73 vol.-% CO ₂ atmosphere [273].	139
6.10.	Coefficients of the simplified devolatilization models for Rhenish Lignite.	140
6.11.	Summary of the simulation parameters for all simulation.	140
6.12.	Composition of the overall volatile yield for a lignite particle under a heating rate of 80 K/ms.	141

6.13. Stoichiometric coefficients of the global char reaction for a particle oxidized at
1400 K in an atmosphere containing 27 Vol.-% O₂ and 73 Vol.-% CO₂. 141

6.14. Particle classified into different size classes for particle histories. 150

A. Grid Sensitivity of the Uniform Source Term Distribution

To analyze the effect of the cell size, simulations using different grids have been performed for different particle number densities (PNDs). Figure A.1 depicts the influence of the grid size on predicting the ignition delay. All three grids are locally refined towards the middle of the simulation domain resulting in $\Delta x \approx \bar{D}_p$, $\Delta x \approx 1.25\bar{D}_p$ and $\Delta x \approx 1.5\bar{D}_p$. Overall, a small influence of the grid on predicting the ignition delay is visible (around 10% difference). Two reasons can explain this: First, the gas phase properties at the particle position are obtained by trilinear interpolation. This interpolation is affected by larger grid sizes, especially when large gradients around the particle occur, which is the case for higher PNDs. In the case of a reactive gas-phase, another issue arises when using coarser grids: The resolution of the progress variable source term. If the progress variable source term is not fully resolved, the history of the progress variable is influenced. In the case of tabulated chemistry the progress variable is used to read the thermochemical state from the flamelet table. This also includes the OH mass fraction, which is used to determine the ignition delay time.

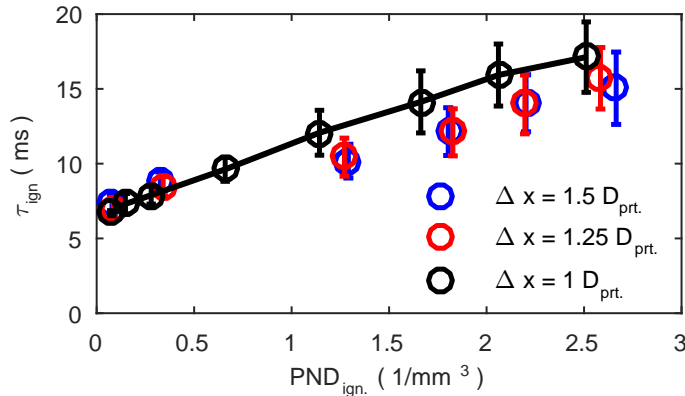


Figure A.1.: Grid dependency study for different particle number densities.

B. RMS Statistics of Laboratory-Scale Burner

Figures B.1, B.2, and B.3 depict the RMS values of the simulations and the experimental data for the three investigated operating conditions. For the non-reactive operating point, illustrated in Figure B.1, similar trends can be observed for the simulation and the experiment. RMS values are significantly lower in the domain center for regions inside the quarl, whereas a rapid increase is visible towards the quarl walls. This holds for all three velocity components. Below the quarl, the domain center exhibits the largest RMS values, which are smaller than those observed inside the quarl. For larger radii, the RMS velocities decrease for all three components. Overall, these trends are predicted very well by the simulation.

For the single-phase reacting operating point, depicted in Figure B.2, similar shapes of the RMS velocities compared to the no reactive case are apparent. However, generally, the peaks are slightly higher for the reactive case. Comparing simulations and experiments, especially at the first height inside the quarl, the RMS values are slightly overpredicted. Further downstream in the quarl, the agreement between the simulation and the experiments is favorable. Below the quarl, the simulation matches the experimental data well.

Figure B.3 illustrates the RMS velocity data for the two-phase reactive case. The out-of-plane component (i.e., tangential velocity) was not available from measurements. Also, measurements inside the diffusor were only possible for the 7kW operating point. Overall, an excellent agreement is found between the simulation and experiment for the RMS values in the quarl region. It is also interesting to note that the RMS values between the simulations with the two different thermal loads are very similar inside the quarl. However, below the quarl, the RMS velocities of the 7kW operating point are slightly higher for the axial component, which is matched by the simulation. For the RMS of the radial component below the quarl, the difference between the two operating conditions vanishes. Also, below the quarl, the simulation can predict the RMS velocity component correctly.

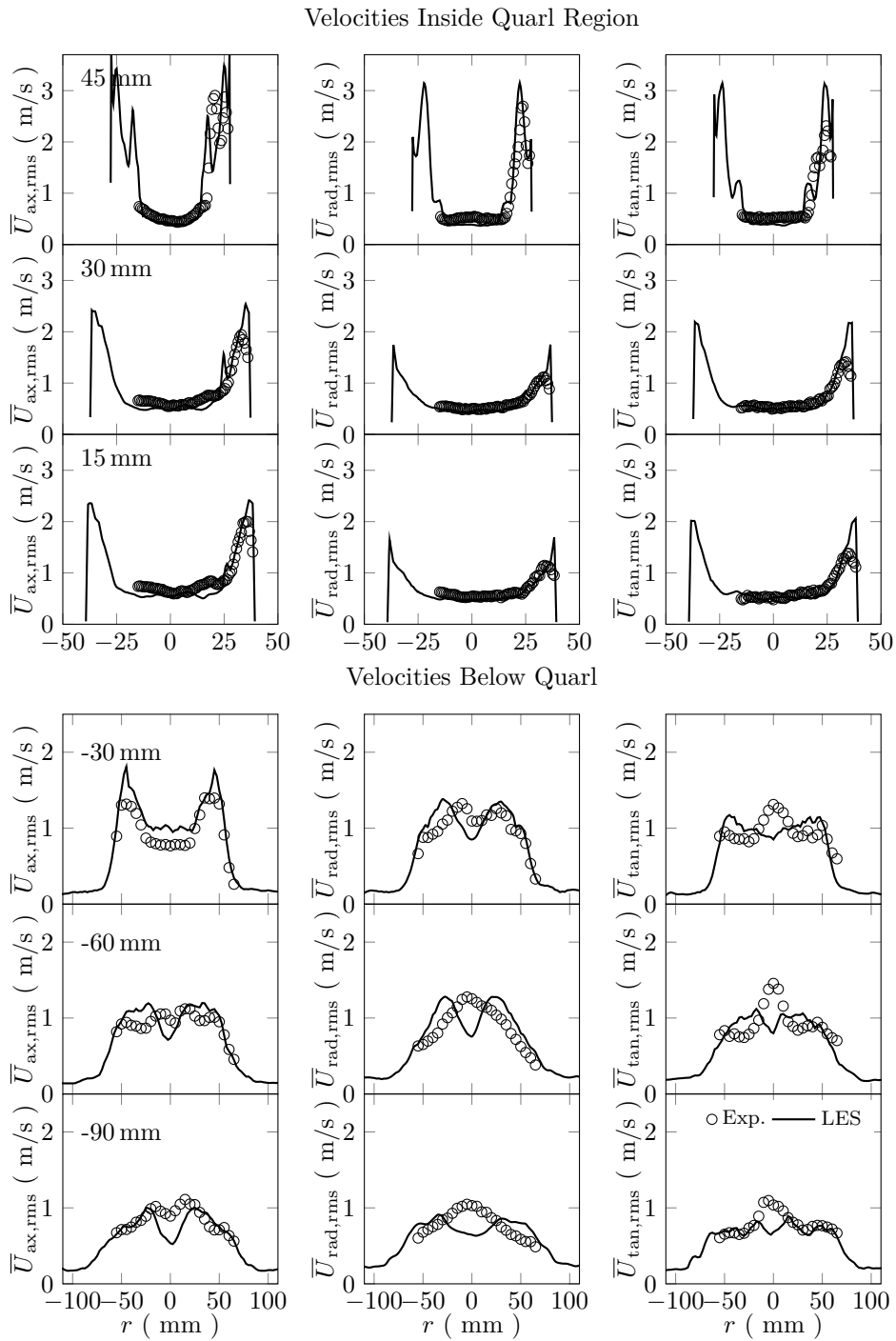


Figure B.1.: Comparison of single-phase non-reactive experimental (dots) and numerical (lines) RMS velocity data. Left: axial velocity component. Middle: radial velocity component. Right: tangential velocity component. Upper three rows: velocity inside quarl. Upper three rows: velocity below quarl.

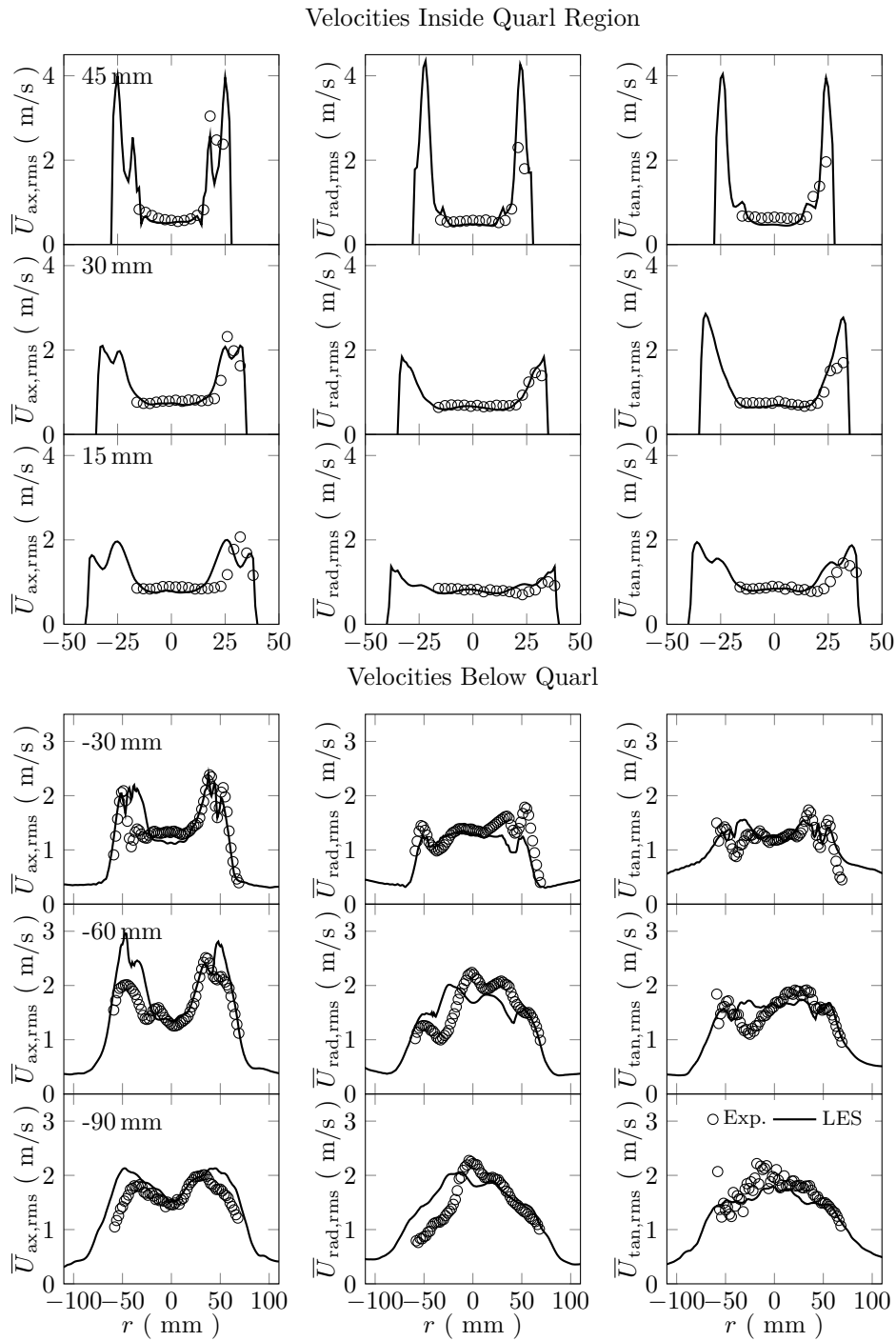


Figure B.2.: Comparison of single-phase reactive experimental (dots) and numerical (lines) RMS velocity data. Left: axial velocity component. Middle: radial velocity component. Right: tangential velocity component. Upper three rows: velocity inside quarl. Upper three rows: velocity below quarl.

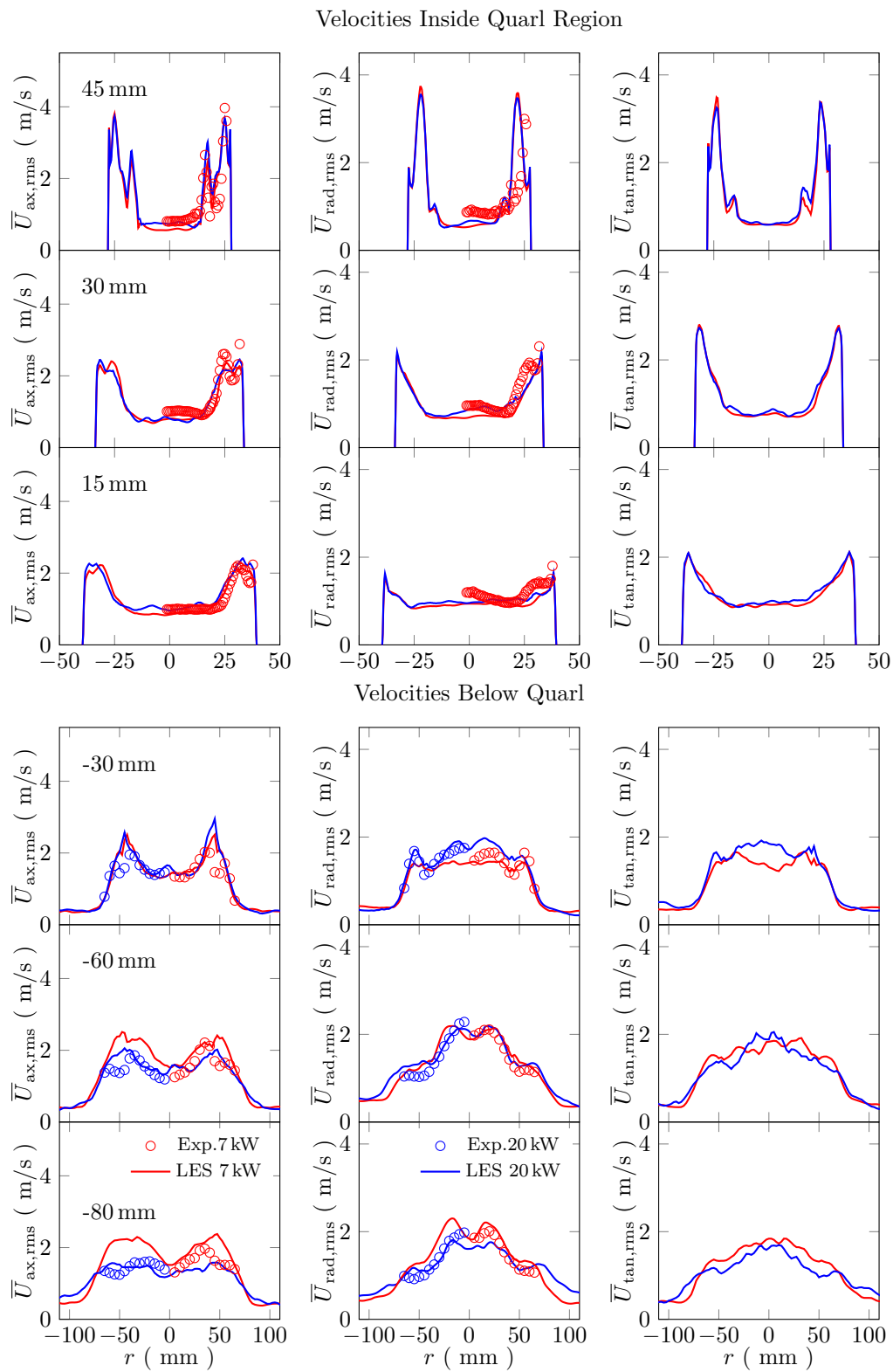


Figure B.3.: Comparison of two-phase reactive experimental (dots) and numerical (lines) RMS velocity data. Left: axial velocity component. Middle: radial velocity component. Right: tangential velocity component. Upper three rows: velocity inside quarl. Upper three rows: velocity below quarl.

C. Influence of the Grid Resolution

Figure C.1 illustrates the comparison of the simulation results for the fine grid and the coarse grid, respectively. Both simulations show similar trends, with the fine grid matching the measured data slightly better with a few exceptions. Overall, the velocities on the coarse grid are slightly higher. This results in an overprediction of the velocities, especially in the recirculation zone.

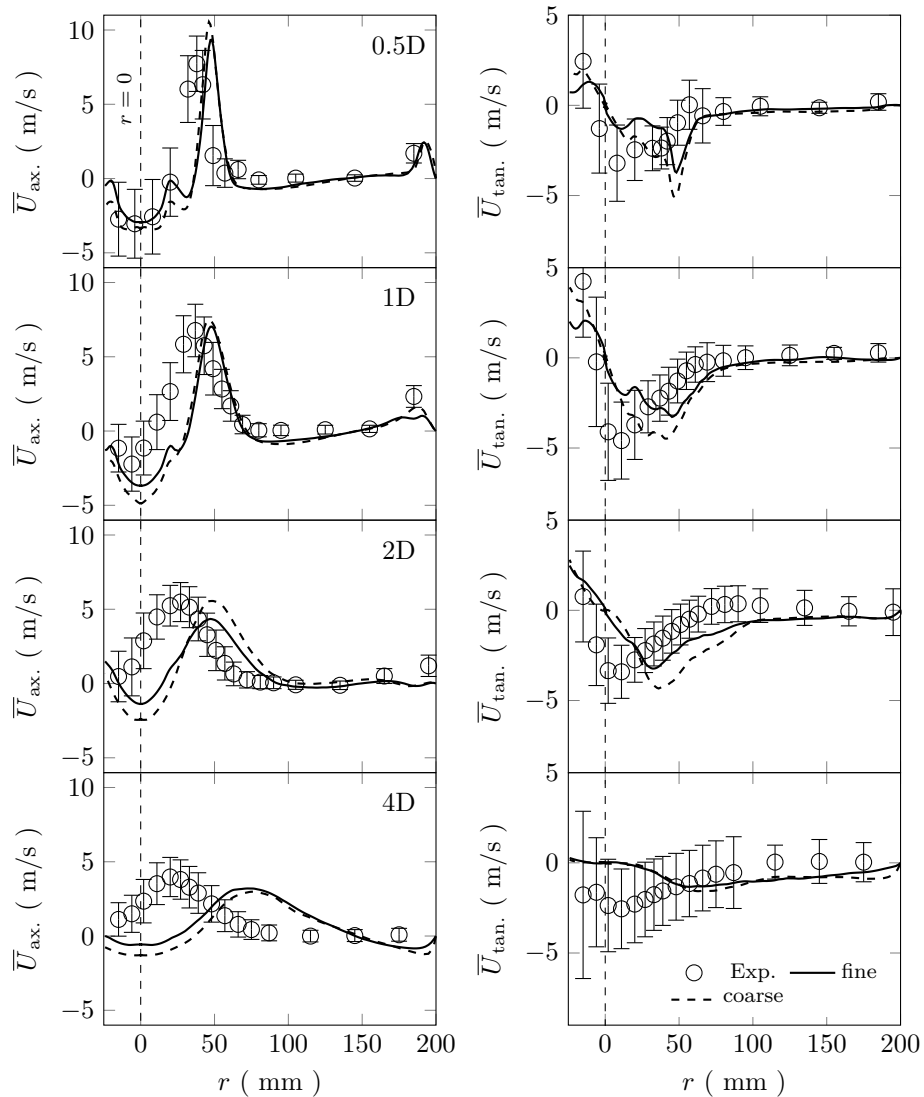


Figure C.1.: Comparison of the mean axial velocity (left) and the mean tangential velocity (right) with experimental data. Solid lines represent the fine grid results, whereas dashed lines indicate the coarse grid results. Different axial locations with increasing distance from the burner port from top to bottom. The vertical dashed line indicates the centerline of the burner.

D. Influence of Radiation

Figure D.1 illustrates the comparison of simulations neglecting and including thermal radiation. A strong heat loss from thermal radiation is apparent, particularly in the downstream regions, where deviation of up to 200 K occur.

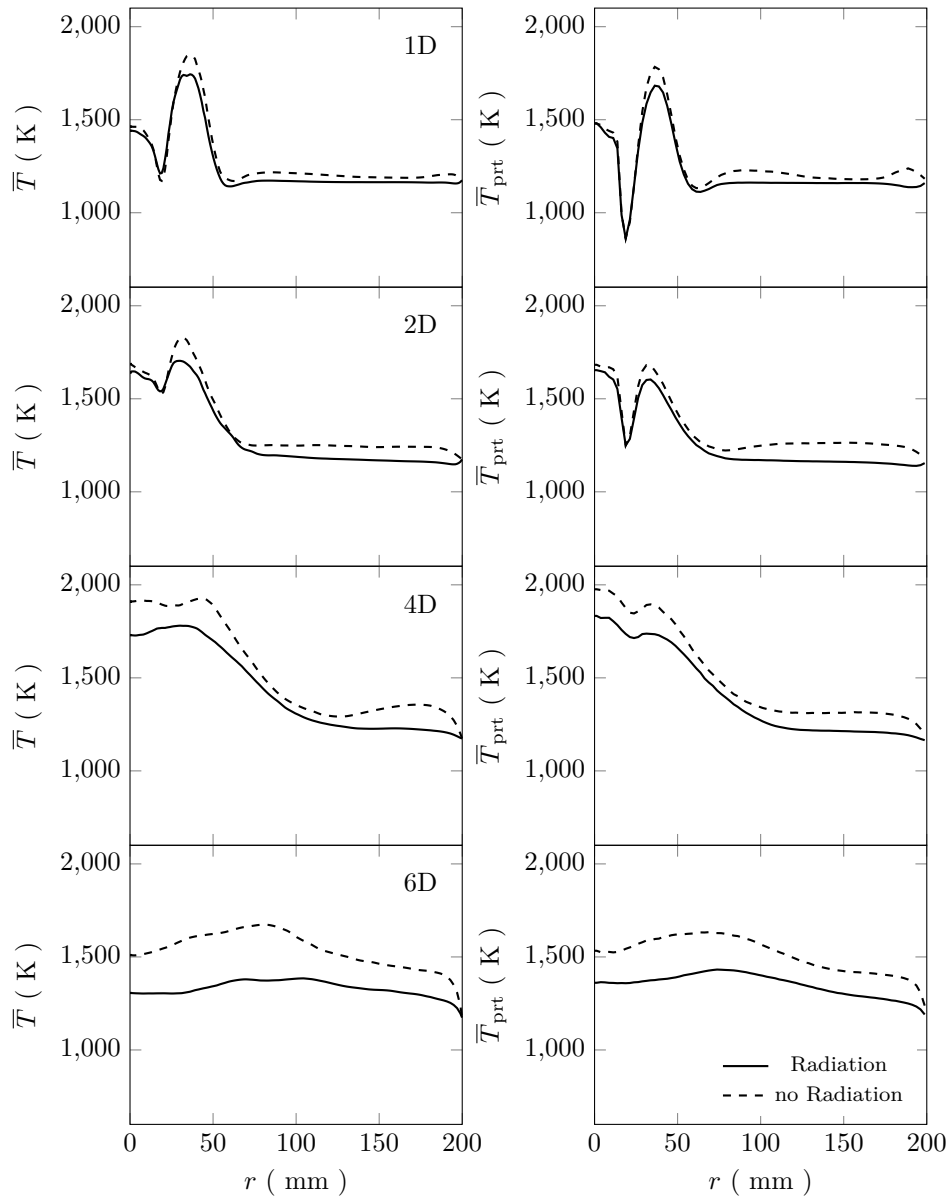


Figure D.1.: Comparison of the mean gas-phase temperature (left) and the mean particle temperature (right) over radius with (solid) and without (dashed) thermal radiation. Different axial locations with increasing distance from the burner port from top to bottom.